Studies of Runaway Electrons during disruptions in the TEXTOR tokamak

Inaugural-dissertation

for the attainment of the title of doctor
in the Faculty of Mathematics and Natural Sciences
at the Heinrich-Heine-Universität Düsseldorf

presented by

Kunaree Wongrach
from Nan (Thailand)

Düsseldorf, September 2015

from the Institute for Laser- and Plasma physics
at the Heinrich-Heine-Universität Düsseldorf

Published by permission of the
Faculty of Mathematics and Natural Sciences at
Heinrich-Heine-Universität Düsseldorf

Supervisor: Prof. Dr. O. Willi
Co-Supervisor: Prof. Dr. U. Samm

Date of the oral examination: 07/12/2015

Abstract

Disruptions are a major threat for fusion devices. In this thesis particular emphasis is put on the runaway electrons generated during disruptions. For this reason, disruptions are initiated by a massive injection of argon gas performed by a special valve; this scenario is rather reproducible and provides a substantial fraction of runaway electrons with energies in the range from a few MeV up to 30 MeV. The lower energy runaways are detected by a scintillator probe. The high energy electrons ($W_{re} \geq 25$ MeV) emit synchrotron radiation which is measured by a fast IR camera.

Despite similar initial conditions, different cases of temporal evolution of runaway electrons are observed. a) There are disruptions, in which no runaway burst in SXR or Mirnov spikes are seen. Surprisingly, in some discharges of this case the subtraction of two consecutive IR images shows stripe structures at the beam edge. These stripes are a characteristic feature of the laminar zone. b) There are spiky disruptions by which the MHD mode is excited. One observes often a small channel connecting the runaway beam to the scintillator probe which is created during the spiky phase when the runaway beam moves close to the probe. c) In other cases of disruptions a significant number or runaway electrons is present after the plateau termination, although the plasma current drops to a few tens of kA.

The radius of the runaway beam of $r_{beam} = 30$ cm amounts to about half of the predisruptive plasma radius. The number of high energy runaway electrons are calculated to be 3.4×10^{16} corresponding to 47 % of the total runaway number. The error in determining the number of the high energy runaways is mainly caused by the estimation of the perpendicular component of the velocity vector of the runaways.

The last experimental campaigns were devoted to the investigations of different techniques to mitigate the effect of runaways or to suppress their generation during disruptions. Means for the mitigation were the use of a) a second fast gas injection or the application of b) magnetic perturbations initiated by the DED 3/1 or 6/2 modes. It was found that the runaway electrons created during a disruption are much more robust against those perturbations than the runaways created during a normal low density discharge. A substantial reduction of REs was achieved only

by gas injection immediately after the disruption is triggered or the start of the ergodization prior to the disruption.

Zusammenfassung

Disruptionen stellen eine große Gefahr für Fusionanlagen dar. In dieser Arbeit werden Runaway-Elektronen untersucht, die in Disruptionen erzeugt wurden. Die Disruptionen werden durch massive Gasinjektion von Argon durch ein spezielles Ventil induziert; das Szenario ist recht reproduzierbar und gewährt eine beträchtliche Anzahl von Runaway-Elektronen im Energiebereich von wenigen MeV bis zu 30 MeV. Der niederenergetischere Anteil der Runaways wird durch eine Szintillator-Sonde erfasst und der höherenergetische Teil ($W_{re} \geq 25$ MeV) über die emittierte Synchrotron Strahlung durch eine schnelle IR-Kamera.

Trotz ähnlicher Anfangsbedingungen zeigt die zeitliche Runaway-Entwicklung deutliche Unterschiede: a) Es gibt ruhige Disruptionen, bei denen in einer Plateau-Phase keine MHD Aktivitäten (z.B. im SXR- oder Mirnov-Signal) beobachtet werden. Überraschender Weise zeigen einige dieser Disruptionen ein Streifenmuster im IR-Bild, wenn man je zwei aufeinander folgende Bilder voneinander subtrahiert. Diese Streifen sind charakteristisch für eine laminare Zone. b) Es gibt Disruptionen mit ausgeprägten MHD Aktivitäten in der Plateau-Phase. Hier beobachtet man häufig dünne Kanäle, die während der MHD-Phase die Runaway-Region mit der Szintillator-Sonde verbindet. c) In wiederum anderen Fällen wird noch eine beträchtliche Anzahl von Runaway-Elektronen beobachtet, obwohl der Plasmastrom nur noch wenige kA beträgt.

Der Radius der Runaway-Zone beträgt etwa 30 cm, etwa die Hälfte des Plasma-Radius vor der Disruption. Die Zahl der hochenergetischen Runaway-Elektronen entspricht etwa 3.4×10^{16}, was 47% der gesamten Zahl der Runaways entspricht. Die wesentliche Unsicherheit bei dieser Abschätzung rührt von der Unsicherheit bei der Abschätzung der senkrechten Komponente des Runaway Geschwindigkeitsvektors.

Der letzte Teil der Arbeit befasst mit Möglichkeiten, die bei der Disruption erzeugten Runaways unschädlich zu machen oder die Erzeugung zu verhindern. Mittel zur Runaway-Unterdrückung sind a) ein zweites Ventil mit massiver Gasinjektion oder b) der Einsatz von einer Magnetfeld-Ergodisierung durch den DED in der 3/1- oder 6/2-Mode. Es wurde gefunden, dass die Runaway-Elektronen, die bei Disruptionen

erzeugt werden, sich wesentlich robuster verhalten als solche, in normalen Niedrig-Dichte-Entladungen erzeugt werden. Nur bei a) sehr hoher Gaszufuhr unmittelbar nach dem Disruptionstrigger oder bei b) Ergodisierung schon vor Einsatz des Injektionstriggers konnte die Runaway-Erzeugung deutlich reduziert werden.

Acknowledgements

I would like to express my sincere gratitude to all those who gave me the possibility to complete this dissertation.

Firstly, I am grateful to Prof. Dr. Oswald Willi, my supervisor, for offering me the opportunity to work in this special and interesting field of research and for his excellent support, guidance and encouragement.

I would like to thank Prof. Dr. Ulrich Samm for his support as my mentor and my co-supervisor.

My deepest thanks go to Dr. Karl Heinz Finken. I have learned a tremendous amount from Dr. Finken. I greatly appreciate his constant encouragement to engage in fruitful conversations, wise suggestion, and all kind supports during my research. It was a great pleasure work with him.

I would like to express my sincere appreciation to Dr. Sadrilla Abdullaev who provided me essential simulations and gave me enormous valuable discussions and supports, particularly in the theoretical part of the work.

My research would not have been possible without support from the TEXTOR team. A special thanks goes to Mr. Albert Hiller and Mr. Dirk Nicolai for their technical supports and for providing me with an excellent working atmosphere at the Institute of Energy and Climate Research of the research center Jülich.

I am indebted to my colleagues, especially Dr. Michael Forster, Nadine Hartmann, Dr. Michael Rack, Dr. Hans Rudolf Koslowski, Dr. Long Zeng and Dr. Oliver Scmitz. I have greatly benefited from all interactions with them. I appreciate their excellent assistance, discussions and hands-on help.

I extend heartfelt thanks to all members of the Institute for Laser- and Plasmaphysics of the Heinrich-Heine University Düsseldorf for making my years in Germany enjoyable. My deepest thanks go to Anna-Marie Schrör for her care and her great help in many aspects.

It is a pleasure to express my gratitude wholeheartedly to my parents and my sister, who supported me to go aboard and complete this PhD study. My deepest appreciation is expressed to them for their love, care, understanding and inspiration.

Finally, I would acknowledge the Thai government scholarship, who supported the opportunity to have a wonderful research experience for all these years. This work was also supported by a Jülich R&D contract, the Trilateral Euregio Cluster (TEC), and the DFG program GRK 1203.

Contents

1 Introduction

One of the biggest challenges in the 21^{st} century is the supply of energy. Global energy demand is estimated to rise by 37% in 25 years [1]. However, the fossil fuel-based energy sources such as coal, natural gas and oil, which are major sources of energy we use today, are limited. Besides shortages of fossil fuels, growing concerns about the environment, climate change and safety over the past few decades play an important role in the development of alternative energy resources.

Renewable energy such as wind, solar and biomass energy fulfills the requirement of sustainability and energy security. Its sources are abundant and it produces only little or no greenhouse gas and waste. However, it has low reliability of supply since it depends on the weather and lacks of production capacity. Another source of energy which is widely used is nuclear power. It is reliable and contributes neither to carbon emission nor air pollution. Nevertheless, the nuclear accidents at Chernobyl and Fukushima Daiichi have drawn interest from people. Radioactive particles were released into the environment and spread over a large area. Many countries, especially Germany, began a nuclear power phase-out due to a safety concern. By 2040, almost 200 reactors will shut down [1].

One of promising candidates for long-term energy production is nuclear fusion energy. Nuclear fusion is a thermonuclear reaction, in which nuclei are fused to form a heavier nuclei. The fusion of the nuclei of atoms lighter than iron generally releases energy. The most feasible fusion reaction initiating on earth is an equal mixture of two isotopes of hydrogen: deuterium and tritium. Deuterium is plentiful since it can be easily extracted from natural water and tritium can be bred from lithium which is found as an ore and in brine deposits. The primary fuels (D and Li) and the

direct end product (^{4}He) are not radioactive. Sources of radioactivity are tritium and the activation of reactor structures by neutrons. Tritium, however, is consumed directly in fusion reactions. In addition to the abundance of fusion fuels and low level of nuclear wastes, fusion reactions do not cause significant ecological and geophysical problems. There is no production of combustion gases, which contribute to the greenhouse effect and the destruction of the ozone layer.

The fusion reaction takes place when two nuclei approach sufficiently close that the short-range nuclear attraction force becomes dominate. In order to overcome the long-range Coulomb repulsion force, the temperatures of the order of 10 keV to 100 keV corresponding to temperatures of 10^8 K to 10^9 K are required. A plasma, a quasi-neutral gas consisting of charge and neutral particles, has to be confined sufficiently long to produce significant fusion reactions. Owing to its high temperature, the plasma cannot be contained by the material walls. Magnetic field confinement has been proposed to keep the plasma away from the wall. In order to do so, a helical magnetic field is required. In a tokamak, the best developed magnetic confinement system, a helical field is obtained by a superposition of the toroidal and poloidal fields. The toroidal field is created by superconducting coils surrounding the vessel while the poloidal field is produced by the toroidal current flowing in the plasma itself. The current is induced by a transformer. The magnetising coils are known as the primary windings while the plasma act as a secondary winding of the transformer. The poloidal field is typically 5 to 15 times smaller than the toroidal field.

Tokamak performance is limited by several operational parameters. Crossing a hard limit leads to a disruption, an abrupt termination of the plasma. Greenwald limit gives a maximum line-averaged density above which magnetohydrodynamics (MHD) instabilities arise. Another well-known limit is the plasma current, i.e. the edge safety factor must be greater than 2. A review of physics instabilities and technical problems which lead to disruptions is given in references [2, 3] and references therein. Two main causes which initiate plasma disruptions are strong radiation from a plasma and the MHD instabilities. A disruption is undesirable since magnetic and thermal energies stored in the plasma are lost suddenly. Intense heat fluxes

are deposited on the vessel wall within a few milliseconds and may cause melting or evaporating of plasma facing components (PFCs). Electromagnetic forces induced by halo and eddy currents pose a serious threat to in-vessel components. Additionally, a high loop voltage during a disruption can lead to a generation of runaway electrons (REs). REs can gain energies upto several tens of MeVs. When they are lost and hit the wall, they can penetrate deep into the plasma facing components and cause significant damage. In the Tore Supra [4], the REs generated during a disruption passed through the graphite shielding and hit a leading edge tube located $\sim$ 20 mm outside the last closed flux surface (LCFS) resulting in a cooling water leak. The situation becomes more severe in the next generation tokamak since it will be operated with a higher plasma current and REs with higher energies are expected.

A number of investigations have been performed in the last decades in order to study the evolution of disruptions and to test the disruption mitigating methods. Impurity injection techniques such as pellet injection (PI) and massive gas injection (MGI) have been commonly used in the studies of disruption mitigation in different tokamaks [5]. A pellet injection technique offers a rapidly insert of impurities [6, 7]. On the one hand, the injected pellet penetrates deep into the plasma core and mitigates the disruption effects. The mechanical loads on in-vessel components and the peak halo current are reduced by up to 50 %. On the other hand, the pellet injection often leads to the generation of REs [8, 9]. Although a massive gas injection technique provides a shallower penetration of the impurities in comparison with the pellet injection technique, a massive injection of noble gas, e.g. helium and neon demonstrates a reduction of runaway generation as well as the halo current and the local heat load on the plasma facing components [10, 11, 12, 13, 14]. Fast injections of helium and mixtures of argon with deuterium provides a runaway-free disruption, whereas an argon injection gives rise to runaway generation [15]. Nevertheless, if an amount of injected argon exceeds $\sim$ 140 times the plasma electron content, the disruption becomes runaway free.

The group of the Institute for Laser- and Plasmaphysics of the Heinrich-Heine University Düsseldorf in collaboration with the Institute of Energy and Climate Re-

search of the research center Jülich (Forschungszentrum Jülich GmbH) focuses on the studies of REs at the TEXTOR tokamak. Different probes have been developed and applied to measure REs. Among these probes, the scintillator probe is the most significant probe and has been used throughout the present work. This probe enables the spectrally, temporally and spatially resolved measurements of REs [16, 17]. The detail of the scintillator probe will be given later. In addition, the synchrotron radiation measurement technique which was invented by one of the colleagues was applied [18]. It is a powerful runaway diagnostic which allows the observation of the structure and dynamics of the runaway beam and the determination of the absolute number of high energy runaways. In low density discharges, runaway generation at different plasma densities was investigated [19]. It has been found that the number of REs decreases with increasing densities because the primary runaway generation is suppressed. Furthermore, the runaway diffusion coefficients as a function of the magnetic field were derived from synchrotron radiation [20]. Unfortunately, in our previous studies, the synchrotron measuring system was available only during the experiments on runaways in low density regimes ($n_e \leq 1 \times 10^{19}$ m^{-3}).

During the investigations of REs in other regimes, i.e. turbulent and perturbed magnetic fields and disruptions, only the scintillator probe was used in addition to the standard diagnostics. Runaway transport and loss in the presence of resonant magnetic perturbations (RMPs) during the low density discharges were investigated [21]. The runaway loss is enhanced when the RMP is applied. The loss rates increases nonlinearly with the amplitude of the perturbation fields. In the disruption scenario, evolution of runaways and their energy spectra as well as the runaway bursts were analysed [22]. Runaway measurements by the other probes, enable the investigations of energies of the lost runaways, an energy deposition on materials and radial decay of runways during disruptions [23, 24].

For the present experimental studies, we have installed a new synchrotron radiation measurement system at TEXTOR and used as a main runaway diagnostic. Together with the scintillator probe, REs at both the plasma core and edge can be observed. Additionally, theses diagnostics detect runaway electrons in different energy ranges, i.e. the scintillator probe is sensitive to REs with energies between 3 MeV and

22 MeV, while the synchrotron radiation measurement system measures the synchrotron radiation emitted by REs with energies $\geq$ 25 MeV. The combination of these techniques allows an observation of REs in a wider energy range and gives an additional information of the temporal evolution, structures and transports of the runaways during induced disruptions which was missing in the previous works. Aims of the present work are: (i) to investigate behaviour of REs during TEXTOR disruptions (ii) to provide an understanding of loss mechanisms of REs in different energy ranges. (iii) to study the application of fast injections of different types of gas, namely helium, neon and argon performed by the disruption mitigation valves in runaway mitigation and (iv) to investigate the impact of the RMPs on the runaway confinement.

Since the main interest of this work was the studies of REs and transient events during disruptions, the IR camera which was used to observe synchrotron radiation emitted by high energy REs was temporally calibrated prior to the experiments. During the experimental investigations reported in this thesis, disruptions were initiated by massive injections of argon into steady state plasmas. This technique provides rather reproducible disruptions with a significant number of REs. In the first part of the experiments, a runaway mitigation technique was not applied. The temporal evolution and the structure of the runaway beam during disruptions were measured. Runaway transport and loss were also investigated. The quantitative analysis of the synchrotron radiation emitted by REs was performed to determine the number of high energy REs. The radius of the runaway beam (r_{beam}) and the pitch angle (θ) were deduced from the 2D synchrotron image. Additionally, the subtraction of two consecutive IR images was carried out in order to enable the observation of rapidly varying small-scale structures of runaway beam.

Next, the effect of various methods on the runaway mitigation were investigated. Runaway disruptions were initiated by argon injection and then the mitigation techniques were applied separately. First, a disruption mitigation valve was used. Here, 3 different types of gases, namely helium, neon and argon were studied. Secondly, the runaway mitigation effect of an argon injection performed by another valve which has a larger orifice and larger volume, and is located closer to the plasma than the

previous valve was investigated. One of these valves was developed and built at the Düsseldorf University. In the last part of the present work, both the influence of the RMPs produced by the DED 3/1 mode and DED 6/2 mode on the runaway confinement were studied.

The thesis is an extended summary of the author's publications and organized as follows. Runaway generation mechanisms, runaway transport and loss are briefly described in chapter 2. Theoretical approaches and novel models which describes behaviour and characteristic features of runaways during disruptions at TEXTOR developed by the colleague from the Institute of Energy and Climate Research of the research center Jülich are also included in this chapter. In chapter 3 characteristics and concepts of the TEXTOR tokamak and diagnostics as well as other scientific instruments which are used in the recent work are presented in detail. Chapters 4 and 5 are devoted to the results of the experimental investigation on the REs during TEXTOR disruptions and their mitigations, respectively. A summary is given in chapter 6. Finally, the author's publications are attached.

2 Runaway electron during tokamak disruptions

As the tokamak plasma has an induced current in it, charged particles in the plasma gain energies from the induced electric field. Electrons with velocities exceeding a critical value are freely accelerated and run away in energy space. Observations of REs in tokamak discharges have been reported in early studies [25, 26]. However, in the normal operating regime of the present day tokamaks REs are rarely generated because the typical toroidal electric field is less than the critical field for RE generation and the toroidal magnetic field is low, i.e. close to the minimum magnetic field required for runaway generation, $B_T \approx 2$ T. Nevertheless, observations of REs during disruptions have been reported in most present day tokamaks.

2.1 Runaway electron generations

The first numerical analysis for RE generation has been performed by Dreicer [27, 28]. The Dreicer generation is a primary runaway generation which can be observed both in the low density regime and during disruptions. The hot tail generation is expected to play an important role during disruptions when the thermal quench (TQ) is sufficiently rapid. Tritium decay and Compton scattering may also lead to primary RE generation. REs can be generated by the primary generation mechanisms even if there were no runaways in the plasma. Runaway avalanche which is a secondary runaway generation mechanism, in contrast, occurs only if REs already exist in the plasma.

2.1.1 Dreicer generation

The Dreicer generation mechanism describes the diffusion of an electron from the collisional region into the runaway region of the velocity space caused by long range collisions. Electrons are slowed down mainly by electron-electron collisions [27, 28]. By setting the electrical force, qE, equal to the friction force, the minimum electric field required for RE generation is obtained

$$E_{cr} = \frac{n_e e^3 \ln \Lambda}{4\pi\epsilon_0^2 mc^2} \qquad \left[\frac{V}{m}\right]. \tag{2.1}$$

n_e is the electron density, lnΛ the Coulomb logarithm and ϵ_0 the vacuum permittivity. For the weak electric field, only the high-energy part of the Maxwell distribution is accelerated and runs away. If the electric field exceeds the Dreicer field

$$E_D = \frac{n_e e^3 \ln \Lambda}{4\pi\epsilon_0 T_e} \qquad \left[\frac{V}{m}\right], \tag{2.2}$$

runaway occurs even for the thermal electrons. The Dreicer generation rate obtained by using non relativistic approach reads [29]

$$\frac{dn_r^{pr}}{dt} = \lambda_r \nu_{ee} n_e. \tag{2.3}$$

where ν_{ee} is the electron-electron collision frequency and λ_r the runaway birth rate [30]

$$\lambda_r = k\epsilon^{-3(1+Z_{eff})/16} \exp\left(-\frac{1}{4\epsilon} - \sqrt{\frac{1+Z_{eff}}{\epsilon}}\right). \tag{2.4}$$

k is a factor of order unity and $\epsilon = |E_\parallel|/E_D$. If the relativistic effects are taken into account the birth rate becomes [31]

$$\lambda_r^{relat} = \lambda_r \exp\left(-\frac{T_e}{m_e c^2}\left(\frac{1}{8}\epsilon^2 + \frac{2}{3}\epsilon^{3/2}\sqrt{1+Z_{eff}}\right)\right). \tag{2.5}$$

The drag force does not fall to zero but remains finite at the speed of light. The runaway birth rate in both cases depends on the electric field E, electron density

n_e, electron temperature T_e and effective ion charge Z_{eff}.

2.1.2 Hot tail generation

Since the collision frequency decreases with increasing velocity, the high energy electrons need longer times to slow down than the low energy ones. During the transient event such as the TQ in a disruption, the high energy electrons may not have enough time for complete thermalization and form a hot tail of the Maxwellian distribution with a decreasing temperature of the rest of the distribution [32]. As the plasma cools down, the critical velocity for runaway acceleration decreases. The electrons in this hot tail can thus become REs resulting in a rapid growth of the runaway population. In references [33, 34] the hot tail runaway generation for certain cooling types was analyzed. The cooling rate is assumed to be proportional to the collision frequency of the thermal electrons. At low temperature in a post-thermal quench the cooling rate is constant or decreasing with time. The hot tail runaway generation for general cooling scenarios is given by [35]

$$\frac{dn_r^{hot}}{dt} \simeq -\frac{du_c}{dt}\frac{2u_c^2 H(-du_c/dt)}{(u_c^3-3\tau)^{1/3}}\int_{u_c}^{\infty}\frac{e^{-u^2}u^2du}{(u_c^3-3\tau)^{2/3}}, \tag{2.6}$$

where $u_c = (v_c^3/v_T^3 + 3\tau)^{1/3}$ and H the Heaviside function.

An experimental study of the hot tail generation was performed in DIII-D [8]. It has been found that during the disruption induced by killer pellet injection, the cooling rate and the final temperature of the plasma has a significant influence on the RE generation.

2.1.3 Runaway avalanche

As the generation rate in equation 2.4 is exponentially small in the parameter ϵ, the runaway generation is negligible for $\epsilon \lesssim 0.03$ [29]. Another production mechanism which is more effective was pointed out by Sokolov [36]. Although a close Coulomb collision, i.e. "hard" collision, has a small probability in plasmas with $\ln\Lambda \gg 1$, this

collision can kick a thermal electron into the runaway region while the colliding RE still stays in the runaway region. The runaway population grows exponentially due to this mechanism. Many studies have been devoted to an analysis of the runaway avalanche [37, 38, 39]. The most complete mathematical treatment of the runaway avalanching process was done by Rosenbluth and Putvinski [39]. The gyrokinetic relativistic Fokker-Planck equation averaged over a particle bounce period can be written as

$$-\frac{eE_{\parallel}\xi}{m_e c}\left(\frac{\partial f}{\partial p}-\frac{2\lambda}{p}\frac{\partial f}{\partial \lambda}\right)=C(f)+S, \tag{2.7}$$

where $p=\gamma v/c$ is the normalized relativistic momentum, $\lambda=(1-\xi^2)/B$ the magnetic moment variable and S the avalanche source of REs. $\gamma=1/\sqrt{1-v^2/c^2}$ is the relativistic factor.

Equation 2.7 was solved analytically in several limits [29]. An interpolation formula for the runaway production rate due to the secondary generation is given as

$$\frac{dn_r^{sec}}{dt}\simeq\frac{(\epsilon^*-1)n_r}{\tau\ln\Lambda}\sqrt{\frac{\pi\varphi}{2(Z_{eff}+5)}}\times\left(1-\frac{1}{\epsilon^*}+\frac{4\pi(Z_{eff}+1)^2}{2\varphi(Z_{eff}+5)(\epsilon^{*2}+4/\varphi^2-1)}\right)^{-1/2}, \tag{2.8}$$

where $\epsilon^*=E_{\parallel}/E_c$ is the normalized electric field, $\tau=(c/v_{th})^3\nu_{ee}^{-1}$ is the collision time for relativistic electrons and $\phi\approx(1+1.46(r/R)^{1/2}+1.72r/R)^1$ describes the effect of finite aspect ratio R/r. In the limit $\epsilon^*\gg 1$, $Z_{eff}=1$ and $r/R\to 0$, a simpler growth rate is obtained:

$$\frac{dn_r^{sec}}{dt}\simeq n_r\sqrt{\frac{\pi}{2}}\left(\frac{\epsilon^*-1}{3\tau\ln\Lambda}\right). \tag{2.9}$$

The secondary generation rate is proportional to the density of the existing REs. The frequency of hard collisions is $1/(\tau\ln\Lambda)$. Runaway avalanche is dominant at a sufficiently weak electric field if there are REs present in the plasma. When a considerable fraction of the initial current is converted to the runaway current, the electric field decreases and the runaway current becomes saturated before it reaches the initial current [40].

During disruptions, the avalanching mechanism is also expected to play a dominant

role in the runaway generation [41, 42].

2.1.4 Other possible primary runaway electron sources

In most of the simulations, the Dreicer and the hot tail generation provide significant number of primary REs and other primary RE sources are negligible. In ITER, however, the tritium decay and Compton scattering of γ-rays cannot be neglected if the Dreicer and the hot tail generation are suppressed [43]. The RE generation rate of both methods depends on the activation of the wall. The activated ITER wall can emit γ-rays with energies of several MeV. Compton scattering of these γ-rays with electrons can lead to runaway generation. The RE generation rate is estimated by

$$\frac{dn_r^\gamma}{dt} = \sigma \Gamma_r n_e, \tag{2.10}$$

where σ is the Compton scattering cross section and Γ_r the γ-ray flux.

The efficiency of each runaway generation mechanisms is mainly influenced by different parameters. The Dreicer generation is sensitive to the initial current, post-thermal quench density and post-thermal quench temperature while the hot tail generation is sensitive to E/E_D and the cooling rate. An increase in post-thermal quench density leads to a reduction of the efficiency of both mechanisms. In JET, the hot tail generation dominates for the thermal quenches faster than 0.3 ms, otherwise the Dreicer mechanism dominates [44]. The most important parameter for the avalanche mechanism is the initial current.

2.2 Runaway energy

Electrons in a tokamak experience an acceleration $a = eE/m$ due to an induced electric field. The energy gained from the toroidal electric field is given by

$$W_{max}(t) = \frac{ec}{2\pi R} \int_0^t V_{loop}(t')dt' = 27\Phi(t) \qquad [MeV]. \tag{2.11}$$

where R is the tokamak major radius, V_{loop} the loop voltage and $\Phi(t)$ the flux swing applied to the plasma. When the electrons diffuse from the collisional region into the runaway region of the velocity space, they have energies close to the critical energy. During the current quench (CQ), REs gain more energy from the high loop voltage and start to emit synchrotron radiation. As the runaways move with higher velocities, the drift of the runaway orbits become more crucial. If they are accelerated further, their orbits will move closer to the wall and finally the orbits will intersect the wall. The runaway confinement time also plays an important role for the maximum runaway energy. The longer they are confined in the plasma, the higher energies they can gain.

The energy limit of the REs is most likely determined by the flux swing of the TEXTOR transformer; since the part of the initial flux swing is consumed for the plasma generation, the remaing flux swing at $t = 2$ s, the time of the disruption, amounts to typically 1.1 Vs. This flux swing limits the maximum runaway energy to about $W_{max} = 30$ MeV.

In principle other reasons could limit the maximum runaway energy: magnetic field ripples, instabilities of relativistic electrons (Parial-Pogutse), pitch angle scattering and the energy loss due to synchrotron radiation. These limits are discussed in detail in [45]. For the experiments discussed below, there are no indication that the instabilities dominate. The synchrotron radiation also limits the maximum energy at 30 MeV (see section 3.1.1). The only dominant loss factor here is ergodization of the magnetic fields and magnetic field braiding. In contrast to the flux swing, which is an overall limitation, the ergodization is local and has a different loss effect for different radii. The core is often little affected.

2.3 Runaway electron transports and losses

In the presence of the magnetic field, an electron gyrates around a magnetic field line with the Larmor radius

$$\rho \quad = \quad \frac{v_\perp}{\omega_c} \quad = \quad \frac{\gamma m_e v_\perp}{eB} \tag{2.12}$$

where ω_{cj} is the cyclotron frequency, B the magnetic field, $v_\perp$ the vertical velocity with respect to the magnetic field and γ the relativistic factor.

The helical magnetic field lines in tokamaks makes the motion of electrons more complex. The electrons experience additional forces causing the outward movement (drift) of the electrons with the velocity v_d. The motion of a RE can be determined by the velocity vector

$$v_{re} = v_{cyc} + v_{gc} + v_d. \tag{2.13}$$

The contribution of the cyclotron is included in the first term on the right hand side, the motion of the guiding center in the second term and the drift in the last term. The guiding center is the center of mass of the electron averaged over its gyromotion.

In collaboration with the Institute of Energy and Climate Research of the research center Jülich (Forschungszentrum Jülich GmbH) models have been developed and theoretical calculations have been performed in order to describe runaway orbits and to study the runaway loss mechanisms during induced disruptions in TEXTOR. The calculations agree well with the experimental results shown in chapter 4.

2.3.1 Relativistic Hamiltonian guiding center equations

In order to reformulate the Hamiltonian equations for guiding-center motion of passing particles such as a RE, the toroidal angle φ is introduced as the independent, time-like variable and the corresponding canonical toroidal momentum p_φ as a new Hamiltonian $K = -p_\varphi$ [46, 47]. The guiding center motion can be determined by the Hamiltonian equations

$$\frac{dq_i}{d\varphi} = \frac{\partial K}{\partial p_i}, \qquad \frac{dp_i}{d\varphi} = -\frac{\partial K}{\partial q_i}, \quad (i = 1, 2). \tag{2.14}$$

with the simplified Hamiltonian function

$$K = -p_\varphi = -Z_q \psi_\varphi - \sigma(R/R_0)u_\varphi. \tag{2.15}$$

where $u_\varphi = \sqrt{\varepsilon_0(\gamma^2 - 1) - 2\omega_R I_R}$. Here, ψ_φ is the normalized vector potential or the poloidal flux, ε_0 a normalized energy of the particle at rest and ω_R the radial gyrofrequency and I_R the action variable. The direction of motion with respect to the toroidal angle φ is determined by the parameter σ, which is equal to -1 in case of REs and equal to 0 for the field line. (R, Z, φ) is a cylindrical coordinate system.

The radial gyromotion energy T_R and the full kinetic energy of a particle T_K can be written as

$$T_R = \sqrt{\varepsilon_0^2 + 2\omega_R I_R} - \varepsilon_0 \tag{2.16}$$

$$T_K = \varepsilon_0(\gamma - 1) \tag{2.17}$$

The ratio between these values $\lambda_I = T_R/T_K$, is considered as the initial parameter of motion. $\lambda \leq 0.1$ was obtained experimentally for TEXTOR [18, 45].

2.3.2 Runaway electron orbits

The toroidal momentum p_φ is a constant of motion in axisymmetrix tokamaks. The electron orbits lie on the so-call drift surfaces. For low relativistic energy electrons with $\gamma \gtrsim 1$, the effective safety factor q_{eff} is equivalent to the safety factor of the equilibrium magnetic field $q(\rho)$, while q_{eff} for high energy electron deviates from the $q(\rho)$. The effective safety factor is determined by a ratio of the increment of the toroidal angle φ per one poloidal turn, i.e. $q_{eff} = \Delta\varphi/2\pi$.

The typical runaway orbits at TEXTOR is shown in figure 2.1. The REs outside the separatrix follow the opened orbits and are not confined. Only the runaway inside the separatrix can be confined. The runaway confined area S_{conf} depends on the electron energy W_{re} and the plasma current I_p. For a given I_p, the S_{conf} shrinks with increasing W_{re} [48]. If the runaway energies exceed the critical value, the REs are no longer confined in the plasma.

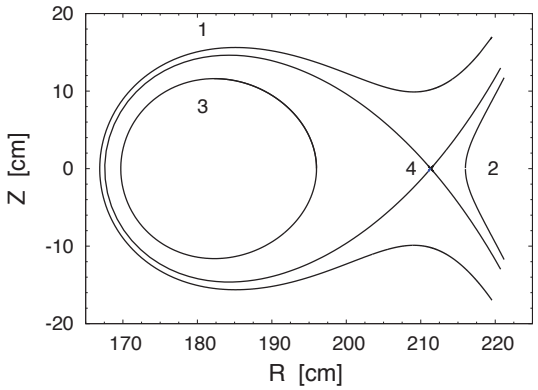

Figure 2.1: (a) Typical runaway orbits in (R,Z) plane for W_{re} = 30 MeV, I_p =100 kA, plasma radius of a = 30 cm. This parameters are taken from the experimental observation of the discharge #117527 at t =2.033 s. Curves 1 and 2 correspond to unconfined electrons, curve 3 the confined electrons and curve 4 the separatrix which separates the confined and unconfined orbits [reproduced with kind permission of S. Abdullaev].

The drift orbits for different runaway energies presented in figure 2.2 have a common intersecting point at the HFS. The drift orbit of REs with energies of 10 keV coincides with the magnetic surface. By increasing the electron energy the corresponding drift surfaces deviate more strongly from the magnetic surface. The radial shift δ of the electron orbit from the magnetic surface obtaining from (2.15) (see figure 2.2) can be written as

$$\delta \approx \frac{(R_o - R_i)W_{re}}{ecR_0B_z} = 2\frac{\widetilde{q}W_{re}}{ecB_0}, \tag{2.18}$$

where R_o and R_i are the outermost and innermost points of the electron orbit, respectively and $\widetilde{q} = rB_0/R_0B_z$, ($r = (R_o - R_i)/2$) is the safety factor in a cylindrical

geometry. This is valid for $\delta \ll a$, and the small radial oscillation energy, $2\omega_R I_R \ll \varepsilon_0(\gamma^2 - 1)$. The initial circular orbits become oval when the electrons gain higher energies.

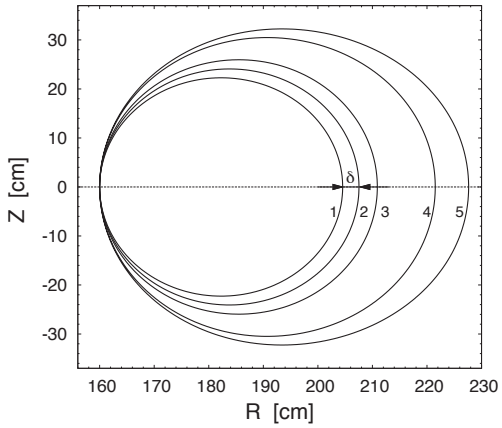

Figure 2.2: The drift orbit of electrons with different energies with $I_P = 300$ kA and $B_t = 2.5$ T. Curves 1−5 correspond to energies of $W_{re} = 10$ keV, 10 MeV, 20 MeV, 40 MeV, and 46 MeV, respectively [reproduced with kind permission of S. Abdullaev].

In addition to the energy of REs, their starting positions also plays an important role in the runaway confinement. In [49], the full orbit development of the RE during disruption is calculated by a mapping method. It has been shown that only the core electrons remain confined throughout the disruption. Electrons with $r > a/2 \approx 20$ cm are lost before they have enough time to gain the minimum energy required for the synchrotron radiation measurement by the system described in subsection 3.1.1.

2.3.3 Runaway orbit drift

Since the magnetic field is curved, electrons experience the centrifugal force leading to the curvature drift, v_R. Additionally, the strength of the magnetic field inside the toroidal coil decreases with the distance from the center. The Larmor radius at the low field side is larger than that at the high field side resulting in the grad-B drift, $v_{\nabla B}$. The total drift is in opposite direction for electrons and ions. However,

the E cross B drift, $v_{E\times B}$ resulting from an electric fields produced by the charge separation can be neglected because the drift of runaways which follow the helical field lines in a tokamak is averaged out. The drift velocity $v_r = v_R + v_{\nabla B}$ is inverse proportional to the aspect ratio R_0/a and the plasma current I_p.

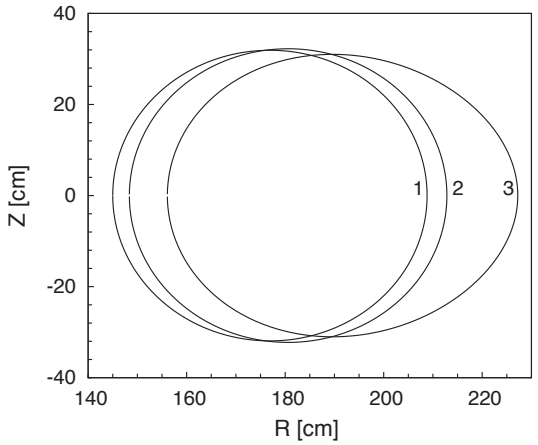

Figure 2.3: Outward drift of electron orbits for the plasma current I_p = 300 kA. Curve 1-3 correspond to t= 0.0 s, t= 0.01 s and t= 0.035 s, respectively. The toroidal magnetic field $B_t = 2.5$, the loop voltage $V_{loop} = 40$ V, the major radius $R_0 = 175$ cm, the minor radius a =46 cm [reproduced with kind permission of S. Abdullaev].

As the toroidal momentum p_φ is a constant of motion, the drift velocity can be written as [50]

$$v_d = \frac{R_0 E_\varphi}{R B_Z^*}\left(1 - \frac{R T_{av}}{R_0 T}\right), \tag{2.19}$$

where $T_{av} = 2\pi q_{eff} R_0/v_\varphi$ is the average transition time, T the transition time and v_φ the toroidal velocity. B_Z^* is the effective poloidal field

$$B_Z^* = B_Z + \frac{\sigma B_\varphi}{Z_q}\left(u_\varphi + \frac{\omega_x I_x}{u_\varphi}\right). \tag{2.20}$$

Figure 2.3 presents the temporal evolution of electron orbits under the assumption

that the induced electric field is constant in time. The outward drift velocities for different plasma currents I_p are shown in figure 2.4 (a). For the higher plasma current, i.e. $I_p = 300$ kA the drift velocity remains nearly constant, whereas the drift velocity for the lower plasma current, i.e. $I_p = 100$ kA increases more strongly with time. In addition to the plasma current, positions of the drift orbits has also a strong influence on the evolution of the drift velocity (see figure 2.4 (b)).

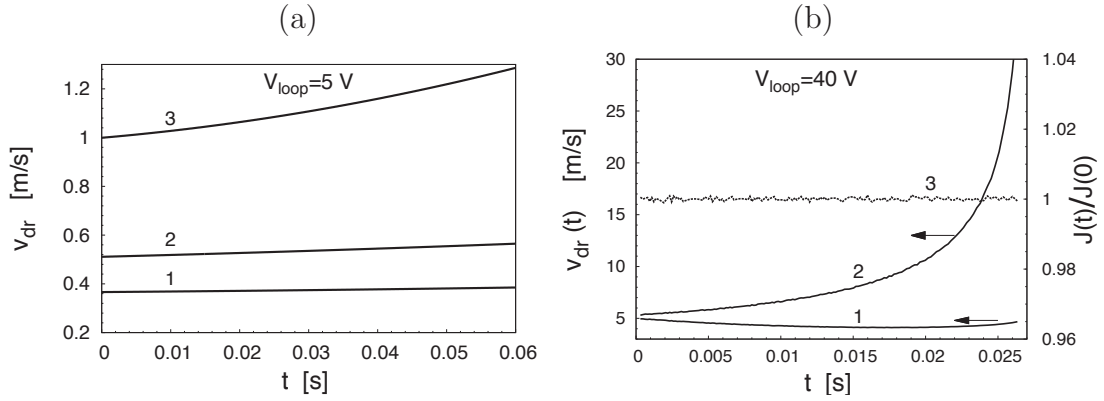

Figure 2.4: The temporal evolution of the drift velocities v_{dr} of electron orbits: (a) for the loop voltage of $V_{loop} = 5$ V. Curves 1-3 correspond to $I_p = 100$ kA, 200 kA and 300 kA, respectively. (b) for $V_{loop} = 40$ V and I_p=150 kA Curves 1 and 2 correspond to the innermost point R_i and the outermost point R_o of electron orbit, respectively. Curve 3 presents the normalized area enclosed by the orbit in one poloidal turn (right hand side axis) [63].

2.3.4 Structure of runway electron orbits

According to the magnetohydrodynamics (MHD) theory, the magnetic topology can be change by breaking and reconnecting the magnetic filed lines owing to the finite resistivity of the plasma. When the so-called tearing mode, which is a resistive MHD instability develops, a spontaneous magnetic reconnection takes place and hence magnetic islands are formed (see figure 2.5). The field line equation can be written as

$$(r - r_s)^2 = \frac{w^2}{8} cos(m\chi) - cos(m\chi_0) \tag{2.21}$$

here, r_s is the radial position of the resonance surface and $\chi = \theta - \frac{n}{m}\phi$ is an angular coordinate orthogonal to the helix. The width of the magnetic island is given by

$$w = 4\sqrt{\frac{rqB_r}{mq'B_\theta}} \tag{2.22}$$

Here, the $'$ denotes a derivative with respect to r.

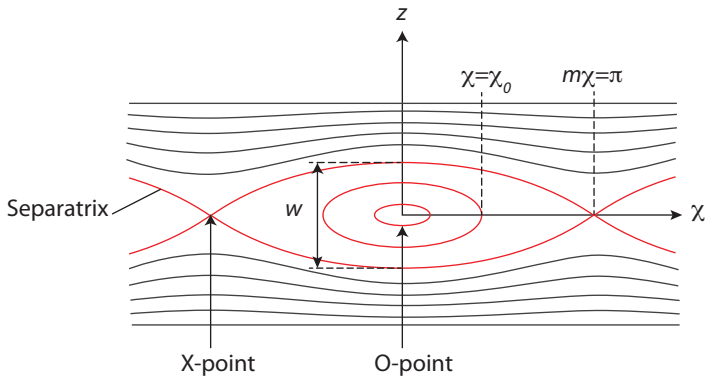

Figure 2.5: Geometry of a magnetic islands resulting from magnetic reconnection.

The current profile developed during the pre-disruption phase is commonly not stable to tearing modes, particularly the $m = 2$ mode. It is sometimes followed by growth of MHD modes. If magnetic islands resulting from the modes are sufficiently large, they can induce significant eddy currents in the vacuum vessel. The induced eddy currents create torques in the opposite direction to the plasma rotation. The plasma rotation is slowed down or even stops [51]. As mode locking occurs, the magnetic islands grow continuously. The overlap of the islands on neighbouring rational surfaces results in an ergodic or stochastic layer; the magnetic field move randomly and fills the volume of the ergodic layer. Both, magnetic islands and ergodic layers degrade the plasma confinement and enhance the radial transport.

The enhanced heat and particle transport in the stochastic layer results in a rapid

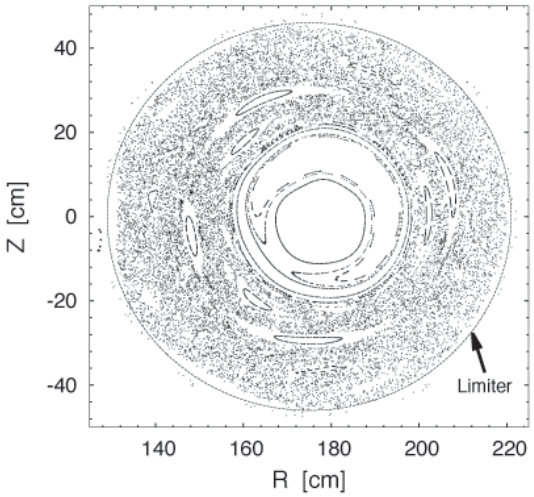

Figure 2.6: Poincaré plot of the guiding center of a runaway electron in the presence of the m/n = 1/1 mode [reproduced with kind permission of S. Abdullaev].

drop of the plasma temperature followed by the current quench (CQ). During disruptions, REs are generated owing to the induced toroidal electric field. The most stable runaway beam can be obtained for plasmas with the central safety factor q(0) < 1 [52, 53]. Interactions of the REs with the MHD mode leads to rapid losses of the REs in the stochastic region. The extent of the stochastic layer depends on: (i) the structure of the magnetic field, (ii) the spectra of the perturbations and (ii) the safety factor (q) profile [52]. Figure 2.6 shows a Poincaré plot of the runaway guiding center during a disruption. In this example, the stochastic layer does not reach the plasma center. The outermost intact magnetic surface is created between the magnetic surfaces $q = 1$ and $q = 5/4$ or $4/3$ which is the closet low-order rational magnetic surface. The REs in the inner region are well confined, whereas the REs in the outer region are lost rapidly.

2.3.5 Runaway electron losses

Since the velocity of REs is close to the speed of light c, they are considered to be insensitive to electrostatic turbulence. Their radial transport is therefore influenced

only by magnetic turbulence. It has been suggested that the radial transport of the REs is mainly due to small-scale fluctuations of the plasma. The rate of radial transport is determined by the diffusion coefficient D_r. In a fully stochastic magnetic field, the magnetic field diffusion coefficient is given by [54]

$$D_M \propto L_{\parallel} \left(\frac{\tilde{B}}{B} \right)^2 \tag{2.23}$$

where $L_{\parallel} \propto \pi q R$ is the correlation length of the fluctuations along the magnetic field and $\tilde{B}$ the magnetic field fluctuations. The runaway diffusion coefficient can be derived from the D_M by using following relation

$$D_r \propto v_{\parallel} D_M. \tag{2.24}$$

Nevertheless, if the magnetic shear is taken into account, the magnetic field lines will no longer follow the Gaussian random walk and the scaling of the runaway diffusion coefficient with $v_{\parallel}$ becomes weaker [55].

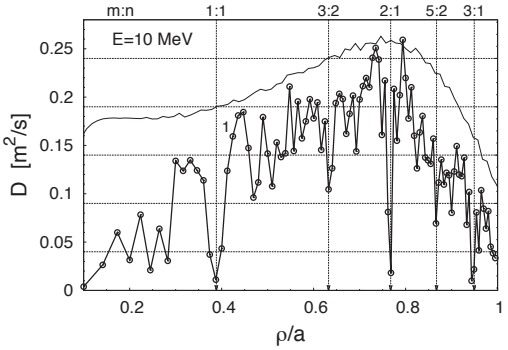

Figure 2.7: Curve 1 presents a numerical calculation of the radial profile of the diffusion coefficient D_r for a runaway electron with an energy of 10 MeV and curve 2 the quasilinear prediction. The vertical lines indicate the positions of the rational drift surfaces [63].

A number of studies has been performed in order to investigate the radial transport of REs in a stochastic magnetic field and the inconsistency between the experimental results and the theoretical models [56, 57, 58, 59, 60, 61]. It has been suggested

that the orbit drift which causes the displacement of the runaway orbits from the magnetic flux surfaces (see subsection 2.3.2) makes the REs less sensitive to the magnetic turbulence. For this reason the effective perturbation of a runaway orbit depends not only on the amplitude of the turbulence at a given surface but also on the width of the spectrum. If the shielding effect is taken into account the diffusion coefficient becomes

$$D_r \simeq \Upsilon \pi q v_{\parallel} R \left(\frac{\delta B}{B} \right)^2 \tag{2.25}$$

where Υ is the shielding factor. For electrons with energies in the range between 1 keV and 1 MeV, the diffusion coefficient D_r grows with increasing energy due to the increase of the parallel velocity $v_{\parallel}$ [61, 62]. The D_r starts to decreases for the runaways with higher energies because of the screening effect, while $v_{\parallel}$ approaches the speed of light c. The orbit averaging is expected to be responsible for the improved confinement of high energy REs.

Direct numerical calculations of diffusion coefficients D_r [63] shows that the radial profiles of D_r are irregular fractal-like functions of the radial coordinate ρ as shown in figure 2.7. The diffusion coefficient D_r near the low-order rational drift surfaces $q_p(\rho_{mn}) = m/n$=1/1, 3/2, 2/1, 5/2,3/1 drops drastically from the quasilinear values. The gaps in the density of these rational drift surfaces are responsible for the reduction of the radial transport [62] and are probably related to the formation of transport barriers for high energy REs.

3 TEXTOR and scientific instruments

Tokamak Experiment for Technology Oriented Research or TEXTOR is a medium sized limiter-tokamak with a circular cross-section. The main focus area is the plasma-wall interaction including the optimization of the wall conditions and plasma boundary. The plasma boundary is defined by the Advanced Limiter Test-II (ALT-II) which removes the particle and heat fluxes beyond the LCFS and prevents the plasma-wall interaction. Additionally, the amorphous film deposited by carbonization, boronization or siliconization processes are used to reduce the impurity influx. The design specifications of TEXTOR is given in table 1. More detailed information on the TEXTOR features is given in [64] and the references therein.

TEXTOR Parameters			
major radius	R_0	1.75	m
minor radius	a	0.46	m
maximum magnetic field	B_{max}	3	T
maximum plasma current	I_{max}	800	kA
maximum pulse duration	t_p	10	s
pulse power	P_p	125	MV
plasma volume	V	7	m^3
auxiliary heating power	NBI, ICRH, ECRH		

TEXTOR has accesses in both tangential and radial directions and is equipped with several plasma diagnostics such as spectroscopy, an IR camera, a magnetic probe and a fast probe. The diagnostics used in the current study are described in section 3.1. Section 3.2 is devoted to the plasma position control system at TEXTOR. The

disruption mitigation valve (DMV) and the Dynamic ergodic diverter (DED) which are used in the study of REs during induced disruptions and runaway mitigations are presented in section 3.3 and 3.4, respectively.

3.1 Diagnostics

3.1.1 Synchrotron radiation measurement system

In the presence of a magnetic field, an electron gyrates around a magnetic field line and emits radiation at the cyclotron frequency $\omega_{c,e}$ and its harmonics perpendicular to the direction of acceleration. For relativistic electrons such as RE the radiation transforms into the continuum synchrotron radiation in the direction of the instantaneous flight. The power emitted by a RE per wavelength interval is given by [65]

$$P_{\lambda}^{e} d\lambda = \frac{4\pi}{\sqrt{3}} \frac{m_e c^3 r_e}{\gamma^2 \lambda^3} \left(\int_{\frac{4\pi R_c}{3\lambda\gamma^3}}^{\infty} K_{5/3}(x) dx \right) d\lambda, \tag{3.1}$$

where $K_{5/3}$ is the modified Bessel function of the order 5/3, r_e the classical electron radius and R_c the radius of curvature of the electron orbit. The emitted power depends on the runaway energy and the radius curvature of the runaway orbit.

In tokamaks, REs move along the curved helix magnetic field lines and emit synchrotron radiation into an narrow cone with the pitch angle θ. The pitch angle can be deduced from the 2D synchrotron radiation image [18]. Figure 3.1 shows that the spectra at lower wavelength λ region increase rapidly with λ while the spectra at the higher λ decrease.

In TEXTOR, a pitch angle of $\theta = 0.12 \pm 0.02$ rad and a radius of the runaway beam of $r_{beam} = 0.20$ - 0.25 m were derived for low density discharges [45] and $\theta = 24 \pm 4$ mrad and $r_{beam} = 0.06 \pm 0.01$ m for disruptions [41].

The synchrotron radiation emission leads to runaway energy losses. The maximum

runaway energy can be obtained from the power balance between the power gain and the power loss due to synchrotron radiation ($P_{gain} - P_{syn} = 0$) because the loss due to friction force for REs is small and can be neglected. According to [45], the maximum energy of ~ 30 MeV is obtained from the typical parameters at TEXTOR : V_{loop} =1 V, R_0=1.75 m, B_T=2.2 T and $\theta = 0.1$.

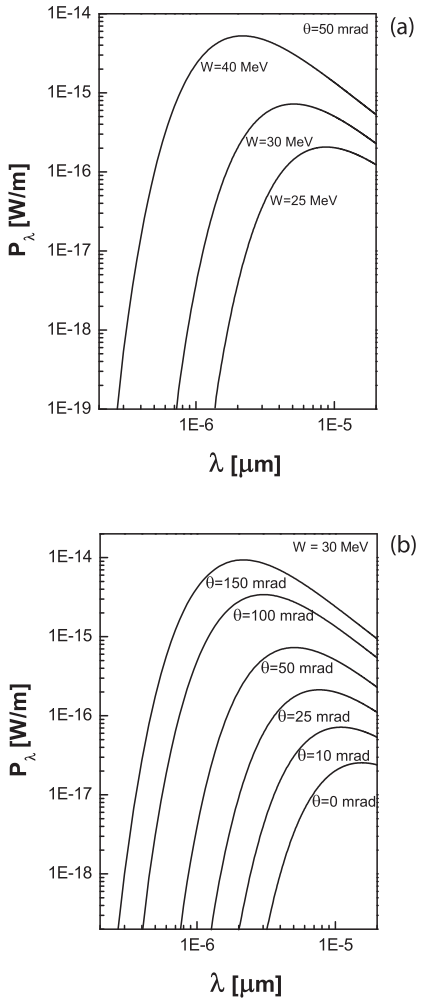

Figure 3.1: Synchrotron radiation spectra of monoenergetic electron with (a) energies of 25 MeV, 30 MeV, 40 MeV and (b) pitch angle of 0 mrad, 10 mrad, 25 mrad, 50 mrad, 100m rad, and 150 mrad.

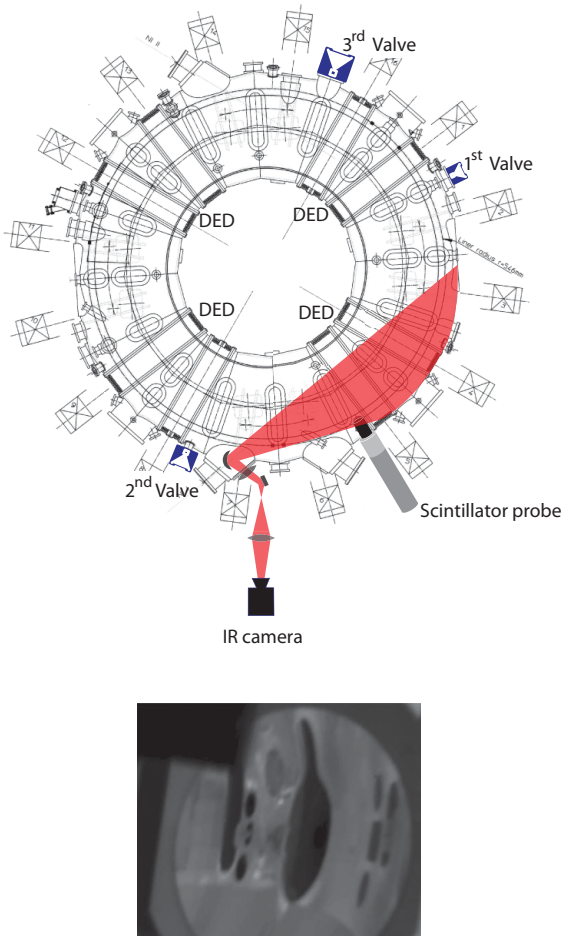

Figure 3.2: *Top:* Schematic top view of TEXTOR with the experimental setup for the measurements of REs. Three fast valves are located at different positions. The scintillator probe is inserted from the low field side (LFS) of the torus at the equatorial plan. The synchrotron radiation as well as the IR radiation from other sources are collected and directed to an IR camera. The red area presents the camera field of view.
Bottom: The camera view: openings for windows and diagnostic ports on the liner are clearly seen.

In order to measure the synchrotron radiation emitted by REs, an IR camera is installed at the equatorial plane on the low field side (LFS) of TEXTOR. It views the plasma tangentially in the electron approach direction. The camera operational wavelength range is between 3 and 5 μm. The lower and upper limits are deter-

mined by the germanium optics of the camera and the InSb detector, respectively. This limit corresponds to REs with energies $\geq$ 25 MeV. The camera is capable of capturing 1253 frames per second in a full frame mode.

The camera detects not only high energy REs but also the thermal radiation and reflections which are directed towards the IR-optics. The stainless steel concave mirror located inside the vacuum chamber collects the radiation from different sources. The radiation is reflected and passes through a CaF_2 window. It is then directed to a CaF_2 lens and consequently the radiation is imaged and recorded by the IR camera. The camera's field of view is indicated by the red area shown in figure 3.2. As the camera is sensitive to different radiation sources, characteristics of each radiation source given below are used to distinguished them from each other:

- **Synchrotron radiation**
  REs emit synchrotron radiation only in the forward direction of their motion with an opening angle θ. Due to its high directivity, only the fraction $\theta/2\pi$ of the superposition of electron orbits can be observed [48]. Since the camera is sensitive to runaways with energies $\geq$ 25 MeV, the runaway beam is observed as soon as they gain the required energy. The change of the synchrotron radiation position is related to the movement of the runaways and it disappears suddenly when REs are lost.

- **Thermal radiation**
  The thermal radiation is emitted mainly by the PFCs. The heated components can emit the thermal radiation over a few seconds if the heat is deposited on the components continuously for a relatively long period of time and propagates into the materials. In contrast, if the components are exposed to the heat flux for a short time, such as during disruptions the duration of the thermal radiation is short. Nevertheless, the thermal radiation lasts longer than the synchrotron radiation. In addition to the heat convection, the plasma radiation and neutral particle bombardment can contribute to the heat load on the wall and consequently results in thermal radiation.

- **Reflection**
  Although the reflection is not a radiation source, it has to be considered carefully. The reflection from the wall, particularly flat parts can make the analysis more complicated. However, the reflection in very localized. If the location of the ports, opening and other components of the vessel wall are known, the reflection can be easily distinguished.

- **Neutral gas**
  In some experiments with massive gas injection, IR radiation emitted by an injected gas has been observed. This radiation is very diffusive and lasts only a few ms after the injection.

3.1.2 Scintillator probe

The scintillator probes were developed at Heinrich-Heine University Düsseldorf in order to study REs in the TEXTOR tokamak [16, 17, 19, 66]. Only the final version of the probe is used in the present work. It consists of 9 YSO crystals and 2 thermocouples separated from each other by stainless steel (see figure 3.3). From the electron approach direction, crystals 1 - 9 are placed behind stainless steel slabs with a thickness of 0 mm, 1 mm, 2 mm, 2.5 mm, 3.5 mm, 4.6 mm, 5.5 mm, 7 mm and 9.5 mm, respectively. The absorbed energy of the YSO crystals is expected to change slowly with the energy of the electron for the electron with energies higher than 100 keV [67]. A drawback of the crystals is that it is sensitive not only to electrons but also to γ-rays. However, the signal produced by electrons is twice as high as the signal generated by γ-rays. The crystals are connected to a set of photomultipliers by using optical fibres. The probe was covered by the 5 mm thick graphite housing which shields the probe from electrons with energies below 4 MeV. The probe is sensitive to REs with energies between 4 MeV and 22 MeV and has an energy resolution of about 2 MeV. The temporal resolution of the probe depends on the RC loading time which can be adjusted by using variable resistors. The absolute calibration of the probe is performed by applying the monoenergetic electron beam generated by the accelerator ELBE at the Forschungszentrum Dresden Rossendorf.

The probe calibration obtained from the GEANT4 simulation shows that the effect of bremsstrahlung and neutrons are negligible.

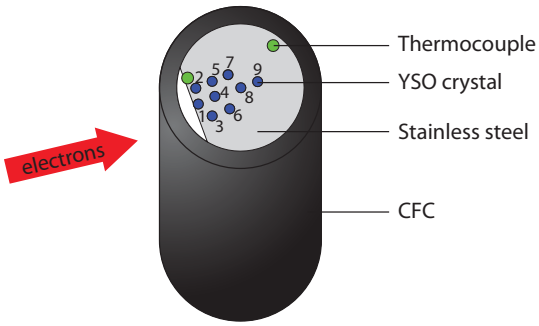

Figure 3.3: Schematic of the final schintillator probe. The probe consists of 9 YSO crystals and 2 thermocouples. Each crystal is separated by a stainless steel slab with different thickness. A tungsten filter is placed on the top of the probe in order to block the electrons coming from the top.

After the use in the disruption experiment [24], a crack was present on the graphite housing. Therefore, in the recent experimental campaigns, a carbon fibre composite (CFC) housing is used instead. Its high temperature tolerance and low thermal expansion makes CFC suitable for the measurement of high energy electrons. The energy deposition by electrons with different initial energies on a 5 mm thick CFC housing is simulated by using the Monte Carlo GEANT4 simulation code [68, 69]. The calculation shows that a larger number of electrons will penetrate the CFC material for higher electron energies. Only 0.4% of the 1 MeV electrons can propagate through the CFC housing and 6.5% in case of electrons with energies of 2 MeV. For electrons with energies of 3 MeV this fraction increases to 50%. The probe has the energy sensitivity range from 3 MeV to about 22 MeV. The scintillator probe is inserted into the LFS of the torus 200 ms before the gas injection and remains at the last closed flux surface (LCFS) until the plasma termination. The fast movable mechanism [17] enables the insertion of the probe along the minor radius on a ms timescale. It provides a direct measurement of the REs near the plasma boundary.

3.1.3 Soft X-ray (SXR) tomography

A measurement of Soft X-ray (SXR) emission is a powerful technique used in the studies of impurity transport and MHD phenomena in tokamaks. Since the tokamak plasma is optically thin for SXR radiation, the SXR detection allows an observation of plasma activities at the core. Moreover, the observation can be simplified into a 2D geometry in a poloidal cross-section of the plasma due to the toroidal symmetry of the plasma.

The SXR tomography system at TEXTOR provides 2D-profiles of the local emission coefficient of the line radiation emitted by impurities [70]. The system consists of 4 SXR pin-diode cameras: 2 cameras view the plasma vertically (2 × 20 channels) and the other two view the plasma horizontally (2 × 16 channels) as shown in figure 3.4. The time resolution of the tomography system is 20 ms. The local emission is reconstructed from the line-integrated signal of the camera by using a tomographic algorithm.

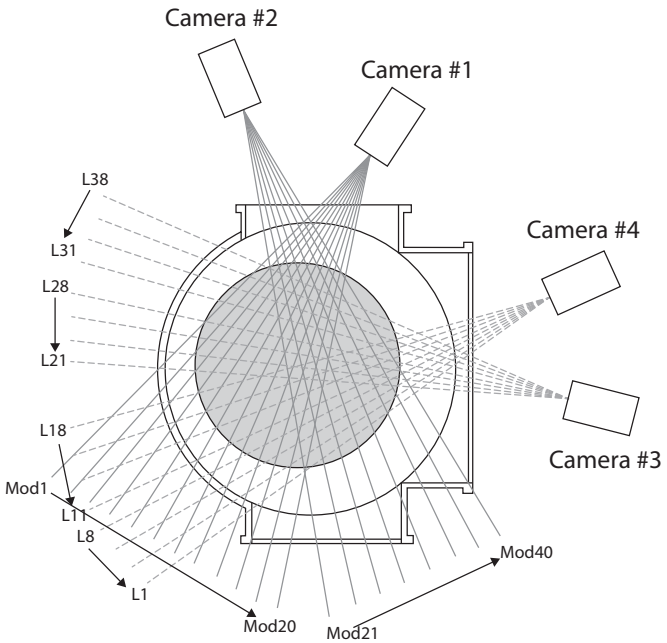

Figure 3.4: Schematic of a setup of soft X-ray pin diode arrays at TEXTOR.

The plasma position and profile can be obtained from spatially resolved measurements of SXR emission. Unfortunately, only some of the SXR channels were available during the current study. It was, therefore, not possible to reconstruct the SXR image. Only the SXR signal from the channel L22 which detects the SXR closed to the plasma center is discussed in chapter 4 and chapter 5.

3.1.4 Mirnov coils

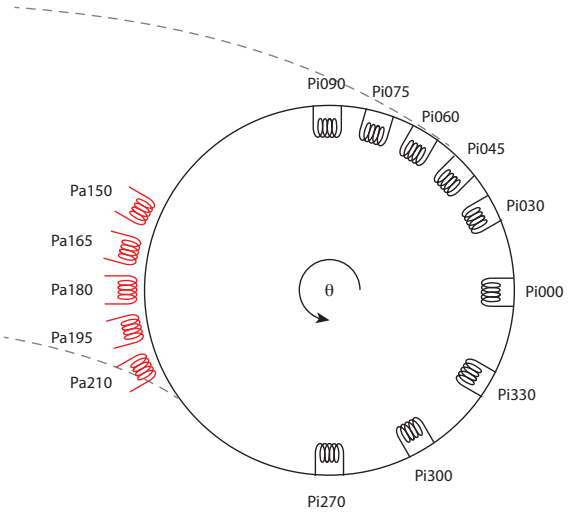

Figure 3.5: Schematic of a poloidal array of Mirnov coils at TEXTOR. "Pi" and "Pa" denotes the internal and external poloidal Mirnov coils, respectively. The numbers indicate the poloidal angle.

A set of small coils called Mirnov coils or pickup coils installed close to the plasma are used to measure the local magnetic fluctuations in tokamaks. According to Faraday's law of induction:

$$\oint_l E \cdot dl = -\frac{d}{dt} \oint_S B \cdot n dA, \tag{3.2}$$

the change in magnetic flux induces the voltage in the coils. Here, E is the induced electric field, B the magnetic field and n the normal to the coil surface area A. The magnetic field averaged over the coil cross section is given by

$$B \cdot n = \frac{1}{NA} \int_{t_0}^{t} U(t)dt \qquad [Tesla]\,. \tag{3.3}$$

where $U(t)$ is a voltage induced by the time varying magnetic field B.

Normally, Mirnov coils are located inside the vacuum vessel in order to reduce the skin effect losses. Moreover, they can measure higher frequencies than the Mirnov coils that located outside the vessel.

At TEXTOR, coils are wound around non-magnetic cores. The cross sectional area of the coils is $A \approx 13 \times 10^{-4}$ m^2 [71]. Figure 3.5 presents 2 sets of poloidal Mirnov coils installed at TEXTOR. The black coils ("Pi") are located inside the liner while the red ones ("Pa") are placed outside the liner. These coils measure the poloidal field component and are used to determine the poloidal MHD mode number, m number. In addition, there are radial coils which measure the normal component of the poloidal field located at a poloidal angle of 0, 30, 60 90, 270, 300 and 330 degrees. The toroidal MHD mode number, n number, can be deduced from signals of the toroidal Mirnov coils which are located at the same poloidal angle but different toroidal angles.

Signals from 2 Mirnov coils separated toroidally are sufficient to identify the n number owing to the toroidal symmetry of the tokamak plasma [72]. The determination of m number is more complex. In addition to the plasma shaping, the Mirnov signals are affected by the eddy currents on the vacuum vessel. Moreover, the mixture of many modes makes it difficult to define a dominant poloidal mode number.

3.2 Position control system

The position control system requires in addition sensors of the instantaneous plasma position. The most often used sensor is the HCN-interferometer for the horizontal position detection and magnetic coils for the vertical position. Other systems such as magnetic coils and spectroscopic signals have been used as well. During disruptions all systems tend to have problems, e.g. phase jumps at the interferometer and signal saturation. Therefore, at the time of a preprogrammed disruption, one can switch from a feedback system of the coil current control to a preprogrammed feed-forward control. This option is often used in the experiments presented in this thesis.

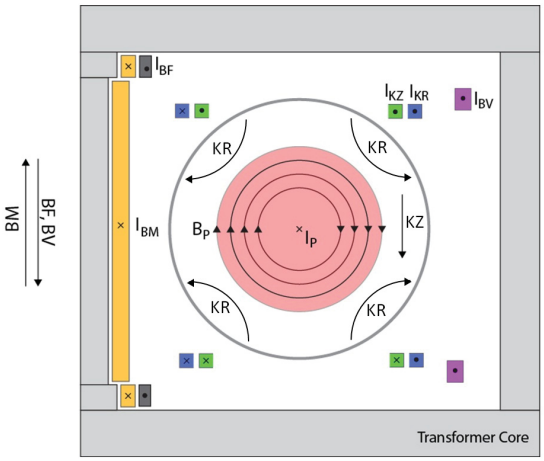

Figure 3.6: Schematic sectional view of TEXTOR: Directions of the plasma current I_p and the poloidal field B_p as well as the magnetic fields - BF, BM, BV, KR and KZ generated by $I_{BF}, I_{BM}, I_{BV}, I_{KR}$ and I_{KZ}, respectively.

An overview of the TEXTOR coil systems is given in figure 3.6. The toroidal coil system consists of 16 water cooled coils with 20 turns each. They are connected in parallel and generate the toroidal field up to 3 T at the plasma center at the maximum current of 82 kA. The poloidal field systems namely, heating coils, shaping coils and the vertical field coils, act independently. The ohmic heating coil with 294 turns acting as the primary winding of the transformer contributes mainly to the iron core flux. The shaping coils compensate the stray field. It produces only a local

effect on the plasma shape, whereas the vertical field coils, BV, generate a field that provides the plasma equilibrium and counteracts the plasma pressure. The vertical field coils consist of 2 coils connected in series with 24 turns each.

The position control coils: KZ coils generate pure vertical fields while KR coils generates radial fields. KR and KZ coils are used to control the vertical and horizontal position of the plasma, respectively. KR coils consist of an equal numbers of turns both clockwise and counterclockwise around the core, and therefore do not magnetize the iron core.

The radial position is controlled by both the BV coils and KZ coils. The maximum current of the BV coils is 20 kA, which is much higher than that of the KZ coils. However, the KZ coils which are located near the vacuum vessel provide a fast position control. More details on this topic can be found in [73, 64]

3.3 Disruption mitigation valve (DMV)

In order to mitigate disruption effects, i.e. heat loads, halo current and REs, disruption mitigation valves (DMVs) have been developed and tested at TEXTOR [74, 75, 76]. A DMV consists of a stainless steel case, an aluminium piston and a pancake-type coil (see figure 3.7). When the valve is triggered, a current flowing in the coil induces the eddy current which activates the piston to open the valve. The stem compresses the gas in the closure volume that acts as a spring. The valve is closed again due to the pressure in the closure volume. A Michelson interferometer in the downstream flow of a guiding vacuum tube allows the characterization of the gas flow [77]. The flow rate and the front of the gas are limited by a valve orifice and by the guiding tube length and diameter. Since the valve does not contain any ferrite material, it is not affected by the magnetic field and can be installed close to the vacuum vessel. This enables a fast reaction of the valve to the disruption.

In the present work, 3 different DMVs have been used. The characteristics of these valves are shown in table 3.1. Valve 1 which is located at the top of TEXTOR is used to initiated disruptions reproducibly. The other valves are used to mitigate

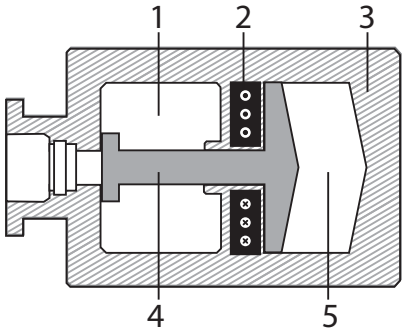

Figure 3.7: Schematic section of the DMV: (1) a working reservoir, (2) a pancake-type coil (3) a stainless steel case (4) an aluminium piston, and (5) a closing gas volume.

REs. Valve 1 is located rather far from the plasma due to technical reasons while valve 2 and valve 3 are installed in the equatorial plane as close to the plasma as possible. The gas path of valve 1 is 0.5 m longer than the path of the other valves. Valve 3 has the largest orifice with gas throughput an order of magnitude higher than that of valve 1. Valve 2 was developed and built at the Düsseldorf University.

Valve	$\emptyset_{orifice}$	Vol	P_{max}	Location
1	8 mm	20 cm^3	3.2 MPa	top of TEXTOR
2	14 mm	30 cm^3	3.0 MPa	equatorial plane
3	28 mm	110 cm^3	15 MPa	equatorial plane

Table 3.1: Characteristics of the valves at TEXTOR - orifice diameter, volume, maximum operating pressure and location of the valves.

3.4 Dynamic Ergodic Divertor (DED)

The primary aim of the DED is to study the effect of the resonant magnetic perturbations (RMPs) on the plasma confinement and rotation as well as the heat and particle transport at the plasma edge [64, 78, 79, 80]. Recently, the RMPs created by the DED have been used as a runaway mitigation method during disruptions.

Regarding the experimental results presented in [81], the runaway avalanche during TEXTOR disruptions is suppressed by the externally applied the RMPs. The loss rate of REs is significantly enhanced if sufficiently strong RMPs are applied. However, a complete runaway suppression cannot be achieved. The experimental results in [82] shows, conversely, no clear effect of the RMPs on the runaway suppression.

The DED consists of 16 helical coils and 2 compensation coils. The helical coils are aligned parallel to the magnetic surface at the high field side (HFS) of the torus, while the compensation coils are placed above and below the helical coils. The compensation coils counteract the vertical force on the plasma caused by the non-ideal coil feeding. The DED can operate in 3 different base modes: m/n = 12/4, m/n = 6/2 and m/n = 3/1 modes. The maximum current in the DED coils depends on the base mode number, i.e. I_{DED}^{max} = 15 kA, 7 kA and 3 kA for the m/n = 12/4, m/n = 6/2 and m/n = 3/1 base modes, respectively.

The magnetic field generated by the DED is resonant to the plasma magnetic field, particularly near the $q = 3$ surface. As the RMPs are applied, the resonant magnetic surfaces are destroyed and the isolated islands are formed. In addition to the base modes, neighbouring modes are generated resulting in a cascade of magnetic islands in the plasma. With an increasing perturbation current (I_{DED}), the magnetic islands develop. If the islands are sufficiently large, they overlap and the magnetic field become ergodic. The so called laminar zone is formed by magnetic field lines which intersect the wall. The loss of particles, especially REs from this area is enhanced. Since the radial penetration of the perturbation field $B_p(r) \approxeq B_p(a) \cdot (\frac{r}{a})^m$, the perturbation of low m modes penetrates more deeply into the plasma in comparison with the high modes. The islands resulting from the m/n = 3/1 base mode can excite the m/n = 2/1 tearing modes [83]. In the studies of runaway mitigation by magnetic perturbations presented in this thesis, only the m/n = 6/2 and the m/n = 3/1 base modes are studied.

4 Experimental investigations of runway electrons at TEXTOR

This chapter focuses on the study of the temporal evolution of REs during unmitigated disruptions. Therefore, no runaway mitigation method was applied in this chapter. The investigations of runaway mitigation techniques will be exploited in the next Section. The combination of the scintillator probe and the synchrotron measurement system was used to measure REs in different energy ranges. The IR camera discussed in subsection 3.1.1 was aimed to measure the synchrotron radiation emitted by the high energy REs and transient events during disruptions. Hence, a temporal calibration of the camera is crucial. The calibration of the camera is described in section 4.1. Section 4.3 presents the experimental results. Finally, runaway parameters deduced from the observations shown in section 4.3 are given in section 4.4.

4.1 Temporal calibration of the IR camera

During the calibration, an electrical spark was used as a radiation source. The spark brightness has a duration of <1 ms with a delay of nanoseconds when it is switched on. The spark was triggered 2, 3 and 4 s after the camera triggering started. It was operated in both a single mode and a periodic mode. Despite the starting-time jitter of the camera of about 20 ms, the time interval between each spark brightness recorded by the camera was consistent with the time interval of the trigger signal in the periodic mode (see figure 4.1). An independent signal

to synchronize between the camera's clock and the timing of other diagnostics is required. The most suitable time marker is the events occurring during the thermal quench (TQ) which is a transient phase. The sudden drop of the plasma current (electron cyclortron emission (ECE) signal) and the thermal radiation emitted by the heated wall (camera observation) are used as time markers for synchronization.

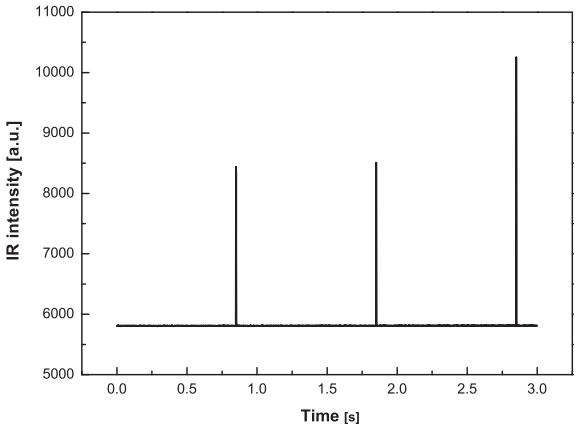

Figure 4.1: Thermal radiation from an electrical spark in a periodic mode observed by the IR camera.

4.2 Plasma disruptions induced by fast gas injection

A rapid plasma termination initiated by fast injection of noble gas has been studied in several tokamaks [15, 84, 85, 86]. This technique mitigates an effect of the halo current and reduces heat loads during disruptions. However, in some cases a significant number of REs are generated. In this section, the comparison between disruptions with and without REs is performed. In the former case disruptions were induced by argon injection, while in the latter case helium was used instead. The discharge conditions are: toroidal field $B_T = 2.4$ T, plasma current $I_P = 350$ kA and line average central density $n_e = 1.5 \times 10^{19}$ m^{-3}.

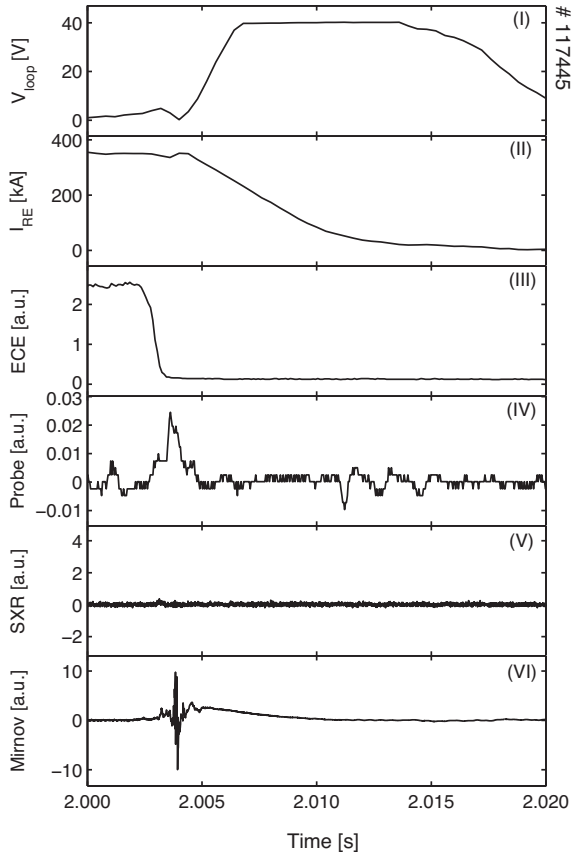

Figure 4.2: Temporal evolution of the disruption of discharges # 117445: (top to bottom) the time trace of the loop voltage, the plasma current, the electron cyclotron emission (ECE) signal, the scintillator probe signal, the soft X-ray (SXR) signal and the Mirnov signal.

A typical runaway-free disruption induced by helium injection at TEXTOR is shown in figure 4.2. As soon as the injected gas reaches the $q = 2$ surface, i.e. ~ 2.3 ms after the valve is triggered, a major disruption takes place. The confinement of both heat and particles is degraded. The plasma temperature drops suddenly as can be seen in figure 4.2 (III). Hence, this phase is called thermal quench (TQ) or energy quench. The sudden collapse of the electron temperature results in expulsion of the trapped poloidal flux followed by a negative voltage spike which is considered as a signature of a major disruption. Runaway electrons which are generated prior to the disruption are lost to the wall. The lost REs are detected by the scintillator

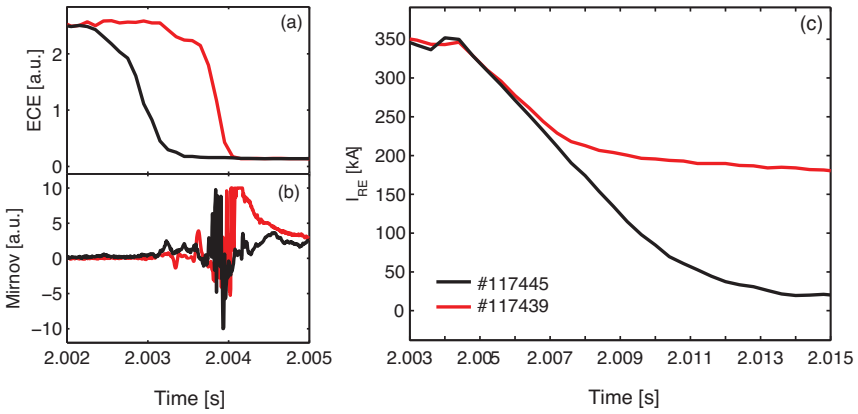

Figure 4.3: The time trace of (a) the electron cyclotron emission (ECE) signal, (b) the Mirnov signal and (c) the plasma current of discharges # 117445 (black) and # 117439 (red).

probe (see figure 4.2 (IV)). An increase in the plasma resistance and probably the impedance resulting from the MHD turbulence during the TQ leads to the plasma current decay and consequently an increases of the loop voltage.

In figure 4.3, the ECE, Mirnov signal and the plasma current of discharge # 117445 (black curve) is plotted on a smaller time scale in comparison with discharge # 117439 (red curve). In discharge # 117439, a disruption is induced by argon injection. During such a disruption REs are generated. Although in both discharges gas is injected at the same time, the TQ of the disruption induced by argon injection (red curve) occurs about 1 ms later than the case of helium injection (black curve). The atomic mass of helium is about 10 times smaller than the atomic mass of argon. Its flow velocity, $v_g \sim 1/\sqrt{A_g}$, is therefore higher. The penetration depth of the injected gas does not depend only on the mass of the gas A_g but also on its ionization rate k_{ion}: $\lg = v_g/(k_{ion} n_e)$ [87, 88]. The calculations given in [53] show that at TEXTOR injected helium and neon can reach the center of the plasma. In case of argon, the penetration depth is much smaller due to its high ionization rate.

The injected helium can penetrate deep into the plasma core and the whole plasma is cooled down. An increase in the plasma resistivity leads to an excitation of tearing modes on the resonant magnetic surfaces. In this case, the TQ phase of the

disruption induced by helium injection ends before the MHD activity is detected (see figure 4.3 (a) and (b) (black curve)). On the contrary, the TQ phase of the disruption induced by argon injection occurs at the same time as the MHD activity (see red curve). An injected argon is ionized mainly at the plasma edge leading to edge cooling and hence to a strong plasma resistivity gradient and a current gradient. The sudden loss during the TQ in this case results from the stochastic magnetic field created by interactions between MHD modes on the magnetic surfaces with $q > 1$. Therefore, the time scale of the TQ in this case is shorter than in case of disruptions induced by helium injection as shown in figure 4.3 (a).

The CQ in both cases begins almost at the same time. However, the current of a runaway-free disruption decays faster than the current of a disruption with REs. The plasma current of a runaway-free disruption decays exponentially, while the runaway plateau is formed in case of disruptions with REs as can bee seen in figure 4.2 (c). The difference between the plasma currents in both cases gives the runaway current. Disruptions with REs will be discussed in more detail in the next section.

4.3 Observation of runaway electrons during disruptions

In order to initiate disruptions with a significant number of REs reproducibly, argon injection is used in the studies presented in this section. When the disruption valve (valve 1) is triggered, argon is injected into the plasma. Since valve 1 is located relatively far away from the vessel, it takes a few ms for argon to travel from the valve to the plasma. As soon as the injected argon reaches the $q = 2$ surface, i.e. $\sim$ 4 ms after the valve is triggered, a major disruption takes place. The confinement of both heat and particles is degraded. The plasma temperature drops suddenly as can be seen in figure 4.4 (III) dashed line (a). Hence, this phase is called thermal quench (TQ) or energy quench. The sudden collapse of the electron temperature results in expulsion of the trapped poloidal flux followed by a negative voltage spike which is considered as a signature of a major disruption. Runaway electrons which

are generated prior to the disruption are lost to the wall and heat it. Figures 4.5 (A) (a) and (B) (a) show the thermal radiation emitted by the heated wall in false color. An increase in the plasma resistance and probably the impedance resulting from the MHD turbulence during the TQ leads to the plasma current decay and consequently an increases of the loop voltage. Runaway electrons are created due to the high loop voltage and form a plateau (see figure 4.4 (II)). Although the same initial conditions were held throughout the study, 3 different cases have been observed. REs in all cases develop similarly during the TQ and the CQ phases. During the runaway plateau phase, cases with and without mode excitations have been observed. In the other case, a substantial number of REs is present after the runaway plateau is terminated.

Case 1

In this case, "quiet" disruptions have been observed. The plasma current decays smoothly over $\sim$ 40 ms. No indications of runaway loss such as runaway bursts, SXR spikes and Mirnov spikes are present during the runaway plateau phase (see figure 4.4 (V) - (VII)). Runaway loss occurs mainly during the TQ and the plateau termination phase consistent with the observation from the IR camera presented in figure 4.5 (A).

According to the operational wavelength range of the synchrotron radiation measurement system of 3 - 5 μm, the runaway energy of $W_{re} \geq 25$ MeV is required. Consequently, a runaway beam is not observed directly after the TQ but about 7 ms later. As soon as REs gain high enough energies, they become visible to the camera at the high field side (HFS) as shown in figure 4.2 (A) (b). The runaway beam can be seen partially because the camera view is vignetted at the HFS.

Special structures have been observed by the IR camera throughout the disruption (see figure 4.5 (A) (b) - (h) white arrows). These structures are localized and coincide with the openings and highly reflective parts of the wall indicating that they are a result of the reflection from the vessel wall and do not originate from the synchrotron radiation. With increasing time, the runaway beam moves toward the

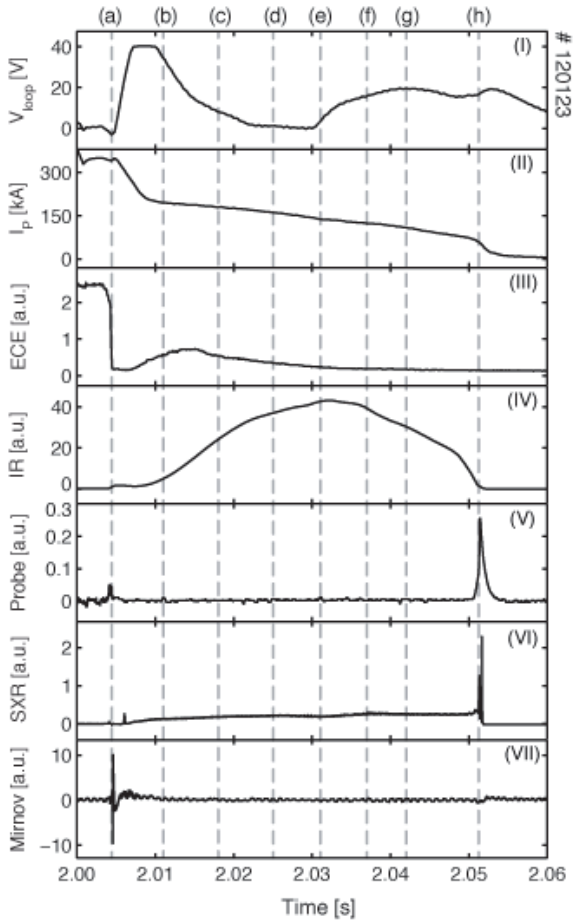

Figure 4.4: Temporal evolution of the disruption of discharge # 120123: (top to bottom) the time trace of the loop voltage, the plasma current, the electron cyclotron emission (ECE) signal, the intensities added over all pixels of the IR image, the scintillator probe signal, the soft X-ray (SXR) signal and the Mirnov signal. Dashed lines (a) - (h) correspond to the sub-figures (a) - (h) in figures 4.5 (A) and (B).

low field side (LFS). A larger part of the beam comes into the camera's field of view and the intensity of the beam increases resulting in a rise in intensities added over all pixels of the IR image shown in figure 4.4 (IV). The intensity at the center of the runaway beam increases continuously. However, after $t = 2.032$ s, the intensities added over all pixels of the IR image start to decrease because the runaway beam moves back to the HFS and the major part of the beam is located outside the field

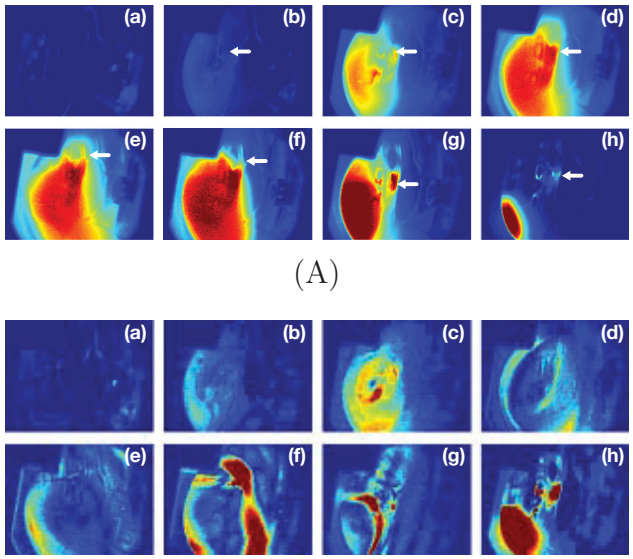

Figure 4.5: IR images in (A) the normal recording mode and (B) the subtraction mode for discharge # 120123 observed by the camera at (a) t = 2.004 s, (b) t = 2.011 s, (c) t = 2.018 s, (d) t = 2.025 s, (e) t= 3.032 s, (f) t = 2.037 s, (g) t = 2.042 s, and (h) t = 2.051 s. White arrows indicates structures from the reflection.

of view. During the runaway plateau phase, neither a rapid runaway loss nor a transient event have been observed by the IR camera.

In order to investigate small variations in the runaway beam, a time derivative of each IR image is taken by subtracting the current image from the previous image (see figure 4.5 (B)). The intensities of the IR images in the subtraction mode are much lower than those in the normal recording mode. Therefore, the maximum value of the color scale for the images in the subtraction mode is reduced by a factor of 10. No runaway loss is observed during the runaway plateau phase except at t = 3.042 s. At this time a channel towards the top is present as shown in figure 4.5 (B) (g). The loss occurs at the plasma edge, whereas the runaways at the plasma core stay almost unaffected. Only a small number of runaway electrons is lost. A major part of runaways remains well confined within the plasma.

In some disruptions of this case, the subtraction of the consecutive IR images shows

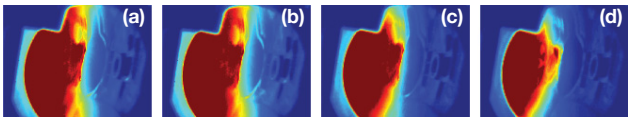

(A)

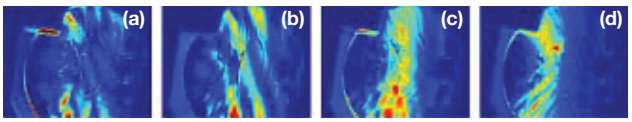

(B)

Figure 4.6: IR images in (A) the normal recording mode and (B) the subtraction mode for discharge # 119874 observed by the camera at (a) $t = 2.044$ s, (b) $t = 2.058$ s, (c) $t = 2.089$ s, and (d) $t = 2.094$ s.

stripe patterns at the plasma edge (see figure 4.6). These structures are typical for laminar zones of the ergodic system [63, 89]. In some images in the subtraction mode such as figure 4.6 (a) and (b), the inclined stripes are in the same direction. In the other images such as figure 4.6 (c) and (d), a superposition of stripes in different directions is observed.

Case 2

In contrast to the previous case, here runaway bursts, the SXR spikes and the Mirnov signal spikes are observed during the runaway plateau phase as shown in figure 4.7 (V) - (VII). The amplitudes of the spikes from different channels of each diagnostic are different indicating that the spikes are anisotropic. Runaway losses occur not equally in all directions. The excitation mode created during this period leads to enhanced runaway and hence the current decay rate increases.

During the disruption presented in figures 4.7 and 4.8, the runaway beam moves toward the LFS allowing the whole beam to be seen. The tip of the scintillator probe which is located at the LFCS is heated continuously by the lost REs and the runaways in the halo of the beam (see figure 4.8 white rings). Despite the increasing loop voltage, the runaway beam does not develop further due to the losses. The intensity at the center of the beam remains almost constant until the end of the

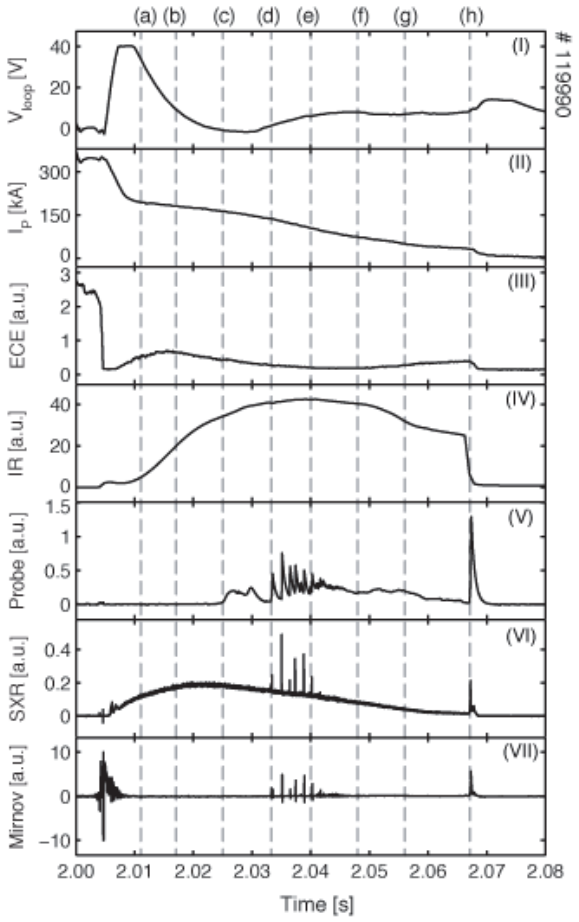

Figure 4.7: Temporal evolution of the disruption of discharge # 119990. Dashed lines (a) - (h) correspond to the sub-figures (a) - (h) in figures 4.8 (A) and (B).

discharge (see figure 4.8 (A)). No rapid change of synchrotron radiation is observed during the spiky phase. This indicates that most of the lost runaways are in the medium and low energy band.

In some disruptions of this case, a small channel connecting between the runaway beam and the probe is created during the spiky phase. In addition to the MHD activities, the generation of the loss channel seems to be influenced by the position of the runaway beam. The loss channel is built up only when the beam moves close to the scintillator probe. In some disruptions the channel last until the end of the

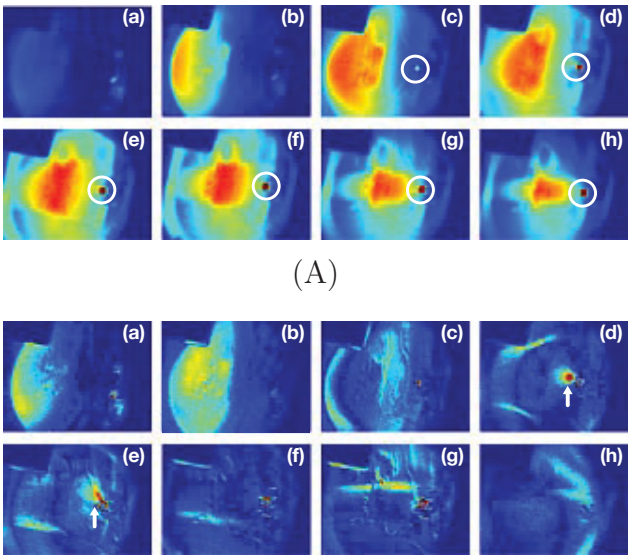

(A)

(B)

Figure 4.8: IR images in (A) the normal recording mode and (B) the subtraction mode for discharge # 119990 observed by the camera at (a) $t = 2.011$ s, (b) $t = 2.017$ s, (c) $t = 2.025$ s, (d) $t = 2.033$ s, (e) t= 3.040 s, (f) $t = 2.048$ s, (g) $t = 2.056$ s, and (h) $t = 2.067$ s. White rings indicate the scintillator probe tip and white arrows indicate areas of the interaction between the runaway beam and the probe.

discharges, while in the others it is present only during the spiky phase. However, no fast variations related to individual spikes are observed. The IR images in figures 4.8 (B) (d) and (e) show that the area of the interaction between the runaway beam and the scintillator probe is limited to a small area near the probe.

Case 3

Disruptions in this case seems to have a much shorter duration than in the other cases. In the example shown in figure 4.9, the plasma current ends apparently at $t \approx 2.015$ s. After this time, the SXR signal, Mirnov signal and the probe signal are zero. Nevertheless, a significant number of the high energy REs is observed by the IR camera (see figure 4.9 (IV)).

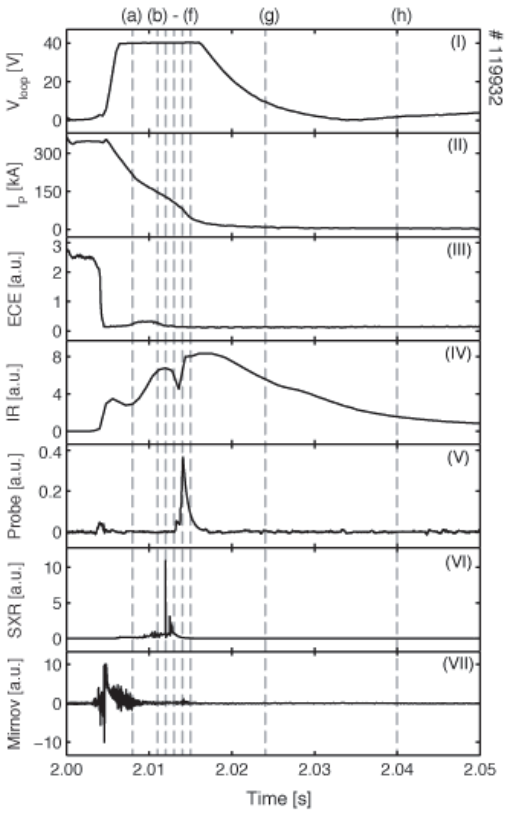

Figure 4.9: Temporal evolution of the disruption of discharge # 119932. Dashed lines (a) - (h) correspond to the sub-figures (a) - (h) in figures 4.10 (A) and (B).

A sharp SXR spike is observed at $t = 2.012$ (dashed line (c) in 4.9). At this time no runaway burst is detected by the probe. It is probably due to the fact that the beam is moved toward the HFS, i.e. away from the probe and hence the lost REs do not strike the probe. Afterwards, the runaway beam appears suddenly at the LFS (see figure 4.10 (A)). Parts of REs are lost and detected by the scintillator probe. The IR images in the subtraction mode in figure 4.10 (B) show that there is a small number of REs located at the LFS. Due to the high loop voltage, the survived REs which have energies only a little lower than 25 MeV are accelerated and become visible suddenly. The runaway beam decays slowly over tens of milliseconds.

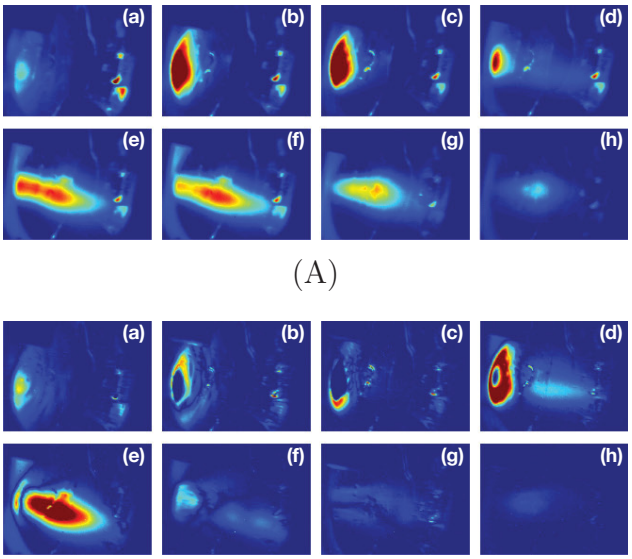

(A)

(B)

Figure 4.10: IR images in (A) the normal recording mode and (B) the subtraction mode for discharge # 119932 observed by the camera at (a) t = 2.009 s, (b) t = 2.011 s, (c) t = 2.012 s, (d) t = 2.013 s, (e) t= 2.014 s, (f) t = 2.015 s, (g) t = 2.024 s, and (h) t = 2.040 s.

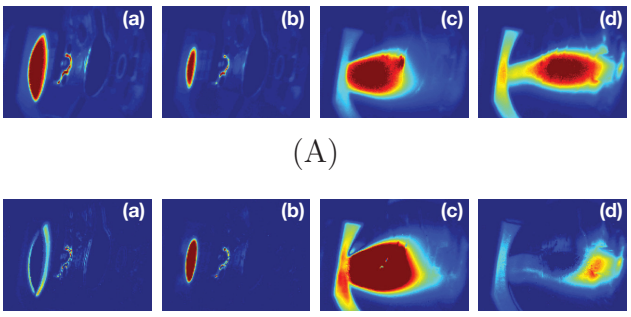

(A)

(B)

Figure 4.11: IR images in (A) the normal recording mode and (B) the subtraction mode for discharge # 117859 observed by the camera at (a) t = 2.020 s, (b) t = 2.024 s, (c) t = 2.027 s, and (d) t = 2.028 s.

It is still not clear whether the sudden appearance of the runaway beam at the LFS results form the acceleration of the REs existing at the LFS or the rapid movement of the beam towards the LFS. In another example shown in figure 4.11, the latter case is favourable. After the disruption is initiated by argon injection, the runaway beam becomes visible and develops at the HFS similar to the other disruptions. Then it moves toward the HFS due to the positive vertical field generated by the position control coils until it the entire beam is located outside the camera's field of view. When the runaway plateau termination takes place, the beam moves suddenly back to the LFS. Afterwards, the horizontally elongated beam stays at the center of the camera's view and decay gradually.

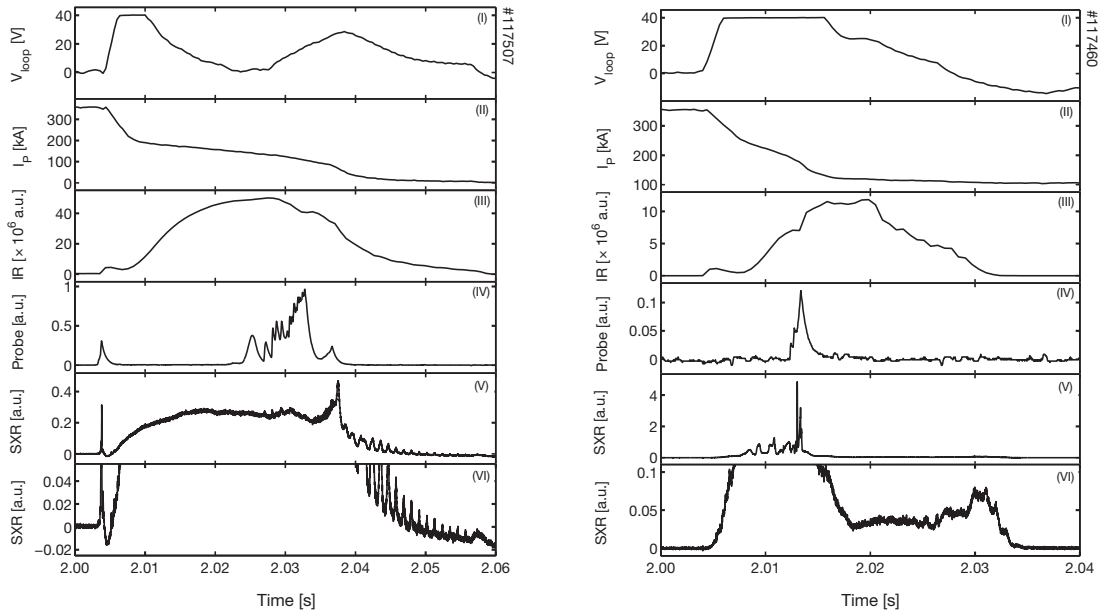

Figure 4.12: Temporal evolution of the disruption of (a) discharge # 117507 and (b) discharge # 117460: (top to bottom) time trace of the loop voltage, the plasma current, the electron cyclotron emission (ECE) signal, the intensities added over all pixels of the IR image, the scintillator probe signal, the soft X-ray (SXR) signal, and the magnified SXR signal.

In some disruptions of this case, the SXR signal is observed after the runaway plateau termination. The SXR signal shown in figure 4.12 (A) (VI) continues after the plateau termination until the runaway beam disappears. The SXR signal in this phase is quite high and can be clearly seen. In another example presented in figure 4.12 (B), conversely, the SXR signal seems to ends with the runaway plateau at $t \approx 2.016$ s. However, if the signal is magnified by a factor of about 50, a small SXR signal is observed. This confirmed that in some disruptions not all of the high energy REs are lost during the runaway plateau termination but a significant part of them is still confined by the plasma current of a few tens of kA.

4.4 Runaway parameters

As mentioned before, runaway parameters such as the radius of the runaway beam and the pitch angle including a position of the runaway beam and the number of the high energy REs can be obtained from the quantitative analysis of the synchrotron radiation emitted by the REs. Special care should be taken in determining the position of the runaway beam since the position of REs obtained from the synchrotron radiation differs from the position of the wall which emits the thermal radiation. It is because the synchrotron radiation is emitted only into the RE approach direction with a pitch angle θ, while the heated materials radiate in the full solid angle of 4π (see subsection 3.1.1). The position of the runaway beam relative to the position of the wall components can be obtained by drawing tangent lines of the runaway orbits. The position of the beam corresponds to the position of the wall components that the tangent line intersect. If the distance between the lens and each component of the wall is known, the position and size of the runaway beam can be determined.

The radial distribution at equatorial plane for discharge # 117527 at $t = 2.033$ s is shown in Fig. 4.13 (b). At this time the runaway beam reaches its maximum intensity and the whole beam is seen. The peak at $R \approx 2220$ mm originates from the thermal radiation emitted by the heated probe tip. Assuming the vertical size of the synchrotron spot is limited by the radius of a runaway beam, the runaway beam

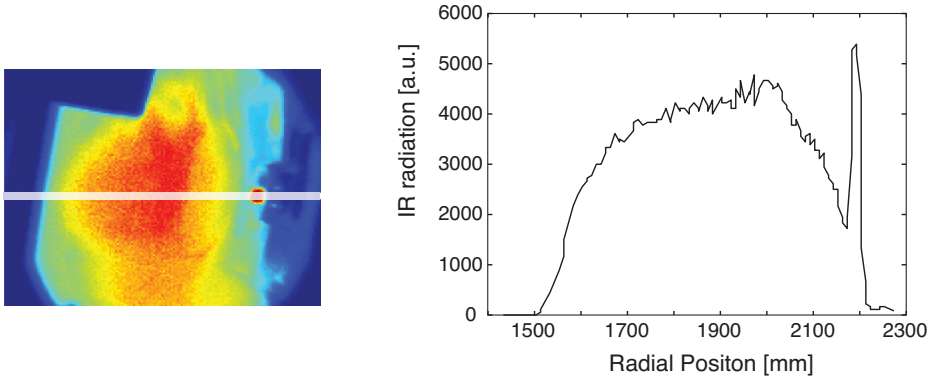

(a) (b)

Figure 4.13: (a) IR 2D image of discharge 117527 at t=2.033. (b) Radial distribution of IR image taken from the white line shown in (a)

of $r_{beam} = 30$ cm and the pitch angle of $\theta = 50$ mrad are deduced. The integration of the synchrotron radiation over the wavelength and the cross section gives the number of the high energy REs:

$$N_{RE} = \frac{L_\lambda A \Omega}{P_\lambda}. \tag{4.1}$$

Here, N is the number of REs, A is the area of the runaway beam cross section, and $\Omega = 2\pi \times 2\theta$. P_λ is the power emitted by one runaway electron described in subsection 3.1.1. The absolute value of the radiance L_λ is obtained by comparing the synchrotron radiation with the thermal radiation from the liner. For $\lambda = 4.5$ μm and $\gamma_{max} = 60$, the number of high energy REs of $N_{re} = 1.6 \times 10^{16}$ is deduced from the IR image shown in figure 4.13 (a).

In runaway-free disruptions, the plasma current decays exponentially. No plateau is formed (see section 4.2). The subtraction of the exponential decay from the plasma current of a runaway disruption gives the runaway current. The total number of runaway electrons can be calculated from the runaway current by using the relation:

$$N_{tot} = \frac{2\pi R_0 I_{re}}{ce}. \tag{4.2}$$

For discharge # 117527, the maximum runaway current is 148 kA. It corresponds to the total number of the runaway electrons of 3.4×10^{16}. The number of the high energy REs is about 47% of the total current.

4.5 Discussions

In order to provide the understanding of the runaway loss mechanisms during disruptions induced by gas injection and to describe the experimental observations presented in section 4.3, a new model has been developed in collaboration with the Institute of Energy and Climate Research of the research center Jülich (Forschungszentrum Jülich GmbH) [52, 53]. The magnetic topology of disruptions without and with REs are presented in figure 4.14 (a) and (b), respectively. In case of helium and neon injections, the injected gas can penetrates deep into the plasma core. The large amplitude $m/n = 1/1$ MHD mode is excited. A stochastic layer extends up to the plasma core. REs generated during the CQ are lost rapidly due to the high radial transport in the stochastic layer. In case of argon injection, on the contrary, the penetration depth of the injected gas is small. Due to a lower amplitude of the $m/n = 1/1$ MHD mode the stochastic layer does not cover the whole plasma but is formed only at the plasma edge.

The extent of the stochastic layer is influenced by the spectra of the perturbations and the radial profile of the safety factor ($q(\rho)$). The perturbations depend mainly on the disruption conditions and are different in each shot leading to a shot to shot variation of the runaway behaviour observed in the recent experiments. In case that the amplitude of the m/n = 1/1 mode is small enough, intact magnetic surfaces are created at the plasma center. The last intact magnetic surface is located between the $q = 1$ surface and the nearest low-order rational surface, e.g. m/n = 5/4 and 4/3.

During the CQ, only a small fraction of REs exists. The plasma current is carried primarily by thermal electrons. As a consequence of the energy loss during the TQ, the plasma temperature is low. The collisional transport dominates. The radial transport in the confined area is caused by small scale magnetic fluctuations. It is

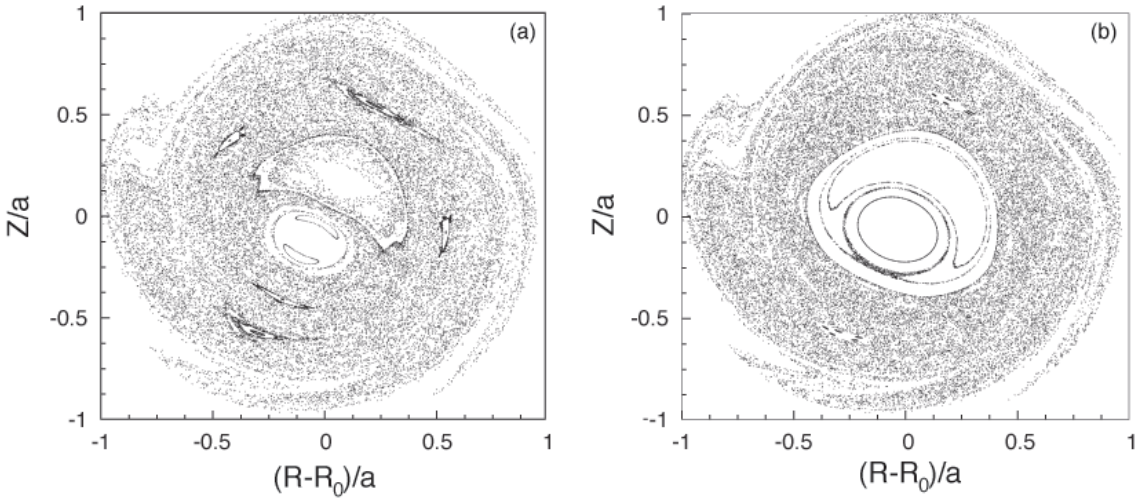

Figure 4.14: Poincaré plots of magnetic field lines for disruptions (a) without REs and (b) with REs. The safety factor at the magnetic axis is $q(0) = 0.8$ and at the plasma edge $q_a = 4.7$ [53].

much lower than the transport in the stochastic layer. Due to the increasing loop voltage REs are generated and accelerated. The REs created at the plasma core are well confined inside the good surfaces and can gain energy up to 30 MeV, while the REs at the plasma edge are lost immediately. This is consistent with the experimental observations shown in the previous sections that the runaway beams occupy only about one half of the initial plasma radius. The current decay rate during the CQ is determined by the radial transport of REs in the stochastic layer which is influenced by the level of magnetic perturbation and charged particle accelerations.

The current decays during the CQ and the runaway plateau phases obtained from the current experiments can be described by linear functions with different decay rates. The current decay rate during both phases as well as the initial runaway current of disruptions induced by argon injection are presented in table 4.1. Figure 4.15 shows the decay rates in both phases plotted as a function of the initial runaway current. The initial runaway current of the disruptions in case 1 (◯) and case 2 (□) varies between 175 kA and 250 kA. The initial runaway currents of these discharges correspond to the outermost intact magnetic surfaces $1 < q < 4/3$ and hence a stable runaway beam is obtained.

Shot No.	I_{re}^{ini} [kA]	dI/dt [MA/s] (CQ)	dI/dt [MA/s] (plateau)	Case
117430	205.8	39.81±0.39	2.76±0.07	2
117431	209.7	38.84±0.96	3.38±0.07	2
117432	205.6	40.24±0.43	2.92±0.07	2
117434	220.1	40.20±0.45	4.63±0.09	2
117438	242.6	37.32±0.11	2.95±0.06	3
117441	204.9	41.19±0.33	2.43±0.11	1
117442	200.2	42.79±0.48	2.77±0.07	1
117443	191.0	43.69±0.45	2.85±0.05	1
117458	170.8	43.71±0.46	17.39±0.06	3
117460	175.1	43.46±1.02	15.15±0.04	3
117507	251.2	42.70±0.71	4.29±0.14	3
117508	211.0	39.72±0.17	2.93±0.06	1
117509	186.7	41.72±0.25	2.54±0.07	1
117517	208.3	41.58±0.60	3.72±0.12	2
117518	215.3	38.83±0.22	3.04±0.17	1
117527	221.9	38.87±0.10	3.86±0.10	2
117528	250.5	39.50±0.53	3.35±0.09	3
117535	208.8	39.73±0.76	3.15±0.09	1
117859	296.0	33.20±1.11	11.70±0.50	3
119868	224.9	40.05±0.31	2.45±0.01	1
119871	221.1	39.90±0.60	2.07±0.11	1
119874	241.3	39.59±0.14	1.35±0.11	1
119932	269.0	37.95±0.69	15.22±0.07	3
119934	219.2	39.01±0.44	2.18±0.07	2
119935	206.0	41.51±0.44	2.17±0.06	2
119937	282.7	36.01±0.37	9.58±0.31	3
119939	222.2	40.53±0.15	2.19±0.06	2
119977	272.9	36.13±0.44	13.77±0.06	3
119978	219.7	38.80±0.76	3.38±0.02	2
119990	218.4	41.98±0.23	3.35±0.03	2
120101	235.0	38.20±0.31	1.54±0.10	2
120102	233.9	37.94±0.39	1.21±0.10	2
120121	213.9	39.60±0.36	1.99±0.08	2
120122	227.2	39.20±0.33	1.29±0.12	1
120123	236.0	36.40±0.47	3.66±0.01	1

Table 4.1: Initial runaway current (I_{re}^{ini}) and averaged current decay rate (dI/dt) during the current quench (CQ) and the runaway plateau phase of disruptions induced by argon injection for different cases.

The current decay rate during the CQ is about an order higher than the decay rate during the plateau phase. The current decay rate during the CQ decreases with increasing initial current. Since the initial current depends on the perturbations which define the extent of the stochastic layer at the plasma edge, this dependence might be affected by a perturbation level during the CQ.

For most of the disruptions in case 3, the initial runaway currents are either lower than 175 kA or higher than 250 kA corresponding to the outermost intact magnetic surfaces close to $q = 1$ and $q = 4/3$, respectively. The runaway beams created during such disruptions are not stable and decay more rapidly than the beams in the other cases (see figure 4.15 (b) (▷)). The runaway plateau is, therefore, very short. During disruptions in this case, sharp SXR spikes and Mirnov signal spikes are often observed.

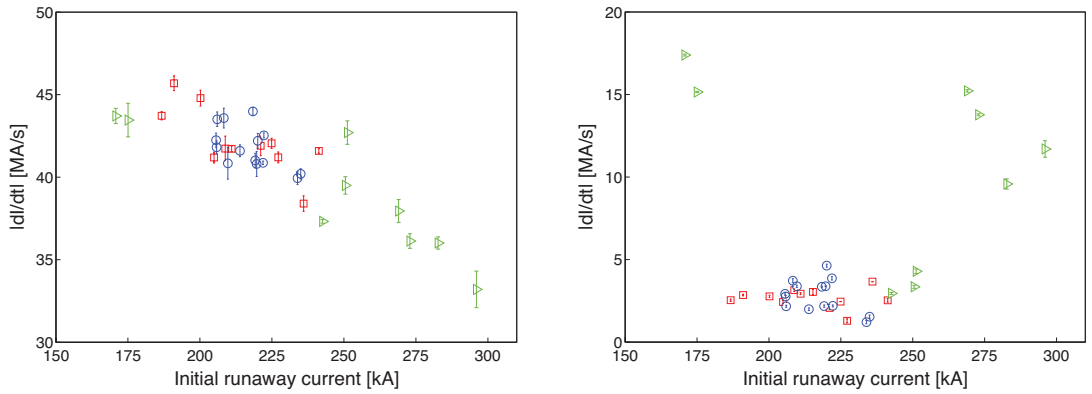

(a) (b)

Figure 4.15: The current decay rate $|dI/dt|$ as a function of the initial runaway current I_{re}^{ini} during (a) the CQ and (b) the runaway plateau phases of disruptions for case 1 (◯), case 2 (□) and case 3 (▷).

During disruptions, the low-mode number MHD modes are excited nonlinearly. Consequently magnetic islands and a stochastic layer are formed at the plasma edge. Only REs which are trapped in the magnetic islands can stay longer in the plasma. A similar effect had been observed earlier by R. Jaspers et al where a large magnetic island was created by pellet injection [90]. The rotation of the stable islands embedded in the stochastic sea following the rotation of the m/n = 1/1 helical magnetic

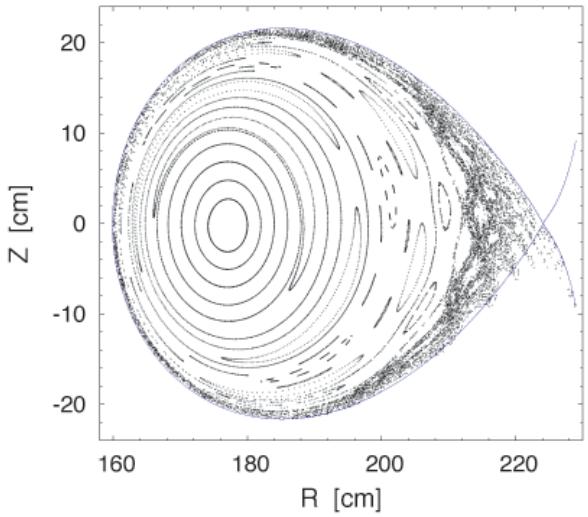

Figure 4.16: Poincaré plot of the RE guiding center for the RE energy of $W_{re} = 20$ MeV and the runaway current of I_{re} =100 kA [53].

perturbation as shown in figure 4.16 is responsible for the observed stripes in case 1 (see figure 4.6). The runaway orbit structures can be observed only when the frequency of the plasma rotation is in the same range as the recording frequency of the camera, i.e. $\sim$ 1 kHz.

For disruptions with loss spikes accompanied by MHD activities as discussed in case 2, a filamented beam which results from tearing mode dominated magnetic islands was expected [22]. In JET [91] the conclusion that the runaway beam is filamented was drawn from the fluctuation of the interaction between runaways and the wall although the soft X-ray image shows a smooth beam. In the recent study, however, no indications of the laminar structures but the diffusive losses of REs have been observed by the IR camera in such disruptions. It is still not clear whether they do not exist or their rotational frequency does not match the camera's capture frequency. The observed structures are, therefore, smeared out and are not detected.

The comparison between the plasma current of a discharge in case 1 (black) and in case 2 (red) presented in figure 4.17 shows that at the beginning of the plateau phase, the currents in both cases decay as a linear function of time with a decay rate

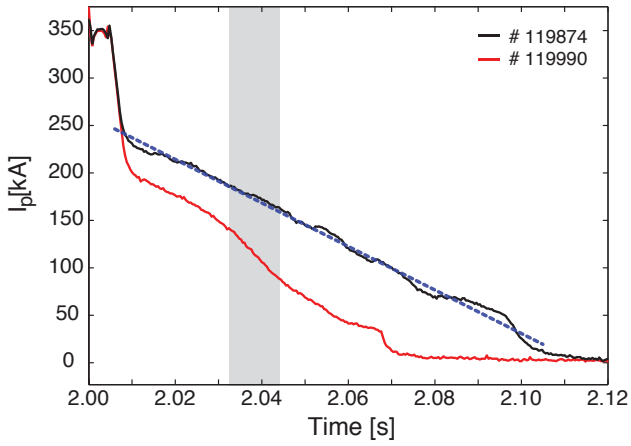

Figure 4.17: The plasma current of the discharges # 119874 (black - quiet disruption) and # 119990 (red - spiky disruption). A dashed blue line represents a linear fit of the current of the discharges # 119874. A gray are indicates the spiky phase.

of about 2.5 MA/s. During the spiky phase, the decay rate of the disruption in case 2 increases to 4.1 MA/s. For the disruption in this case, the MHD activities during the runaway plateau phase are normally accompanied by a stepwise reduction of the plasma current which indicates a significant loss of REs.

Despite an enhanced runaway loss, the observed synchrotron radiation changes only slightly (see figure 4.8) indicating that the major part of the high energy REs are well confined within the plasma while the REs in the low energy range are lost. This agrees well with results presented in the previous study [22]. The analysis of the signal from different crystals of the scintillator probe shows that the spectrum of the lost runaways can be described by an exponential decay function with an exponent of $n_{r_0} \sim 10$ MeV. The number of lost runaways in the low energy range is much higher than those from the high energy range.

During the spiky phase a loss channel which connects between the runaway beam and the probe is created if the runaway beam is located close to the probe. The loss channel is observed only during the spiky disruptions. The creation of the loss channel seems to be influenced by the location of the beam and the MHD activities. In case that the beam moves toward the wall at the HFS, the MHD activities are

also observed. Unfortunately, this area is located outside the camera's field of view. Nevertheless, it is suspected that a loss channel connecting between the beam and the wall is created as well.

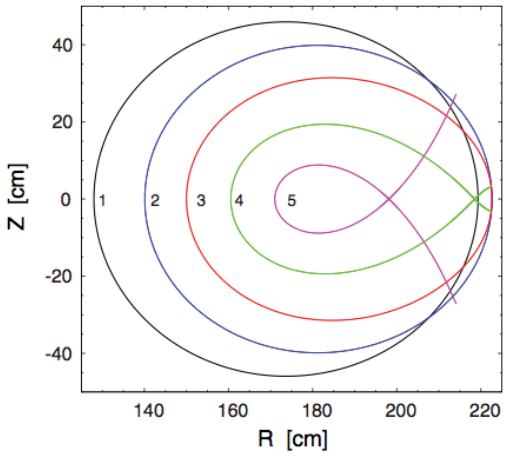

Figure 4.18: Separatrices of the orbits of REs with energies of 1 MeV, 5 MeV, 10 MeV, 20 MeV and 40 MeV [48].

The theoretical calculation shows that the runaway confined area decreases with increasing runaway energy as can be seen in figure 4.18. Only the REs located inside the separatrix can be confined. Otherwise they are lost rapidly. In case 1 and case 2, stable runaway beams are created. The beams decay gradually due to the outward drift of runaway orbits (see 2.3.3) and the shrinkage of the confined area as the energies of REs increase. In case 2, a rapid loss of a part of REs during the plateau phase results from an interaction between MHD modes and REs.

As already mentioned in section 2.3 that the ergodization of the orbits of the low energy REs is stronger than that of the high energy ones. This is consistent with the experimental observation. For disruptions in case 3, the runaway beams are not stable and hence a significant part of REs are lost rapidly. The lost REs are mainly the super thermal electrons and the low energy REs which carry a large fraction of plasma current. The loss of these electrons results in a strong drop of the plasma current leading to an increase in the loop voltage. The high energy REs which survive the plateau termination are accelerated further as can be seen in figures 4.10 and

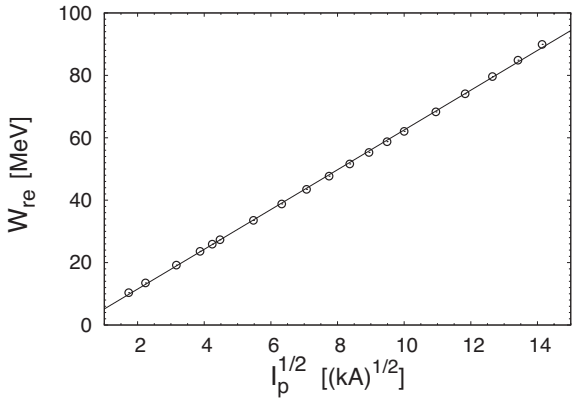

Figure 4.19: Numerical calculation results of the maximum runaway current W_{re} that can be confined by a given plasma current plotted as a function of square root of plasma current I_p (symbols $\odot$). The solid line presents the fitting line: $W_{re} = a + bI_p^{1/2}$ with $a = 3.53924$ and $b = 6.86593$ [48].

4.11. A rapid outward movement of the runaway beam is often observed during the disruptions in case 3. A significant number of REs are still observed although the plasma current drops to almost zero. According to the theoretical calculation presented in [48], a plasma current of only $\sim$ 20 kA is required to confine REs with energy of 25 MeV. In the examples discussed in case 3, the current after the plateau termination drops to a few tens of kA. The current is still higher than the critical current and is sufficient to confine high energy REs which survive the plateau termination. The minimum plasma current required to confine REs increases with increasing runaway energy (see figure 4.19). The relationship between the runaway energy W_{re} and the minimum plasma current I_p is given by: $W_{re} = a + bI_p^{1/2}$, where a and b are constants. For $a = 3.5$ and $b = 6.9$. For the disruptions in case 1 and in case 2, no REs are observed after the plateau termination because either the plasma current is too low or the runaway beam might move toward the LFS and touch the wall. REs are, therefore, lost instantaneously.

5 Runaway mitigations

This chapter presents the study of the effects of the runaway mitigation techniques, namely fast gas injection and resonant magnetic perturbation (RMP). First, disruptions are initiated by an argon injection at $t = 2$ s under the same conditions as the previous chapter. Next, the runaway mitigation methods are applied separately in order to enhance the runaway loss. REs which are generated during the disruptions should be deconfined before they have time to gain high energies and hence the damage to the wall and other components caused by the high energy REs is reduced.

In addition to valve 1 which is used as a disruption initiation valve, valve 2 and valve 3 have been developed and applied at TEXTOR in order to mitigate the disruption effects. Valve 2 successfully suppressed REs generated in low density discharges [92]. It is, therefore, expected that valve 2 is sufficient to suppress REs during disruption as well. The runaway mitigation effect of the fast gas puff performed by valve 2 is presented in section 5.1. Additionally, the influence of the injected gas performed by valve 3, which has a larger orifice diameter, on the runaway confinement is investigated in section 5.2.

Another technique used to suppress REs at TEXTOR is the RMPs. In low density discharges, the runaway loss is increased when the RMP field created by the DED 6/2 mode is applied [93]. The application of the DED 6/2 mode and 3/1 mode in the runaway mitigation during disruptions are discussed in section 5.3 and 5.4, respectively.

5.1 Fast gas injection performed by valve 2

In the previous study on runaway mitigation [76], helium injection was used because the deposition of helium in the wall is small. Additionally, a mixing efficiency of low-Z impurities in the plasma is higher than the high-Z impurities. However, its radiative cooling is lower by three orders of magnitude than that of an argon puff [15]. In the recent study the application in runaway mitigation during disruptions of injection of helium which can suppress the REs during runaway discharges in the low density regime, as well as higher Z impurities such as neon and argon are investigated.

Figure 5.1 shows the mitigation effect of a neon puff in comparison with that of an argon puff. 2.2×10^{22} atoms of gas are injected at $t = 2.015$ s. In case of neon (black curves), the first SXR peak is present at $t = 2.019$ s, i.e. 4 ms after the gas injection (dashed line (a)). 3 ms later, the MHD activities accompanied by enhanced runaway losses are observed (see figure 5.1 dashed line (b)). The runaway current decreases in a stepwise pattern. Shortly thereafter, the scintillator probe signal and SXR signal which are an indication of runaway losses are detected throughout the runaway plateau phase. When the runaway plateau is terminated, a SXR signal peak is present, while no runaway burst is observed by the scintillator probe. Since the probe is located at the last closed flux surface (LFCS), it can detect only the REs that are lost toward the location of the probe. During the plateau termination, the REs may be lost in other directions and do not hit the probe.

At $t = 2.022$ s when the MHD activities are detected, the intensity at the center of the beam decreases instantaneously (see figure 5.2 (A)). The losses occurred during this event inhibit the development of runaway beam. Thereafter, intensity at the center of the beam does not increase further but remains almost constant whereas the intensity at the edge of the beam fluctuates as can be seen in figure 5.2 (B) (c) and (d). These fluctuations, which are not observed in typical induced disruptions, represent the perturbations initiated by the injected gas.

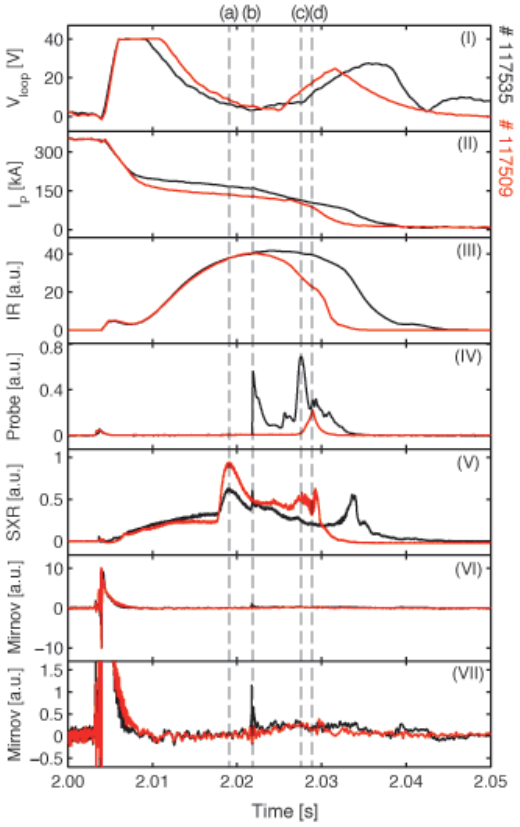

Figure 5.1: Temporal evolution of the disruptions mitigated by an injection of 2.2 $\times 10^{22}$ atoms of neon (black) and argon (red): (top to bottom) time trace of the loop voltage, the plasma current, the intensities added over all pixels of the IR image, the scintillator probe signal, the soft X-ray (SXR) signal, the Mirnov signal, and the magnified Mirnov signal. Dashed lines (a) - (d) correspond to the sub-figures (a) - (d) in figure 5.2 (A) and (B) and figure 5.3 (A) and (B).

In comparison with the case of neon injection, the effect of injected argon is detected a little bit later because argon needs a longer time to travel from the valve to the plasma. In figure 5.1, it is clearly seen that an argon injection provides a stronger effect on the runaway confinement. Although the same amount of gas is injected at the same time for both cases, the runaway plateau length in case of argon is $\sim$ 30 ms shorter than the plateau length in case of neon.

During the plateau phase, no peak in the probe signal or Mirnov signal is present. Only SXR peaks are observed until the runaway plateau termination indicating that REs are lost continuously. At $t = 2.029$ s when the runaway plateau is terminated, a runaway burst is present followed by a SXR peak.

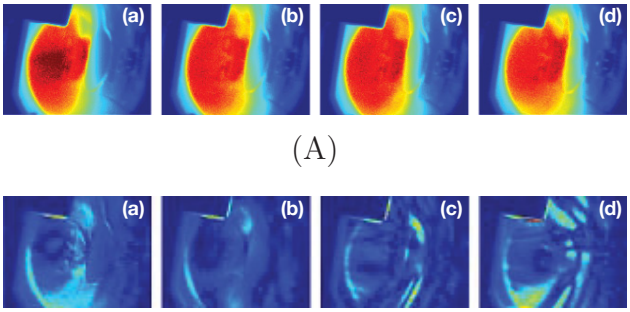

Figure 5.2: IR images in (A) the normal recording mode and (B) the subtraction mode for discharge # 117535 observed by the camera at (a) $t = 2.019$ s, (b) $t = 2.022$ s, (c) $t = 2.027$ s, and (d) $t = 2.029$ s.

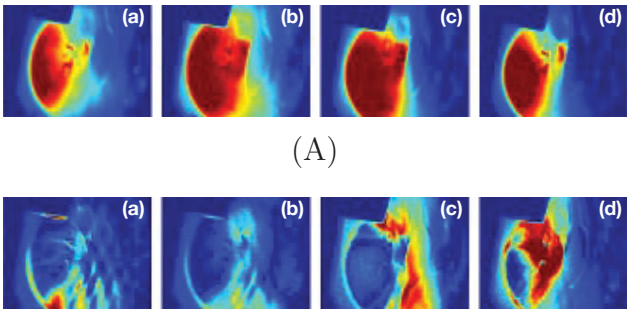

Figure 5.3: IR images in (A) the normal recording mode and (B) the subtraction mode for discharge # 117509 observed by the camera at (a) $t = 2.019$ s, (b) $t = 2.022$ s, (c) $t = 2.027$ s, and (d) $t = 2.029$ s.

The evolution of the runaway beam observed by the IR camera during a disruption mitigated by an argon injection is shown in figure 5.3 (A). In contrast to the previous example, no rapid change is observed here. During the plateau phase, the beam intensity increases gradually with time. All REs are lost suddenly at $t \approx 2.031$ s when the plateau termination takes place.

Figure 5.2 (B) (a), which is obtained from consecutive image subtraction, presents stripe patterns similar to the stripes observed during typical induced disruptions case 1 (see also figure 4.6 (B)). These stripes appear shortly after the beam becomes visible to the camera. Their patterns change with time. After the first SXR peak is detected, the stripes slowly disappear. In this example, the intensity fluctuations at the edge of the beam which indicate the presence of the perturbations are not observed. However, the runaway beam shrink faster than that in the previous example.

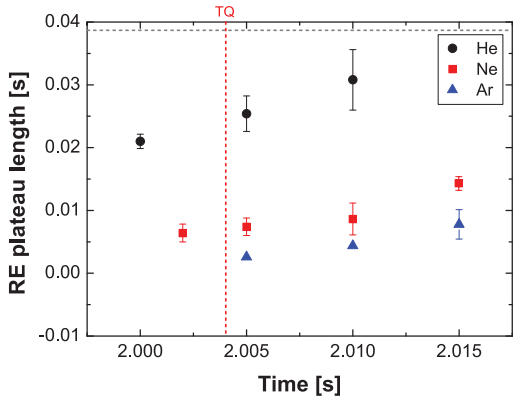

Figure 5.4: Averaged runaway plateau length of the induced disruptions mitigated by gas puffs of helium (black), neon (red) and argon (blue). 2.2 $\times 10^{22}$ atoms of gas are injected by valve 2 at different times. The x-axis indicates the time when valve 2 is triggered. A grey dashed line presents an averaged plateau length of typical induced disruptions and a red dashed line the TQ time.

Figure 5.4 illustrates an effect of the injected gas on the runaway plateau length which is determined by the width of the runaway current curve. The abscissa is the runaway plateau length and the ordinate the time when the gas is injected by valve 2. 2.2 $\times 10^{22}$ atoms of argon, neon and helium are injected separately at different times. For each conditions, 2-5 measurements have been curried out. The plateau lengths presented here are average values of the plateau lengths observed in all discharges under the same condition and the error bars demonstrate the standard deviations. Runaway plateaus of the mitigated disruptions for all conditions are lower than the

average runaway plateau length of unmitigated ones (a gray dashed line). It has been found that the earlier the gas is injected after the start of the disruption, the stronger the mitigation effect is obtained. Among these different types of gas, argon provides the strongest effect. However, the fast injection performed by valve 2 is not sufficient to completely suppress REs.

5.2 Fast argon injection performed by valve 3

In this section, helium and neon injections are excluded due to their weaker influence on the runaway confinement in comparison with argon injections. Only the runaway mitigation effect of argon injections performed by valve 3 is investigated. Different amounts of argon from 2.7×10^{21} atoms up to 5.3×10^{22} atoms are injected at different times.

Figure 5.5 presents the temporal evolution of two disruptions which are mitigated by an injection of 1.3×10^{22} atoms of argon. In discharge # 119989 (black curves), argon is injected at $t = 2.004$ s, i.e. when the TQ takes place. The length of the plateau is much shorter than that of unmitigated disruptions. A SXR spike and a Mirnov spike are present at 7 ms after the mitigation valve is triggered (dashed line (a*)). However, no runaway burst is observed at this time. At the plateau termination phase, a runaway burst and a SXR spike are detected (dashed line (c*)). Afterwards, the IR signal increases indicating that a part of runaway electron survives the plateau termination. This has been also observed before in unmitigated disruptions discussed in section 4.3 case 3. However, this part of REs in this discharge decays faster than that in the unmitigated disruptions.

The IR images in figure 5.6, shows that the runaway beam in this example becomes visible and stays at the HFS throughout the runaway plateau phase. When the plateau termination takes place, the main part of REs are lost, while a small part

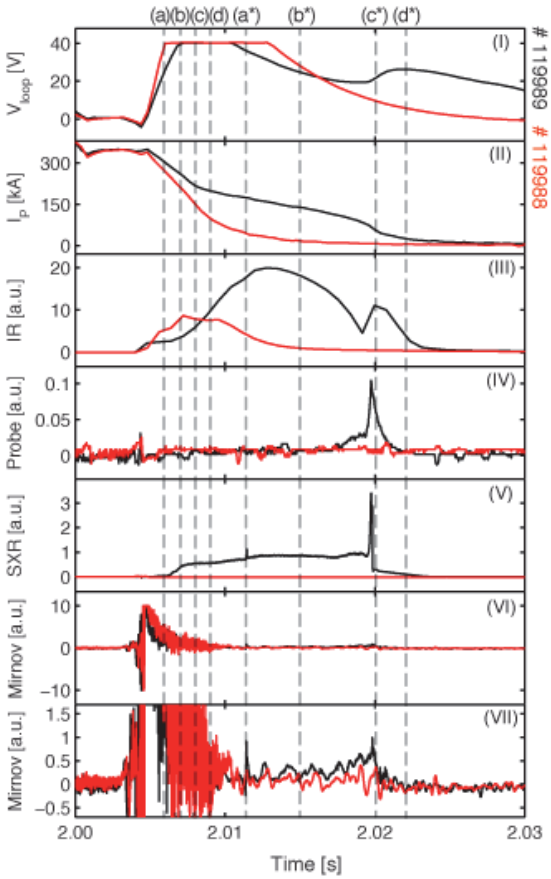

Figure 5.5: Temporal evolution of the disruption of discharge mitigated by an injection of 1.3×10^{22} atoms of argon at $t = 2.004$ s (black) and $t = 2.003$ s (red). Dashed lines (a*) - (d*) correspond to the sub-figures (a) - (d) in figures 5.6 (A) and (B). Dashed lines (a) - (d) correspond to the sub-figures (a) - (d) in figures 5.7 (A) and (B).

remains confined in the plasma. Considering figures 5.6 (A) (d) and (d) and (B) (c) and (d), it seems that the remaining part moves suddenly to the LFS similar to the observations discussed in section 4.3 case 3 (see figure 4.11).

In discharge # 119988, argon is injected 1 ms earlier than the previous example. Here, no indication of the presence of REs is observed (see figure 5.5 (red curves)). The plasma current decays exponentially. No runaway plateau is present. Neither RE burst nor a SXR spike nor a Mirnov oscillation is detected. An increase in

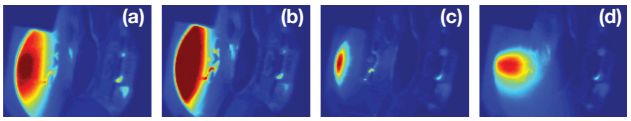

(A)

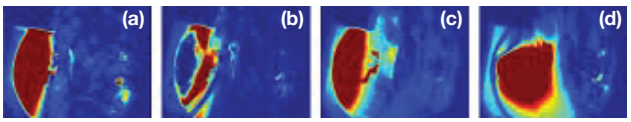

(B)

Figure 5.6: IR images in (A) the normal recording mode and (B) the subtraction mode for discharge # 119989 observed by the camera at (a) $t = 2.011$s, (b) $t = 2.015$ s, (c) $t = 2.020$ s, and (d) $t = 2.022$ s.

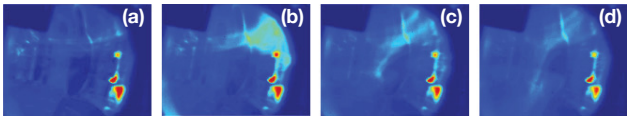

Figure 5.7: IR images in (A) the normal recording mode and (B) the subtraction mode for discharge # 119988 observed by the camera at (a) $t = 2.006$ s, (b) $t = 2.007$ s, (c) $t = 2.008$ s, and (d) $t = 2.009$ s.

the intensity of the IR radiation is originated from the IR radiation emitted by the injected gas and from the thermal radiation emitted by the heated wall.

The runaway mitigation effect of the argon injection performed by valve 3 shown in figure 5.8 has a similar trend as in case of the argon injection performed by valve 2. A shorter runaway plateau length is obtained by the earlier injection. Owing to the fact that valve 3 is installed closer to the plasma than valve 2 and has a larger orifice diameter, valve 3 provides stronger effects. In case of runaway mitigation by valve 2, a complete suppression cannot be achieved. Despite a smaller amount of gas injected by valve 3, it is sufficient to provide runaway-free disruptions if the gas is injected early enough. The minimum amount of injected argon required for complete runaway suppression is $\sim 1.3 \times 10^{22}$ atoms. These impurities has to be injected at ≤ 3 ms after the disruption is triggered, otherwise the effect is minor.

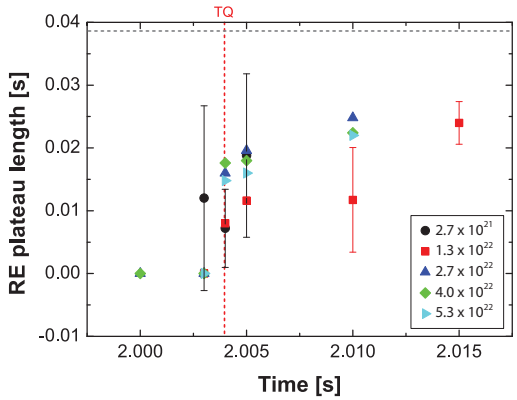

Figure 5.8: Averaged runaway plateau length of the induced disruptions mitigated by argon puff: 2.7 $\times 10^{21}$ atoms (black), 1.3 $\times 10^{22}$ atoms (red), 2.7 $\times 10^{22}$ atoms (blue), 4.0 $\times 10^{22}$ atoms (green), 5.3 $\times 10^{22}$ atoms (light blue). Gas puffing is performed by valve 3. The x-axis indicates the time when valve 3 is triggered. A grey dashed line presents an averaged plateau length of typical induced disruptions and a red dashed line the TQ time. The large error bars are caused by the strong deviation of the plateau lengths of some shots from the average values.

5.3 DED 6/2 mode

In this section, the runaway mitigation effect of the RMPs created by the DED 6/2 mode is studied.The DED with currents from a few kA up to 7 kA is applied at different times before disruptions are triggered by argon injections.

Temporal evolutions of the disruptions mitigated by the DED 6/2 mode with its maximum current of 7 kA applied at $t = 2.00$ s (black curves) and at $t = 1.7$ s (red curves) are illustrated in figure 5.9. Since it takes 90 ms to reach the maximum current after the DED is triggered, the DED current is not constant during the disruption in the former discharge (discharge # 120103). In the later discharge (discharge # 1201114), the DED current reaches its maximum before the a disruption is triggered and is kept constant throughout the disruption.

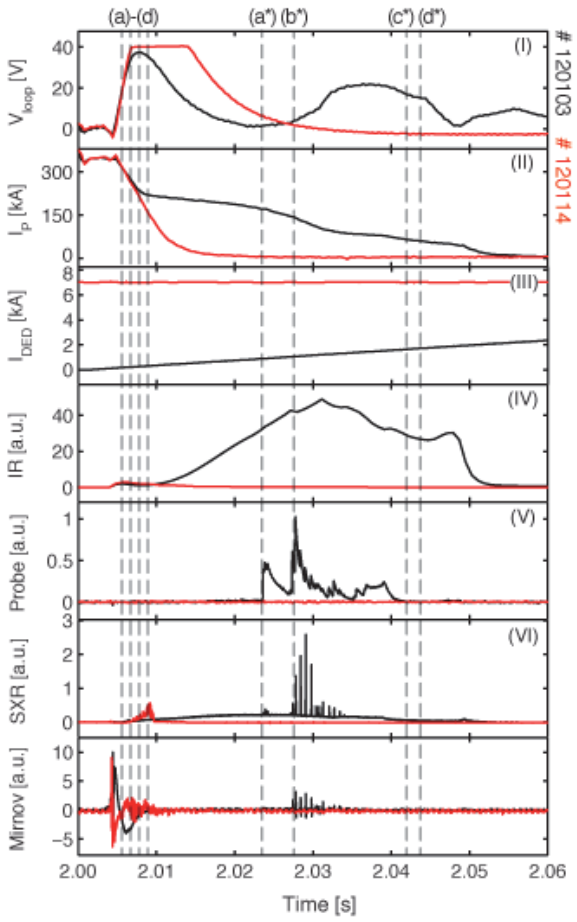

Figure 5.9: Temporal evolution of the disruption mitigated by the DED 6/2 mode with its maximum current of 7 kA applied at $t = 2.00$ s (black) and $t = 1.70$ s (red): (top to bottom) time trace of the loop voltage, the plasma current, the DED current, the intensities added over all pixels of the IR image, the scintillator probe signal, the soft X-ray (SXR) signal, and the Mirnov signal. Dashed lines (a*) - (d*) correspond to the sub-figures (a) - (d) in figures 5.10 (A) and (B). Dashed lines (a) - (d) correspond to the sub-figures (a) - (d) in figures 5.11 (A) and (B).

In discharge # 120103, sharp SXR and Mirnov spikes including runaway bursts are detected during the plateau phase from $t = 2.024$ s to $t = 2.039$ s. The stepwise reduction of the plasma current is observed at $t = 2.027$ s (dashed line (b*)), at which the highest peak of the scintillator signal is present. Additionally, the intensities

added over all pixels of the IR image also drop slightly. This indicates that at this time a significant amount of REs in both the lower energy range and the higher energy range are lost. At the end of the discharge, the intensities added over all pixels of the IR image drop suddenly to zero. All REs are lost. However, no spikes in the probe signal, SXR signal and Mirnov signal are observed.

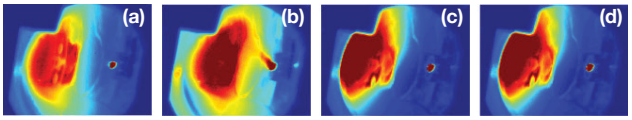

(A)

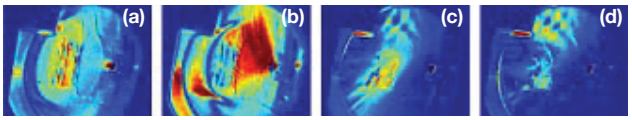

(B)

Figure 5.10: IR images in (A) the normal recording mode and (B) the subtraction mode for discharge # 119989 observed by the camera at (a) $t = 2.024$s, (b) $t = 2.027$ s, (c) $t = 2.042$ s, and (d) $t = 2.044$ s.

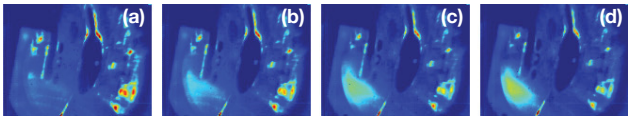

Figure 5.11: IR images in (A) the normal recording mode and (B) the subtraction mode for discharge # 119988 observed by the camera at (a) $t = 2.006$ s, (b) $t = 2.007$ s, (c) $t = 2.008$ s, and (d) $t = 2.009$ s.

The observation of the radiation by the IR camera indicates that REs are lost continuously from the beginning of the runaway plateau phase. Shortly after the runaway beam becomes visible at the HFS, the thermal radiation emitted by the heated probe is detected. Although only the halo of the runaway beam touches the probe, the IR intensity at the scintillator probe tip increases gradually. When the beam moves close to the probe, a narrow channel which connects the runaway beam to the probe is created (see figure 5.10) and the spiky phase begins. This narrow channel has been also observed in unmitigated disruptions and is discussed

in section 4.3 case 2. Sharp SXR spikes and Mirnov spikes including runaway bursts are observed until the beam is moved away from the probe. The channel then slowly disappears. After the spiky phase, strip patterns are observed in the IR images in the subtraction mode (see figure 5.10) (B) (c) and (d). These stripes are similar to the stripes observed previously both in unmitigated disruptions and the disruptions mitigated by argon injection discussed in section 4.3 case 1 and section 5.1, respectively.

Considering the red curves in figure 5.9, the plasma current, the intensities added over all pixels of the IR image, the probe signal and the Mirnov signal do not show any indications of the presence of the REs. Nevertheless, a small SXR peak is present directly after the TQ phase. Additionally, a small number of REs are observed by the IR camera as shown in figure 5.10. The runaway beam becomes visible at the HFS at $t \approx 2.006$ s. A few milliseconds later, it disappears instantaneously.

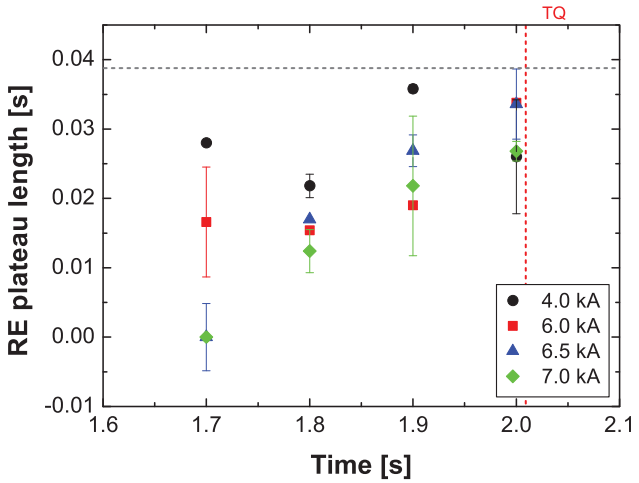

Figure 5.12: Averaged runaway plateau length of the induced disruptions mitigated by the DED 6/2 mode. DED currents of 4 kA (black), 6 kA (red), 6.5 kA (blue) and 7 kA (green) are applied (separately) at different times. The x-axis indicates the time when the DED is applied. A grey dashed line presents an averaged plateau length of typical induced disruptions and a red dashed line the TQ time.

Figure 5.12 presents the influence of the applied DED 6/2 mode on the runaway confinement time, i.e. the runaway plateau length. REs are quickly lost when the

DED with current $I_{DED} \geq 6.5$ kA is applied at $t \leq 1.7$ s. The effect of the DED on the runaway confinement decreases drastically if the DED is applied later. Since a disruption is a transient event, a prompt response is required for runaway mitigation. This technique is, therefore, not suitable for runaway mitigation during disruption because the DED has to be switched on at least 0.3 s before a disruption takes place. However, it is still not sufficient to provide a runaway-free disruption.

5.4 DED 3/1 mode

When DED in the 3/1 mode is applied to the plasma, the tearing modes are created in the plasma when the DED current exceeds about 0.7 kA. The core electron temperature drops as shown in figure 5.13. This is a characteristic for the tearing mode excitation. After the DED 3/1 mode is activated, the DED current increases slowly and reaches 1 kA at 20 ms after the activation time. The ECE starts to decrease exponentially at 100 ms after DED is switched on. At the time that the TQ takes place, the ECE drops drastically. The ECE then rises when the REs are

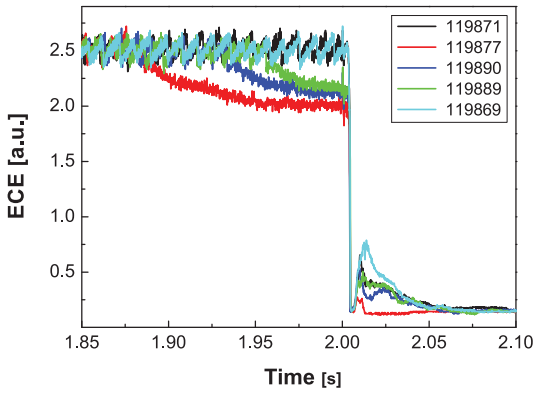

Figure 5.13: Temporal evolution of ECE signal of discharge # 119871 (black) : without DED, discharge # 119877 (red) : DED of 2 kA applied at t = 1.8 s, discharge # 119890 (blue) : DED of 1 kA applied at t = 1.82 s, discharge # 119889 (green) : DED of 1 kA applied at t = 1.84 s, and discharge # 119869 (light blue) : DED of 1 kA applied at t = 2.01 s.

generated. Figure 5.13 shows that the ECE peak after the TQ decreases when the DED is applied. The earlier the DED is triggered, the stronger runaway suppression is observed. If the DED is applied after the TQ, the ECE peak is even higher than in the typical induced disruption.

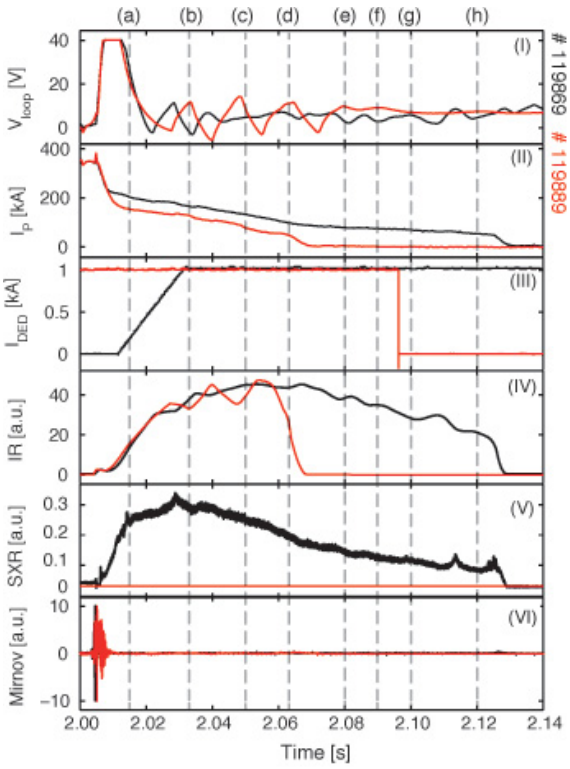

Figure 5.14: Temporal evolution of the disruption of discharge # 119869 (black) and discharge # 119889 (red): (top to bottom) time trace of the loop voltage, the plasma current, the DED current, the intensities added over all pixels of the IR imagel, the soft X-ray (SXR) signal, and the Mirnov signal. The DED 3/1 mode with the current of 1 kA triggered at $t =$ 2.01 s and $t = 1.82$ s in discharge # 119869 and discharge # 119889, respectively. Dashed lines (a) - (h) correspond to the sub-figures (a) - (h) in figures 5.15 (A) and (B). Dashed lines (a) - (d) correspond to the sub-figures (a) - (d) in figures 5.16 (A) and (B). In these discharges, the scintillator probe is not applied.

In discharge # 119869, the DED is applied at $t = 2.01$ s, i.e. after the disruption is triggered. Contrary to the expectation, the late injection results in an improvement of the RE confinement (see figure 5.14 (black curves)). A long runaway plateau is present. This is consistent with the observation of the ECE signal discussed above. Since the loop voltage remains around zero, no sudden runaway acceleration takes place. The runaway current decays slowly and no SXR spike or Mirnov spike is observed. Here, the scintillator probe is not applied.

During the runaway plateau phase, the runaway beam moves slightly forth and back. No sudden change in the beam intensity or the beam shape is observed (see figure 5.15 (A)). In contrast to the IR images in the normal recording mode, spectacular structures have been observed in the images in the subtraction mode (see figure 5.15 (B)). The structure reaches deep into the runaway beam as expected. These structures could either result from the external ergodization of the DED or the internal ergodization by the mode.

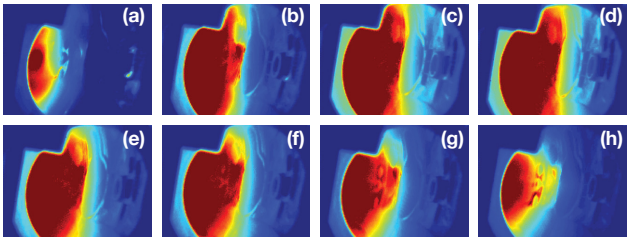

(A)

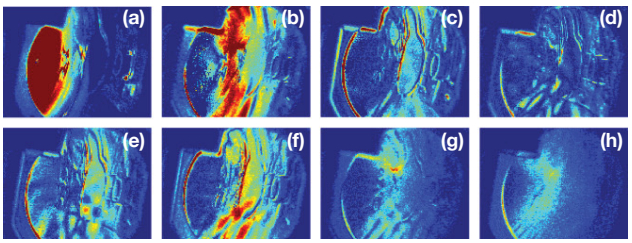

(B)

Figure 5.15: IR images in (A) the normal recording mode and (B) the subtraction mode for discharge # 119869 observed by the camera at (a) $t = 2.015$s, (b) $t = 2.035$ s, (c) $t = 2.050$ s, (d) $t = 2.063$ s, (e) $t = 2.080$ s, (f) $t = 2.092$ s, (g) $t = 2.10$ s, and (h) $t = 2.12$ s.

When the DED 3/1 mode is applied earlier, a suppression of the REs is achieved (see figure 5.14 (red curves)). In this discharge, the DED 3/1 is triggered at $t = 1.82$ s. In contrast to the previous example, here the DED current is constant throughout the disruption. The runaway plateau length in this discharge is much shorter than that in the previous one. The fluctuation presented in the intensities added over all pixels of the IR image is caused by the movement of the runaway beam. The plasma current is also affected by the movement. The stepwise reduction of the plasma current is observed when the beam moves towards the HFS. No Mirnov spike is observed. Unfortunately, the data acquisition system for SXR signal failed in this discharge. Therefore, the information of SXR is not available. Shortly before the end of the discharge, REs at the edge of the runaway beam are lost and the beam becomes elongated horizontally (see figure 5.16 (A) (d)). An intensity fluctuation at the edge of the beam is present in the IR images in the subtraction mode as shown in (see figure 5.16 (B) (c) and (d)), This fluctuation has been observed before in the disruption mitigated by neon injection (see figure 5.2 (B)). However, the fluctuation observed here is located deeper inside the beam in comparison with the fluctuations detected in case of neon injection.

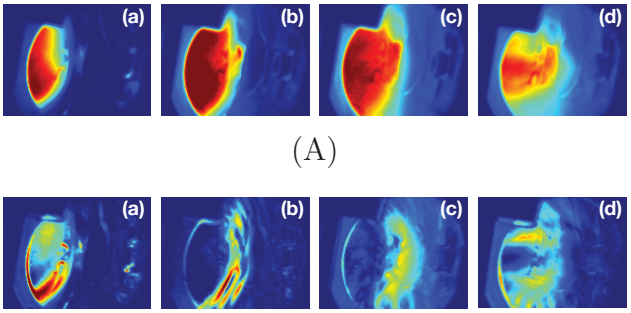

Figure 5.16: IR images in (A) the normal recording mode and (B) the subtraction mode for discharge # 119889 observed by the camera at (a) $t = 2.015$s, (b) $t = 2.035$ s, (c) $t = 2.050$ s, and (d) $t = 2.063$ s.

Figure 5.17 shows that the length of the runaway plateau decreases when DED is applied except in the case when the DED of 1 kA is applied after the TQ. The length of the runaway plateau increases with increasing trigger time. If the DED is

applied after the TQ, the runaway confinement time increases, possibly because a barrier has formed. The effective impact of DED 3/1 mode on the RE confinement can be achieved if DED is applied at $t \leq 1.8$ ms. DED 3/1 mode provides a shorter response time than the 6/2 mode. It causes the generation of tearing modes at the plasma edge. Moreover, it can penetrate deeper into the plasma leading to a higher loss rate. A complete RE suppression could not be achieved.

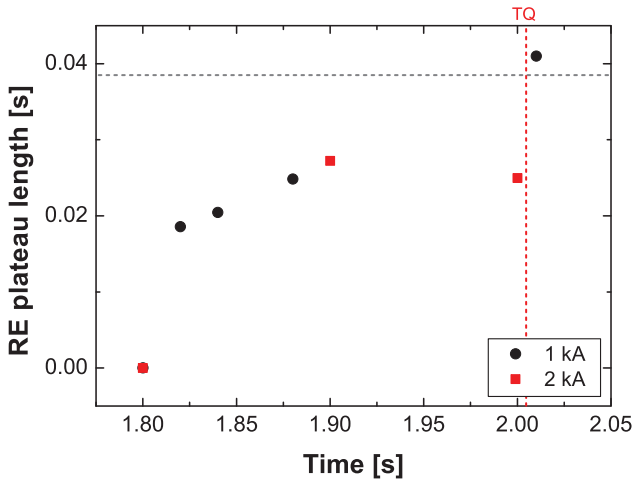

Figure 5.17: Runaway plateau length of the induced disruptions (black) and the disruptions mitigated by DED 3/1 mode. DED of 1 kA (red), and 2 kA (blue) are applied (separately) at different times. The x-axis indicates the time when the DED is applied. A grey dashed line presents an averaged plateau length of typical induced disruptions and a red dashed line the TQ time as a function of the initial runaway current.

5.5 Discussions

The experimental results show that the REs generated during disruptions are robust and cannot be easily eliminated by a fast gas injection or RMPs. Figure 5.18 shows the current decay rates $|dI/dt|$ during disruptions mitigated by different runaway techniques. The disruptions without runaway plateau are not included in these plots. In all cases, the decay rate during the CQ decreases with increasing initial runaway current similar to that in case of unmitigated disruptions. The rates of

change of the current decay rate as a function of the initial runaway current in all case are almost the same, i.e. ~ 70 s^{-1}. During the runaway plateau phase, the current decay rates of disruptions mitigated by the DED lay between a few MA/s and 5 MA/s. In case of fast gas injection, the decay rates during this phase are higher.

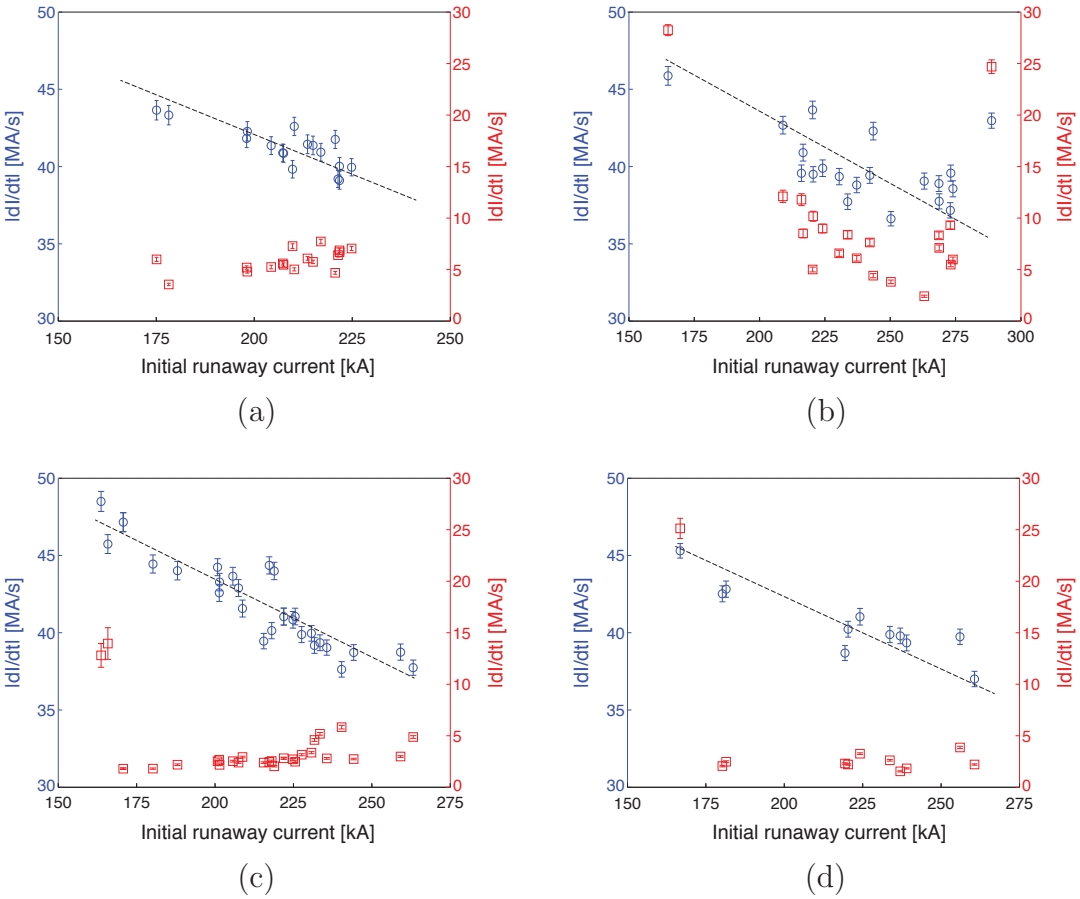

Figure 5.18: The decay rate $|dI/dt|$ as a function of the initial runaway current I_{re}^{ini} during the CQ (◯) and the runaway plateau phases (□) of disruptions mitigated by (a) fast injection performed by valve 2, (b) fast injection by valve 3, (c) DED 6/2 mode and (d) DED 3/1 mode. Dashed black lines indicate the rate of change of the decay rate during the CQ.

For the initial runaway currents of about 160 MA/s and 290 MA/s, the decay rates during the plateau phase are much larger than the decay rates for the initial runaway currents of $160 < I_{re}^{ini} < 290$ MA/s. These currents correspond to the safety factor $q \approx 1$ and $q \approx 4/3$, respectively. As mentioned before, a stable runaway beam is obtained if the outermost intact magnetic surfaces is located between $1 < q < 4/3$. In these discharges the corresponding safety factor are close to the borders and hence the runaway beam is not stable. The MHD modes corresponding to low-order resonant magnetic surfaces within the runaway beam are excited. Interactions between these modes leads to the formation of the stochastic layer and consequently REs are lost rapidly.

It can be clearly seen that a fast gas injection, especially an injection performed by valve 3, increases the runaway loss rate during the plateau phase. Interactions between the drift orbits of REs and the perturbations initiated by injected gas lead to the formation of the stochastic layer which extends deep into the central region of the runaway beam and hence the runaway loss is enhanced.

In case of the DED, the m/n = 1/1 component of the DED 3/1 mode and the m/n = 2/2 component of the DED 6/2 mode are resonant to the $q = 1$ magnetic surface [53]. According to the configuration of the DED coils at TEXTOR, the maximum of the spectrum of the generated magnetic field is located near the $q = 3$ surface which is far from the resonant components. Therefore, the amplitudes of these components the perturbation fields are relative small. Although the perturbation fields created by the DED 3/1 mode can penetrate deeper into the plasma than the fields generated by the DED 6/2 mode owing to its lower poloidal mode number m (see section 3.4), its amplitude is not high enough to create the stochastic layer and hence the late applied DED does not effect much on the runaway loss.

The applied runaway mitigation techniques affect mainly the low energy REs. Since the orbits of the high energy REs deviated more strongly from the resonant magnetic field than the orbits of the low energy ones (see figures 2.2 and 2.3), the influence of the magnetic turbulence induced by the runaway mitigation methods on the confinement of the high energy REs is strongly reduced. The runaway diffusion coefficient D_r is also decreased due to the shielding effect (see equation 2.25). Therefore, the

mitigation methods have to be applied as soon as possible in order to deconfine REs before they have time to gain high energies. After the TQ phase, the loop voltage is so high that REs can gain energies up to 30 MeV within less than 10 ms and hence the mitigation effects drops drastically due to the shielding effect for later injections.

6 Summary

Tokamak plasmas are prone to disruptions resulting in a sudden loss of energy confinement. During disruptions, the energy stored in the plasma are released rapidly. Consequently, large forces and heat loads are exerted to the vessel wall. One of the major threats of disruptions is runaway electrons (REs) which have energies in the order of tens of MeV. A substantial part of the plasma current can be converted to the runaway current. The plasma behaviour is, therefore, influenced by REs. When they are lost, the impact of these relativistic electrons on the plasma facing components (PFCs) are crucial, especially in high current disruptions. The multi-MA beam of REs has a great impact on the vessel components so that they cannot withstand numerous disruptions. REs, therefore, have to be prevented or mitigated. In order to do so, information of runaway parameters and structures as well as an understanding of the runaway behaviour during each phase of the disruption is required.

During TEXTOR disruptions, REs can gain energies up to 30 MeV. Since they travel along helical magnetic field lines, they emit synchrotron radiation in the IR range in the forward direction. In order to observe the confined REs at the plasma center, a new synchrotron measurement system has been installed at TEXTOR. It is capable of capturing up to 1253 frames per second at the full frame size. The operational wavelength range of the system is between 3 and 5 μm. This corresponds to REs with energies $\geq$ 25 MeV. The measurement of the synchrotron radiation provides important information about runaway dynamics and structures. Additionally, runaway parameters, namely radius of the runaway beam (r_{beam}) and the pitch angle (θ) can be deduced from the 2D IR image. Typical runaway parameters during a TEXTOR disruption are: $r_{beam} = 28 \pm 3$ cm and $\theta = 52 \pm 10$ mrad. The number

of the high energy REs is about 30 - 47 % of the total current. This number is affected by an error in the estimation of θ which plays an important role in the determination of the synchrotron radiative power.

Additionally, the scintillator probe developed at Institute for Laser- and Plasmaphysics of the Heinrich-Heine University Düsseldorf was applied. In the recent experimental campaign the damaged graphite housing was replaced by a new CFC housing. The minimum detectable energy was decreased to 3 MeV. The calibration of the probe is then no longer valid. However, the probe provides a qualitative measurement of the lost REs at the plasma edge. The combination of the synchrotron measuring system and the scintillator probe, in addition to the standard diagnostics, allows observations of both low and high energy REs.

Under the same experimental conditions, the REs display different behaviours. The evolution of REs during typical induced disruptions in TEXTOR can be classified into 3 cases. In all cases, disruptions take place at 4 ms after the argon injection. REs were not observed directly after the thermal quench but a few milliseconds later. When they gain the required energy, they become visible at the HFS. In case 1, the runaway beam develops and decays smoothly during the runaway plateau phase. Neither a MHD activity or rapid loss is observed. Surprisingly in some discharges of this case, the IR images in the subtraction mode show stripe patterns at the edge of the runaway beam. These stripes are associated with a laminar zone and can be described by the rotation of the mix topological structures of the REs in the plasma. In case 2, filamentary structures of the runaway beam are expected owing to the runaway bursts, SXR spikes and Mirnov spikes observed during the runaway plateau phase. Nonetheless, a smooth runaway beam is observed. It could be either because the structures do no exist or the rotation speed of the beam is too low or too high for the camera. In some discharges, a small channel connected between the runaway beam and the scintillator probe tip is seen when the beam is moved close to the probe. The channel lasts until the end of the spiky phase and sometimes even longer. This channel is observed only in spiky disruptions. The influence of the MHD activities on the low and high energy runaways is different. During the spiky phase, loss of low energy REs is enhanced, while the high energy ones remain

almost unaffected.

All REs are lost simultaneously during the runaway plateau termination in case 1 and 2. On the contrary, in case 3 a significant number of REs is observed after the runaway plateau is terminated although the plasma current drops to almost zero. The minimum current required for confinement of the 25 MeV REs is only about 20 kA [48]. It is still not clear whether the sudden appearance of a considerable number of REs at the LFS is caused by a rapid movement of the beam towards the LFS or an immediate acceleration of REs with energies slightly lower than 25 MeV that already exist at the LFS.

The new model developed in collaboration with the Institute of Energy and Climate Research of the research Center Jülich (Forschungszentrum Jülich GmbH) agrees well with the experimental observations and can explain RE formation and loss mechanisms [52, 53]. In case of helium and neon injections, an injected gas can penetrate deep into the plasma core. The stochastic layer created by interactions between excited MHD modes extends up to the central region of the runaway beam and hence REs created during disruptions are lost suddenly and no runaway beam is formed. On the contrary, the injected argon is ionized mainly at the plasma edge. The outermost intact surface of a stable runaway beam located between magnetic surfaces $1 < q < 3/4$ is formed. Only the REs in the plasma core are confined. The REs created in the stochastic layer outside this region are lost suddenly. Therefore, the radius of the runaway beam created during disruption induced by argon injection is only about one half of the initial plasma radius. Additionally, the new model can also describe the stripe structures observed at the edge of the runaway beam in case 1. The REs at the outer layer which are trapped inside stable magnetic islands embedded in a stochastic sea can gain high energies and become visible to the camera. The rotation of these islands gives rise to the observed stripes. It should be noted that these structures can be observed only in case that the rotation speed of the islands matches the recording speed of the IR camera.

In order to mitigate REs during disruptions, several techniques are applied. The main idea of mitigation methods investigated in this thesis is to initiate the magnetic turbulence or perturbation fields which cause an enhancement of the RE loss. REs

are then deconfined before they have time to gain high energies. The application in runaway mitigation of gas injection performed by valve 2 is tested first. Then the runaway mitigation effect of an injection performed by valve 3 is investigated. Among the test gas (helium, neon and argon), argon which has the highest Z number provides the strongest effect on runaway suppression. The similar trend of the effect of the injection time on the runaway confinement time is found for both valves. The early injection provide a strong influence on the runaway confinement. If the valve is triggered later, e.g. after the TQ phase, the effect of the injected gas on the REs confinement drops significantly. Although a larger amount of argon is injected by valve 2, valve 3 provides a stronger runaway mitigation effect due to its larger orifice diameter and closer location to the plasma. It is capable of providing runaway free disruptions if argon of 1.3×10^{22} atoms is injected at ≤ 3 ms.

An alternative option to create perturbation fields is the dynamic ergodic divertor (DED). The perturbation fields are resonant with the specific magnetic surface giving rise to the ergodization. In the ergodic layer, the radial transport of the particles and energy are enhanced. The runaway confinement time is shortened considerably if the DED is applied before the disruption is triggered. The radial penetration of the perturbation fields created by the DED 3/1 mode is larger than the perturbations initiated by the DED 6/2 mode.

REs during disruptions are more robust against the attempt to mitigate them in comparison with REs in low density discharges. Additionally, it is more difficult to suppress high energy REs than the low energy ones because the orbits of high energy REs deviate more from the magnetic surface. They are, therefore, less affected by the magnetic perturbations. Among all mitigation techniques investigated in this thesis, argon injection performed by valve 3 provides the strongest influence on the runaway confinement time. However, the gas has to be injected as close as possible to the first injection, i.e. when the disruption is triggered. Otherwise the REs cannot be removed either by the gas injection or by the magnetic perturbations.

Bibliography

[1] *World Energy Outlook 2014 - Executive Summary*, International Energy Agency, Paris Cedex 15, France (2014) *https://www.iea.org/publications/freepublications/publication/world-energy-outlook-2014—executive-summary.html*

[2] P.C. de Vries, M.F. Johnson, B. Alper, P. Buratti, T.C. Hender, H.R. Koslowski, V. Riccardo and JET-EFDA Contributors, *Nucl. Fusion* **51**, 053018 (2011)

[3] H.R. Koslowski, *Trans. Fusion Sci. Technol.* **49**, 147 (2006)

[4] R. Nygren, T. Lutz, D. Walsh, G. Martin, M. Chatelier, T. Loarer and D. Giulhem, *J. Nucl. Mat.* **241**, 522 (1997)

[5] Y. Neyatani, R. Yoshino, Y. Nakamura and S. Sakurai, *Nucl. Fusion* **39**, 559 (1999)

[6] G. Pautasso, K. Buchl, J.C. Fuchs, O. Gruber, A. Herrmann, K. Lackner, P.T. Lang, K.F. Mast, M. Ulrich and H. Zohm, *Nucl. Fusion* **36**, 1291 (1996)

[7] R. Yoshino, T. Kondoh, Y. Neyatani, K. Itami, Y. Kawano and N. Isei, *Plasma Phys. Control. Fusion* **39**, 313 (1997)

[8] P.L. Taylor, G.G. Kellman, T.E. Evans, D.S. Gray, D.A. Humphreys, A.W. Hyatt, T.C. Jernigan, R.L. Lee, J.A. Leuer, S.C. Luckhardt, P.B. Parks, M.J. Schaffer, D.G. Whyte and J. Zhang, *Phys. Plasmas* **6**, 1872 (1999)

[9] V.M. Timokhin, V. Yu. Sergeev and B. V. Kuteev, *Tech. Phys. Lett.* **27**, 795 (2001)

[10] D.G. Whyte, T.C. Jernigan, D.A. Humphreys, A.W. Hyatt, C.J. Lasnier, P.B.

Parks, T.E. Evans, P.L. Taylor, A.G. Kellman, D.S. Gray and E.M. Hollmann, *J. Nucl. Mater.* **313**, 1239 (2003)

[11] C. Reux, J. Bucalossi, F. Saint-Laurent, C. Gil, P. Moreau and P. Maget, *Nucl. Fusion* **50**, 095006 (2010)

[12] M. Bakhtiari, Y. Kawano, H. Tamai, Y. Miura, R. Yoshino and Y. Nishida, *Nucl. Fusion* **42**, 1197 (2002)

[13] A.J. Thornton, K.J. Gibson, I.T. Chapman, J.R. Harrison, A. Kirk, S.W. Lisgo, M. Lehnen, R. Martin, R. Scannell, A. Cullen and the MAST Team, *Nucl. Fusion* **52**, 063018 (2013)

[14] V. Riccardo, P. Andrew, L.C. Ingesson and G. Maddaluno, *Plasma Phys. Control. Fusion* **44**, 905 (2002)

[15] S.A. Bozhenkov, M. Lehnen, K.H. Finken, M.W. Jakubowski, R.C. Wolf, R. Jaspers, M. Kantor, O.V. Marchuk1, E. Uzgel, G. Van Wassenhove, O. Zimmermann, D. Reiter and the TEXTOR team, *Plasma Phys. Control. Fusion* **50**, 105007 (2008)

[16] T. Kudyakov, K.H. Finken, M. Jakubowski, M. Lehnen, Y. Xu, and O. Willi, *Rev. Sci. Insrum.* **79**, 10F126 (2008)

[17] T. Kudyakov, K.H. Finken, M. Jakubowski, M. Lehnen, Y. Xu, B. Schweer, T. Toncian, G. van Wassenhove and O. Willi, *Nucl. Fusion* **48**, 122002 (2008)

[18] K.H. Finken, J.G. Watkins, D. Rüsbuldt, W.J. Corbett, K.H. Dippel, D.M. Goebel, and R.A. Moyer, *Nucl. Fusion* **30**, 859 (1990)

[19] T. Kudyakov, *Spectral measurements of runaway electrons in the TEXTOR tokamak*, Universitäts- und Landesbibliothek Düsseldorf, URN 061-20090825-094300-9, PhD thesis, Heinrich-Heine Universität Düsseldorf, Düsseldorf, Germany (2009)

[20] T. Kudyakov, S.S. Abdullaev, S.A. Bozhenkov, K.H. Finken, M.W. Jakubowski, M. Lehnen, G. Sewell, O. Willi, Y. Xu and the TEXTOR team, *Nucl. Fusion* **52**, 023025 (2012)

[21] M. Forster, S.S. Abdullaev, K.H. Finken, T. Kudyakov, M. Lehnen, G. Sewell, O. Willi, Y. Xu, and the TEXTOR team, *Nucl. Fusion* **52**, 083016 (2012)

[22] M. Forster, K.H. Finken, T. Kudyakov, M. Lehnen, O. Willi, Y. Xu, L. Zeng, and the TEXTOR team, *Phys. Plasmas* **19**, 092513 (2012)

[23] M. Forster, K.H. Finken, M. Lehnen, O. Willi, Y. Xu, and TEXTOR Team, *Phys. Plasmas* **19**, 052506 (2012)

[24] M. Forster, K.H. Finken, M. Lehnen, J. Linke, B. Schweer, C. Thomser, O. Willi, Y. Xu and the TEXTOR team, *Nucl. Fusion* **51**, 043003 (2011)

[25] E.P. Gorbunov, G.G. Dolgov-Savel'ev, V.S. Mukhovatov, V.S. Strelkov, and N.A. Yavlinskii, *Sov. Phys.-Tech. Phys.* **5**, 1089 (1961)

[26] V.V. Matveev, A.D. Sokol'ov and L.A. Suchkova, *Sov. Phys.-Tech. Phys.* **8**, 530 (1963)

[27] H. Dreicer, *Phys. Rev.* **115**, 238 (1659)

[28] H. Dreicer, *Phys. Rev.* **117**, 329 (1660)

[29] P. Helander, L.-G. Efiksson and F. Andersson, *Plasma Phys. Control. Fusion* **44**, B247 (2002)

[30] R.H. Cohen, *Phys. Fluids* **19**, 239 (1967)

[31] J.W. Connor and R.J. Hastie, *Nucl. Fusion* **15**, 415 (1975)

[32] R.W. Harvey, V.S. Chan, S.C. Chiu, T.E. Evans, M.N. Rosenbluth, and D.G. Whyte, *Phys. Plasmas* **7**, 4590 (2000)

[33] P. Helander, H. Smith, T. Fülöp, and L.-G. Eriksson, *Phys. Plasmas* **11**, 5704 (2004)

[34] H. Smith, P. Helander, L.-G. Eriksson, and T. Fülöp, *Phys. Plasmas* **12**, 122505 (2005)

[35] H. M. Smith and E. Verwichte, *Phys. Plasmas* **15**, 072502 (2008)

[36] Y. A. Sokolov *JETP Letters* **29** 218 (1979)

[37] N.T. Besedin and I.M. Pankratov, *Nucl. Fusion*, **26**, 807 (1986)

[38] R. Jayakumar, H.H. Fleischmann, and S.J. Zweben, *Phys. Lett. A* **172**, 447 (1993)

[39] M.N. Rosenbluth and S.V. Putvinski, *Nucl. Fusion* **37**, 1355 (1997)

[40] T. Fülöp, H.M. Smith, and G.Pokol, *Phys. Plasmas* **16**, 022502 (2009)

[41] R. Jaspers, N.J. Lopes Cardozo, F.C. Schüller, K.H. Finken, T. Grewe, and G. Mank, *Nucl. Fusion* **36**, 367 (1996)

[42] H. Smith, P. Helander, L.-G. Eriksson, D. Anderson, M. Lisak, and F. Andersson, *Phys. Plasmas* **13**, 102502 (2006)

[43] T. Fehér, H.M. Smith, T. Fülöp, and K. Gál, *Plasma Phys. Control. Fusion* **53**, 035014 (2011)

[44] H.M. Smith and E. Verwichte, *Phys. Plasmas* **15**, 072502 (2008)

[45] R. Jaspers, *Relativistic Runaway Electrons in Tokamak Plasmas*, CIP- DATA Koninklijke Bibliotheek, Den Haag, ISBN 90-386-0474-2, PhD thesis, Eindhoven University of Technology, The Netherlands (1995)

[46] S.S. Abdullaev and K.H. Finken, *Phys. Plasmas* **9**, 4193 (2002)

[47] A. Wingen, S.S. Abdullaev, K.H. Finken, M. Jakubowski and K.H. Spatschek, *Nucl. Fusion* **46,** 941 (2006)

[48] K. Wongrach, K.H. Finken, S.S. Abdullaev, R. Koslowski, O. Willi, L. Zeng, and the TEXTOR team, *Nucl. Fusion* **54**, 043011 (2014)

[49] K. Wongrach, K.H. Finken, S.S. Abdullaev, O. Willi, L. Zeng, Y. Xu, and the TEXTOR team, *Nucl. Fusion* **55**, 053008 (2015)

[50] S.S. Abdullaev, *Phys.Plasmas* **22**, 030702 (2015)

[51] M.F.F. Nave, J.A. Wesson, *Nuclear Fusion* **30**, 2575 (1990)

[52] S.S. Abdullaev, K. H. Finken, K. Wongrach, M. Tokar, H. R. Koslowski, O. Willi, L. Zeng and TEXTOR team, *Phys.Plasmas* **22**, 040704 (2015)

[53] S.S. Abdullaev, K.H. Finken, K. Wongrach, M. Tokar, H.R. Koslowski, O. Willi, L.Zeng and the TEXTOR team, *J. Plasma Phys.* **81**, 475810501 2015)

[54] A.B. Rechester and M.N. Rosenbluth, *Phys. Rev. Lett.* **40**, 38 (1978)

[55] M. de Rover, A.M. Schilham, A. Montvai, and N.J. Lopes Cardozo, *Phys. Plasmas* **6**, 2443 (1999)

[56] H.E. Mynick and J. Strachan, *Phys. Fluids* **24**, 695 (1981)

[57] J.R. Myra and P.J. Catto, *Phys. Fluids B* **4**, 176 (1992)

[58] J.R. Myra, P.J. Catto, H.E. Mynick, and R.E. Duvall, *Phys. Fluids B* **5**, 1160 (1993)

[59] M. de Rover, N.J. LopesCardozo, and A. Montvai, *Phys. Plasmas* **3**, 4478 (1996)

[60] T. Hauff and F. Jenko, *Phys. Plasma* **16**, 102308 (2009)

[61] S.S. Abdullaev, K.H. Finken, T. Kudyakov, and M. Lehnen, *Contrib. Plasma Phys.* **50**, 929 (2010)

[62] S.S. Abdullaev, K.H. Finken, and M. Forster, *Phys. Plasmas* **19**, 072502 (2012)

[63] S. S. Abdullaev *Magnetic Stochasticity in Magnetically Confined Fusion Plasmas*, Springer-Verlag, Cham, Heidelberg (2014)

[64] O. Neubauer, G. Czymek, B. Giesen, P.W. Hüttemann, M. Sauer, W. Schalt, and J. Schruff, *Fusion Sci. and Technol.* **47**, 76 (2005)

[65] J. Schwinger, *Phys. Rev.* **75**, 1912 (1949)

[66] T. Kudyakov, A. Jochmann, K. Zeil, S. Kraft, K.H. Finken, U. Schramm, and O. Willi, *Rev. Scient. Instrum* **80,** 076106 (2009)

[67] M. Balcerzyk, M. Moszynski, M. Kapusta, D. Wolski, J. Pawelke, and C.L. Melcher, *IEEE Trans. Nucl. Sci.* **47** 1319 (2000)

[68] S. Agostinelli, J. Allison, K. Amako, J. Apostolakis, H. Araujo, P. Arce, M. Asai, D. Axen, S. Banerjee, G. Barrand, F. Fehner, L. Bellagamba, J. Boudreau, L. Broglia, A. Brunengo, H. Burkhardt, S. Chauvie, J. Chuma, R. Chytracek, G. Cooperman, G. Cosmo , P. Degtyarenko, A. Dell'Acqua, G. Depaola, D. Dietrich,

R. Enami, A. Feliciello, C. Ferguson, H. Fesefeldt, G. Folger, F. Foppiano, A. Forti, S. Garelli, S. Giani, R. Giannitrapani, D. Gibin and J.J. Gómez Cadenas, *Nucl. Instrum. Meth. A* **506**, 250 (2003)

[69] J. Allison, K. Amako, J. Apostolakis, H. Araujo, P.A. Dubois, M. Asai, G. Barrand, R. Capra, S. Chauvie, R. Chytracek, G.A.P. Cirrone, G. Cooperman, G. Cosmo, G. Cuttone, G.G. Daquino, M. Donszelmann, M. Dressel, G. Folger, F. Foppiano, J. Generowicz, V. Grichine, S. Guatelli, P. Gumplinger, A. Heikkinen, I. Hrivnacova, A. Howard, S. Incerti, V. Ivanchenko, T. Johnson, F. Jones, T. Koi, R. Kokoulin, M. Kossov, H. Kurashige, V. Lara, S. Larsson, F. Lei, O. Link, F. Longo, M. Maire, A. Mantero, B. Mascialino, I. McLaren, P.M. Lorenzo, K. Minamimoto, K. Murakami, P. Nieminen, L. Pandola, S. Parlati, L. Peralta, J. Perl, A. Pfeiffer, M.G. Pia, A. Ribon, P. Rodrigues, G. Russo, S. Sadilov, G. Santin, T. Sasaki, D. Smith, N. Starkov, S. Tanaka, E. Tcherniaev, B. Tome, A. Trindade, P. Truscott, L. Urban, M. Verderi, A. Walkden, J.P. Wellisch, D.C. Williams, D. Wright, and H. Yoshida *IEEE Trans. Nucl. Sci.* **53(1)**, 270 (2006)

[70] A.J.H. Donné , M.F.M. de Bock, I.G.J. Classen, M.G. von Hellermann, K. Jakubowska, R. Jaspers, C.J. Barth, H.J. van de Meiden, T. Oyewaar, M.J. van der Pol, S.K. Varshney, G. Bertschinger, W. Biel, C. Busch, K.H. Finken, H.R. Koslowski, A. Krmer-Flecken, A. Kreter, Y. Liang, H. Oosterbeek, O. Zimmermann, G. Telessca, G. Verdoolaege, C.W. Domier, N.C. Luhmann jr., E. Mazzucato, T. Munsat, H. Park, M. Kantor, D. Kouprienko, A. Alexeev, S. Ohdachi, S. Korsholm, P. Woskov, H. Bindslev, F. Meo, P.K. Michelsen, S. Michelsen, S.K. Nielsen, E. Tsakadze, and L. Shmaenok, *Fusion Sci. Technol.* **47**, 220 (2005)

[71] C. Wiegman, *Real-time detection of magnetohydrodynamic equilibria at the nuclear fusion experiment textor*, Diploma thesis, Bayerische Julius-Maximillians Universität Würzburg, Würzburg, Germany (2006)

[72] J.S. Kim, D.H. Edgell, J.M. Greene. E.J. Strait, and M.S. Chance, *Plasma Phys. Control. Fusion* **41**, 1399 (1999)

[73] M. Mitri, *Schriften des Forschungszentrums Jülich Reihe Energie & Umwelt / Energy & Environment* Band / Volume **33**, Forschungszentrum Jülich, Jülich,

Germany (2009)

[74] A. Savtchkov, K.H. Finken, and G. Mank, *Rev. Sci. Instrum.* **70**, 3490 (2002)

[75] S.A. Bozhenkov, K.H. Finken, M. Lehnen and R.C. Wolf, *Rev. Sci. Instrum.* **78**, 033503 (2007)

[76] K.H. Finken, M. Lehnen and S.A. Bozhenkov, *Nucl. Fusion* **51**, 033077 (2011)

[77] K.H. Finken, M. Lehnen and S.A. Bozhenkov, *Nucl. Fusion* **48**, 115001 (2008)

[78] K.H. Finken, S.S. Abdullaev, A. Kaleck, and G.H. Wolf, *Nucl. Fusion* **39**, 637 (1999)

[79] K.H. Finken amd S.S. Abdullaev, T. Eich, D.W. Faulconer, M. Kobayashi, R. Koch, G. Mank, and A. Rogister, *Nucl. Fusion* **41**, 503 (2001)

[80] K.H. Finken, S.S. Abdullaev, M. Jakubowski, M. Lehnen, A. Nicolai, and K.H. Spatschek. *Schriften des Forschungszentrums Jülich Reihe Energietechnik / Energy Technology* Band / Volume **45**, Forschungszentrum Jülich, Jülich, Germany (2005)

[81] M. Lehnen, S.A. Bozhenkov, S.S. Abdullaev, and M.W. Jakubowski, *Phys. Rev. Lett.* **100**, 55003 (2008)

[82] H.R. Koslowski, L. Zeng, M. Lehnen, A. Lvovskiy, K. Wongrach and TEXTOR Team, *41st EPS conference on Plasma Physics* **P 5.028** (2014)

[83] H.R. Koslowski, Y. Liang, A. Krämer-Flecken, K. Löwenbrück, M. von Hellermann, E. Westerhof, R.C. Wolf, O. Zimmermann and the TEXTOR team, *Nucl. Fusion* **46**, L1 (2006)

[84] G. Pautasso, C.J. Fuchs, O. Gruber, C.F. Maggi, M. Maraschek, T. Pu tterich, V. Rohde, C. Wittmann, E. Wolfrum, P. Cierpka, M. Beck and the ASDEX Upgrade Team, *Nucl. Fusion* **47**, 900 (2007)

[85] G.M. Olynyk, R.S. Granetz, M.L. Reinke, D.G. Whyte, T. Golfinopoulos, J.W. Hughes, J.R. Walk, V.A. Izzo, S.K. Combs, S.L. Milora and M.W. Brookman, *Nucl. Fusion* **53**, 092001 (2013)

[86] E.M. Hollmann, M.E. Austin, J.A. Boedo, N.H. Brooks, N. Commaux, N.W. Eidietis, D.A. Humphreys, V.A. Izzo, A.N. James, T.C. Jernigan, A. Loarte, J. Martin-Solis, R.A. Moyer, J.M. Muñoz-Burgos, P.B. Parks, D.L. Rudakov, E.J. Strait, C. Tsui, M.A. Van Zeeland, J.C. Wesley and J.H. Yu, *Nucl. Fusion* **53**, 083004 (2013)

[87] M. Koltunov and N.Z. Tokar, *Plasma Phys. Control. Fusion* **53**, 065015 (2011)

[88] N.Z. Tokar and M. Koltunov, *Plasma Phys. Control. Fusion* **55**, 045013 (2013)

[89] K.H. Finken, S.S. Abdullaev, M. Jakubowski, R. Jaspers, M. Lehnen and O. Zimmermann, *Nucl. Fusion* **46**, S139 (2006)

[90] R. Jaspers, N. J. Lopes Cardozo, K. H. Finken, B. C. Schokker, G. Mank, G. Fuchs, and F. C. Schüller, *Phys. Rev. Lett.* **72**, 4093 (1994)

[91] R.D. Gill, B. Alper, A.W. Edwards, L.C. Ingesson, M.F. Johnson and D.J. Ward, *Nucl. Fusion* **40**, 163 (2000)

[92] K.H. Finken, G. Mank, A. Krämer-Flecken and R. Jaspers, *Nucl. Fusion* **41**, 1651 (2001)

[93] M. Forster, *Runaway Electrons in Disruptions and Perturbed Magnetic Topologies of Tokamak Plasmas*, Universitäts- und Landesbibliothek Düsseldorf, URN 061-20121026-131219-6, PhD thesis, Heinrich-Heine Universität Düsseldorf, Düsseldorf, Germany (2012)

[94] X. Guan, H. Qin, and N. Fisch, *Phys. Plasmas* **17**, 092502 (2010)

List of abbreviation

ALT-II	Advanced limiter test-II
CFC	carbon fibre composite
CQ	Current quench
DED	Dynamic ergodic divertor
DMV	Disruption mitigation valve
ECE	Electron cyclotron emission
HFS	High field side
LCFS	Last closed flux surface
LFS	Low field side
MGI	Massive gas injection
MHD	Magnetrohydrodynamics
PFC	Plasma facing component
PI	Pellet injection
RE	Runaway electron
RMP	Resonant magnetic perturbation
SXR	Soft X-ray
TQ	Thermal quench

List of author's publications

Peer reviewed journals

1. L. Zeng, H. R. Koslowski, Y. Liang, A. Lvovskiy, M. Lehnen, D. Nicolai, J. Pearson, M. Rack, H. Jaegers, K. H. Finken, K. Wongrach, Y. Xu, and the TEXTOR team, *Experimental Observation of a Magnetic-Turbulence Threshold for Runaway-Electron Generation in the TEXTOR Tokamak*, Phys Rev. Lett. **110**, 235003 (2013)

2. K. Wongrach, K.H. Finken, S.S. Abdullaev, R. Koslowski, O. Willi, L. Zeng, and the TEXTOR team, *Measurement of synchrotron radiation from runaway electrons during the TEXTOR tokamak disruptions*, Nucl. Fusion **54**, 043011 (2014)

3. K. Wongrach, K.H. Finken, S.S. Abdullaev, O. Willi, L. Zeng, Y. Xu, and the TEXTOR team, *Runaway electron studies in TEXTOR*, Nucl. Fusion **55**, 053008 (2015)

4. S.S. Abdullaev, K. H. Finken, K. Wongrach, M. Tokar, H. R. Koslowski, O. Willi, L. Zeng and TEXTOR Team, *Mechanism of runaway electron beam formation during plasma disruptions in tokamaks*, Phys.Plasmas **22**, 040704 (2015)

5. L. Zeng, H. R. Koslowski, Y. Liang, A. Lvovskiy, M. Lehnen, D. Nicolai, J. Pearson, M. Rack, P. Denner, K. H. Finken, K. Wongrach and the TEXTOR team, *Experimental observation of hot tail runaway electron generation in TEXTOR disruptions*, J. Plasma Phys. **81**, 475810402 (2015)

6. S.S. Abdullaev, K.H. Finken, K. Wongrach, M. Tokar, H.R. Koslowski, O.

Willi, L.Zeng and the TEXTOR team, *Mechanisms of plasma disruption and runaway electron losses in the TEXTOR tokamak*, J. Plasma Phys. **81**, 475810501 2015)

Conference proceedings

7. K. Wongarch, K.H. Finken, R. Koslowski, S.S. Abdullaev, O. Willi and L. Zeng, *Synchrotron radiation pattern of the runaway beam during induced disruptions in TEXTOR*, 40^{th}EPS conference on Plasma Physics **P 5.128** (2013)
8. L. Zeng, H.R. Koslowski, Y. Liang, A. Lvovskiy, M. Lehnen, D. Nicolai, J. Pearson, M. Rack, P. Denner, K.H. Finken, K. Wongrach, and the TEXTOR team, *Experimental observation of runaway electron related relaxation phenomena during disruptions in the TEXTOR tokamak*, 40^{th}EPS conference on Plasma Physics **P 5.169** (2013)

Submitted articles

9. K. Wongrach, K.H. Finken, S.S. Abdullaev, O. Willi, L. Zeng and Y. Xu *Structure of the runaway electron loss during induced disruptions in TEXTOR*, Submitted to Physics of plasmas

Author's contribution to the publications

The work presented in this thesis and the related publications have been performed in close collaboration with Dr. Finken and the Institute of Energy and Climate Research of the research center Jülich (Forschungszentrum Jülich GmbH).

Publication 1, 5 and 8

The author's colleagues (the first authors of the publications) performed the experiment and wrote the manuscripts. The author was responsible for acquisition and interpretation of the experimental data obtained from synchrotron radiation measurements including the approval of the version to be submitted to the publishers.

Publication 2, 3, 7, and 9

The author carried out the experiments by using the synchrotron measurement system developed by Dr. Finken. In publication 3, the scintillator probe developed at the Düsseldorf University by Dr. Kudyakov was used as a main diagnostic in addition to the synchrotron measurement system. The experimental data from the main diagnostics were acquired and analysed by the author. Additionally, the author prepared and revised the manuscripts with the assistance of Dr. Finken. The theoretical calculations and the related figures and texts were provided by Dr. Abdullaev.

Publication 4, 6

The author performed the experiments, analysed the experimental data and provided parameters used in the calculations which were made by Dr. Abdullaev. The manuscript was written by Dr. Abdullaev.

PUBLICATION 1

Experimental Observation of a Magnetic-Turbulence Threshold for Runaway-Electron Generation in the TEXTOR Tokamak

L. Zeng,[1,2] H. R. Koslowski,[1] Y. Liang,[1] A. Lvovskiy,[1] M. Lehnen,[1,3] D. Nicolai,[1] J. Pearson,[1] M. Rack,[1] H. Jaegers,[1] K. H. Finken,[4] K. Wongrach,[4] Y. Xu,[5] and the TEXTOR team

[1]*Forschungszentrum Jülich GmbH, Institute of Energy and Climate Research—Plasma Physics (IEK-4), Association EURATOM-FZJ, Trilateral Euregio Cluster, 52425 Jülich, Germany*

[2]*Institute of Plasma Physics, Chinese Academy of Sciences, 230031 Hefei, China*

[3]*ITER Organization, Route de Vinon sur Verdon, 13115 St Paul Lez Durance, France*

[4]*Institut für Laser- und Plasmaphysik, Heinrich-Heine-Universität Düsseldorf, 40225 Düsseldorf, Germany*

[5]*Laboratoire de Physique des Plasmas—Laboratorium voor Plasmafysica, Association 'Euratom-Belgian state', Ecole Royale Militaire—Koninklijke Militaire School, Trilateral Euregio Cluster, 1000 Brussels, Belgium*

(Received 22 March 2013; published 5 June 2013)

Magnetic turbulence is observed at the beginning of the current quench in intended TEXTOR disruptions. Runaway electron (RE) suppression has been experimentally found at magnetic turbulence larger than a certain threshold. Below this threshold, the generated RE current is inversely proportional to the level of magnetic turbulence. The magnetic turbulence originates from the background plasma and the amplitude depends strongly on the toroidal magnetic field and plasma electron density. These results explain the previously found toroidal field threshold for RE generation and have to be considered in predictions for RE generation in ITER.

DOI: 10.1103/PhysRevLett.110.235003 PACS numbers: 52.55.Fa, 52.27.Ny, 52.35.Ra

Introduction.—Runaway electron (RE) currents of several mega ampere are expected to be generated in ITER disruptions due to avalanche multiplication [1]. An uncontrolled loss of these high energetic electrons to the plasma facing components might cause serious damage [2]. The occurrence of REs depends on various factors and no definite RE generation dependence on plasma parameters is given in theory or found in present experiments. In tokamak experiments it is observed that RE generation occurs only above a threshold for the toroidal magnetic field of about 2 T, as has been found, independent on machine size, on JET [3], JT-60U [4], Tore Supra [5], and TEXTOR [2]. As a possible explanation for this behavior the whistler wave instability has been proposed [6]; however, no clear experimental evidence has been found yet. Above the 2 T threshold, the RE generation shows an exponential dependence on the toroidal magnetic field [7].

Magnetic fluctuations cause strong RE losses and can even prevent RE generation [8]. A variety of analytical models and numerical simulations address the effect of magnetic fluctuations on RE generation and find that a magnetic turbulence level of $\delta B/B_t > 0.1\%$ suppresses the RE avalanche during disruptions [8–11]. The effect of externally applied magnetic perturbations (e.g., resonant magnetic perturbations) on RE generation has been studied in JT-60U [12] and TEXTOR [13]. Both publications conclude that RE production is completely suppressed above a certain amplitude of the applied perturbation field. The magnetic fluctuation level is correlated with the hard X-ray signal after the disruption in JET, showing that larger X-ray levels are obtained when magnetic fluctuations are lower [3]. The influence of intrinsic magnetic turbulence on the de-confinement of REs has recently been analyzed at TEXTOR during the flattop phase of low density discharges [14] where RE losses have been utilized to probe the spatial amplitude of magnetic fluctuations. In this letter, we will report evidence from the TEXTOR tokamak showing that intrinsic magnetic turbulence strongly correlates with the toroidal field threshold for RE generation during the disruption current quench.

Experimental setup and results.—Disruptions are deliberately triggered by injection of large amounts of Argon using a fast disruption mitigation valve (DMV) on TEXTOR [15]. Using the same experimental setup as in Ref. [13], the experiments were carried out with the following parameters: the toroidal magnetic field $B_t = 1.7$–2.5 T, the plasma current $I_P = 300$–350 kA, the edge safety factor $q_a = 2.9$–5, the line averaged central density $n_e = 2.0 \times 10^{19}$ m^{-3}, the major radius $R = 1.75$ m, the minor radius $a = 0.46$ m, and number of injected Argon particles N_{Ar} changing from 2.3×10^{21} to 1.9×10^{22}.

Figure 1 compares two discharges, one develops a RE current plateau during the current quench and the other does not. The DMV is triggered at $t = 2.0$ s. After 3–4 ms the thermal quench occurs. During the following current quench, the plasma current decreases as shown in Fig. 1(a). In some situations a RE current plateau forms (#117833) which has been observed to last up to 170 ms. Meanwhile, obvious magnetic turbulence is seen in signals from magnetic pick-up coils with the sampling rate of 1 MHz, shown in Fig. 1(b) and 1(c). The magnetic turbulence appears at the beginning of the current quench and lasts from 4 to

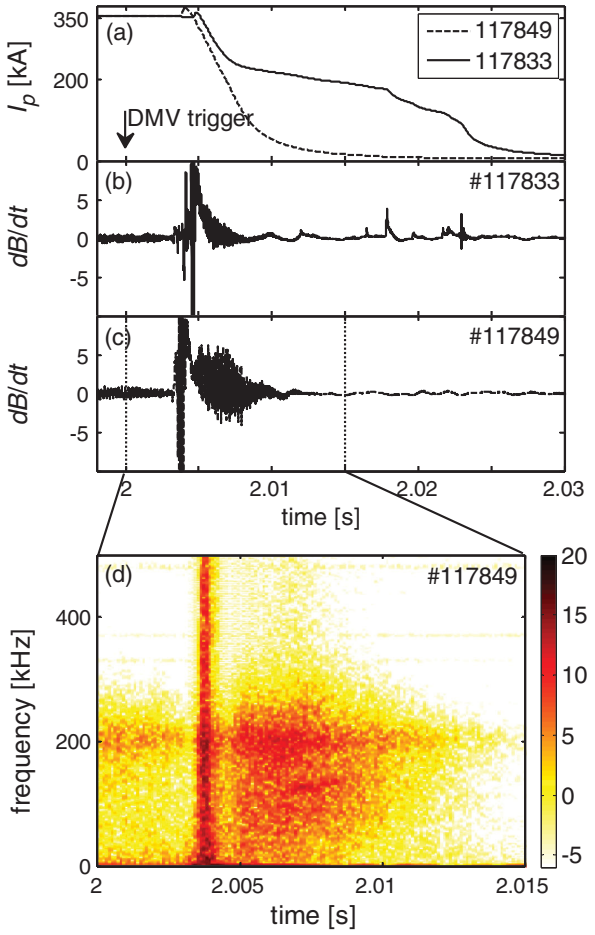

FIG. 1 (color online). Time traces from two discharges differing in the current quench phase showing (a) plasma current I_P, (b) magnetic turbulence dB/dt in shot 117833, (c) magnetic turbulence dB/dt in shot 117849, and (d) spectrum of magnetic turbulence in shot 117849. The current quench occurs at about 4.5 ms after triggering the DMV in shot 117849.

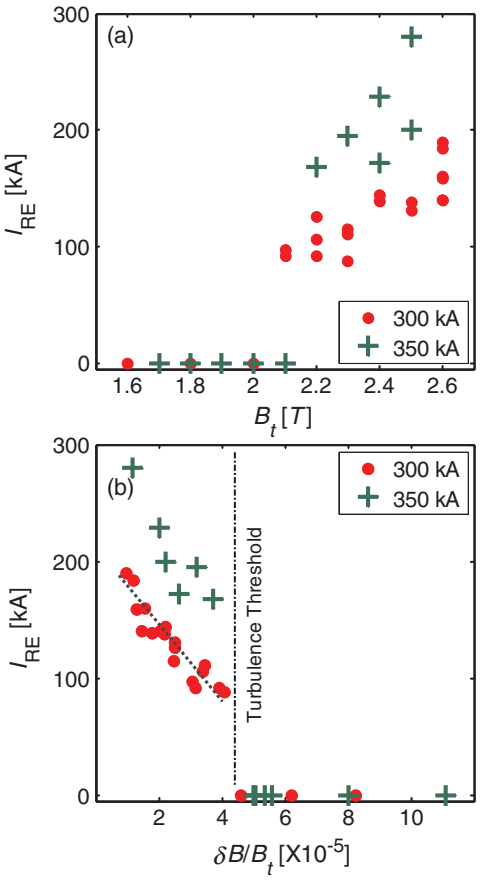

FIG. 2 (color online). RE current in TEXTOR disruptions as a function of (a) toroidal field (b) normalized magnetic turbulence level.

8 ms. The level initially increases and then decreases. A typical frequency spectrum of magnetic turbulence is shown in Fig. 1(d).

The parameters of both shots 117833 and 117849 are the same except for the toroidal magnetic field, but the RE generation is totally different. The magnetic turbulence level with $B_t = 1.8$ T is at least twice of that with $B_t = 2.4$ T. Anomalous RE losses due to magnetic turbulence with $B_t = 1.8$ T are therefore much larger than with $B_t = 2.4$ T. This suggests that magnetic turbulence during the current quench plays the dominant role in this stage and is the cause of the different observed RE tails.

In Fig. 2(a), a survey of several discharges shows that REs occur after a disruption when the value of B_t exceeds the threshold and that the RE current increases at high toroidal magnetic field. However, the RE tail is not always reproducible, even with the same toroidal magnetic field. This could be due to the difference in the magnetic turbulence level (δB), as seen later in the spread of δB for the same value of B_t in Fig. 4(b). One possible reason for the difference in δB is the triggering of the disruptions at random phases of the sawtooth cycle, which locally changes the plasma parameters. The RE current is estimated by subtracting the current evolution of a disruption without any RE generation. RE current is given in Fig. 2(b) as a function of the maximum magnetic turbulence during the current quench. The amplitude of magnetic turbulence is calculated by filtering the signal with a high pass filter (> 2 kHz), integrating, and then determining the maximum of the envelope. In TEXTOR the RE plateau is always visible unless the normalized magnetic turbulence level exceeds the threshold of about $\delta B/B_t \sim 4.8 \times 10^{-5}$ for $I_p = 300$, 350 kA and the REs (which may be produced in the current quench) get quickly lost within the first 5 ms of the current quench. This value of the critical turbulence level is of the same order as JET result (Fig. 3 in Ref. [3]). The threshold dependence on different currents is not obvious from the measured data. For shots with lower magnetic turbulence level than the threshold it is found that the RE current (I_{RE}) decreases linearly with $\delta B/B_t$ for $I_p = 300$ kA and also for $I_p = 350$ kA but in the latter

case the RE current is larger. The value of the critical fluctuation amplitude seems to depend only on the toroidal field and not on the plasma current. From the analysis above it follows that there is clear evidence that the development of a RE beam depends strongly on the level of magnetic turbulence during the current quench.

Figure 2(b) suggests that a good empirical relation for the RE current dependence on $\delta B/B_t$ below the threshold is given by

$$I_{\mathrm{RE}} \propto -\alpha \delta B/B_t.$$

Here α is a function of the plasma current decay rate or the electric field. It cannot be excluded at present that α depends on the pre-disruption plasma parameters. Magnetic turbulence appears after the thermal quench and it is only possible to cause RE losses but not the generation. The resultant RE current depends on both, electric field (RE generation) and magnetic turbulence (RE losses).

Magnetic turbulence.—In the following some basic aspects of magnetic turbulence are analyzed. The amplitude of the measured magnetic turbulence during the current quench is $\delta B/B_t \sim 10^{-5}$–$10^{-4}$, which is much weaker than that during the thermal quench [Fig. 1(d)]. The spectrum shows that the frequencies of the turbulence form a wide distribution and most of the power is in the range from 60 to 260 kHz. This excludes that it originates from macroscopic magnetohydrodynamics (MHD) activity though the origin of the magnetic turbulence is not yet clear and requires future investigations.

Comparing the signals of different Mirnov coils distributed along the poloidal circumference of the liner (= first wall) shows that the magnetic turbulence is poloidally asymmetric (Fig. 3). The level at the top of the inner wall is about 7 times larger than that at the low field side. Indeed, the magnetic fluctuations decay as $r^{-(m+1)}$ in the vacuum. Here, r is the minor radius and m is the poloidal mode number. Poloidal asymmetry during the current quench could be an indication that the plasma is shrinking and moving inward. If we assume $m = 10$ (here m is an average value because the poloidal mode number is a function of both time and frequency during the current quench) and the plasma movement to be inward by 8 cm, the simulated signals agree with the measured ones, as shown in Fig. 3. REs are always generated on the high field side as has been observed by measuring the synchrotron emission with an infrared camera in TEXTOR [16], which is also consistent with the assumptions for our simulations.

Clear evidence of the relation between the magnetic turbulence and plasma density can be drawn from Fig. 4 in which measured magnetic turbulence is plotted versus the amount of injected gas. In a series of experiments the number of injected Argon atoms has been varied from 2.3×10^{21} to 1.9×10^{22}. The impurity ion density in

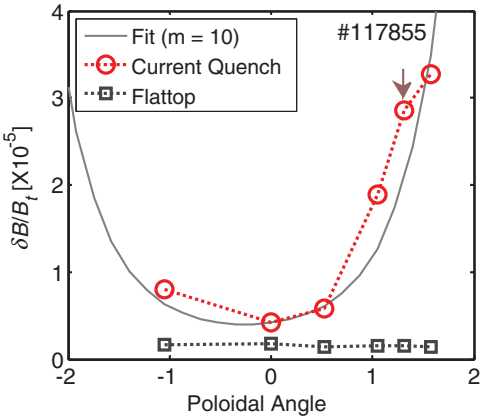

FIG. 3 (color online). Comparison of magnetic turbulence level at different poloidal angles: Circles correspond to measured values during the current quench ($t = 2.0065$ s) and squares correspond to the values before the disruption ($t = 2.0$ s). The fitting line is simulated assuming the plasma moves inwards by 8 cm. Poloidal angle "0" is at the low field side and the magnetic turbulence value used in this Letter is from the coil in the poloidal angel of 1.3, marked by the arrow in the figure.

MGI disruptions on TEXTOR is proportional to the number of injected atoms [17]. Figure 4(a) shows that, the relative level of magnetic turbulence is proportional to the square root of post-MGI plasma density both for $B_t = 1.9$ T and $B_t = 2.4$ T. This result is in agreement with a scaling law obtained in the Tore Supra tokamak [18]. In order to compare the fluctuation level with $B_t = 2.4$ T to the one with $B_t = 1.9$ T, the first value is multiplied by a factor $(2.4/1.9)^2$ yielding a good agreement of both data sets [Fig. 4(a)]. The level of magnetic turbulence is a decreasing function of the toroidal magnetic field as can be seen from Fig. 4(b). The influence of the plasma current is again not clear. Both parameter scans can be summarized as

$$\delta B/B_t \propto \sqrt{n_e} \quad \text{and} \quad \delta B \propto B_t^{-2}.$$

The level of magnetic turbulence does strongly dependent on the toroidal magnetic field. The lower the magnetic field, the larger is the level of the magnetic turbulence and more RE losses occur. The turbulence also depends on the plasma density of which REs are only a small fraction. This supports that magnetic turbulence is mainly contributed from the background plasma.

Discussion.—The magnetic turbulence can cause RE losses due to increased radial transport and the characteristic diffusion time associated with magnetic turbulence can be written as $\tau_{\delta B} = (a^2/\nu_{\parallel} D_M)\gamma^5$, where $\nu_{\parallel}$ is the parallel electron velocity, γ is the relativistic scaling factor (γ^5 represents the phase-averaging effect of electron orbits deviating from flux surfaces), and D_M is the magnetic diffusion coefficient, given by $D_M \approx \pi q R (\delta B/B_t)^2$, where q is the safety factor [8–10]. Since the RE diffusion

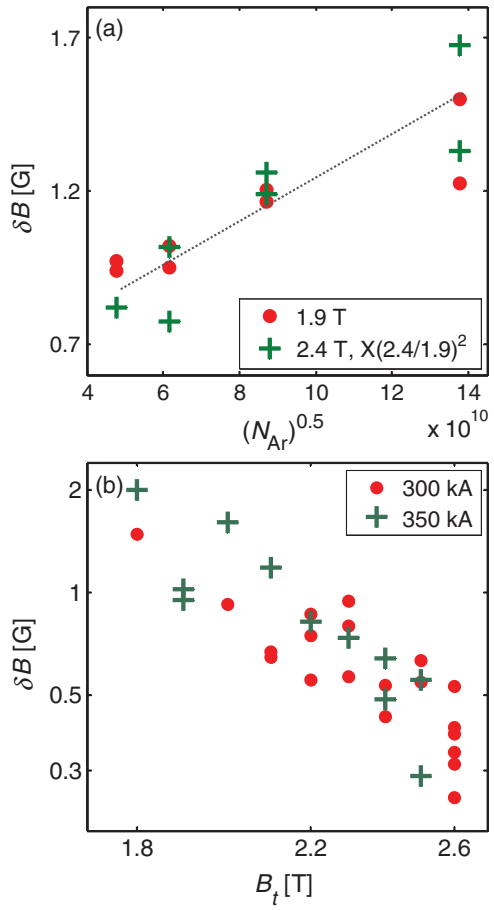

FIG. 4 (color online). (a) Magnetic turbulence levels for $B_t = 1.9$ T and $B_t = 2.4$ T versus number of injected Argon atoms. In order to compare both data sets the amplitudes measured at $B_t = 2.4$ T are multiplied by a factor $(2.4/1.9)^2$. (b) Magnetic turbulence level for $I_P = 300$ kA and $I_P = 350$ kA versus toroidal field.

is dominated by the magnetic turbulence, the RE diffusion time τ_{loss} can be approximately regarded as the magnetic turbulence induced diffusion time $\tau_{\mathrm{loss}} \approx \tau_{\delta B}$. A 0D model of the current quench including RE generation n_{RE} and magnetic turbulence loss is applied in [17]:

$$\frac{dn_{\mathrm{RE}}}{dt} = f_{\mathrm{prim}} + (1/\tau_{\mathrm{RE}} - 1/\tau_{\mathrm{loss}})n_{\mathrm{RE}}.$$

Here, f_{prim} is Dreicer generation and τ_{RE} is the avalanche growth time. With high magnetic turbulence the RE diffusion time should be shorter than the avalanche growth time and thus suppress avalanche generation of REs. In fact, $1/\tau_{\mathrm{RE}} \sim 260\ \mathrm{s}^{-1}$ for typical TEXTOR parameters ($B_t = 2.4$ T, $N_{\mathrm{Ar}} = 3.8 \times 10^{21}$, $R = 1.67$ m, $a = 0.35$ m, $q = 2$, $\nu_{\parallel} \approx c = 3 \times 10^8$ m/s, and $\gamma = 3$ at the beginning of the current quench). The corresponding threshold of magnetic turbulence is $\sim 2.2 \times 10^{-3}$. Previous modeling studies also find that $dB/B_t > 10^{-3}$ suppresses the RE avalanche [8–11]. This value is much larger than the measured magnetic turbulence amplitude $\sim 4.8 \times 10^{-5}$ using the Mirnov coils. This can be explained by the inward movement of the plasma and a shrinking of the minor radius during the current quench. Assuming an average poloidal mode number $m \sim 10$, a movement of 8 cm and a reduction of the minor radius to 0.35 m, the estimated level of magnetic turbulence at the plasma edge amounts $\delta B/B_t \approx 2.4 \times 10^{-3}$. This value is in good agreement with calculated value needed to explain the experimentally observed increase in RE transport.

Conclusions.—Magnetic turbulence (broadband frequency) is observed at the beginning of the current quench in deliberate TEXTOR disruptions. The analysis carried out in this Letter shows that RE suppression has been experimentally found only when the magnetic turbulence exceeds a certain threshold. Below this threshold, the RE current is inversely proportional to the level of magnetic turbulence. Magnetic turbulence is mainly contributed from the background plasma and the level does strongly dependent on the toroidal magnetic field and plasma density. The results reported in this Letter support evidence for a new threshold for RE suppression due to magnetic turbulence and should be considered when making predictions on RE generation in devices such as ITER.

Support from the Helmholtz Association in the frame of the Helmholtz-University Young Investigators Group VH-NG-410 and the National Magnetic Confinement Fusion Science Program of China under Contract No. 2013GB106003 is gratefully acknowledged.

[1] T. C. Hender *et al.*, Nucl. Fusion **47**, S128 (2007).
[2] M. Lehnen, S. S. Abdullaev, G. Arnoux, S. A. Bozhenkov, M. W. Jakubowski, R. Jaspers, V. V. Plyusnin, V. Riccardo, and U. Samm, J. Nucl. Mater. **390–391**, 740 (2009).
[3] R. D. Gill, B. Alper, M. de Baar, T. C. Hender, M. F. Johnson, V. Riccardo, and contributors to the EFDA-JET Workprogramme, Nucl. Fusion **42**, 1039 (2002).
[4] R. Yoshino, S. Tokuda, and Y. Kawano, Nucl. Fusion **39**, 151 (1999).
[5] G. Martin, in *Proceedings of the 25th European Physical Society Conference on Plasma Physics, Prague, 1998* (European Physical Society, Prague, Czech Republic, 1998), Vol. 22C, P.3.006.
[6] T. Fülöp, H. M. Smith, and G. Pokol, Phys. Plasmas **16**, 022502 (2009).
[7] V. Riccado *et al.* (JET EFDA contributors), Plasma Phys. Controlled Fusion **45**, A269 (2003).
[8] P. Helander, L.-G. Eriksson, and F. Andersson, Phys. Plasmas **7**, 4106 (2000).
[9] R. W. Harvey, V. S. Chan, S. C. Chiu, T. E. Evans, M. N. Rosenbluth, and D. G. Whyte, Phys. Plasmas **7**, 4590 (2000).
[10] J. R. Martín-Solís, R. Sánchez, and B. Esposito, Phys. Plasmas **7**, 3369 (2000).
[11] T. Féher, H. M. Smith, T. Fülöp, and K. Gál, Plasma Phys. Controlled Fusion **53**, 035014 (2011).

[12] R. Yoshino and S. Tokuda, Nucl. Fusion **40**, 1293 (2000).
[13] M. Lehnen, S. A. Bozhenkov, S. S. Abdullaev, TEXTOR Team, and M. W. Jakubowski, Phys. Rev. Lett. **100**, 255003 (2008).
[14] I. Entrop, N. J. LopesCardozo, R. Jaspers, and K. H. Finken, Phys. Rev. Lett. **84**, 3606 (2000).
[15] S. A. Bozhenkov, K.-H. Finken, M. Lehnen, and R. C. Wolf, Rev. Sci. Instrum. **78**, 033503 (2007).
[16] K. H. Finken, J. G. Watkins, D. Rusbüldt, W. J. Corbett, K. H. Dippel, D. M. Goebel, and R. A. Moyer, Nucl. Fusion **30**, 859 (1990).
[17] S. A. Bozhenkov *et al.*, Plasma Phys. Controlled Fusion **50**, 105007 (2008).
[18] L. Colas, X. L. Zou, M. Paume, J. M. Chareau, L. Guiziou, G. T. Hoang, Y. Michelot, and D. Grésillon, Nucl. Fusion **38**, 903 (1998).

PUBLICATION 2

IOP Publishing | International Atomic Energy Agency Nuclear Fusion
Nucl. Fusion **54** (2014) 043011 (9pp) doi:10.1088/0029-5515/54/4/043011

Measurement of synchrotron radiation from runaway electrons during the TEXTOR tokamak disruptions

K. Wongrach[1], K.H. Finken[1,2], S.S. Abdullaev[2], R. Koslowski[2], O. Willi[1], L. Zeng[2,3] and the TEXTOR Team

[1] Institut für Laser- und Plasmaphysik, Heinrich-Heine Universität Düsseldorf, Germany
[2] Institut für Energie- und Klimaforschung, Forschungszentrum Jülich GmbH, EURATOM Association, Jülich, Germany
[3] Institute of Plasma Physics, Chinese Academy of Sciences, 230031 Hefei, People's Republic of China

E-mail: kunaree.wongrach@uni-duesseldorf.de

Received 30 June 2013, revised 16 January 2014
Accepted for publication 30 January 2014
Published 12 March 2014

Abstract

Investigations of runaway electrons (REs) during induced disruptions are performed at the TEXTOR tokamak. The synchrotron radiation generated by REs in the plasma core is detected using an infrared camera. The measurements enable the observation of the structure and dynamics of the runaway beam. In particular, the runaway beam is investigated as a function of the vertical and horizontal control fields. From the plasma current a runaway number of 4.33×10^{16} was calculated. The number of REs with energies exceeding 25 MeV is 6.4×10^{15} according to the synchrotron measurement at the end of the current quench phase. The mean pitch angle of the >25 MeV runaways is found to be 52 mrad which is smaller than in the low density discharge scenario. In addition, the synchrotron measurements show for the first time that a significant number of the high energy REs can survive after the end of the current plateau phase. In order to understand this, runaway orbit calculations have been performed which are in good agreement with the measurements.

Keywords: runaway electrons, synchrotron, tokamak, disruption

(Some figures may appear in colour only in the online journal)

1. Introduction

The presence of the inductive electric fields in tokamaks leads to electron acceleration in the toroidal direction. On the other hand, the frictional force due to collisions slows down the electrons. The collision frequency, however, decreases with increasing electron velocity. Hence, the electrical driving force exceeds the collisional drag force for electrons with high velocities and are freely accelerated and run away. The study of runaway electrons (REs) is important in many aspects. First, the collisionless REs can be used as a probe to investigate the non-collisional transport in tokamaks [1]. Second, a substantial part of the plasma current can be converted into a runaway current. REs, therefore, play a crucial role in determining the plasma behaviour [2]. Moreover, they are one of the major concerns for tokamak fusion reactors [3]. Since these REs can gain energies of several tens of MeV [4], they may cause severe damage to plasma facing components (PFCs).

REs have been observed in different tokamaks. It has been found in the Frascati Tokamak Upgrade that REs can carry up to 80% of the predisruptive current [5]. Preferentially runaways are observed at increased toroidal magnetic fields (typically $B_T > 2$ T). Only in the KSTAR tokamak runaways are found down to magnetic fields of 1.3 T [6].

The presence of the REs can be detected by different diagnostics. In principle, the REs can be inferred from x-rays emitted when REs interact with PFCs, or scatter off ions [7], or photons and neutrons generated during photo-nuclear processes [8]. These methods are indirect measurements of unconfined REs. In order to directly detect the runaways at the plasma edge specialized probes have been developed [9, 10]. Additionally, the detection of the synchrotron radiation is one of the most powerful methods used to study REs [11, 12]. REs with energies greater than 25 MeV emit synchrotron radiation in the IR as a result of their helical orbits [13]. This enables the observation of runaways inside the plasma.

REs can be generated at the start up of the discharge, during normal operation, and during a disruption. In TEXTOR, REs are typically generated during normal operation in the low-density discharge regime [13–15]. During

these discharges, the line averaged electron density is kept below $1.0 \times 10^{19}\,\mathrm{m}^{-3}$. Typical runaway parameters in TEXTOR are a runaway beam radius of $r_{\mathrm{beam}} = 0.20$–$0.25\,\mathrm{m}$ and a maximum energy of $W_{\mathrm{max}} \approx 30\,\mathrm{MeV}$ [16]. In addition, measurements of runaways during disruptions by synchrotron radiation have been reported [17]. It has been found that, after disruptions, $r_{\mathrm{beam}} = 0.06 \pm 0.01\,\mathrm{m}$ and $W_{\mathrm{max}} \approx 20\,\mathrm{MeV}$.

In this paper, we discuss the runaway structure of the high energy part during a disruption employing an infrared (IR) camera for detection of the synchrotron radiation. After a short introduction of the experimental setup in section 2, we will present an overview of the synchrotron measurement technique and the plasma position control system in sections 3 and 4, respectively . IR images for different cases of the magnetic control coils are presented and discussed in section 5. Finally, the number of high energy runaways as well as their orbits will be modelled in sections 6 and 7.

2. Experimental setup

The IR camera was installed at the equatorial plane on the low field side (LFS) of the limiter tokamak TEXTOR ($R_0 = 1.75\,\mathrm{m}$, $a = 0.46\,\mathrm{m}$). The camera views the plasma tangentially in the electron approach direction. Figure 1(*a*) shows the schematic of the experimental setup for the synchrotron measurements. The camera is sensitive to wavelengths between 3 and 5 μm where the lower limit is given by the germanium optics of the camera and the upper limit by the InSb detector. The camera viewing area is indicated by the shadowed cone shown in figure 1(*a*) and covers more than half of the plasma cross-section; however, not all runaways are seen from this area, but only those which emit radiation directed towards the IR-optics (see next section). In addition to synchrotron radiation also thermal Planck radiation and the reflection are recorded. Therefore, the graphite tiles of the toroidal pump limiter surface ALT-II and diagnostic ports are recognized (see figure 1(*b*)). The IR camera allows a full-frame image capture of up to 1253 frames per second.

TEXTOR is equipped with a heatable liner allowing an absolute calibration of the IR camera to be performed by heating the liner up to 300 °C and then cooling it down to 150 °C. Images of the liner and, in particular, of the ALT-II limiter for different temperatures have been recorded. The radiation of the graphite tiles is very close to the black body radiation such that the integration over the sensitive band of the camera gives accurately the number of photons.

Since we are interested in the fast varying events of disruptions, a calibration of the temporal behaviour of the camera is important. This was done by using a source of IR radiation. An electrical spark was used which is triggered by a fast high voltage source. The spark brightness has a delay of nanoseconds after the trigger signal and a duration of less than 1 ms, which is the exposure time of the IR camera during the calibration. During the calibration process the spark was triggered in both a single mode and a periodic mode with delays of 2, 3 and 4 s after the switch-on of the camera. The time interval between each spark brightness recorded by the camera agrees well with the time interval of the trigger signal in the periodic mode. However, we have observed that after the 'start signal' the camera has a jitter of about 20 ms. Therefore

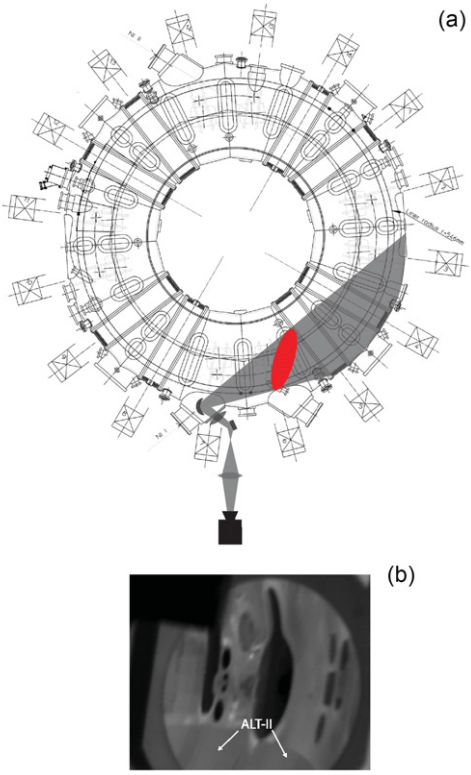

Figure 1. (*a*) Schematic top view of TEXTOR with the experimental setup for synchrotron radiation measurements. The synchrotron radiation as well as IR radiation from other sources are collected and reflected by the stainless steel concave mirror (inside the vacuum chamber) and pass through a CaF_2 window. They are then imaged by a CaF_2 lens and directed to an IR camera. The ellipse indicates the position of the synchrotron radiation which can be observed by the IR camera. (*b*) The camera views the diagnostic ports and the graphite tiles of the toroidal pump limiter surface ALT-II which are seen at the bottom of the 2D IR image (indicated by white arrows).

an independent signal indicating the start of the disruption is required; a suitable signal is the heat pulse at the thermal quench which has a fast rise time and is reproducible.

The main purpose of the camera is to detect the synchrotron radiation. However, the camera detects all the IR radiation emitted in the wavelength region between 3 and 5 μm. This technique is only useful if the synchrotron radiation is the dominant source, or if the other radiation sources can be subtracted. Therefore, the characteristics for synchrotron radiation as compared e.g. to the thermal radiation and radiation from dense gases or dense plasmas (line radiation, continuum radiation), which both are observed during a massive gas injection (MGI), are shortly discussed.

- Synchrotron radiation is only emitted in the electron flight direction with a small opening angle (more details see below in section 3); the light is a continuum. In the given IR band between 3 and 5 μm, an electron energy of at least 25 MeV is required. Therefore runaways are not seen directly after their birth but only after an acceleration phase where the electrons have gained the required energy. After the runaways are lost, no synchrotron radiation is emitted any more.
- Thermal radiation arises predominantly from PFCs, in particular from protruding edges. If the heat flux lasts

relatively long as during a normal discharge, the deposited heat propagates into the material and therefore the objects can radiate for seconds. If the thermal power is deposited in a short time as in a disruption, the heat from the surface disappears relatively quickly, but in general lasts longer than the synchrotron radiation. In addition to the preferred heating of edges due to heat convection one also observes a diffuse heating of the surface due to plasma radiation and/or neutral particle bombardment of the vessel surface. Diffuse heating is found during MGI experiments.

– Reflections do not represent a heat source but can complicate the analysis of the measurements e.g. of the synchrotron radiation. The reflections originate preferentially from flat parts of the walls e.g. at flange locations. A characteristic feature is that the reflections remain spatially well localized.
– A neutral gas or a dense plasma can also emit IR radiation. During the experiments with a MGI by a fast valve, this radiation is indeed the dominant IR source. It has not been investigated whether it is line or continuum radiation. The radiation appears very quickly, namely between 1 and 2 ms after the activation of the valve and it is very diffuse.

The different IR radiation sources have characteristic features such that they can easily be distinguished. In the following we describe only those disruptions where synchrotron radiation can well be analysed.

The fast valve [18] located at the top of TEXTOR is used to induce the disruption by a fast injection of Ar-gas. It has a volume of 250 ml with a typical operating pressure of 1 bar. During the disruption the magnetic control fields are switched in different ways. One aim was to optimize the runaway lifetime in the vessel in order to study their shape and their movement.

3. Synchrotron radiation in a tokamak

Since the measurement of synchrotron radiation is not an often applied technique, a short summary is given here. The synchrotron radiation has some specific properties. Synchrotron radiation is generated by relativistic electrons. If one considers electrons spiralling around a magnetic field with higher and higher energies, they emit at first only one line at ω_{ce}, then more and more harmonics are emitted. Finally they merge at the relativistic limit into a continuum. A characteristic feature at relativistic energies is that the radiation is emitted into the forward direction. The natural opening angle of such an emission is about $\theta \approx 1/\gamma$ where γ is the relativistic factor. The power emitted by one RE per wavelength interval is [19]

$$P_\lambda^e \mathrm{d}\lambda = \frac{4\pi}{\sqrt{3}} \frac{m_e c^3 r_e}{\gamma^2 \lambda^3} \left(\int_{\frac{4\pi R_c}{3\lambda\gamma^3}}^{\infty} K_{5/3}(x)\,\mathrm{d}x \right) \mathrm{d}\lambda, \qquad (1)$$

where $K_{5/3}$ is the modified Bessel function of the order 5/3, m_e the electron rest mass, r_e the classical electron radius and R_c the instantaneous radius of curvature of the electron orbit.

The radiated power per electron depends on the energies of the REs and on the radius of curvature of their orbits. The orbit of the REs is a curved helix, namely a superposition of a toroidal orbit along the magnetic field lines and the Larmor motion around the field lines.

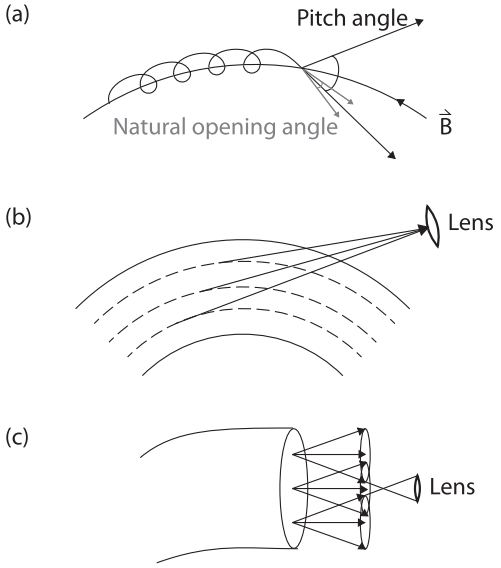

Figure 2. Schematic sketch of (*a*) the pitch angle of the synchrotron radiation from RE and the natural opening angle of the synchrotron radiation (*b*) Toroidal cut: synchrotron radiation emitted by REs from different drift surfaces (*c*) Poloidal cut: synchrotron radiation emitted by REs from different areas. Only the synchrotron radiation within the emission cone is collected by the lens.

The synchrotron radiation is emitted into a narrow cone with the natural opening angle. However, the gyromotion of the REs leads to an increase in the emission angle of the synchrotron radiation. The runaways will fill the emission cone with the pitch angle $\theta = v_\perp/v_\parallel$, which is larger than the natural emission angle (see figure 2). From the analysis of the shape of the synchrotron radiation image the pitch angle can be derived [14]. The radius of curvature of the electron orbits and the direction of the velocity vector of the RE change along its path, therefore, the pitch angle deduced from the 2D image is an average value.

Due to the high directivity of the synchrotron radiation, only the fraction $\theta/2\pi$ of the superposition of gyro and toroidal electron orbits can be seen, indicated by the encircled area in figure 1. The dependences of the emitted power as a function of the wavelength λ for different runaway energies and pitch angles are shown in figures 3(*a*) and (*b*), respectively. At the lower λ region, the spectra drop strongly with decreasing λ. The spectra are dominated by the highest energy and the largest pitch angle. Figure 3(*b*) shows the strong dependence on θ, in particular for low values of θ. Typical runaway parameters in TEXTOR for low density discharges are $\theta = 0.12 \pm 0.02$ rad, $r_{beam} = 0.20$–0.25 m and $W_{max} \approx 30$ MeV [16]. For disruptions, we derive $\theta = 24 \pm 4$ mrad, $r_{beam} = 0.06 \pm 0.01$ m and $W_{max} \approx 20$ MeV [17].

4. Plasma position control systems in TEXTOR

The TEXTOR plasma has a circular symmetry shape. A set of vertical position control coils generates the control field for the plasma vertical position. The horizontal position is determined by the sum of the vertical fields generated by the vertical field coils and the fast radial position control coils. The position control systems have a lower inductivity and a faster response on the plasma than the vertical field coil systems.

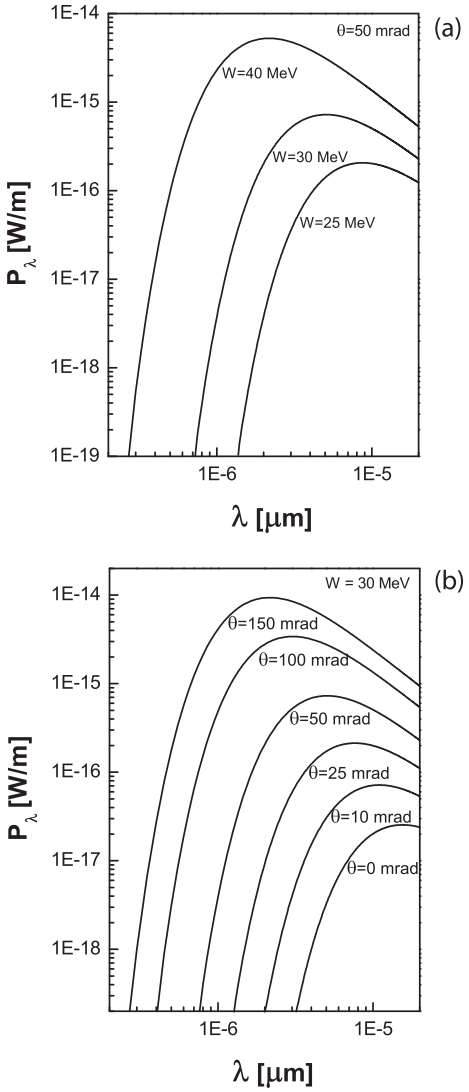

Figure 3. Spectra of the synchrotron radiation for monoenergetic electrons with (*a*) energies up to 40 MeV and (*b*) the pitch angles from 0 to 10 rad.

The feedback signal is measured by using either magnetic sensors or interferometry. During disruptions, the magnetic loop control systems show errors because the integrating systems of the magnetic coils saturate. Additionally, the interferometric measurement is affected by fringe shifts which occur during disruptions. This leads to counting errors. Therefore, during pre-programmed disruptions the control coils are mostly operated in feed-forward mode. There are different modes of operation because the different coils have independent power supplies. In the next section the runaway distribution in the plasma will be described depending on the handling of the control coils. More details of the technical systems of TEXTOR are found in [20, 21].

5. Measurement of REs during disruptions

During the steady state phase of an ohmic discharge, 0.25 bar l of argon is injected into the vacuum vessel using the fast valve at $t = 2$ s to initiate the disruption. This procedure provides a rather reliable generation of REs [22]. In the following subsections, runaway beams in different scenarios of the control coil systems are investigated.

Case I. In the discharge 117830, the current of the radial position control coils is switched to its limiting value of +3.5 kA and the current of the vertical position control coils is set to +1 kA shortly after the initiation of the disruption. Figures 4(*a*)–(*f*) present the IR radiation observed by the camera at different times. As mentioned in section 2, the camera views a partial cross-section of the runaway beam, i.e. the LFS of the torus can be seen while the HFS of the torus is vignetted. Therefore, the beam information at the HFS is lost. Since the beam is partially observed, it is difficult to determine the exact shape and the pitch angle of the beam. The radius of the runaway beam and the pitch angle given in section 6 are deduced from the discharges, in which the runaway beam was shifted to the LFS and the whole beam was observed.

IR radiation is seen at 4 ms after the gas injection and remains nearly unchanged over 5 ms (see figure 4(*a*)). This radiation is the thermal radiation emitted from the heated PFCs during the thermal quench phase. At $t = 2.009$ s, REs have gained enough energy to become visible at the left side of the image as shown in figure 4(*b*). The rapid change of the IR radiation pattern developing after the thermal quench indicates that the IR emission is synchrotron radiation emitted by REs.

The runaway beam builds up at the left side of the IR images. The runaway beam reaches its maximum brightness at about 2.021 s (see figure 4(*c*)). After that the radius of the runaway beam shrinks with time. Decreases of the intensity and size of the beam indicate the loss of high energy REs. In figures 4(*b*)–(*d*) one sees an 'ear like structure' (indicated by white arrows); this structure is not generated by the runaways but is a reflection from one of the big opening ports of TEXTOR (see also figure 1(*b*)). The radiation pattern of this part is very localized and its intensity changes with the movement of the beam. In contrast, figures 4(*e*) and (*d*) do not show any structure which is related to the surface of the vessel wall or the diagnostic ports. Additionally, the position of the IR radiation changes rapidly. Thus the IR radiation in figures 4(*e*) and (*f*) are neither the reflection nor the thermal radiation but the synchrotron radiation.

In figure 5, the intensities added over all pixels of the IR image (I), plasma current (II), loop voltage (III), SXR (IV), the horizontal field (V), the total vertical field (VI) and ECE (VII) are plotted against time. The dashed lines (*a*)–(*f*) indicate the time corresponding to figures 4(*a*)–(*f*), respectively. The thermal quench takes place at $t = 2.004$ s (dashed line (*a*)). The plasma energy is rapidly lost accompanied by a sudden drop of the plasma temperature (see figure 5(VII)). The energy is deposited on the PFCs leading to thermal radiation of the heated components as shown above. The thermal quench time is, therefore, used to synchronize the camera timing with the timing of the other diagnostics. After that the rapid rise of the loop voltage followed by the current drop is observed (see figures 5(II) and(III)). Figure 5(I) shows that during the current quench phase, IR radiation builds up exponentially and gains energy from the induced E-field. At the loss phase (after dashed line (*d*)), the plasma current drops rapidly accompanied by a positive peak of the thermal IR signal. The increase in IR radiation is caused by the movement of the runaway beam.

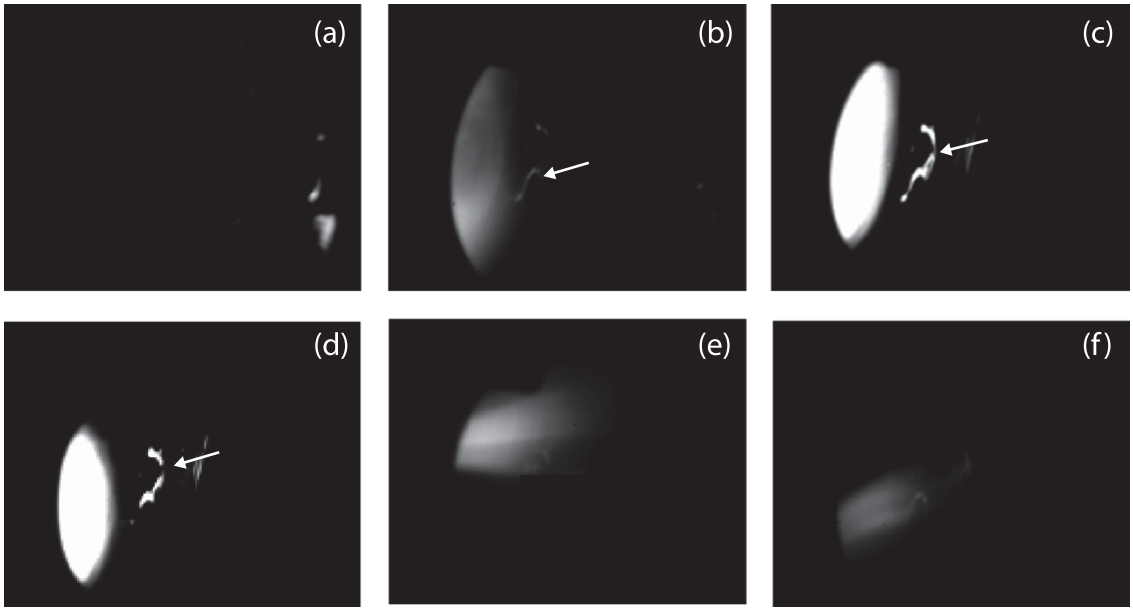

Figure 4. IR radiation observed by the camera of the discharge 117830. Images are taken at (*a*) $t = 2.004$ s when the thermal quench takes place, (*b*) $t = 2.010$ s, the synchrotron radiation emitted by REs becomes visible, (*c*) $t = 2.021$ s, runaway beam has its maximum intensity, (*d*) $t = 2.027$ s, (*e*) $t = 2.034$ s and (*f*) $t = 2.042$ s. The HFS is on the left side of the images, whereas the LFS is on the right side. White arrows indicate the 'ear like' structure from the reflection.

Since the beam moves rapidly towards LFS, larger parts of the beam expose to the camera's field of view. After this phase, the IR radiation decays gradually. The SXR spikes between dashed lines (b) and (d) in figure 5(IV) correspond to a decrease of the IR signal. This confirms that during the current plateau parts of REs are lost.

The horizontal field shown in figure 5 (V) oscillates between -3.5×10^{-3} T and $+3.5 \times 10^{-3}$ T because one of the vertical position control coil systems failed. At $t = 2$ s the horizontal field (B_H) is around zero. 15 ms later it drops to ≈ -3.5 kA. The runaway beam then moves a little bit upward because shortly thereafter the B_H increases to +3.5 kA. With increasing time the beam move more and more downward (see figure 4(*d*)). At $t \approx 2.028$ s the B_H drops to ≈ -3.5 kA, therefore, the beam move upward as shown in figure 4(*e*). As the B_H increases to +3.5 kA, the beam moves again downward.

Case II. The position control coils are operated by independent power supplies. One may fail during a disruption. This leads to an inhomogeneous field and will cause oscillations of the beam. Since a circular plasma is vertically stable, we are able to switch off the vertical position control system during the following case in order to avoid potential problems with feedback control.

In the discharge 117859, the current of the radial position control coils is also set to +3.5 kA. However, the current of the vertical field coils is higher than that in the discharge 117830. In the absence of the force exerted by the horizontal field, the vertical position of the beam does not change significantly over time as can be seen in figure 6.

Similar to the previous discharge, the beam becomes visible and develops at the HFS as shown in figure 6(*b*). However, the higher total vertical field (see figure 7(VI)) causes an inward movement of the beam after it evolves over 6 ms. This indicates that the positive vertical field moves the runaway

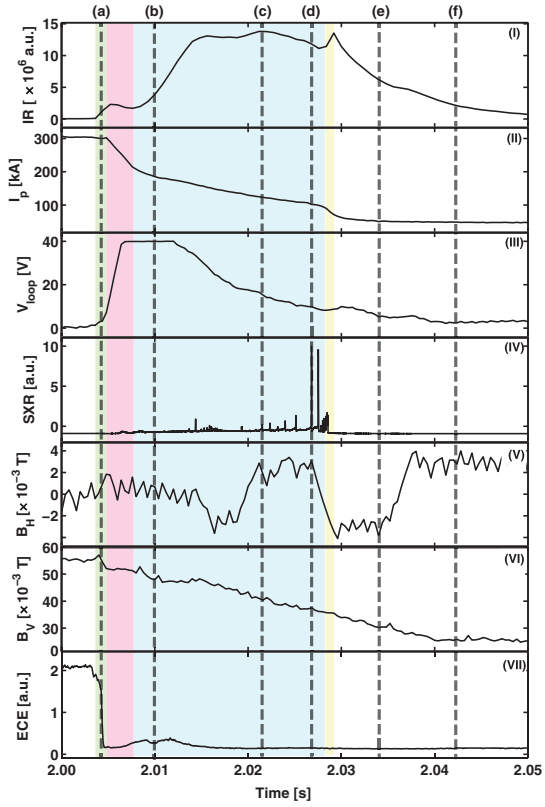

Figure 5. Temporal evolution of the discharge 117830: (top to bottom) the intensities added over all pixels of the IR image, plasma current, loop voltage, soft x-ray emission (SXR), the horizontal field, the total vertical field, and electron cyclotron emission (ECE) during an induced disruption. The dashed lines indicate the times corresponding to the IR 2D images shown in figure 4. The green area indicates the thermal quench (TQ), the pink area the current quench (CQ), the blue area the runaway plateau and the yellow area the runaway plateau termination.

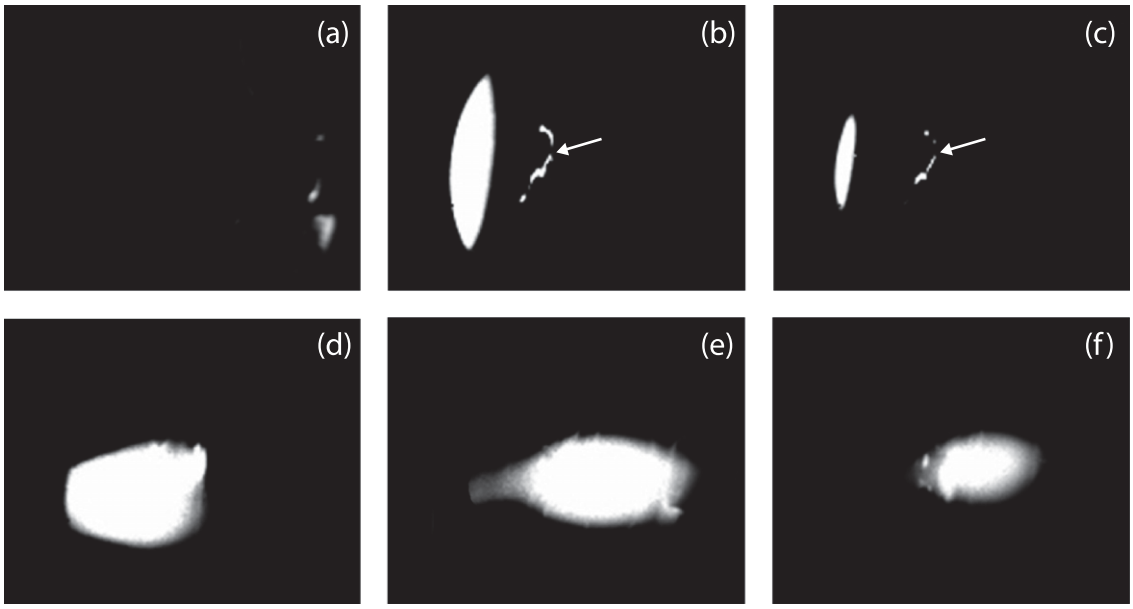

Figure 6. IR radiation observed by the camera of the discharge 117859. Images are taken at (*a*) $t = 2.004$ s when the thermal quench takes place, (*b*) $t = 2.020$ s, the runaway beam starts to move towards HFS, (*c*) $t = 2.024$ s, shortly before the beam move completely out of the camera view, (*d*) $t = 2.027$ s, the runaway beam moves towards LFS, (*e*) $t = 2.028$ s, the runaway beam has its maximum intensity and (*f*) $t = 2.039$ s. White arrows indicate the 'ear like' structure from the reflection.

beam towards HFS. At $t = 2.025$ s, the runaway beam moves completely out of the camera view. Shortly thereafter, the beam moves back to the LFS as shown in figure 6(*d*). The shape of the runaway beam changes rapidly. The beam then slowly moves further away from the HFS. After the beam reaches its maximum intensity at $t = 2.028$ s (see figure 6(*e*)), no further change in the beam position is observed. The REs are gradually lost and completely disappear at $t \approx 2.050$ s.

During the current quench phase (pink area), the temporal evolution of the IR radiation intensity presented in figure 7(I) is similar to the previous case (see also figure 5(I)). The maximum intensity during this phase in both cases is comparable. In contrast, the intensity of IR radiation during and after the plateau termination phase (dashed lines (*c*)–(*e*)) increases strongly. The maximum IR radiation intensity during this phase is ≈2.5 times higher than the intensities during the current plateau phase. The reason for this is that during the current plateau phase a major part of the beam is located at the HFS, i.e. outside the camera's field of view. However, the high IR intensity originating from synchrotron radiation indicates that a large fraction of the high energy RE survives the runaway plateau termination. After the beam reaches its maximum intensity at $t = 2.028$ s (dashed line (*e*)), the IR radiation smoothly decays to zero. The loop voltage after the current drop is relatively high (see figure 7(III)). SXR signal in figure 7(IV) shows that losses occur during the current plateau phase and during the runaway plateau termination (dashed lines (*a*)–(*d*)). After the plateau termination (dashed lines (*d*)–(*f*)), by contrast, no SXR spike is observed.

In this scenario (figures 6 and 7), the high energy runaways survive about 30 ms. However, their vertical extension is rather limited. Shortly before the runaway plateau termination takes place, the plasma current is relatively high. The sudden drop of the current during the runaway plateau termination leads to the rise of the loop voltage. The high loop voltage accelerates the REs that survive the runaway plateau termination. As the energies of the REs are further increased, the runaway orbit drifts outwards (see figures 6(*d*)–(*e*)). This agrees well with the calculation shown in section 7. In addition, the poloidal field generated by the plasma current decreases rapidly due to the strong current drop during the runaway plateau termination. For lack of poloidal field the vertical electric field is generated due to the charge separation. The $E \times B$ force moves the beam outwards. Nevertheless, the drift velocity of the runaway orbits due to the parallel acceleration induced by loop voltage is one order larger than the $E \times B$ drift [23]. This effect is therefore negligible.

In both cases discussed above no MHD activity is observed after the plateau termination. The synchrotron radiation detected by the IR camera is an only proof of the existence of the REs after the runaway plateau termination. However, in some discharges the continuing MHD activity has been observed after the current drops to almost zero. The MHD activity measured in the soft x-ray regime is present until the runaway beam disappears (see figure 8). This confirms that REs survive the plateau termination. A detailed analysis of the soft x-ray signals will be provided in another paper in preparation.

6. Number of REs

As discussed in section 3, synchrotron radiation is emitted only in a cone with an angle θ, while the thermal radiation is emitted into the full solid angle of 4π. The position of the runaway beam, therefore, deviates from the position of the ports and PFCs shown in figure 1(*b*). The position of the runaway beam is determined by drawing a line tangent to a runaway orbit from the entrance lens to the vessel wall. The position of the runaway beam on the line corresponds to the position of the wall where it intersects the line. As the background position

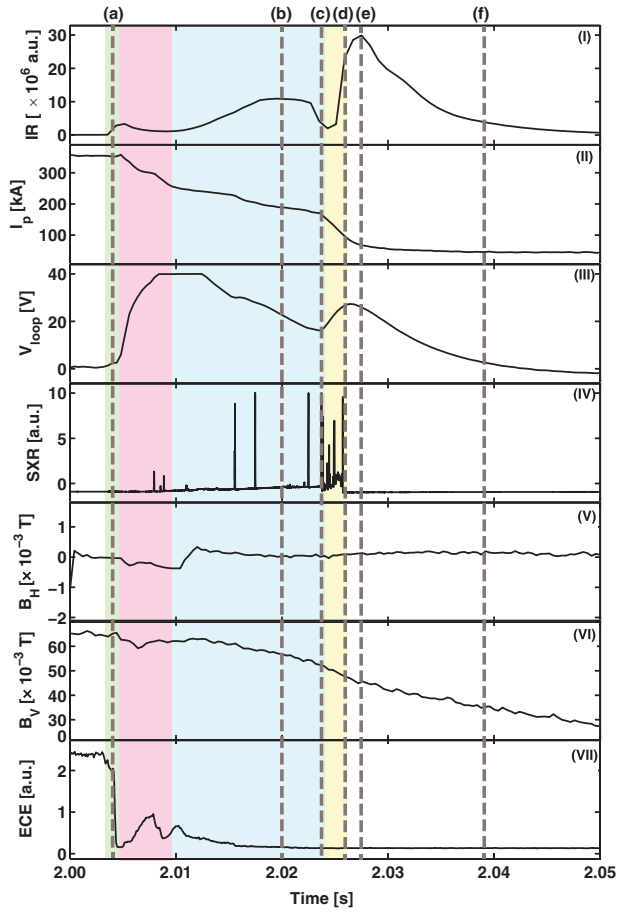

Figure 7. Temporal evolution of the discharge 117859: (top to bottom) the intensities added over all pixels of the IR image, plasma current, loop voltage, soft x-ray emission (SXR), the horizontal field, the total vertical field, and electron cyclotron emission (ECE) during an induced disruption. The dashed lines indicate the times corresponding to the IR 2D images shown in figure 6. The green area indicates the thermal quench (TQ), the pink area the current quench (CQ), the blue area the runaway plateau and the yellow area the runaway plateau termination.

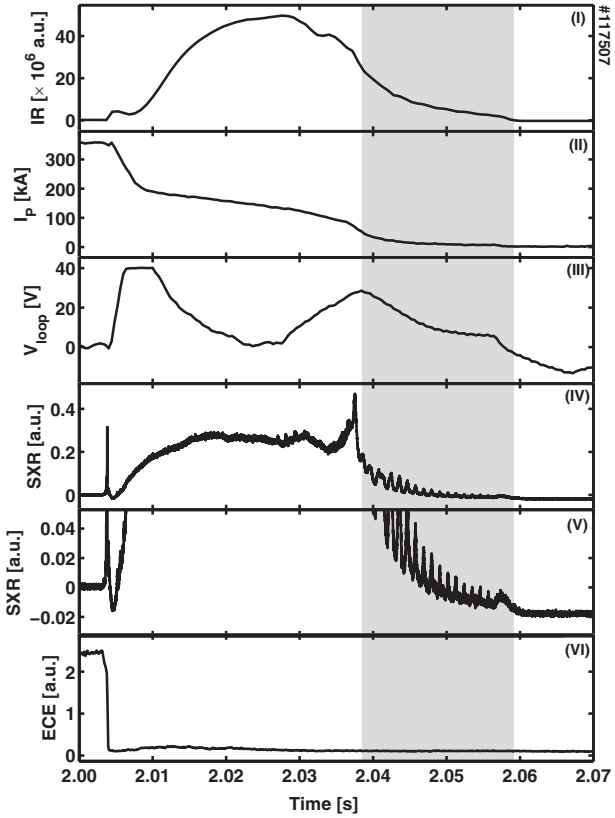

Figure 8. Temporal evolution of the discharge 117507: (top to bottom) the intensities added over all pixels of the IR image, plasma current, loop voltage, soft x-ray emission (SXR), magnified SXR, and electron cyclotron emission (ECE) during an induced disruption. The grey area indicates the phase after the runaway plateau termination.

relative to the lens is known, the position of the runaway beam can be obtained.

For deducing the number of REs from the synchrotron radiation, the radius of curvature of the runaways must be known. The procedure is described in detail in references [13–15].

Typical runaway parameters during an induced disruption in TEXTOR are $r_{\mathrm{beam}} = 28 \pm 3\,\mathrm{cm}$ and $\theta = 52 \pm 10\,\mathrm{mrad}$. The number of the high energetic REs can be retrieved from the synchrotron radiation integrated over the wavelength and the cross section according to the equation

$$N_{\mathrm{RE}} = \frac{L_\lambda A \Omega}{P_\lambda} \tag{2}$$

where N is the number of REs, A the area of the runaway beam cross section, $\Omega = 2\pi \times 2\theta$, P_λ the power emitted by one RE and L_λ the absolute value of the radiance. Comparing the synchrotron radiation with the thermal radiation from the liner gives rise to the absolute value of the radiance.

Figure 9(*a*) shows the IR image of the discharge 117859 at $t = 2.029\,\mathrm{s}$ when the whole runaway beam is observed and the runaway beam has its maximum intensity. The radial distribution of the runaway beam is plotted in figure 9(*b*). For $\lambda = 4.5\,\mu\mathrm{m}$ and $\gamma_{\mathrm{max}} = 60$, we obtain $N_{\mathrm{re}} = 6.40 \times 10^{15}$.

The total number of REs can be estimated from the runaway current:

$$N_{\mathrm{tot}} = \frac{2\pi R_0 I_{\mathrm{re}}}{ce}. \tag{3}$$

The I_{re} obtained from figure 7 (II) is 189 kA corresponding to the total number of the REs of 4.33×10^{16}. The ratio of the number of the REs which survive the current drop to the total runaway number is 0.15. It is affected by an error margin of about 20%.

7. REs orbits

It is assumed that REs are generated during the high voltage phase shortly after the current quench, then they are accelerated and form a plateau in the plasma current, and at the end of this plateau they are lost when the current decreases again. To our knowledge, our synchrotron measurements show for the first time that high energy REs can survive the current decay phase for a considerable time (see figures 4–7), even though the plasma current is already close to zero. As seen in figures 5 and 7, sometimes the high energy runaways are indeed lost at the expected time but in other cases not.

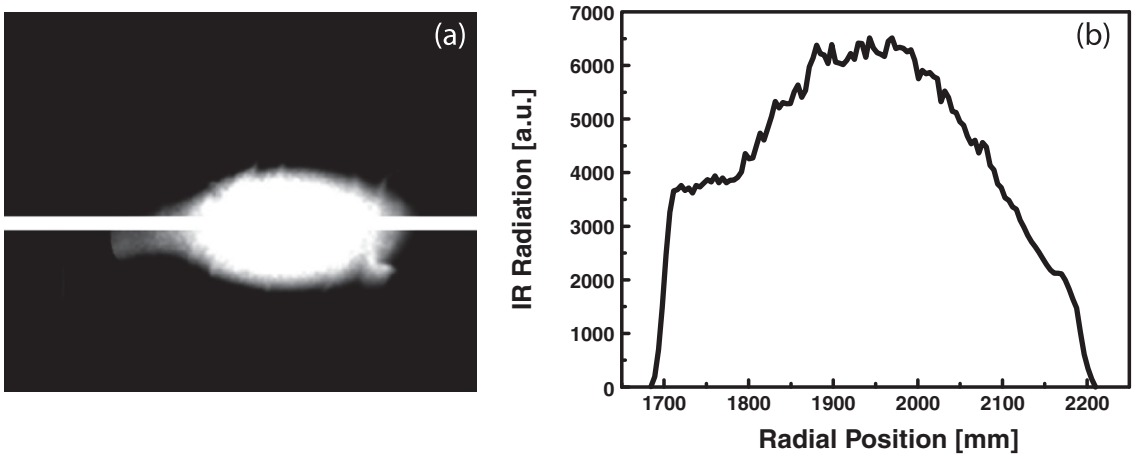

Figure 9. (*a*) An IR 2D image of the discharge 117859 at $t = 2.029$ s. (*b*) Radial distribution of the IR image taken from the slit shown in (*a*).

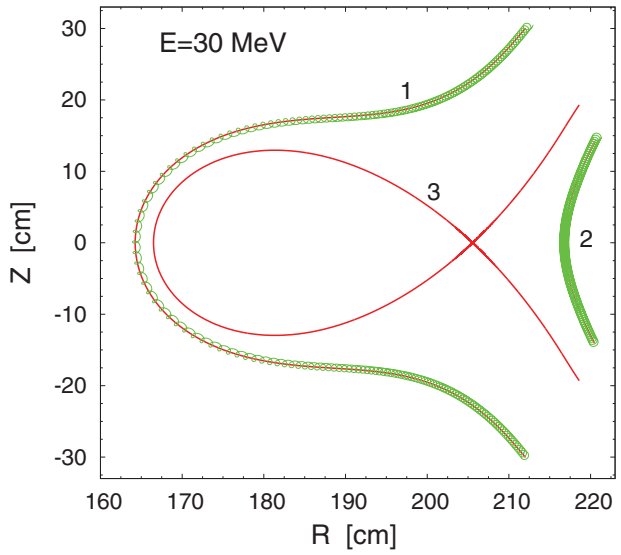

Figure 10. Typical RE orbits in the (R, Z) plane for $E = 30$ MeV at $t = 2.027$ s of the discharge 117859. The plasma current is $I_p = 94$ kA. The plasma radius is taken equal to $a = 30$ cm. Curves 1 and 2 correspond to the unconfined electrons and curve 3 corresponds to the curve (the separatrix) separating the confined and unconfined orbits.

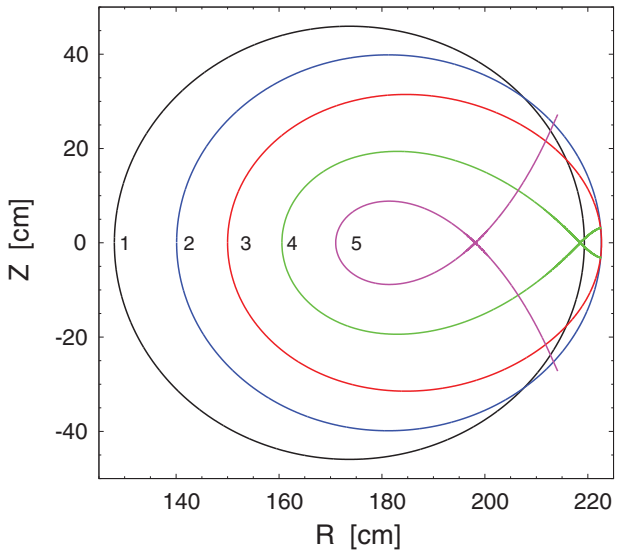

Figure 11. Separatrices of RE orbits for the five values of the electron energies: curves 1–5 correspond to $E = 1$ MeV, 5 MeV, 10 MeV, 20 MeV and 40 MeV, respectively. The plasma parameters are the same as in figure 10.

In order to study this process, a direct numerical calculation of RE orbits at the different currents is performed. For this we have used the relativistic Hamiltonian equations for the gyrating particles and the guiding centre motion developed in references [24, 25]. For the magnetic field we have used the model presented in [26].

The typical gyrating orbits and guiding centre orbits of REs in the (R, Z)-plane are shown in figure 10 for the plasma parameters corresponding to the discharge 117859 at $t = 2.027$ s. The electron energy is taken $E = 30$ MeV, and the plasma radius $a = 30$ cm. The plasma current is centred at $R = 172$ cm.

As seen from figure 10 the unconfined orbits (curves 1 and 2) are located outside the separatrix, i.e. the boundary separating the confined and the loss orbits (curve 3). The area S_{conf} of confined orbits depends on the electron energy E and the plasma current I_p. At the given current the confined particle's area shrinks with increasing energy E. This tendency is shown in figure 11 where the separatrices of the guiding centre orbits are plotted for the five different values of the electron energies: curves 1–5 correspond to the energies 1 MeV, 5 MeV, 10 MeV, 20 MeV and 40 MeV, respectively.

The particles with the energy E exceeding the critical value E_{cr} are not confined in the plasma. The value E_{cr} depends on the plasma current I_p. The numerical calculations show that E_{cr} grows as a square root of I_p. The dependence of E_{cr} on the square root of the current I_p is plotted in figure 12. This dependence can be fitted by the linear function (solid curve) $E_{cr} = a + bI_p^{1/2}$ with the constant coefficients a and b. Such a dependence is in agreement with the qualitative theoretical estimation given in [27].

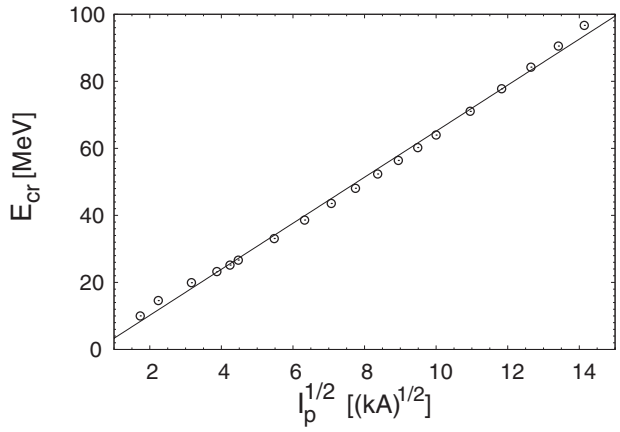

Figure 12. Critical energy E_{cr} versus square root of plasma current I_p: the symbols ⊙ correspond to the numerical calculations, the solid line corresponds to the fitting by the straight line $E_{cr} = a + bI_p^{1/2}$ ($a = -3.539\,24$, $b = 6.865\,93$).

8. Summary and conclusions

Detection of the synchrotron radiation is a powerful tool to study runaway electrons in tokamak disruptions. With this technique we detect the high energy part of the distribution function of the runaways and find that the runaway energy becomes of the order of 30 MeV even for the medium size tokamak TEXTOR. For the quantitative analysis of the runaways from synchrotron radiation we have to estimate the radius of curvature of the orbit. Our analysis shows that the pitch angle θ amounts to about 52 mrad, which is about 2 times smaller than the pitch angle in low density runaway discharges. As can be seen from figure 3(*b*), the pitch angle has a significant influence on the radiative power. The calculated number of high energy runaways is therefore affected by the error associated with the estimation of θ.

In many tokamak disruption studies [17, 28, 29], the runaway termination is determined by the time the plasma current drops rapidly to almost zero. The runaway electrons are completely lost to the wall when the current plateau is terminated. Nevertheless, in 23 disruptions of our experimental campaign we have observed a significant number of high energy runaway electrons after the runaway plateau termination. In some of these disruptions the existence of the runaway electrons in this phase is evidenced by both the synchrotron radiation and the MHD activity.

To our knowledge, it has been shown for the first time that high energy runaway electrons can survive the runaway plateau termination. When the current drops to tens of kA, only the runaway electrons outside the confined orbits are lost (see figure 11). It is striking that the high energy runaways (25 MeV) can still be confined by a plasma current of about 20 kA (see figure 12).

The decrease in current is accompanied by the increase in the loop voltage which can lead to the runaway electron acceleration or further runaway generation [30]. With increasing time the runaway electrons gain more energy. The high energy runaway electrons drift towards LFS while the runaway confined area becomes smaller. The runaway electrons are therefore lost gradually.

The control of the runaway beam offers an opportunity to moderate the consequential effects of the runaway loss in case that the runaway suppression does not work, for instance, on ITER. The beam positioning can help improve the stability of the beam. The runaways then decay gradually instead of being dumped on to a localized area.

Acknowledgments

This work was supported by the Royal Thai Government, an R&D contract, the Trilateral Euregio Cluster (TEC) and the DFG program GRK 1203. The authors thank O. Schmitz and the TEXTOR team for their support.

References

[1] Hauff T. and Jenko F. 2009 *Phys. Plasmas* **16** 102308
[2] Yoshida Z. 1990 *Nucl. Fusion.* **30** 317
[3] Plyusnin V.V. *et al* 2006 *Nucl. Fusion* **46** 277
[4] Helander P. *et al* 2002 *Plasma Phys. Control. Fusion* **44** B247
[5] Martin-Solis J.R. *et al* 2006 *Phys. Rev. Lett.* **97** 165002
[6] Chen Z.Y. *et al* 2013 *Plasma Phys. Control. Fusion* **55** 035007
[7] Savrukhin P.V. 2002 *Phys. Plasmas* **9** 3421
[8] Esposito B. *et al* 2003 *Phys. Plasmas* **10** 2350
[9] Kudyakov T. *et al* 2008 *Nucl. Fusion* **48** 122002
[10] Forster M. *et al* 2011 *Nucl. Fusion* **51** 043003
[11] Shi Y. *et al* 2010 *Rev. Sci. Instrum.* **81** 033506
[12] Yu J.H. *et al* 2013 *Phys. Plasmas* **20** 042113
[13] Finken K.H. *et al* 2007 *Nucl. Fusion* **47** 91
[14] Finken K.H. *et al* 1990 *Nucl. Fusion* **30** 859
[15] Entrop I. *et al* 1999 *Plasma Phys. Control. Fusion* **41** 377
[16] Jaspers R. 1995 Relativistic runaway electrons in tokamak plasmas *PhD Thesis* Technical University Eindhoven, The Netherlands
[17] Jaspers R. *et al* 1996 *Nucl. Fusion* **36** 367
[18] Savtchkov A. *et al* 2002 *Rev. Sci. Instrum.* **70** 3490
[19] Schwinger J. 1949 *Phys. Rev.* **75** 1912
[20] Mitri M. 2009 *Real-time Digital Control of Plasma Position and Shape on the TEXTOR Tokamak: Environment & Energy* vol 33 (Jülich, Germany: Forschungszentrum Jülich)
[21] Neubauer O. *et al* 2005 *Fusion Sci. Technol.* **47** 76
[22] Lehnen M. *et al* 2008 *Phys. Rev. Lett.* **100** 255003
[23] Guan X. *et al* 2010 *Phys. Plasmas* **17** 092502
[24] Abdullaev S.S. and Finken K.H. 2002 *Phys. Plasmas* **9** 4193
[25] Wingen A. *et al* 2006 *Nucl. Fusion* **46** 941
[26] Finken K.H. *et al* 2005 *The Structure of magnetic field in the TEXTOR-DED: Energy Technology* vol 45 (Jülich, Germany: Forschungszentrum Jülich)
[27] Knoepfel H. *et al* 1979 *Nucl. Fusion* **19** 785
[28] Gill R. 1993 *Plasma Phys. Nucl. Fusion* **33** 1613
[29] Eidietis N.W. *et al* 2012 *Phys. plasmas* **19** 056109
[30] Loarte *et al* 2011 *Nucl. Fusion* **51** 073004

PUBLICATION 3

OPEN ACCESS
IOP Publishing | International Atomic Energy Agency Nuclear Fusion
Nucl. Fusion **55** (2015) 053008 (12pp) doi:10.1088/0029-5515/55/5/053008

Runaway electron studies in TEXTOR

K. Wongrach[1], K.H. Finken[1], S.S. Abdullaev[2], O. Willi[1], L. Zeng[3], Y. Xu[4] and the TEXTOR Team

[1] Institut für Laser-und Plasmaphysik, Heinrich-Heine Universität Düsseldorf, Germany
[2] Institut für Energie-und Klimaforschung, Forschungszentrum Jülich GmbH, Jülich, Germany
[3] Institute of Plasma Physics, Chinese Academy of Sciences, Hefei, People's Republic of China
[4] Southwestern Institute of Physics, Chengdu, People's Republic of China

E-mail: kunaree.wongrach@uni-duesseldorf.de

Received 23 October 2014, revised 19 February 2015
Accepted for publication 26 February 2015
Published 15 April 2015

Abstract

The evolution of runaway electrons in disruptive plasmas in TEXTOR is determined by observing the synchrotron radiation (hard component $E > 25$ MeV) and by measuring the runway electrons with an energy of a few MeV using a scintillator probe. Disruptions are initiated by a massive argon gas injection performed by a fast valve. The observed runaway beam of the high energy component (synchrotron radiation) fills about half of the diameter of the original plasma. The beam is smooth and shows no indication of filamentation. The initial conditions are in all cases very similar. The temporal development of the runaway electrons, however, is different: one observes cases with and without subsequent mode excitation and other cases in which the hard runaway component survives the apparent end of the runaway plateau. Several methods are applied to remove the runaway electrons including massive gas injection from two additional valves of different sizes as well as external and internal ergodization by inducing a tearing mode. The mitigation is only marginally successful and it is clearly found that the runaways in disruptions are substantially more robust than runaways created in stationary, low density discharges.

Keywords: runaway, mitigation, disruption, TEXTOR, tokamak

(Some figures may appear in colour only in the online journal)

1. Introduction

During a disruption, a sudden loss of magnetic confinement, the energy stored in the plasma is rapidly lost to the plasma facing components (PFCs) [1]. The damage to the machine following the disruption is caused by: (a) the transient heat load during the thermal quench (TQ), (b) the high forces applied to the PFCs and the vessel resulting from the halo and eddy currents, and (c) the energetic runaway electrons (REs). Several methods have been proposed in order to mitigate the effects of disruptions. It has been shown in several tokamaks that the damaging effects of disruptions are significantly reduced by early injection of impurity species [2]. Killer pellet injection is one of the methods for rapid insertion of impurities into a tokamak plasma. Experiments on disruption mitigation by using pellets of neon, argon and methane have been performed in several tokamaks [3–6]. The pellet increases the radiated power and reduces the mechanical loads on the vessel wall by up to 50%, the thermal flux on the divertor by 25–40%, and the peak halo current by 50%. Nevertheless, the production of REs has been caused also by the pellet injection [5, 6]. Another potential candidate for disruption mitigation is a massive gas injection [7]. A gas injection system creates a subsonic gas jet which delivers a large quantity of neutral gas ($>10^{22}$ atoms) into the vacuum vessel within $\leqslant 5$ ms [8]. The rapid shutdown by puffing noble gases, e.g. helium, neon or argon, in JET [9], ASDEX upgrade [10], DIII-D [11], Tore-Supra [12], JT-60U [13] and TEXTOR [14] demonstrates the mitigation of the halo current and the significant reduction of the heat load during TQ by enhanced radiation. Massive helium injection effectively suppresses REs [12]. Argon injection, in contrast, is prone to runaway generation. However, the TEXTOR disruptions initiated by argon injection can become runaway free if the number of atoms exceeds $14 \pm 2 \times 10^{21}$, i.e. around 140 times the plasma electron content [14]. Additionally, the injection of mixtures of argon with hydrogen [13] or deuterium [14] also provides runaway-free disruptions.

Several experiments have been dedicated to the study of runaway generation and suppression during disruptions in different tokamaks [14–16]. Most studies of runaway mitigation concentrate on a massive gas injection. In next-generation tokamaks such as ITER, REs with energies of the order of a few hundred MeV are expected [17]. In order

to avoid runaway generation during ITER disruptions, either 1.5×10^{25} molecules of helium gas or 1.8×10^{24} molecules of argon gas have to be delivered within a few milliseconds [18]. This requirement cannot be achieved by the present-day devices. Moreover, the injection of a large amount of gas may affect the vacuum system. It has been shown in [19] that a fast gas puff with a moderate amount of helium leads to the loss of the existing REs and the plasma current decay time is shortened. Magnetic perturbations are another method applied to mitigate the REs. The suppression of the runaway avalanche during TEXTOR disruptions is observed when a perturbation field with $n = 1$ and $n = 2$ is applied [20].

In this paper, we present initially some examples of the evolution of runaways without additional mitigation methods and then a systematic study of different runaway mitigation methods used in TEXTOR including a gas puff and mitigation by the dynamic ergodic divertor (DED). The mitigation approaches are applied to disruptions initiated by a fast argon puff. The paper focuses in particular on the observation of the IR-synchrotron radiation which is sensitive to runaways with energies $E_r \gtrsim 25$ MeV and the measurement of the runaway probe which is sensitive to runaways leaving the plasma with energies between 3.5 and 22 MeV. An overview of the different observations detected by these diagnostics is given.

2. Experimental Setup

The experimental measurements were carried out in TEXTOR (a tokamak with circular cross section, $R_0 = 1.75$ m, $a = 0.46$ m) operated in a pure ohmic mode without additional heating. The discharge conditions are: toroidal field: $B_T = 2.4$ T, plasma current: $I_P = 350$ kA and line average central density: $n_e = 1.5 \times 10^{19}$ m^{-3}. When the discharge is in the steady state condition, i.e. 2 s after the start of the discharge, 9.7×10^{20} atoms of argon are injected in order to trigger a disruption in a reproducible way. Beyond the standard diagnostics of TEXTOR the following diagnostics and equipment are used: an infrared (IR) camera for observing the synchrotron radiation from highly relativistic electrons, a runaway probe for energetic electrons leaving the plasma, different fast valves for initiating disruptions and for mitigating the runaways created during the disruptions, and the ergodization system of TEXTOR (the DED) for possibly reducing the runaway damage at the walls.

2.1. The IR detection system

An IR camera is used to observe the synchrotron radiation emitted by the REs. It is located of the equatorial mid-plane of TEXTOR. The camera is oriented to the direction of electron approach such that it is sensitive to the synchrotron radiation of REs. Its field of view covers the low field side (LFS) of the torus. The camera is sensitive for wavelengths between 3 and 5 μm. It is operated at a frame rate of 1253 frames per second with an integration time of 2 μs. Since the REs emit synchrotron radiation into the forward direction with a small opening angle, the camera detects the confined REs with energies higher than 25 MeV only from the area where the orbit of the runaways is directed towards the entrance lens of the IR optics. Analysis of synchrotron radiation has been described in detail elsewhere [21].

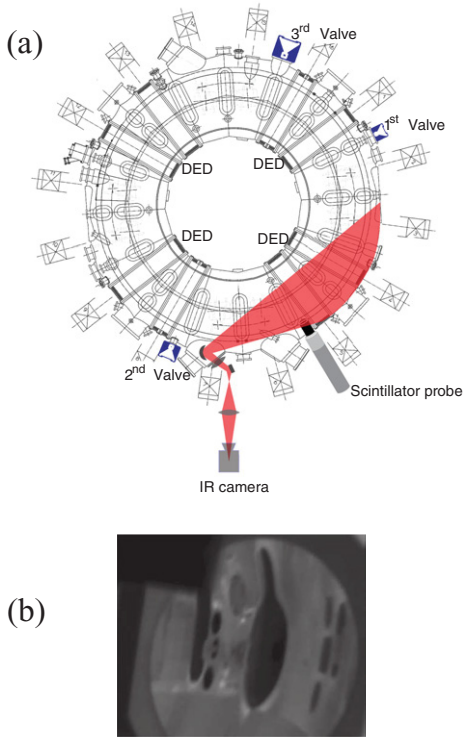

Figure 1. (*a*) Schematic top view of TEXTOR with the experimental setup for the measurements of REs. Three fast valves are located at different positions. The scintillator probe is inserted from the LFS of the torus at the equatorial plan. The synchrotron radiation as well as the IR radiation from other sources are collected and directed to an IR camera. The red area presents the camera field of view. (*b*) The camera view: openings for windows and diagnostic ports on the liner are clearly seen.

In addition, the camera measures also the thermal radiation of the wall components. A view of the wall, heated up to 150 °C without plasma, is shown in figure 1(*b*). One clearly sees the liner with openings for windows and diagnostic ports. The background thermal objects enable the reconstruction of the location from where the synchrotron radiation is emitted. Details of observation of synchrotron radiation have recently been reported in [22]. The structure and dynamics of the runaway beam have been observed.

2.2. Scintillator probe

A scintillator probe measures the REs at the plasma edge. The probe is inserted from the LFS shortly before the disruption is triggered and remains at the edge of the plasma at the minor radius $a = 0.46$ m until the plasma termination. Only the REs with energies exceeding 3.5 MeV can penetrate through the CFC housing and reach the scintillating crystals inside the probe. The probe consists of nine scintillating crystals connected via glass fibre cables to photomultipliers. Each crystal measures the REs at a different energy range; the probe is sensitive in an energy range between 3.5 and 22 MeV. The details of the probe are described in [23].

2.3. The valves

TEXTOR is equipped with three fast valves [24]. The valves are activated by an eddy current, which is induced by a current

Table 1. Characteristics of the valves at TEXTOR—orifice diameter, volume, maximum operating pressure and location of the valves.

Valve	$Ø_{\text{orifice}}(mm)$	Vol (cm^3)	P_{max} (MPa)	Location
1	8	20	3.2	top of TEXTOR
2	14	30	3.0	equatorial plane
3	28	110	15	equatorial plane

flowing in a pancake-type coil. Since the valves do not contain any ferrite materials, they can be installed very close to or even inside the vacuum vessel with its full magnetic field. The characteristics of these valves are shown in table 1. Valve 1 has been installed in order to create and study disruptions. Its gas flow has been characterized by a Michelson interferometer in the downstream flow of a guiding vacuum tube [25]. The flow rate and, in particular, the front of the gas are limited by a valve orifice of 8 mm and by the guiding tube length and diameter. If the valve is filled with 0.2 MPa of argon, disruptions with runaway generation are produced reproducibly. The gas reservoir volume of the valve amounts to 250 cm^3; however here it is reduced by an insert to 20 cm^3 only.

Valve 2 has a gas reservoir of 30 cm^3. Only half of the gas in the reservoir is released because the valve closes quickly after the activation. The valve is mounted close to the plasma such that there is only a small delay in the flow. Previously, even a smaller valve has successfully been applied to expel REs from a low density discharge [26]. The valve was operated with helium gas. After the gas injection, the REs were expelled even before the TQ took place. One aim of the following experiments is to test whether the injection of such an amount of gas will also suppress the runaways created during disruptions or whether the behaviour of REs in low density discharges is different.

Valve 3 has the largest orifice such that the gas can be quickly released. The gas throughput is about an order of magnitude higher than by valve 1. It is designed for a pressure up to 3.2 MPa in order that a moderate gas reservoir provides a high amount of gas. Here only low gas pressures are used. Therefore, the volume of the gas reservoir is reduced from more than 1 dm^3 to 110 cm^3 by adding an insert, similar as in valve 1 [27]. The valve has been mounted close to the plasma inside the TEXTOR vessel such that the delay due to the gas flow is minimal.

In order to suppress the runaway generation completely by fast gas injection, an argon gas density of more than $5 \times 10^{22}\,m^{-3}$ is required [28]. This corresponds to a gas pressure in the vessel of about 0.207 kPa. In TEXTOR, the valve would have to inject 3.5×10^{23} atoms of argon. Here, valve 1 is used only to initiate runaway disruptions, while valve 2 and valve 3 are applied to suppress the REs. Valve 2 and valve 3 are mounted at a vessel flange in the equatorial plane as close to the plasma as possible. This minimizes the flow time of the gas. For technical reasons the gas path of valve 1 is 0.5 m longer. Therefore the time delay between the valve trigger and the arrival time of the gas at the plasma surface is about 2 ms longer than the time delay of the other valves [27].

2.4. Ergodization

Another approach for RE mitigation is the DED of TEXTOR. The DED is a set of magnetic perturbation coils. Sixteen individual coils and two compensation coils are wound around the torus at the high field side (HFS) following the direction of the equilibrium magnetic field lines [29]. The electrical current in the coils generates a magnetic field which is resonant to the plasma magnetic field in particular near the $q = 3$ surface. The DED coils can be connected in different ways such that the dominant base modes $m/n = 12/4$ or $m/n = 6/2$ or $m/n = 3/1$ can be excited. In addition to the base modes, also neighbouring modes are generated which lead to a cascade of magnetic islands in the plasma. If the islands are wide enough such that they overlap, the magnetic field becomes ergodic which means that a magnetic field line is not restricted to a surface but fills the whole volume. The so-called laminar zone is formed by those field lines which intersect limiters or the wall. Particles, in particular the collisionless runaways, are lost practically immediately from this area.

The radial penetration of the perturbation field B_{p} scales with about $B_{\text{p}}(r) \approxeq B_{\text{p}}(a) \cdot (\frac{r}{a})^m$; therefore, the penetration of modes with high m—numbers is very limited while the $m/n = 3/1$ penetrates deeply into the plasma. The islands resulting from the $m/n = 3/1$ base mode can be a seed for $m/n = 2/1$ tearing modes in the plasma [30]. The dynamic option, allowing for a rotation of the perturbation field, is not applied here.

3. Typical induced disruptions in TEXTOR

In order to induce a disruption, 9.7×10^{20} atoms of argon were injected by valve 1 into the plasma at $t = 2$ s after the start-up. The TQ took place when the edge of plasma up to the $q = 2$ surface had been cooled. A significant number of REs was generated during such disruptions. During all discharges presented in this section, no additional mitigation methods are applied. Under the same initial conditions, three types of disruption evolutions have been observed.

3.1. Runaway disruptions without mode excitation

The start of a disruption is characterized with respect to the IR camera by a flash of thermal radiation from the vessel wall. For the given valve and gas feeding line, this is about 4 ms after the argon injection. At this time, the wall is heated by the lost electrons and ions during the TQ (see figures 2$(A)(a)$ and 2$(B)(a)$). We use this flash as the time marker of the disruption. After the REs have gained a sufficiently high energy, the RE beam becomes visible at the HFS. The width of the runaway beam in the vertical direction is about one half of the original plasma diameter. In the horizontal direction, the camera view is vignetted, therefore, we cannot see the whole beam. The RE beam then grows and moves towards the LFS. The structures which are seen in figures 2$(A)(b)$–(f) (indicated by white arrows) result from the reflection from the vessel wall. At $t = 2.032$ s, the position control system generates the magnetic fields such that the RE beam is pushed back to the HFS. As the loop voltage increases, the REs are accelerated. The intensity at the centre of the beam increases. However, the beam radius decreases. This indicates that with increasing energy, only the REs at the centre are well confined while the REs at the edge are lost.

In addition to the IR image from the IR camera, we calculate a time derivative of each IR image by subtracting

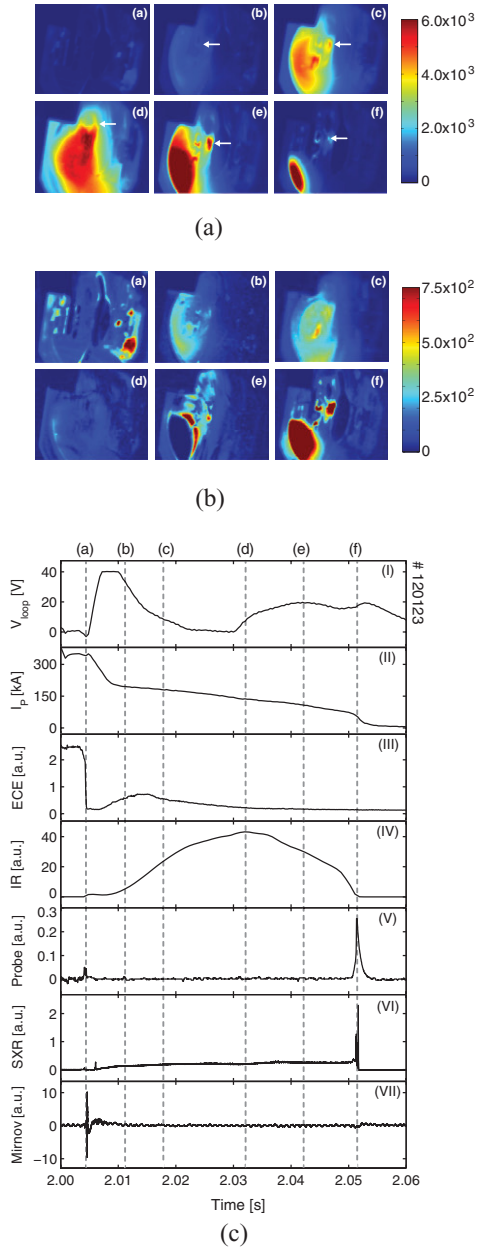

Figure 2. (*A*) IR images observed by the camera and (*B*) the images obtained from subtracting consecutive images for discharge #120123 at (*a*) $t = 2.004$ s, (*b*) $t = 2.011$ s, (*c*) $t = 2.018$ s, (*d*) $t = 2.032$ s, (*e*) $t = 3.042$ s and (*f*) $t = 2.051$ s. White arrows indicate structures from the reflection. (*C*) Temporal evolution of the disruption of discharge #120123: (top to bottom) time trace of the loop voltage, the plasma current, the ECE signal, the intensities added over all pixels of the IR image, the scintillator probe signal, the SXR signal and the Mirnov signal. Dashed lines (a)–(f) correspond to the sub-figures (*a*)–(*f*) in (*A*) and (*B*).

the image from the previous image. This representation is very sensitive to relatively small but fast variations of the RE distribution. The absolute values of consecutive image subtractions corresponding to figures 2(*A*)(*a*)–(*f*) are shown in figures 2(*B*)(*a*)–(*f*), respectively. Of particular interest is the loss phase of the REs, namely sub-figures (*e*) and (*f*). One sees that the core of the REs is hardly affected in this phase and that the loss occurs as a peeling of the RE beam edge, especially in sub-figure (*e*), a loss channel towards the top is observed.

Figure 2(*C*) shows the evolution of the characteristic signals during the disruption. Displayed from top to bottom are: the loop voltage, the plasma current, the electron cyclotron emission (ECE) signal, the integrated synchrotron radiation, the runaway probe signal, the soft x-ray (SXR) signal and the Mirnov signal. During the TQ (dashed line (*a*) in figure 2(*C*)), a negative loop voltage spike and a sudden drop of the ECE signal as well as a strong Mirnov signal oscillation are observed. A runaway burst and a SXR spike which indicate the runaway loss are consistent with the loss observed by the IR camera shown in figure 2(*A*)(*a*).

In a 'quiet' disruption such as discharge #120123, neither the SXR spikes nor Mirnov signal spikes are present during the runaway plateau phase. The level of the probe signal in figure 2(*C*)(V) is rather low with the exception of a small spike at the TQ and at the termination of the runaway plateau. The plasma current shown in figure 2(*C*)(II) decays smoothly. This confirms that the major part of REs is well confined within the plasma. A decrease in the intensities added over all pixels of the IR image shown in figure 2(*C*)(IV) is caused by the movement of the beam. At the end of the discharge, the runaway beam disappears rapidly. Sharp SXR spikes and a RE burst are observed. All REs are lost immediately.

3.2. Runaways with mode excitation

The 'quiet' disruption belongs to one class of observations. In another class, mode excitation is observed as seen, for instance, in discharge #119990. In this case, the runaway beam is located at the centre of the camera view and is not vignetted. The runaway beam becomes visible and develops at the HFS similar to the first case (see figure 3(*A*)). However, in this case the runaway beam continues moving towards LFS. The beam touches the scintillator probe and heats it up as can be seen in figures 3(*A*)(*b*)–(*f*).

Despite the increasing loop voltage shown in figure 3(*C*)(I) dashed line (c), the intensity of the beam at the centre does not change significantly. Only slight changes obtained from subtracting two consecutive images are present (see figure 3(*B*)). The runaway bursts, the SXR spikes and Mirnov signal spikes are present as can be seen in figures 3(*C*)(V)–(VII), respectively. The excitation mode created during the runaway plateau phase leads to losses and inhibits the runaway beam development.

Even though the probe signal is enhanced and the decay rate of the plasma current increases, the IR signal in (IV) varies only slightly. This indicates that the loss in the medium and low energy band is substantially higher than in the high energy band. The beginning of the mode excitation seems to be dependent on the position of the runaway beam. The mode excitation is observed when the runaway beam touches the wall or the probe. However, the mode excitation sometimes appears longer or shorter than the contact time.

Although the runaway currents in both cases are comparable, the maximum intensity of the runaway beam is about 20% lower than in the previous case. The runaway beam becomes smaller with increasing time. During the runaway plateau termination, all REs are lost. The IR signal drops

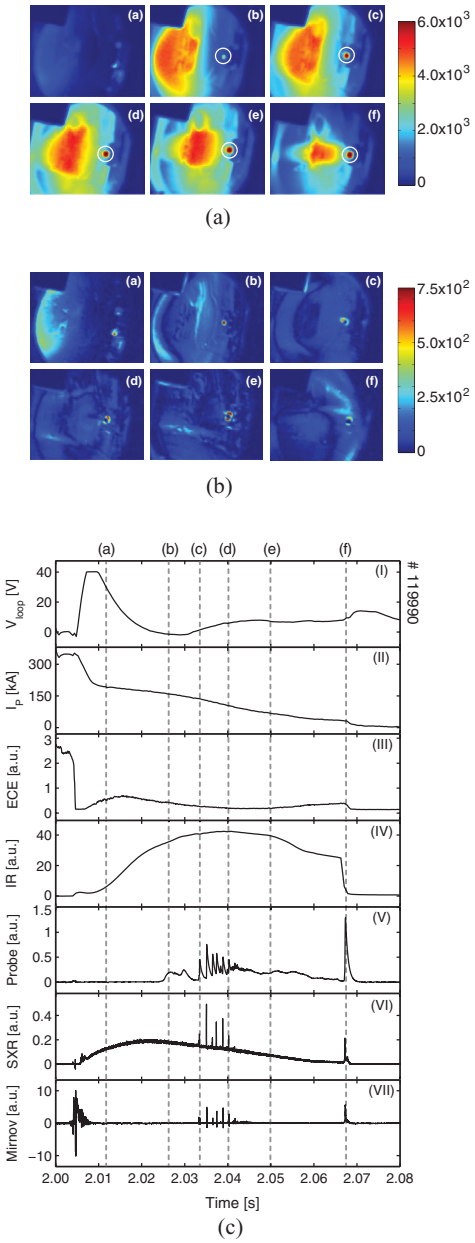

Figure 3. (*A*) IR images observed by the camera and (*B*) the images obtained from subtracting consecutive images for discharge #119990 at (*a*) $t = 2.011$ s, (*b*) $t = 2.027$ s, (*c*) $t = 2.033$ s, (*d*) $t = 2.040$ s, (*e*) $t = 3.050$ s and (*f*) $t = 2.067$ s. White rings indicate the scintillator probe tip. (*C*) Temporal evolution of the disruption of discharge #119990: (top to bottom) time trace of the loop voltage, the plasma current, the ECE signal, the intensities added over all pixels of the IR image, the scintillator probe signal, the SXR signal and the Mirnov signal. Dashed lines (a)–(f) correspond to the sub-figures (*a*)–(*f*) in (*A*) and (*B*).

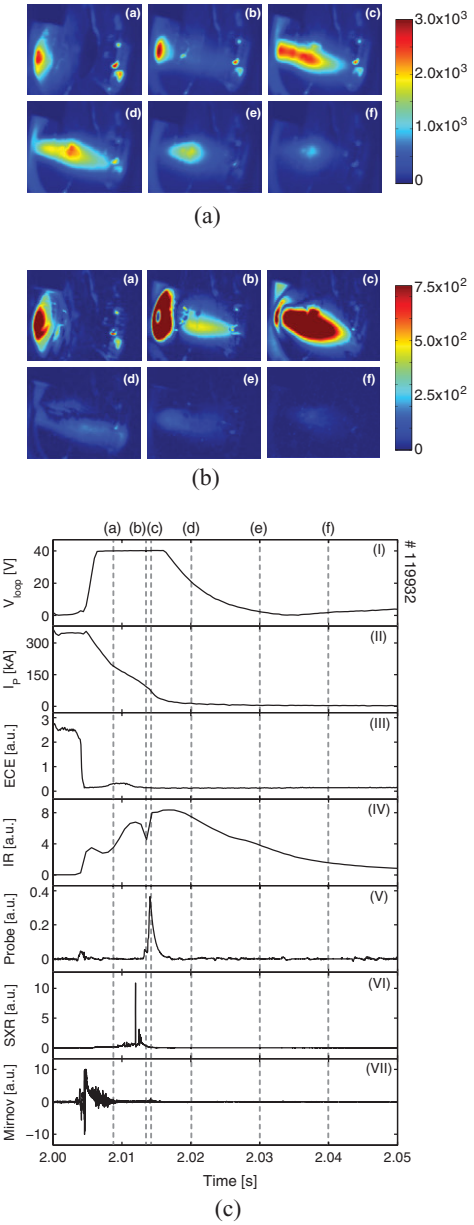

Figure 4. (*A*) IR images observed by the camera and (*B*) the images obtained from subtracting consecutive images for discharge #119932 at (*a*) $t = 2.009$ s, (*b*) $t = 2.013$ s, (*c*) $t = 2.014$ s, (*d*) $t = 2.020$ s, (*e*) $t = 3.030$ s and (*f*) $t = 2.040$ s. (*C*) Temporal evolution of the disruption of discharge #119932: (top to bottom) time trace of the loop voltage, the plasma current, the ECE signal, the intensities added over all pixels of the IR image, the scintillator probe signal, the SXR signal and the Mirnov signal. Dashed lines (a)–(f) correspond to the sub-figures (*a*)–(*f*) in (*A*) and (*B*).

suddenly accompanied by a RE burst, a sharp SXR spike and a Mirnov signal spike (see figures 3(*C*)(V)–(VII) dashed line (f)).

3.3. REs survive the runaway plateau termination

In the third class of observations, the high energy part of the runaway beam survives longer than one expects from the conventional traces such as the plasma current or SXR signals. After the runaway beam is generated and develops at the HFS, it moves more and more towards the HFS due to the positive vertical field (see figures 4(*A*)(*a*) and (*b*)). SXR spikes are present during the runaway plateau phase but no probe signal is observed because in this case the plasma is shifted away from the probe (see figures 4(*C*)(V) and (VI) dashed line (a)). The runaway plateau termination takes place at $t = 2.015$ s. A runaway burst is observed followed by a sudden appearance of the REs at the LFS. In figure 4(*A*)(*c*), it seems like the beam moves rapidly towards the LFS. However, the image obtained

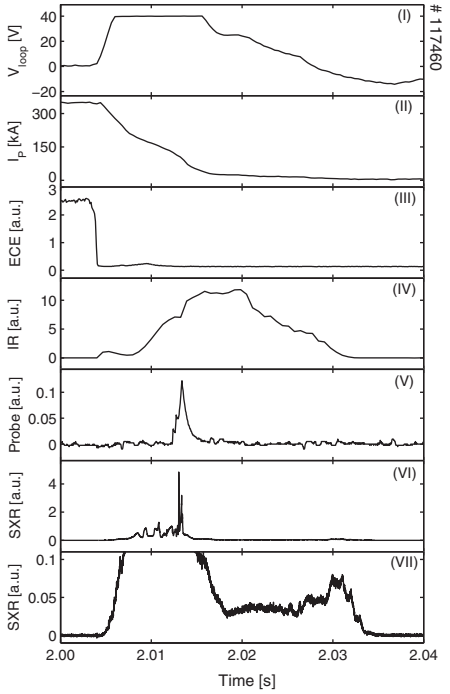

Figure 5. Temporal evolution of the disruption of discharge #117460: (top to bottom) time trace of the loop voltage, the plasma current, the ECE signal, the intensities added over all pixels of the IR image, the scintillator probe signal, the SXR signal and the magnified SXR signal.

from consecutive image subtraction in figure 4(*B*)(*c*) shows that a small amount of REs already exists at the LFS. When the current drops to almost zero these REs as well as the REs which have energies a bit lower than 25 MeV are accelerated and become visible.

Although the plasma current drops to almost zero (see figure 4(*C*)(II)), a significant number of REs can still be confined. The runaway beam then decays gradually over several tens of ms. During this phase neither the SXR nor the probe shows any signal as the loss rate of the REs is too low. The intensity of the runaway beam in this case is much smaller than in previous cases because the runaway plateau phase, in which the REs are accelerated, is much shorter. The REs do not have enough time to gain high energies. In this example, the MHD activity stops at $t \approx 2.014$ s (see figure 4(*B*) dashed line (c)) while the synchrotron radiation continues to be emitted by the REs over a few tens of ms. Observations of significant number of REs after runaway plateau termination have been reported previously [22]. There are other examples where the SXR signal continues when the plasma current has apparently ended, however, with a strongly reduced amplitude. Figure 5 is an example in which the plasma current seems to finish already at $t = 2.015$ s while the IR-synchrotron signal continues for 15 ms. Other characteristic runaway signals like the probe signal and the SXR signal seem to stop with the plasma current at $t = 2.015$ s. However, if the SXR signal is enhanced by a factor of 50, one sees that the signal continues to the end of the IR radiation (see figure 5 (VI)). The presence of the SXR signal at this phase confirms that the REs can survive the runaway plateau termination and can be confined by the plasma current of a few tens of kA.

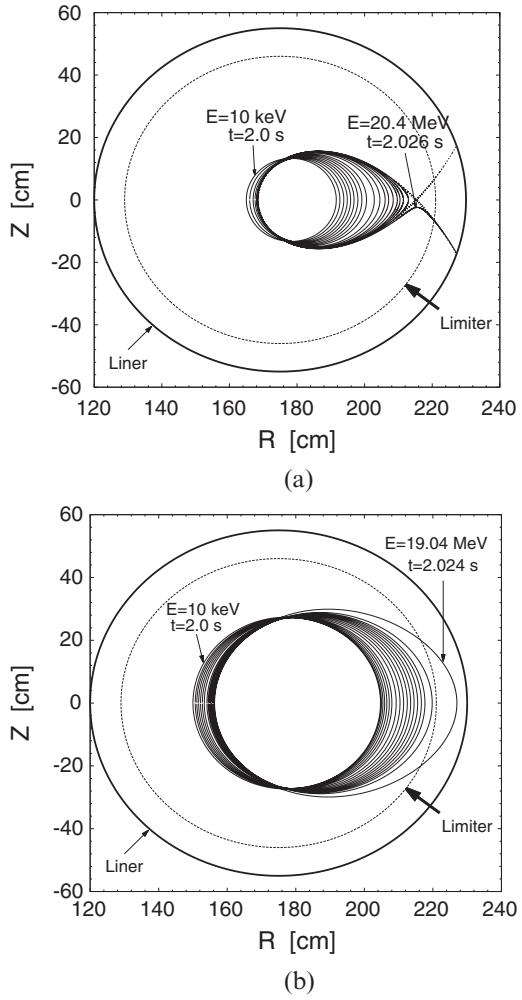

Figure 6. The evolution of the orbits for electrons of discharge #117859 starting at (*a*) $R = 165$ cm and (*b*) $R = 150$ cm.

4. Runaway orbits

Runaway orbits during disruptions are so far calculated for a constant energy. In a new approach, the full orbit development in the given toroidal electric field of the disruption is calculated by a mapping method. Since of course the calculation of the full orbit evolution would be extraordinarily time consuming, smaller parts of the orbit are computed and the evolution extrapolated in the next step followed by another orbit mapping etc.

The method allows for a visualization of the history of the electron acceleration, i.e. which electrons can gain energy and which electrons are lost during the acceleration phase. A typical loop voltage and plasma current are taken from the experiment. Figure 6(*a*) shows the evolution of the orbits for an electron in the core and figure 6(*b*) the orbit more outside. In figure 7 the energy gain of the electrons is shown for electrons of different starting positions; the major radius of the TEXTOR axis amounts to 175 cm. Only the core electrons remain confined throughout the disruption while electrons with $r > a/2 \approx 20$ cm are quickly lost before they gain sufficient energy to emit synchrotron radiation in the operating wavelength range of the camera. In addition, the right axes of figure 7 show the loop voltage and the plasma current; the

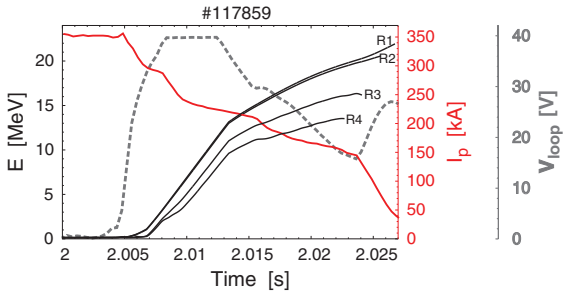

Figure 7. Temporal evolution of the disruption of discharge #117859: energy gain of the electrons starting at $R_1 = 172$ cm, $R_2 = 165$ cm, $R_3 = 150$ cm and $R_4 = 140$ cm (black), the plasma current (red), and the loop voltage (dashed grey).

loop voltage is cut at about 40 V due to the limitation of the data logger. Therefore, the final energy of the core electrons could reach 25 MeV, consistent with the limit required that the synchrotron radiation can be observed. The orbits of the outer electrons clearly hit the wall before they can reach such energies. The energy of about 25 MeV, however, is also the upper limit which is given by $\int E(t)\,\mathrm{d}t$ during the current decay.

The orbit radii remain nearly unchanged but drifts to the LFS as expected. The shift amounts to about $\delta = \frac{\langle q\rangle W}{ecB_\phi}$, where $\langle q\rangle = \langle \frac{r}{B_\theta}\rangle \frac{B_\phi}{R}$, and W the runaway energy. This shift is identical with the shift from the resonant magnetic surface and visualizes the shielding of the runaways from the magnetic perturbation.

If we neglect other boundaries, then the limiting orbit shows an X-point towards the LFS. Beyond the X-point, the orbits are open and the runaways are quickly lost. For a given experiment, it depends on the details of the vessel whether the X-point is the limitation of the runaway orbits or whether it is the orbit shift towards a limiter or the wall which leads to the loss of the runaways. In case of TEXTOR disruptions, both limits are nearly identical.

5. Induced disruptions with runaway mitigation methods applied

The following examples show effects of various mitigation methods on the behaviour of REs during induced disruptions. All disruptions presented in this section are triggered by an argon injection performed by valve 1 at $t = 2$ s. First, valve 2, which is sufficient to remove runaways from a low density runaway discharge, was applied. Then valve 3 capable of a massive gas injection is applied. Finally, the option of runaway removal by ergodization of the magnetic field lines are tested.

5.1. Fast gas injection performed by valve 2

As already discussed above, valve 2 is used because of its ability to suppress REs during low density discharges. The effect of 3 different types of gas puffs, namely helium, neon and argon, on the runaway confinement is investigated. 2.2×10^{22} atoms of gas are injected by valve 2 at different times. In discharge #117535, valve 2 injects 2.2×10^{22} atoms of neon at 15 ms after the first injection. The runaway beam develops at the HFS similarly as in typical induced disruptions. At $t = 2.022$ s the runaway beam expands suddenly and the intensity at the centre of the beam decreases as can be seen in figures 8(A)(b) and 8(B)(b). At this time, a Mirnov signal spike is observed (see figure 8(C)(VII) (black curve) dashed line (b)). As the RE loss is enhanced, the current decay rate increases accompanied by runaway bursts and SXR spikes (see figure 8(C) (black curve)). The IR images in figures 8(A)(c)–(f) show that the beam does not develop further due to the loss. The beam becomes smaller while the intensity at the centre of the beam does not change significantly. At the edge, intensity fluctuations of the beam are observed as shown in figures 8(B)(b)–(f) (white arrows). These fluctuations, which are not present in typical induced disruptions, indicate the perturbations initiated by the gas puff. The SXR signal rises again during the runaway plateau termination but no runaway burst is observed by the scintillator probe. When the plasma is terminated, the REs are lost to the wall and may not hit the probe.

In discharge #117509, 2.2×10^{22} atoms of argon are injected at 15 ms after the first injection. No sudden expansion of the runaway beam is observed. The temporal evolution of the beam is similar to the first case of a typical induced disruption without mode excitation (see figure 9(A)). The runaway beam is generated and develops at the HFS. The beam intensity at the centre increases with time while the beam shrinks. The filamented structures are also present in figure 9(B) which is obtained from consecutive image subtraction. However, the argon injection results in an enhancement of the runaway loss. During the plateau phase, peaks in the SXR are observed. All the REs are lost at 16 ms after the injection. In comparison with the previous example, the runaway confinement time is shorter (see figure 8(C) (red curve) compared with (black curve)). The runaway plateau is terminated ~30 ms earlier. It agrees with the synchrotron radiation observed by IR camera. The effect of argon injection is detected later than that of neon injection because argon needs a longer time to travel from the valve to the plasma.

In figure 10, the averaged runaway plateau lengths of the disruptions mitigated by different types of gas are plotted against a time scale of the discharge, at which valve 2 is triggered. A plateau length is determined from the width of the runaway current, which is obtained by subtracting the exponential current decay from the plasma current. For each condition, we made 2–5 measurements. The data plotted in this figure are obtained by averaging the plateau lengths of all discharges under the same condition. The error bars present the standard deviations.

2.2×10^{22} atoms of argon, neon and helium are injected separately at different times. The earlier the gas is injected, the stronger the effect is obtained. Argon provides the strongest effect. Nevertheless, the effect is not strong enough to effectively suppress the REs. To us the result was a surprise, because the runaways are regularly and quickly expelled from normal runaway discharges. This means obviously the runaways are much more robust in the current decay phase of a disruption than in a normal runaway discharge.

5.2. Argon injection performed by valve 3

Since argon, in comparison with helium and neon, provides the strongest effect on the runaway suppression, this section

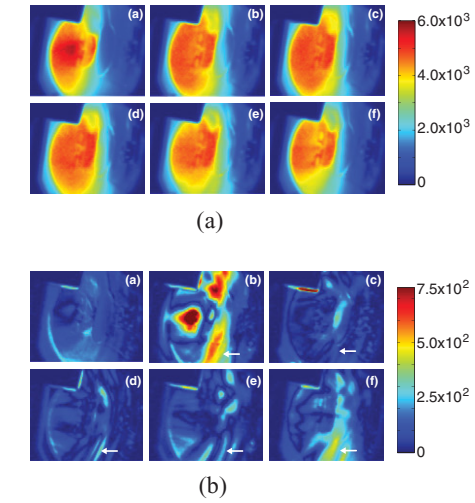

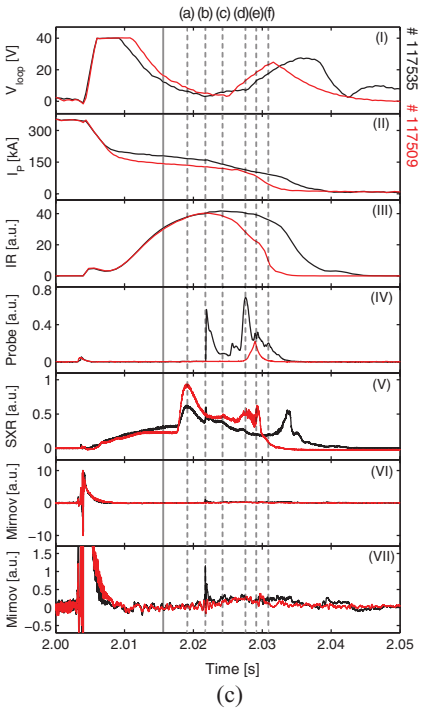

Figure 8. (*A*) IR images observed by the camera and (*B*) the images obtained from subtracting consecutive images for discharge #117535 at (*a*) $t = 2.019$ s, (*b*) $t = 2.022$ s, (*c*) $t = 2.024$ s, (*d*) $t = 2.027$ s, (*e*) $t = 2.029$ s and (*f*) $t = 2.031$ s. White arrows indicate the fluctuations, which are not present in the typical induced disruptions. (*C*) Temporal evolution of the disruption of discharges #117535 (black curve) and #117509 (red curve). In discharge #117535, 2.2×10^{22} atoms of neon are injected at $t = 2.015$ s. In discharge #117509, argon is used instead. A grey line indicates the time at which the gas puffs are injected. Dashed lines (a)–(f) correspond to the sub-figures (*a*)–(*f*) in figures 8(*A*), 8(*B*), 9(*A*) and 9(*B*).

focuses only on the influence of an argon puff injected by valve 3 on runaway mitigation. Up to 5.3×10^{22} atoms of argon are injected at different times. In discharge #119989, 1.3×10^{22} atoms of argon are injected at $t = 2.004$ s. The runaway beam evolves and remains at the HFS. In comparison with typical induced disruptions, the beam develops more slowly. At $t = 2.011$ s, a SXR and a Mirnov signal spikes are present

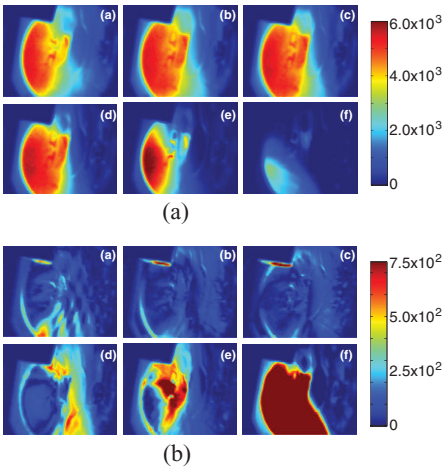

Figure 9. (*A*) IR images observed by the camera and (*B*) the images obtained from subtracting consecutive images for discharge #117509 at (*a*) $t = 2.019$ s, (*b*) $t = 2.022$ s, (*c*) $t = 2.024$ s, (*d*) $t = 2.027$ s, (*e*) $t = 2.029$ s and (*f*) $t = 2.031$ s.

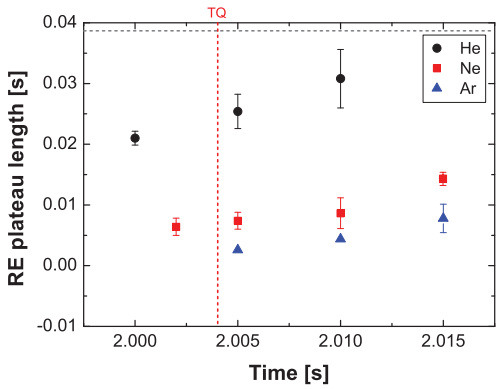

Figure 10. Averaged runaway plateau length of the induced disruptions mitigated by gas puffs of helium (black), neon (red) and argon (blue). 2.2×10^{22} atoms of gas are injected by valve 2 at different times. The x-axis indicates the time when valve 2 is triggered. A grey dashed line presents an averaged plateau length of typical induced disruptions and a red dashed line the TQ time.

as shown in figures 11(*C*) dashed line (a). The intensity of the runaway beam at the centre increases suddenly (see figures 11(*A*)(*a*) and (*B*)(*a*)). However, the radius of the beam does not change significantly. After that only small Mirnov oscillations are observed. Neither the SXR spike nor the probe signal is present. REs are well confined within the plasma. A small fluctuation of the runaway beam intensity is observed 10 ms after the fast argon injection (see figures 11(*B*)(*b*) and (*c*)). As the runaway plateau is terminated, the plasma current drops to almost zero and the REs suddenly appear at the LFS. It is still not clear whether the REs observed at the LFS afterwards are the existing REs which move suddenly towards the LFS or a new population of REs develops at the LFS. Some discharges seem to favour the first scenario and others the alternative (see subsection 3.3). The runaway burst and the SXR spike at the runaway plateau termination indicate the runaway loss (see figures 11(*C*)(IV) and (V) dashed line (e)). However, a significant number of the REs survives as presented in figure 11(*C*)(III) (black curve). The beam remains visible over 5 ms and the SXR signal decays slowly to zero.

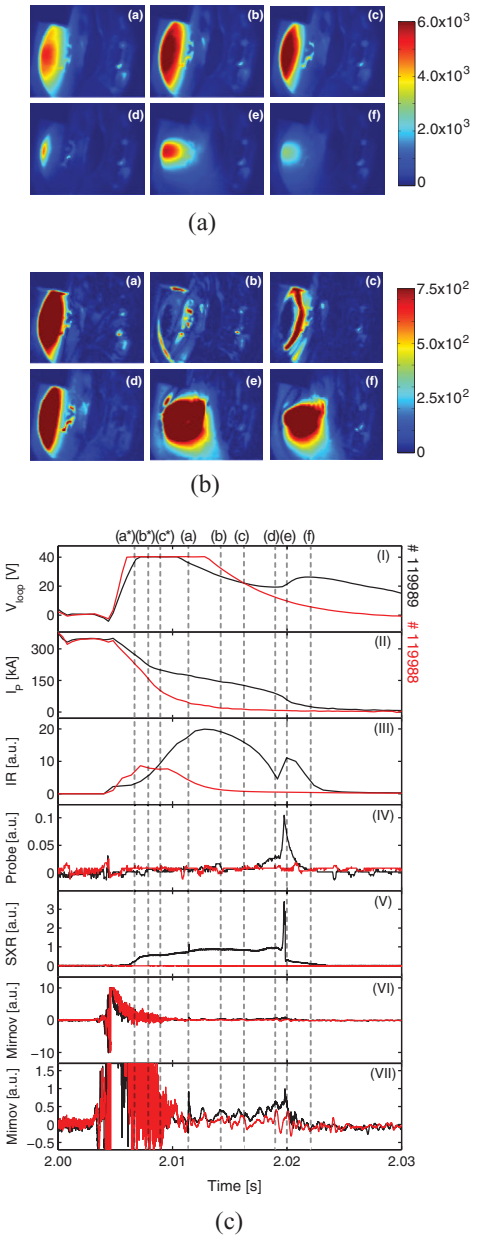

Figure 11. (*A*) IR images observed by the camera and (*B*) the images obtained from subtracting consecutive images for discharge #119989 at (*a*) $t = 2.011$ s, (*b*) $t = 2.014$ s, (*c*) $t = 2.016$ s, (*d*) $t = 2.019$ s, (*e*) $t = 2.020$ s and (*f*) $t = 2.022$ s. (*C*) Temporal evolution of the disruption of discharge #119989 (black) and discharge #119988 (red), in which 1.3×10^{22} atoms of argon are injected at $t = 2.004$ s and $t = 2.003$ s, respectively. The lowest sub-figure presents the magnified Mirnov signal. Dashed lines (a*)–(c*) correspond to the sub-figures (*a*)–(*c*) in figure 12. Dashed lines (a)–(f) correspond to the sub-figures (*a*)–(*f*) in (*A*) and (*B*).

The disruption of discharge #119988 is runaway free. In this discharge, 1.3×10^{22} atoms of argon are injected at $t = 2.003$ s. The probe and the SXR signal are zero. Additionally, neither synchrotron radiation emitted by the REs nor the runaway plateau is observed. The IR peak presented in figure 11(*C*)(III) (red curve) is IR emitted by the injected gas and thermal radiation originating from the wall, which is heated during the TQ (see figure 12). The IR radiation originates from a neutral gas is very diffuse. This means that

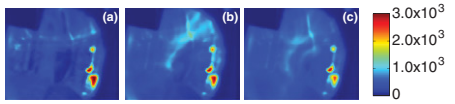

Figure 12. IR radiation observed by the camera of discharge #119988 at (*a*) $t = 2.007$ s, (*b*) $t = 2.008$ s, (*c*) $t = 2.009$ s. The IR observed here is emitted by the injected gas and is the thermal radiation from the heated wall.

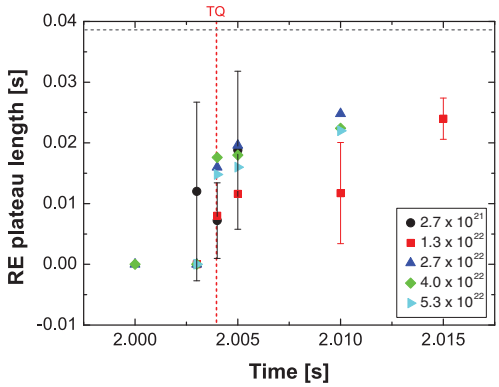

Figure 13. Averaged runaway plateau length of the induced disruptions mitigated by argon puff: 2.7×10^{21} atoms (black), 1.3×10^{22} atoms (red), 2.7×10^{22} atoms (blue), 4.0×10^{22} atoms (green), 5.3×10^{22} atoms (light blue). Gas puffing is performed by valve 3. The x-axis indicates the time when valve 3 is triggered. A grey dashed line presents an averaged plateau length of typical induced disruptions and a red dashed line the TQ time. The large error bars are caused by the strong deviation of the plateau lengths of some shots from the average values.

the gas injection of valve 3 suppresses the runaway generation completely. However, a later argon injection into a disruption with already existing REs does not eliminate them.

Similar to the effect of the gas puff (valve 2), if the gas is injected earlier, the effect is stronger (see figure 13). Since valve 3 is located as close to the plasma as possible (closer than valve 2), the gradient of the gas flow hitting the plasma surface is higher than with valve 2. In addition, the area of orifice diameter is twice as large as the one of valve 2. The injected gas, therefore, penetrates deeper into the plasma. The runaway-free disruptions are achieved when $\geqslant 1.3 \times 10^{22}$ atoms of argon are injected at $\leqslant 3$ ms after the disruption is triggered. The effect of the argon puff decreases drastically if the gas is injected after the TQ.

5.3. Dynamic ergodic divertor (DED) 6/2 mode

In discharge #120103 (figure 14), the DED is applied in the 6/2 mode at $t = 2.00$ s (at the same time as the argon is injected by valve 1). Because of its substantial inductivity, the rise time of the DED current amounts to about 60 ms. Therefore, the current is not constant during the disruption, unless it is switched on prior to the disruption. In this case, REs are also generated at the HFS. However, the runaway beam develops more slowly in comparison with typical induced disruptions. The runaway beam is broadened. REs are then lost to the LFS and hit the probe. IR radiation at the probe position is present at the very beginning of the disruption as shown in figure 14(*A*) (white rings). The IR intensity at the probe position increases with time, i.e. REs are lost continuously. The runaway plateau

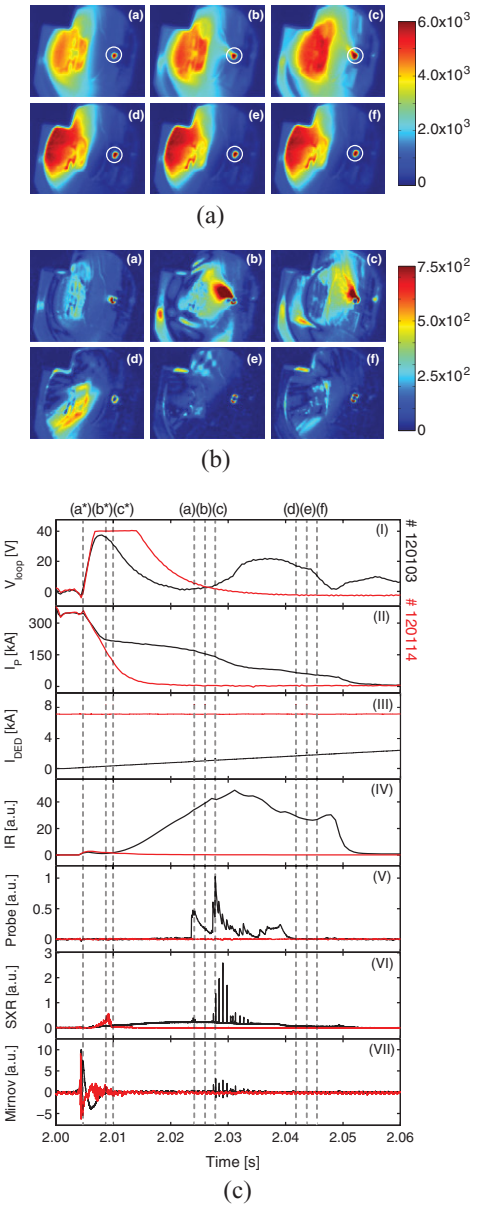

Figure 14. (*A*) IR images observed by the camera and (*B*) the images obtained from subtracting consecutive images for discharge #120103 at (*a*) $t = 2.023$ s, (*b*) $t = 2.025$ s, (*c*) $t = 2.027$ s, (*d*) $t = 2.042$ s, (*e*) $t = 2.044$ s and (*f*) $t = 2.046$ s. White rings indicate the scintillator probe tip. (*C*) Temporal evolution of the disruption of discharge #120103 (black) and discharge #120114 (red), in which the DED current of 7 kA is applied on at $t = 2.00$ s and $t = 1.70$ s, respectively. The DED currents are shown in sub-figure (III). Dashed lines (a*)–(c*) correspond to the sub-figures (*a*)–(*c*) in figure 15. Dashed lines (a)–(f) correspond to the sub-figures (*a*)–(*f*) in (*A*) and (*B*).

termination takes place at $t = 2.05$ s accompanied by a sudden loss of REs. The intensity profile of the runaway beam is affected by the applied DED. It is no longer smooth as shown in figure 14(*B*). In contrast to the previous cases of gas injection, the filamentary structure is observed not only at the edge of the beam but also in the beam centre. It is most likely that the 'filamentary structure' originates from the modes which are induced by the external DED field.

The time traces of the loop voltage, the plasma current, the DED current, the intensities added over all pixels of the

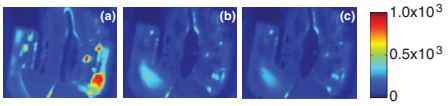

Figure 15. IR radiation observed by the camera of discharge #120114 at (*a*) $t = 2.005$ s, (*b*) $t = 2.009$ s, (*c*) $t = 2.010$ s.

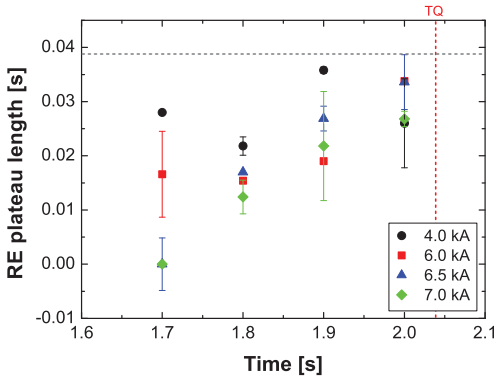

Figure 16. Averaged runaway plateau length of the induced disruptions mitigated by the DED 6/2 mode. DED currents of 4 kA (black), 6 kA (red), 6.5 kA (blue) and 7 kA (green) are applied (separately) at different times. The x-axis indicates the time when the DED is applied. A grey dashed line presents an averaged plateau length of typical induced disruptions and a red dashed line the TQ time.

IR image, the scintillator probe signal, the SXR signal and the Mirnov signal of the discharge #120103 are shown in figure 14(*C*) (black curve). As the DED current reaches 1 kA at $t \approx 2.03$ s, a small-stepwise reduction of plasma current is observed (see figure 14(*C*)(II) dashed line (d)). Additionally, RE bursts, SXR and Mirnov signal spikes are present. The intensity of the runaway beam decreases while the IR intensity at the probe tip increases. Therefore, the intensity added over all pixels of the IR image decreases slightly. The runaway beam moves a little towards the LFS at $t = 2.047$ s. Since a larger area of the beam is in the camera's field of view, the intensity added over all pixels of the IR image increases. The intensity of the runaway beam, in contrast, continues to decrease. The DED leads to REs loss before REs gain high energies. However, a significant number of REs is still confined in the plasma.

In the discharge #120114, the DED is switched on at $t = 1.70$ s. The DED current reaches the maximum value of 7 kA at $t = 1.90$ s. The runaway beam develops and remains at the HFS. The beam does not touch the probe, therefore, no probe signal is present (see figure 14(*C*)(IV) (red curve)). Although no runaway plateau is present, a small number of REs is observed by the IR camera as can be seen in figure 15. Additionally, the SXR signal is also present. However, REs are lost rapidly shortly after the TQ. It is shown in figure 16 that the earlier the DED is switched on, the stronger the effect on REs suppression is obtained. The impact on the RE confinement in discharges, in which the DED is applied at $t = 1.70$ s, is much stronger than in case where the DED is applied at $t = 1.80$ s although the DED current of both cases are the same, i.e. 7 kA, when the argon puff is injected.

In order to obtain a significant effect of the DED on the RE confinement, the DED has to be applied at least 0.3 s

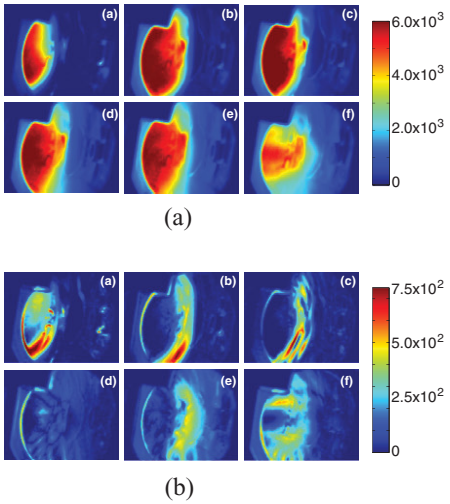

Figure 17. (*A*) IR images observed by the camera and (*B*) the images obtained from subtracting consecutive images for discharge #119889 at (*a*) $t = 2.015$ s, (*b*) $t = 2.026$ s, (*c*) $t = 2.033$ s, (*d*) $t = 2.047$ s, (*e*) $t = 2.050$ s and (*f*) $t = 2.063$ s. Here, the DED current of 1 kA is applied at $t = 1.82$ s.

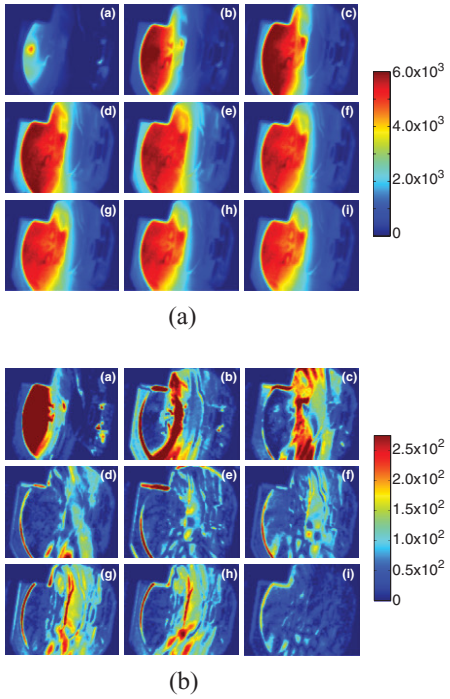

Figure 18. (*A*) IR images observed by the camera and (*B*) the images obtained from subtracting consecutive images for discharge #119869 at (*a*) $t = 2.013$ s, (*b*) $t = 2.022$ s, (*c*) $t = 2.033$ s, (*d*) $t = 2.045$ s, (*e*) $t = 2.065$ s, (*f*) $t = 2.080$ s, (*g*) $t = 2.085$ s, (*h*) $t = 2.087$ s and (*i*) $t = 2.091$ s. Here, the DED current of 1 kA is applied at $t = 2.01$ s.

before the disruption takes place. Otherwise the effect is minor as can be seen in figure 16. This method is rather impractical for disruption mitigation since a disruption is a transient event and the method that provides a fast response is required. Additionally, complete runaway suppression cannot be achieved. Although the perturbations generated by the DED, in comparison with the case of the gas puff, can penetrated deeper into the runaway beam, it is not strong enough to eject all REs from the plasma.

5.4. Dynamic ergodic divertor (DED) 3/1 mode

The influence of the resonant magnetic perturbation (RMP) produced by the DED 3/1 mode on the runaway suppression in the TEXTOR tokamak has been investigated by Lehnen [20] and Koslowski [31]. It has been shown in [20] that the loss rate of REs is significantly enhanced if sufficiently strong RMPs with $n = 1, 2$ are applied. However, a complete runaway suppression cannot be achieved. The experimental results in [31] shows, conversely, no clear effect of the RMPs on the runaway suppression. Here we will discuss only the results observed by the IR camera.

Figure 17, shows the temporal evolution of the runaway beam of discharge #119889, in which the DED current of 1 kA is applied at 1.82 s. The DED is constant during the whole disruption. The fluctuation of the beam intensity distribution as present in the case of the gas puff injection (valve 2) is observed (see figures 17(*A*) and (*B*)). However, the perturbations penetrate deeper into the runaway beam than the perturbations initiated by the gas puff (valve 2). A different runaway behaviour is found in discharge #119869, in which the DED is applied at $t = 2.01$ s, i.e. after the disruption is triggered. The RE confinement is improved. A runaway is confined longer in the plasma than in the previous case. Figure 18(*A*) shows that the runaway beam changes only slightly over a long period of time. No sudden loss is observed. In this discharge, different structures are observed as shown in figure 18(*B*). At the beginning of the discharge structures are present only at the edge of the runaway beam. As the perturbations penetrate deep into the beam centre, the intensity of the beam starts to decrease.

It is still not clear whether a tearing mode is also induced if the DED is applied during the disruption. In any case, one finds a rich 'filamentary' structure in particular in the different sequence of figure 18(*B*); the structure reaches deep into the runaway beam as one might expect for the $m/n = 3/1$ mode. This structure could either result from the external ergodization of the DED or the internal ergodization by the mode.

6. Summary and conclusions

In order to study the development of runaway electrons in disruptive discharges, a massive gas injection of argon is applied by valve 1. Key diagnostics are IR-synchrotron radiation measurements for the high energy runaway component ($E > 25$ MeV) and a runaway probe in particular for the runaways with energies of a few MeV up to 22 MeV. The disruption starts with the TQ and an initial exponential decay of the plasma current which is then followed by a characteristic plateau phase in which the runaway beam develops and a runaway plateau termination phase.

Even though the experimental conditions are identical, the runaways can show a quite different time evolution. In the simplest case, the disruption is 'smooth' without mode excitation. A runaway beam with a diameter of about one half of the original plasma diameter develops. The beam size agrees well with the one that is obtained from modelling [22]. In other cases, MHD activity is observed during the plateau

phase. Even though the plasma current shows typical decay steps during this phase, the synchrotron image shows neither special structures in the image of the high energy electrons nor a strong loss. On the contrary, the synchrotron radiation can even still increase. The reason is most likely that low and high energy runaways are not influenced in the same way by MHD perturbations. The orbit of the low energy runaways shows only a small displacement and is close to 'its' resonant magnetic surface and much more perturbed than the high energy ones which have strongly displaced orbits. The high energy runaways are thus shielded from perturbations. Therefore, the loss of the low energy runaway electrons is substantially higher than that of the high energy ones. Since the high energy runaways are confined for a relatively long time in the plasma they can gain more energies and may cause the severe damage to the PFCs when they are lost. Nevertheless, the runaway confinement time depends also on the starting position of the REs. The REs at the core remain confined throughout the disruption while the REs in the outer part are quickly lost because their orbits intersect the limiter or wall. Sometimes, a runaway loss channel towards the wall is observed.

Additionally, we have observed cases, in which the high energy runaways seemed to survive longer than the plasma current. A very low current of between 10 and 20 kA is, in agreement with modelling [22], sufficient to confine 25 MeV runaway electrons. The low current indicates that again the high energy component of the runaways can survive magnetic perturbations and can remain dangerous, in particular for fusion devices, even in late times of the disruption.

Various methods were applied in order to mitigate the effect of the REs. The runaway loss was expected to be initiated by the applied mitigation method and the REs should be lost before they have time to gain high energy. The argon injection performed by valve 3 provides the best results. A complete runaway suppression can be achieved if a moderate amount of gas is injected early enough, i.e. as close as possible to the first injection performed by valve 1 initiating the disruption. Otherwise the mitigation effect is minor. The ergodization during the disruption helps slightly to shorten the runaway confinement time. This indicates that the runaways created during disruptions are very robust, much more than in a low density runaway discharge.

In summary:

- High energy runaways are more difficult to remove than low energy runaways.
- Runaways generated during disruptions are rather robust against attempts to remove them. Fast gas injection and ergodization are effective only if they are applied as close as possible to the first valve trigger and with a large number of injected atoms or with the highest ergodization amplitude available.
- To our experience runaways generated during disruptions can be avoided by either a fast and massive argon injection of the order of 10^{22} atoms (TEXTOR) or by a pre-existing $m/n = 2/1$ tearing mode.

Acknowledgments

This work was supported by the Royal Thai Government, a Jülich R&D contract, the Trilateral Euregio Cluster (TEC) and the DFG program GRK 1203. The authors would like to thank Dr H.R. Koslowski, M. Forster, M. Rack, Dr O. Schmitz and the TEXTOR Team for their support.

References

[1] Schüller F.C. 1995 *Plasma Phys. Control. Fusion* **37** A135
[2] Neyatani Y. *et al* 1999 *Nucl. Fusion* **39** 559
[3] Pautasso G. *et al* 1996 *Nucl. Fusion* **36** 1291
[4] Yoshino R. *et al* 1997 *Plasma Phys. Control. Fusion* **39** 313
[5] Taylor P.L. *et al* 1999 *Phys. Plasmas* **6** 1872
[6] Timokhin V.M. *et al* 2001 *Tech. Phys. Lett.* **27** 795
[7] Whyte D.G. *et al* 2002 *Phys. Rev. Lett.* **89** 055001
[8] Hollman E.M. *et al* 2005 *Nucl. Fusion* **45** 1046
[9] Lehnen M. *et al* 2011 *J. Nucl. Fusion* **51** 123010
[10] Pautasso G. *et al* 2009 *Plasma Phys. Control. Fusion* **51** 124056
[11] Whyte D.G. *et al* 2003 *J. Nucl. Mater.* **313** 1239
[12] Reux C. *et al* 2010 *Nucl. Fusion* **50** 095006
[13] Bakhtiari M. *et al* 2002 *Nucl. Fusion* **42** 1197
[14] Bozhenkov S.A. *et al* 2008 *Plasma Phys. Control. Fusion* **50** 105007
[15] Plyusnin V.V. *et al* 2006 *Nucl. Fusion* **46** 277
[16] Chen Z.Y. *et al* 2013 *Plasma Phys. Control. Fusion* **55** 035007
[17] Martin-Solis J.R. *et al* 1995 *Phys. Plasmas* **6** 238
[18] Hender T.C. *et al* 2007 *Nucl. Fusion* **47** S128–202
[19] Finken K.H. *et al* 2001 *Nucl. Fusion* **41** 11
[20] Lehnen M. *et al* 2008 *Phys. Rev. Lett.* **100** 55003
[21] Kudyakov T. *et al* 2012 *Nucl. Fusion* **52** 023035
[22] Wongrach K. *et al* 2014 *Nucl. Fusion* **54** 043011
[23] Kudyakov T. *et al* 2008 *Rev. Sci. Instrum.* **79** 10F126
[24] Savtchkov A. *et al* 2002 *Rev. Sci. Instrum* **70** 3490
[25] Finken K.H. *et al* 2008 *Nucl. Fusion* **48** 115001
[26] Finken K.H. *et al* 2003 *J. Nucl. Mater.* **313–316** 1247
[27] Finken K.H. *et al* 2011 *Nucl. Fusion* **51** 033007
[28] Lehnen M. *et al* 2009 *J. Nucl. Mater.* **390** 740
[29] Finken K.H. *et al* 2005 *The Structure of Magnetic Field in the TEXTOR-DED: Energy Technology* vol 45 (Jülich: Forschungszentrum Jülich)
[30] Koslowski H.R. *et al* 2006 *Nucl. Fusion* **46** L1
[31] Koslowski H.R. *et al* 2014 *41st EPS Conf. on Plasma Physics* P 5.028 http://ocs.ciemat.es/EPS2014PAP/pdf/P5.028.pdf

PUBLICATION 4

Mechanism of runaway electron beam formation during plasma disruptions in tokamaks

S. S. Abdullaev,[1] K. H. Finken,[2] K. Wongrach,[2] M. Tokar,[1] H. R. Koslowski,[1] O. Willi,[2] L. Zeng,[3] and TEXTOR Team
[1]*Forschungszentrum Jülich GmbH, Institut für Energie- und Klimaforschung—Plasmaphysik, D–52425 Jülich, Germany*
[2]*Institut für Laser- und Plasmaphysik, Heinrich-Heine Universität Düsseldorf, Düsseldorf, Germany*
[3]*Institute of Plasma Physics, Chinese Academy of Sciences, 230031 Hefei, China*

(Received 22 January 2015; accepted 15 April 2015; published online 24 April 2015)

A new physical mechanism of formation of runaway electron beams during plasma disruptions in tokamaks is proposed. The plasma disruption is caused by a strong stochastic magnetic field formed due to nonlinearly excited low-mode number magnetohydrodynamic (MHD) modes. It is conjectured that the runaway electron beam is formed in the central plasma region confined inside the intact magnetic surface located between $q = 1$ and the closest low–order rational magnetic surfaces [$q = 5/4$ or $q = 4/3$,…]. It results in that runaway electron beam current has a helical nature with a predominant $m/n = 1/1$ component. The thermal quench and current quench times are estimated using the collisional models for electron diffusion and ambipolar particle transport in a stochastic magnetic field, respectively. Possible mechanisms for the decay of the runaway electron current owing to an outward drift electron orbits and resonance interaction of high–energy electrons with the $m/n = 1/1$ MHD mode are discussed. [http://dx.doi.org/10.1063/1.4919253]

The runaway electrons (REs) generated during the disruptions of tokamak plasmas may reach a several tens of MeV and may contribute to the significant part of post–disruption plasma current. The prevention of such RE beams is of a paramount importance in future tokamaks, especially in the ITER operation, since it may severely damage a device wall.[1–5]

The mitigation of REs by massive gas injections (MGI) and externally applied resonant magnetic perturbations (RMPs) have been extensively discussed in literature (see, e.g., Refs. 6–8 and references therein). However, no regular strategy to solve this problem has been developed because up to now the physical mechanisms of the formation of REs during plasma disruptions are not well understood. In spite of the numerous dedicated experiments to study the problem of runaway current generation during plasma disruptions in different tokamaks (see, e.g., Refs. 7–15), no clear dependence of RE formation on plasma parameters has been established. These numerous experiments show the complex nature of plasma disruption process especially the formation of RE beams.

One of the important features of the formation of RE beams is the irregularity and variability of the beam parameters from one discharge to another one. This is an indication of the sensitivity of RE beam formations on initial conditions which is the characteristic feature of nonlinear processes, particularly, the chaotic system. Therefore, one expects that *ab initio* numerical simulations of the RE formation process may not be quite productive to explain it because of complexity of computer simulations of nonlinear processes.[16] The problems of numerical simulations of plasma disruptions are comprehensively discussed in Ref. 17.

In this work, we propose a new physical mechanism of formation of RE beams during plasma disruptions in tokamaks. It is based on the analysis of numerous experimental results, mainly obtained in the TEXTOR tokamak and the ideas of magnetic field stochasticity.[18] The mechanism explains many features of plasma disruptions accompanied by RE generations.

It is believed that the plasma disruption starts with the excitation of magnetohydrodynamic (MHD) modes with low poloidal m and toroidal n numbers, ($m/n = 1/1$, 2/1, 3/2, 5/2,…) that lead to a large–scale magnetic stochasticity (see, e.g., Refs. 19–22 and references therein). The heat and particle transports in the strongly chaotic magnetic field cause the fast temperature drop and cease the plasma current. This process depends on the structure of the stochastic magnetic field which depends on the spectra of magnetic perturbations and on the safety factor profile $q(\rho)$ (ρ is the minor radius of the magnetic surface). At certain conditions, the stochastic magnetic field may not extend up to the central plasma region due to the creation of the outermost intact magnetic surface ρ_c. The electrons confined by this magnetic surface are accelerated by the toroidal electric field induced by the current decay from the outer plasma region, which leads to the formation of the RE beam. The initial RE current $I_p^{(RE)}$ is mainly determined by the pre-disruption plasma current distribution $I_p(\rho)$ confined by the outermost intact magnetic surface ρ_c, i.e., $I_p^{(RE)} \approx I_p(\rho_c)$.

The lifetime of the RE beam mainly depends on two effects: the outward drift of RE orbits induced by the toroidal electric field E_φ[32,33] and the resonant interactions of REs with helical magnetic perturbations. The first one is responsible for the smooth decay of the RE current, while the second one cause the sudden RE losses. The outward drift velocity v_{dr} is determined by E_φ and the RE current, $v_{dr} \propto E_\varphi / I_p^{(RE)} \propto E_\varphi / \rho_c^2$.[32,33] The most stable of the RE beams is expected to form when the corresponding drift velocity is lowest and the low–order rational surfaces within the RE beam are absent or one.

Consider, for example, the pre-disruption plasma with a monotonic safety factor profile $q(\rho)$ with $q(0)<1$. Then the most stable RE beam can be formed when the outermost intact magnetic surface is located between magnetic surface $q=1$ and the nearest low–order rational surfaces $q=5/4$ [or $q=4/3,\ldots$]. It occurs at the sufficiently small amplitude of the $m/n=1/1$ mode. There is only one rational magnetic surface $q=1$ within the RE beam that is resonant to the large–scale magnetic perturbations, particularly, to the RMPs. Such RE beams are relatively stable, since low–energetic REs (up to 10–15 MeV) are not destabilized due to absence of a large scale stochasticity. The loss of REs mainly occurs due to the outward drift of RE orbits and the stochastic instability of high–energetic REs due to the interactions of high–mode harmonics of the $m/n=1/1$ mode of magnetic perturbations.

In the case of plasma disruptions with $q(0)>1$, the intact magnetic surface ρ_c would be smaller while the toroidal electric field E_φ would be larger than in the ones with $q(0)<1$. Due to the large outward drift velocity v_{dr}, such RE beams would cease faster.

The two possible distinct generic structures of a stochastic magnetic field before the current quench (CQ) with the RE-free discharge and with the RE discharge are shown in Figs. 1(a) and 1(b) by the Poincaré sections of magnetic field lines. It is assumed that the perturbation magnetic field contains several low–mode number m/n MHD modes with equal amplitudes B_{mn}: (a) the amplitude B_{11} of the $m/n=1/1$ mode is equal to others; (b) B_{11} is four times smaller than the amplitudes of other modes. As seen from Fig. 1(a) for the large amplitude of the $(m/n=1/1)$ mode, the stochastic magnetic field extends up to the central plasma region destroying the separatrix of the $m=n=1$ island. For the low–amplitude of the $(m/n=1/1)$ mode shown in Fig. 1(b), the stochastic magnetic field does not reach the $q=1$ magnetic surface. The last intact drift surface (red dots) is located between the resonant surfaces $q=1$ and $q=5/4$ (blue curves).

The existence of an intact magnetic surface and its location depends on the radial profile of the safety factor and on the spectrum of magnetic perturbations. The latter sensitively depend on the plasma disruption conditions and vary unpredictably from one discharge to another during plasma disruptions. This makes RE formation process unpredictable and may explain a shot–to–shot variability of the parameters of RE beams.

This conjecture on the mechanism of RE beam formation agrees with the important features of the experimental observations in the TEXTOR tokamak. In the experiments, the plasma disruptions were triggered by gas injections (see, e.g., Refs. 9–11,23): the disruptions with REs were triggered by argon (Ar) injection and the RE–free disruptions with Ne injection. The injection of these gases may finally give rise to different spectra of amplitudes of MHD modes. One can expect that the amplitude of the $m/n=1/1$ MHD mode excited by the He/Ne injection is higher than in the case of Ar gas injection.

The plasma current decay in the CQ and the RE plateau regimes for all discharges is well approximated by the linear function of time $I_p=I_{p0}+bt$, with the average CQ rate $b=\langle dI_p/dt\rangle$ as shown in Fig. 2(a). The current decay rates $|\langle dI_p/dt\rangle|$ in the CQ stage and the RE plateau stage versus the initial RE current $I_p^{(RE)}$ for a number discharges are plotted Fig. 2(b). The plausible radial profiles of $I_p(\rho)$ and the corresponding safety factor $q(\rho)$ are plotted for the two values of $q(0)$ in Fig. 3.

Since ρ_c is located between the magnetic surfaces ρ_1 and ρ_3 corresponding to $q(\rho_1)=1$ and $q(\rho_3)=4/3$, the RE current $I_p^{(RE)}$ should take values in the finite interval. This expectation is supported by the experimental values of the plasma current $I_p^{(RE)}$ as seen from Figs. 2(a) and 2(b). These values of $I_p^{(RE)}$ also lie in the region between the resonance magnetic surfaces $q(\rho_1)=1$ and $q(\rho_3)=4/3$ [or $q(\rho_2)=3/2$] as shown in Fig. 3 where the radial profile of the pre–disruption equilibrium plasma current $I_p(\rho)$ (curve 1) and the corresponding safety factor profile $q(\rho)$ (curve 2) are plotted.

The average values of $\langle|dI_p/dt|\rangle$ for almost all discharges are confined in the interval (2.2, 5.6) MA/s, i.e., in one order lower than the current decay rate in the CQ stage. The values of $I_p^{(RE)}$ are in the range between 170 kA and 260 kA (see Fig. 2(b)). These values of $\langle|dI_p/dt|\rangle$ and $I_p^{(RE)}$ are close to the ones observed in the similar experiments in the DIII-D tokamak (see, e.g., Ref. 15).

As seen from Fig. 2(a), there are untypical discharges with the highest and lowest values of $I_p^{(RE)}$ that correspond to

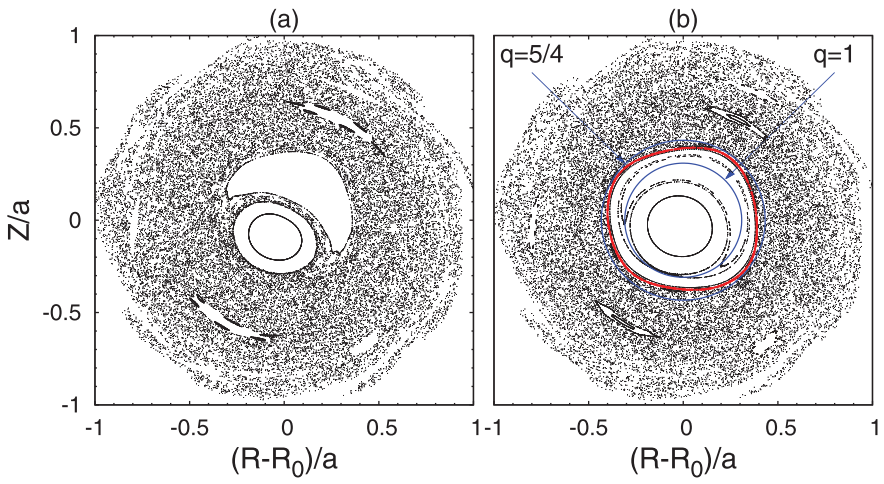

FIG. 1. Poincaré sections of magnetic field lines in a pre–disruption plasma caused by several m/n MHD modes, $(n=1,\ 2,\ 3;\ m=1,\ldots 8)$: (a) all mode amplitudes B_{mn} are equal; (b) the amplitude B_{11} of the $m/n=1/1$ mode is four times smaller than B_{mn}. The safety factor at the magnetic axis $q(0)=0.8$ and at the plasma edge $q(a)=4.7$.

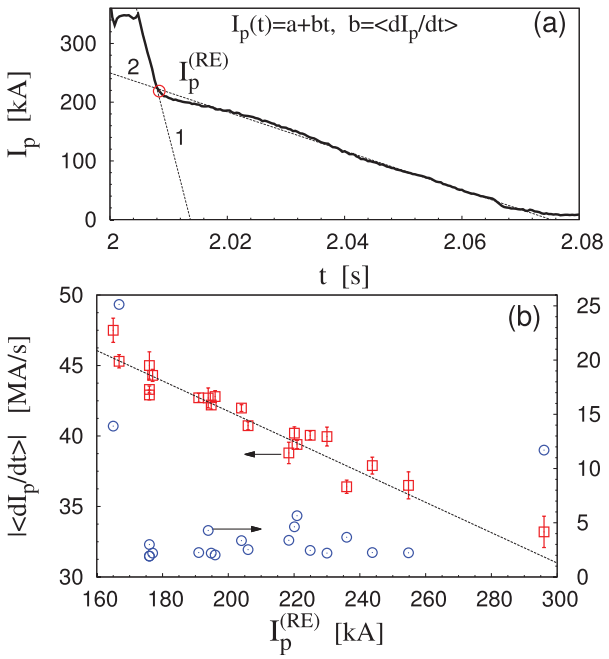

FIG. 2. (a) Typical time evolution of the plasma current with RE current. The average current decay rates $\langle dI_p/dt\rangle$ at the CQ and the RE plateau stages are determined by fitting with a linear function $I_p(t) = a + bt$. Symbol $\odot$ corresponds to the plasma current $I_p^{(RE)}$ at the initial stage of the RE plateau. (b) The decay rates $|\langle dI_p/dt\rangle|$ versus $I_p^{(RE)}$. Symbols $\boxdot$ (red) correspond to the CQ rate (lhs axis), and $\odot$ (blue)—the RE plateau (rhs axis).

ρ_c at the borders of region $\rho_1 < \rho < \rho_3$. For these discharges, the CQ rates $\langle|dI_p/dt|\rangle$ take highest or lowest values. The RE current decay rates of these discharges take the highest values. They have the shortest duration time of RE currents. One expects that the presence of several low–order $m/n = 4/3$, $m/n = 3/2$, and $m/n = 1/1$ resonant magnetic surfaces within the RE beam for the discharge with the highest $I_p^{(RE)}$ may lead to excitations of the corresponding MHD modes. The interactions of these modes may lead to the quick loss of REs due to the formation of a stochastic zone at the edge of the RE beam.

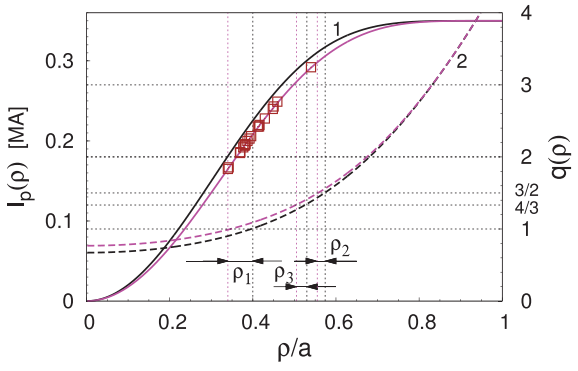

FIG. 3. Radial profile of the plasma current $I_p(\rho)$ (solid curves 1 on lhs axis) and the corresponding safety factor profile $q(\rho)$ (dashed curves 2 on rhs axis). The rectangular (red) dots correspond to the experimentally measured values of $I_p^{(RE)}$ for several TEXTOR discharges. The plasma parameters are $I_p = 350$ kA, $B_0 = 2.4$ T, $R_0 = 1.75$ m, and $a = 0.46$ m. The values of $q(0)$ are 0.7 (solid black curves) and 0.8 (dashed magenta curves), respectively. The radii ρ_1, ρ_2, and ρ_3 are the positions of the rational magnetic surfaces $q(\rho_1) = 1$, $q(\rho_2) = 3/2$, and $q(\rho_3) = 4/3$, respectively.

The existence of the intact magnetic surface ρ_c between the $q = 1$ and $q = 4/3$ rational magnetic surfaces and its location depends on the level magnetic perturbation ϵ_{MHD} (more exactly on the spectrum B_{mn}). With increase of ϵ_{MHD}, the radius ρ_c shrinks and it can be broken at the certain critical perturbation level ϵ_{cr}. It leads to the total destruction of confinement of electrons and ions. This is in agreement with experimental observations of the existence of critical magnetic perturbations from which on runaway beams are not generated.[10]

The shrinkage of ρ_c with increasing the magnetic perturbation ϵ_{MHD} leads to the decrease of the RE current $I_p^{(RE)}$ since $I_p^{(RE)} \approx I_p(\rho_c)$. On the other hand, if one assumes that the plasma current decay is caused by the radial transport of particles in the stochastic magnetic field, the CQ rate dI_p/dt should be proportional to the square of the magnetic perturbation level ϵ_{MHD}, $|\langle dI_p/dt\rangle| \propto |\epsilon_{MHD}|^2$. Therefore, one expects that to the higher values of $|\langle dI_p/dt\rangle|$ correspond the lower values of the RE current $I_p^{(RE)}$. This expectation is in agreement with the experimental measured values of these quantities presented in Fig. 2(b).

The formation of the RE beam inside the intact magnetic surface can be also confirmed by the spatial profiles of the synchrotron radiation of high–energy REs with energies exceeding 25 MeV. One observes that the radiation is localized within a finite radial extent in the central plasma region.

The strong radial transport along the stochastic magnetic field lines causes the losses of heat and plasma particles from the stochastic zone. The TQ can be explained by the fact that the anomalously large heat transport in a stochastic magnetic field is mainly determined by the electron diffusion. The CQ is determined by the particle transport in a stochastic magnetic field and has an ambipolar nature. Using the collisional test particle transport model in a stochastic magnetic field,[24] we estimated the heat conductivity $\chi_r(\rho)$ and the ambipolar diffusion coefficient D_p of particles.

For typical magnetic perturbations and pre-disruption plasma temperatures (0.5–1.0 keV), the magnitude of $\chi_r(\rho)$ has the order of several 10^2 m^2/s. The characteristic heat diffusion time $\tau_H = a^2/2\chi_r$ is of the order of 10^{-4} s that agrees with the experimentally observed times. The quantitative analysis based on the numerical solution of the heat diffusion equation also gives similar values for τ_H.

The ambipolar particle transport in a stochastic magnetic field is strongly collisional due to the low plasma temperature (from 5 eV to 50 eV) after the TQ. At these plasma temperatures, the corresponding diffusion time $\tau_p = a^2/D_p$ of particles changes from 1 s to 0.3 s. Since the diffusion coefficient $D_p \propto B_{mn}^2$ and therefore $\tau_p \propto B_{mn}^{-2}$, then τ_p can be reduced to one order smaller value for a three times larger perturbation than in Fig. 1. This timescale is still much longer than the experimental values. However, the collisional model does not take into account the effect of the toroidal electric field. One expects that the acceleration of electrons and ions by the toroidal electric field increases the radial transport of particles. To include this effect in the collisional model, one can assume that the effective temperature of the plasma is

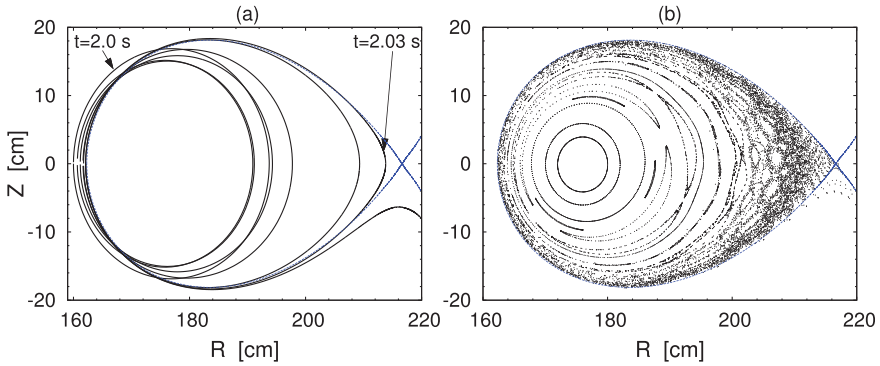

FIG. 4. (a) Evolution of a RE orbit in the (R, Z)-plane for the TEXTOR discharge No. 117527. (b) Poincaré section of RE orbit of energy 11.7 MeV in the (R, Z)-plane. The plasma current $I_p = 50$ kA.

higher than the measured one. The particle diffusion time τ_p at the effective temperature 2 keV is about 8×10^{-3} s. This timescale gives the average current decay rate $dI_p/dt \approx I_p/\tau_p = 0.35/(8.0 \times 10^{-3}) \approx 44.0$ MA/s which is order of the experimental measured one given in Fig. 2(b).

In general, the transport of heat and particles in the presence of RMPs is a three–dimensional problem. Particularly, a stochastic magnetic field with the topological structures likes the ones in Fig. 1 leads to poloidally and toroidally localized heat and particle deposition patterns on the wall (see, e.g., Ref. 21) similar to those in ergodic divertor tokamaks (see, e.g., Ref. 18).

From the described scenario of plasma disruption, it follows that a typical runaway beam current is localized inside the area enclosed by the last intact magnetic surface. In general, the distribution of the current density j would depend not only on the radial coordinate ρ but also vary along the poloidal θ and the toroidal φ angles due to the presence of the $(m/n = 1/1)$ magnetic island. This agrees with the analysis of numerous disruptions in the JET tokamak.[25] One can assume that the radial profiles of the RE current density averaged along poloidal and toroidal angles are almost uniform. This gives the value of the safety factor at the beam axis $q(0)$ is less than unity. This assumption is supported by a number of experimental measurements of the current profile after the sawtooth crashes in the TEXTOR, the TFTR, and JET tokamaks.[26–31]

The toroidal electric field accelerates electrons to higher energies. With increasing electrons energy, their orbits drift outwardly[32,33] and eventually hit the wall. It is illustrated in Fig. 4(a). This effect may be one of mechanisms of slow RE current decay. Calculations show that the outward drift velocity v_{dr} is of the order of a few m/s for typical discharges in TEXTOR. The RE current decay rate dI_p/dt due to outward drift RE orbits can be roughly estimated as follows. This loss mechanism is mainly caused by the shrinkage of the beam radius a. The rate of such a shrinkage da/dt is of the order of the average outward velocity v_{dr}. Since $I_p \propto a^2$, we have $dI_p/dt \propto (2I_p/a)da/dt = (2I_p/a)v_{dr}$. For the typical values of $I_p \approx 0.2$ MA, $a \approx 0.2$ m, and $v_{dr} \sim 1$ m/s, one has $dI_p/dt \approx 4$ MA/s. This estimation is in the order of the experimentally measured average decay rate of the runaway current plotted in Fig. 2(b).

The effect of magnetic perturbation on RE beams depends on their safety factor profile q. The latter varies in the interval $[q(0) < 1, q(a)]$ with its edge value $q(a)$ less than 3/2 [or 4/3, 5/3]. Such a RE beam is relatively stable to the effect of magnetic perturbations. The single $m/n = 1/1$ mode does not create the stochastic layer at the beam edge for REs with energies up to several MeVs, since their drift surfaces are close to magnetic surfaces. With increasing the energy of electrons, the drift surfaces strongly deviate from magnetic ones and thus create the perturbation harmonics with higher mode numbers $m > 1$. The interactions of several resonance modes of perturbations may form the stochastic zone at the beam edge, which leads to fast RE losses as illustrated in Fig. 4(b). This process may explain the sudden RE current drop accompanied by magnetic activity and RE bursts observed in experiments (see, e.g., Refs. 4 and 9).

Based on the analysis of numerous experimental data obtained in the TEXTOR tokamak, we have proposed the mechanism of RE beam formation during the plasma disruption. The plasma disruption starts due to a large–scale magnetic stochasticity caused by nonlinearly excited of MHD modes with low (m, n) numbers ($m/n = 1/1$, 2/1, 3/2, 5/2,…). The RE beam is formed in the central plasma region confined by the intact magnetic surface. Its location depends on the safety factor profile $q(\rho)$ and the spectrum of MHD modes. In the cases of plasmas with the monotonic profile of $q(\rho)$ and at sufficiently small amplitude of the $m/n = 1/1$ mode, the most stable RE beams are formed by the intact magnetic surface located between the magnetic surface $q = 1$ and the closest low–order rational surface $q = m/n > 1$ ($q = 5/4$, $q = 4/3$, or $q = 3/2$).

This mechanism reproduces well the essential features of the measurements. Particularly, the TQ and the CQ are determined by the strong electron diffusion and ambipolar transport of particles in a stochastic magnetic field, respectively. The slow decay of the RE current is due to the outward drift of RE orbits induced by a toroidal electric field, and the spiky quick decay of REs is due to resonant interaction of high–energy REs with the $m/n = 1/1$ MHD mode. The effect of external resonant magnetic perturbations on low-energy electrons (up to 5–10 MeV) is weak and does not cause their loss. This is in agreement with the recent experiments in the TEXTOR tokamak.[34] The detailed description of the mechanism of RE formation and the evolution of RE current based on the analyses of experimental observations will be given in a separate publication.[35]

The authors gratefully acknowledge valuable discussions with W. Biel, S. Brezinsek, O. Marchuk, Ph. Mertens, D. Reiser, D. Reiter, A. Rogister, and U. Samm. Authors also thank Ph. Mertens for improving the English.

[1]J. Wesson, R. Gill, M. Hugon, F. Schüller, J. Snipes, D. Ward, D. Bartlett, D. Campbell, P. Duperrex, A. Edwards *et al.*, Nucl. Fusion **29**, 641 (1989).
[2]R. D. Gill, Nucl. Fusion **33**, 1613 (1993).
[3]F. Schüller, Plasma Phys. Controlled Fusion **37**, A135 (1995).
[4]R. D. Gill, B. Alper, A. W. Edwards, L. C. Ingesson, M. F. Johnson, and D. J. Ward, Nucl. Fusion **40**, 163 (2000).
[5]G. Papp, T. Fülöp, T. Fehér, P. C. de Vries, V. Riccardo, C. Reux, M. Lehnen, V. Kiptily, V. V. Plyusnin, B. Alper *et al.*, Nucl. Fusion **53**, 123017 (2013).
[6]T. C. Hender, J. C. Wesley, J. Bialek, A. Bondeson, A. H. Boozer, R. J. Buttery, A. Garofalo, T. P. Goodman, R. S. Granetz, Y. Gribov *et al.*, Nucl. Fusion **47**, S128 (2007).
[7]E. Hollmann, N. Commaux, N. W. Eidietis, T. E. Evans, D. A. Humphreys, A. N. James, T. C. Jernigan, P. B. Parks, E. J. Strait, J. C. Wesley *et al.*, Phys. Plasmas **17**, 056117 (2010).
[8]M. Lehnen, A. Alonso, G. Arnoux, N. Baumgarten, S. A. Bozhenkov, S. Brezinsek, M. Brix, T. Eich, S. N. Gerasimov, A. Huber *et al.*, Nucl. Fusion **51**, 123010 (2011).
[9]M. Forster, K. Finken, T. Kudyakov, M. Lehnen, O. Willi, Y. Xu, L. Zeng, and the TEXTOR Team, Phys. Plasmas **19**, 092513 (2012).
[10]L. Zeng, H. R. Koslowski, Y. Liang, A. Lvovskiy, M. Lehnen, D. Nicolai, J. Pearson, M. Rack, H. Jaegers, K. H. Finken, K. Wongrach, and Y. Xu, Phys. Rev. Lett. **110**, 235003 (2013).
[11]K. Wongrach, K. Finken, S. S. Abdullaev, R. Koslowski, O. Willi, L. Zeng, and the TEXTOR Team, Nucl. Fusion **54**, 043011 (2014).
[12]Z. Y. Chen, W. Kim, Y. Yu, A. England, J. Yoo, S. Hahn, S. Yoon, Y. Lee, Y. K. Oh, J. Kwak, and M. Kwon, Plasma Phys. Controlled Fusion **55**, 035007 (2013).
[13]V. V. Plyusnin, V. Riccardo, R. Jaspers, B. Alper, V. Kiptily, J. Mlynar, S. Popovichev, E. de La Luna, F. Andersson, and JET EFDA Contributors, Nucl. Fusion **46**, 277 (2006).
[14]N. Commaux, L. R. Baylor, S. K. Combs, N. W. Eidietis, T. E. Evans, C. R. Foust, E. M. Hollmann, D. A. Humphreys, V. A. Izzo, A. N. James *et al.*, Nucl. Fusion **51**, 103001 (2011).
[15]E. M. Hollmann, M. E. Austin, J. A. Boedo, N. H. Brooks, N. Commaux, N. W. Eidietis, D. A. Humphreys, V. A. Izzo, A. N. James, T. C. Jernigan *et al.*, Nucl. Fusion **53**, 083004 (2013).
[16]L. P. Kadanoff, *Perspectives in Computational Science* (IEEE-CS and AIP, 2004), March/April p. 57.
[17]A. H. Boozer, Phys. Plasmas **19**, 058101 (2012).
[18]S. S. Abdullaev, *Magnetic Stochasticity in Magnetically Confined Fusion Plasmas* (Springer, Cham, 2014).
[19]B. B. Kadomtsev, Plasma Phys. Controlled Fusion **26**, 217 (1984).
[20]J. Wesson, *Tokamaks*, 3rd ed. (Clarendon Press, Oxford, 2004).
[21]S. E. Kruger, D. D. Schnak, and C. R. Sovinec, Phys. Plasmas **12**, 056113 (2005).
[22]V. A. Izzo, D. A. Humphreys, and M. Kornbluth, Plasma Phys. Controlled Fusion **54**, 095002 (2012).
[23]S. A. Bozhenkov, M. Lehnen, K. H. Finken, M. W. Jakubowski, R. C. Wolf, R. Jaspers, M. Kantor, O. V. Marchuk, E. Uzgel, G. VanWassenhove, O. Zimmermann, D. Reiter, and TEXTOR Team, Plasma Phys. Controlled Fusion **50**, 105007 (2008).
[24]S. S. Abdullaev, Phys. Plasmas **20**, 082507 (2013).
[25]S. N. Gerasimov, T. Hender, J. Morris, V. Riccardo, L. Zakharov, and JET EFDA Contributors, Nucl. Fusion **54**, 073009 (2014).
[26]H. Soltwisch, W. Stodiek, J. Manickam, and J. Schlüter, in *Proceedings of the 11th IAEA Conference on Plasma Physics and Controlled Fusion Research, Kyoto, 13–20 November, 1986* (IAEA, Vienna, 1987), Paper No. IAEA-CN-47/A-V-1, Vol. 1, pp. 263–273.
[27]M. Yamada, F. Livinton, N. Pomphrey, R. Budny, J. Manickam, and Y. Nagayama, Phys. Plasmas **1**, 3269 (1994).
[28]H. Soltwisch and H. R. Koslowski, Plasma Phys. Controlled Fusion **37**, 667 (1995).
[29]J. O'Rourke, Plasma Phys. Controlled Fusion **33**, 289 (1991).
[30]H. R. Koslowski, H. Soltwisch, and W. Stodiek, Plasma Phys. Controlled Fusion **38**, 271 (1996).
[31]H. Soltwisch and H. R. Koslowski, Plasma Phys. Controlled Fusion **39**, A341 (1997).
[32]X. Guan, H. Qin, and N. Fisch, Phys. Plasmas **17**, 092502 (2010).
[33]S. S. Abdullaev, Phys. Plasmas **22**, 030702 (2015).
[34]H. R. Koslowski, L. Zeng, M. Lehnen, A. Lvovskiy, K. Wongrach, and TEXTOR Team, in *Proceedings of the 41st EPS Conference on Plasma Physics*, Berlin, June 22–28, 2014, No. P5.028.
[35]S. S. Abdullaev *et al.*, "Mechanisms of plasma disruption and runaway electron losses in tokamaks," J. Plasma Phys. (to be published).

PUBLICATION 5

J. Plasma Physics (2015), *vol.* 81, 475810402
doi:10.1017/S0022377815000380

Experimental observation of hot tail runaway electron generation in TEXTOR disruptions

L. Zeng[1,†], H. R. Koslowski[2], Y. Liang[2], A. Lvovskiy[2], M. Lehnen[3], D. Nicolai[2], J. Pearson[2], M. Rack[2], P. Denner[2], K. H. Finken[4], K. Wongrach[4] and the TEXTOR team

[1]Institute of Plasma Physics, Chinese Academy of Sciences, 230031 Hefei, China
[2]Forschungszentrum Jülich GmbH, Institute of Energy and Climate Research – Plasma Physics (IEK-4), 52425 Jülich, Germany
[3]ITER Organization, Route de Vinon sur Verdon, 13115 St Paul Lez Durance, France
[4]Institut für Laser- und Plasmaphysik, Heinrich-Heine-Universität Düsseldorf, 40225 Düsseldorf, Germany

(Received 13 January 2015; revised 10 March 2015; accepted 10 March 2015; first published online 14 April 2015)

Experimental evidence supporting the theory of hot tail runaway electron (RE) generation has been identified in TEXTOR disruptions. With higher temperature, more REs are generated during the thermal quench. Increasing the RE generation by increasing the temperature, an obvious RE plateau is observed even with low toroidal magnetic field (1.7 T). These results explain the previously found electron density threshold for RE generation.

1. Introduction

RE currents of several mega ampere are expected to be generated in ITER disruptions due to avalanche multiplication (Hender et al. 2007). An uncontrolled loss of these high energetic electrons to the plasma facing components might cause serious damage (Lehnen et al. 2009). The occurrence of REs depends on various factors and no definite RE generation dependence on the plasma parameters is given in the theory or found in the present experiments. In tokamak experiments, it is observed that RE generation occurs only above a threshold for the toroidal magnetic field (B_t), as has been found on JET (Lehnen et al. 2011), JT-60U (Yoshino et al. 1999), Tore Supra (Martin 1998), ASDEX Upgrade (Pautasso 2007), and TEXTOR (Lehnen et al. 2009). The B_t threshold on JET is about 1.8 T and that on other tokamaks is about 2 T. REs appear only in discharges with low electron density in JT-60U (Yoshino et al. 1995) and ASDEX Upgrade (Pautasso 2007), which has been named the density threshold. The B_t threshold has been well understood by the magnetic turbulence during the current quench (Zeng et al. 2013), but the density threshold is still not clear.

The physics behind RE generation is the excess of the driving force on electrons, over the collisional drag force from plasma particles, which results in the acceleration of electrons. Several mechanisms can cause electrons to run away, including Dreicer generation (Dreicer 1959; 1960), hot tail RE generation (Chiu et al. 1998; Harvey et al. 2000; Helander et al. 2004; Smith et al. 2005; Smith and Verwichte 2008;

† Email address for correspondence: zenglong@ipp.ac.cn

Féher 2011), runaway avalanching (Rosenbluth and Putvinski, 1997), tritium decay, and Compton scattering of γ rays from the activated wall. In the present work, only the first three of these runaway generation processes are discussed. In a disruption, the Dreicer generation and the hot tail processes are the primary RE mechanisms, creating a RE seed population that is amplified by the secondary runaway avalanche mechanism. The Dreicer generation and RE avalanching processes have been well discussed both in the theory and present experiments. However, to our knowledge, the hot tail RE generation has also been proposed by the theory but has not been clearly isolated as the cause of RE seeds in experiments up to now.

A variety of analytical models and numerical simulations investigate the formation of a high-energetic tail during a disruption if the thermal quench time is short enough, which yield a population of seed REs for the following RE avalanche process (Chiu et al. 1998; Harvey et al. 2000; Helander et al. 2004; Smith et al. 2005; Smith and Verwichte 2008; Féher et al. 2011). If the duration of the thermal quench is shorter than the collision time for electrons near the RE threshold energy, the energetic electrons do not have time to cool down and equilibrate. Instead, they will form a high-energy tail and the number of electrons close to the RE threshold energy will be enhanced. Moreover, simulations for ITER in previous work (Smith and Verwichte 2008) show that hot tail generation will dominate over Dreicer generation when the thermal quench time is around 1 ms, which is the value predicted for ITER (ITER Physics Basis Editors et al. 1999). In this paper, we will report evidence from the TEXTOR tokamak which suggests that hot tail RE generation is likely to occur during disruptions and strongly correlates with the density threshold.

2. Experimental setup and results

Disruptions are deliberately triggered by injection of large amounts of Argon using a fast disruption mitigation valve (DMV) on TEXTOR (Bozhenkov et al. 2007). Using the same experimental setup as in Lehnen et al. 2008, the experiments were carried out with the following parameters: toroidal magnetic field $B_t = 1.5 - 2.4$ T, plasma current $I_P = 200 - 350$ kA, edge safety factor $q_a = 3.5 - 7.3$, line averaged central density $n_e = (0.8 - 3.3) \times 10^{19}$ m^{-3}, major radius $R = 1.75$ m, minor radius $a = 0.46$ m, and number of injected Argon particles $N_{Ar} = 7.3 \times 10^{20}$.

Figure 1 compares three discharges, one does not develop a RE current plateau during the current quench while the others do, but the RE currents are different. REs are seen as a plateau in the current decay due to the current carried by them, non-thermal electron cyclotron emission (ECE), and bursts or continuous soft X-ray emission. The DMV is triggered at $t = 2.0$ s. After $3 \sim 4$ ms the thermal quench occurs as a result of radiation cooling due to influx of the injected gas. The duration of the thermal quench (τ_2) measured by the ECE radiometer is about 0.2 ms in TEXTOR, independent of the plasma parameters (as will be shown in Fig. 5(a)). The temperature of the background plasma after the thermal quench is $\sim$10 eV (Lehnen et al. 2009). During the following current quench, the plasma current decreases as shown in Fig. 1(a). In some situations a RE current plateau forms (#119 336 and #119 342) which has been observed to last up to 170 ms in TEXTOR.

The parameters of the three ohmic discharges are the same except for the plasma electron density and the corresponding electron temperature, shown in Fig. 1(b), but the RE generation is totally different. All discharges have a toroidal field of $B_t = 1.7$ T and the plasma current of $I_p = 260$ kA. The plasma line-averaged densities in the three discharges are $n_e = 0.8 \times 10^{19}$, 1.0×10^{19} and 1.5×10^{19} m^{-3}, and the corresponding

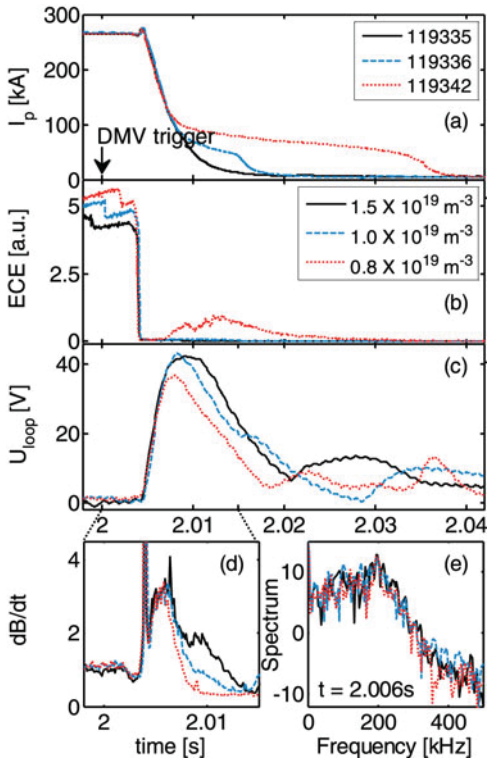

FIGURE 1. Time traces from three discharges differing in the current quench phase showing (a) plasma current I_P, (b) electron temperature, (c) toroidal loop voltage U_{loop}, (d) magnetic turbulence dB/dt, and (e) the frequency spectrum of magnetic turbulence at t = 2.006 s. The envelope of magnetic turbulence is calculated by filtering the signal with a high pass filter (passband >2 kHz). The thermal quench occurs about 4.0 ms after triggering the DMV in these discharges.

temperature decreases for each step. Higher RE currents are observed in discharges with higher temperature.

During the disruptions, the maximum loop voltage is about 50 V and the corresponding electric field is about 5 V m^{-1}. The maximum density is around 10^{20}m^{-3} and the corresponding Connor-Hastie electric field threshold is about 0.2 V m^{-1}, which is the same as the critical electric field necessary for avalanching. Both of them are much less than the measured electric field, although the critical electric field for Dreicer generation is a factor of 10–12 times above Connor-Hastie electric field threshold during the flattop (Connor and Hastie 1975). Both, the Dreicer generation and the avalanche process, need to be considered for RE generation. The number of injected Argon particles in the three discharges is the same. The maximum electron density mainly depends on the number of injected Argon particles (Bozhenkov et al. 2008; Lvovskiy et al. 2015). Meanwhile, the loop voltages in the three discharges, measured by the flux loop mounted internal to the vacuum vessel and shown in Fig. 1(c), are similar, but the loop voltage in shot 119 342 remains slightly lower because part of the plasma current is quickly replaced by RE current. So the primary Dreicer generation due to the electric field is almost the same for the three discharges. The avalanche rate, mainly depending on the plasma current, is also the same for the three discharges. The magnetic turbulence is measured by Mirnov coils and causes the

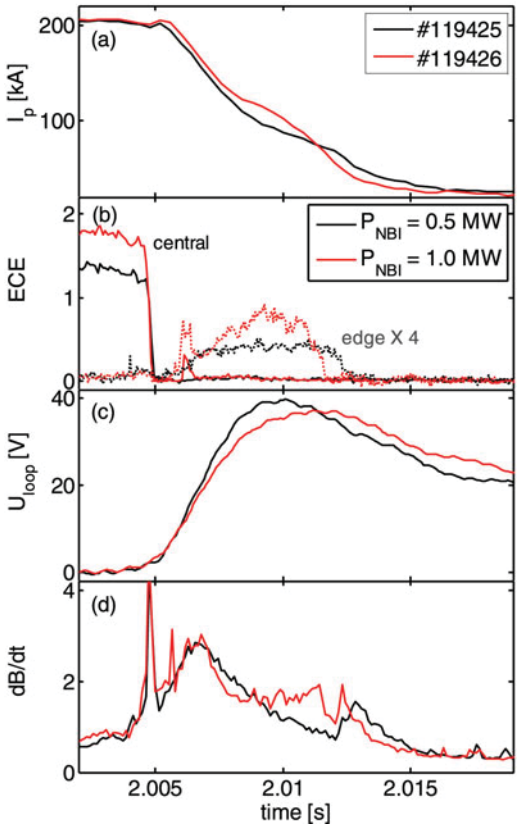

FIGURE 2. Time traces from two discharges differing in the current quench phase showing (a) plasma current I_P, (b) the central electron temperature (solid line) and the edge temperature (dashed line), (c) toroidal loop voltage U_{loop}, and (d) magnetic turbulence dB/dt.

loss of REs due to enhanced radial diffusion. Previous work gives the evidence that the generated RE current is inversely proportional to the level of magnetic turbulence during the current quench (Zeng et al. 2013). The detected levels and the frequency spectrum of the magnetic turbulence during the fast current quench, shown in Figs 1(d) and (e), are similar, so the corresponding transport loss of REs are almost the same. The critical density for flat-top RE generation in TEXTOR is below 0.7×10^{19} m^{-3}, lower than minimum density (0.8×10^{19} m^{-3}) of the experiments, and no REs are generated during the flat-top phase (Granetz et al. 2015). This shows that the plasma temperature and its evolution during the thermal quench plays the dominant role in this stage and is the cause of the different observed RE tails.

More RE generation with higher temperature has also been observed during disruptions in neutral beam injection (NBI) discharges. The parameters of both shots 119 425 and 119 426 are the same except the temperature which changes with the NBI power, shown in Fig. 2 at 2.01 s. Both target plasmas have a toroidal field of $B_t = 2.4$ T, a plasma current of $I_p = 200$ kA, and a plasma line-average density of $n_e = 2.0 \times 10^{19}$ m^{-3}. The NBI powers in the two discharges are 0.5 and 1.0 MW, which correspond to the temperature T_e of 1.4 and 1.8 keV, respectively (Fig. 2(b)). The NBI is switched off at the time of triggering the DMV. RE tails are observed in both discharges but the currents are different, shown in Fig. 2(a). The RE current in

the discharge with higher temperature is larger, consistent with the electron cyclotron emission measured by an edge ECE radiometer, shown in Fig. 2(b). The density during the current quench is about 10^{20} m^{-3}, so the second harmonic 130 GHz ECE is cut off and the detected emission originates from REs. Moreover, the toroidal loop voltage and magnetic turbulence level during the current quench are similar (Figs 2(c) and (d)). Comparison of the two discharges gives the same conclusion, namely that the discharges with higher temperature will generate more REs. Again, the difference in the RE tail is likely to be caused by the plasma temperature and its evolution during the thermal quench.

Both of the two cases present that the plasma temperature and its evolution during the thermal quench is the cause of the different observed RE tails, suggesting the hot tail RE generation mechanism. The experiment with variation in NBI heating power at constant electron density shows the primary importance of the electron temperature. The plasma temperature decreases to about 10 eV of the background plasma during the thermal quench of $\sim$0.2 ms from the initial temperature of several keV. The energetic electrons, especially in the tail of the initial Maxwellian distribution, need more time to slow down than the low energy part of the velocity distribution and do not equilibrate with a Maxwellian distribution of $\sim$10 eV (Smith and Verwichte 2008). Instead, they will form a high-energy tail and the number of electrons in the RE region will be enhanced. There are more energetic electrons close to the runaway threshold in the higher-temperature plasma and more RE seeds remain during the thermal quench.

Obvious RE plateaus are observed with $B_t = 1.7$ T when the electron density is below 1.0×10^{19} m^{-3} (#119 336 and #119 342). The value of B_t is slightly lower than in the previously published experimental observation of a toroidal magnetic field threshold of about $B_t = 2$ T for RE generation in tokamak disruptions (Zeng et al. 2013). As mentioned in Zeng et al. 2013, the toroidal magnetic field could mainly affect RE losses by magnetic turbulence and does not influence RE generation. When the hot tail RE generation is enhanced by increasing the temperature and the total RE generation exceeds the RE losses, the RE tail can be obtained even at lower toroidal field.

A study of several ohmic discharges shows that RE generation after a disruption occurs in the region of high toroidal field and low electron density, shown in Fig. 3(a). Clear thresholds of toroidal field and density on RE generation are observed in TEXTOR disruptions. For discharges with the same electron density (parallel to X-axis direction in Fig. 3(a)), there is a toroidal magnetic field threshold for RE generation, which has been explained by the magnetic turbulence threshold during the current quench (Zeng et al. 2013). For discharges with the same toroidal field (parallel to Y-axis direction in Fig. 3(a)), there is a density threshold for RE generation, which can be understood by hot tail RE generation. Moreover, the density threshold increases with the toroidal field but the toroidal magnetic field threshold decreases with the density. As we have seen in Fig. 2, there is a temperature threshold instead of the density threshold, but the electron density is the quantity controlled in the experiments and therefore plotted in Fig. 3(a). With higher temperature, more REs are generated via the hot tail mechanism during the thermal quench, which creates more seed REs for the following RE avalanche process. The degree of conversion of thermal current to RE current has been accurately fitted empirically in Fig. 3(b) as a function of the toroidal magnetic field and electron density before the disruptions. More RE currents are obtained in the region of high toroidal field and low electron density (high plasma temperature). The exponent 3 on B_t results from

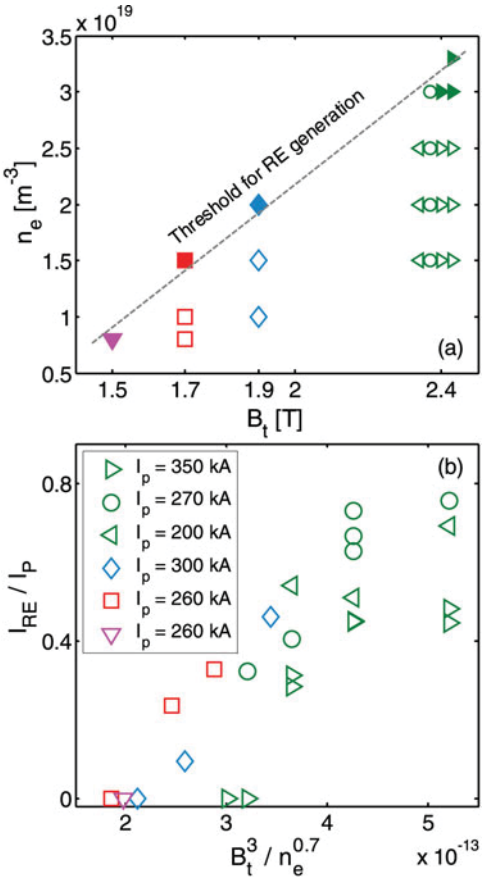

FIGURE 3. (a) The parameter space for RE generation in terms of toroidal magnetic field and electron density for TEXTOR disruptions. Open data points mean observation of RE plateau and filled ones have no RE plateau. The dashed line indicates the boundary for RE generation. (b) The degree of conversion of thermal current to RE current in TEXTOR disruptions as a function of toroidal field and electron density before the disruptions.

the influence of magnetic turbulence, which is consistent with the scaling in Zeng et al. 2013.

3. Discussion

Hot tail RE generation is caused by incomplete thermalization of the electron velocity distribution during rapid plasma cooling. If the thermal quench rate is rapid compared with the collision frequency at the RE threshold velocity, the energetic electrons in the tail of the initial Maxwellian distribution could be converted into REs (Chiu et al. 1998; Harvey et al. 2000; Helander et al. 2004; Smith et al. 2005; Smith and Verwichte 2008; Féher et al. 2011). After the thermal quench, the electron velocity distribution in the plasma consists of two parts: (i) a Maxwellian distribution with the temperature of about 10 eV; (ii) the tail of the former Maxwellian distribution with the temperature in the range of several keV. The second part contributes to the hot tail RE generation. A simple estimate for hot tail RE density generated during

the thermal quench can be obtained by neglecting RE losses (Smith and Verwichte 2008),

$$n_{\text{RE-HT}} = n_0 \frac{2}{\sqrt{\pi}} u_c e^{-u_c^2},$$

accompanied by the temporal evolution of the temperature $T = T_{\text{final}} + (T_0 - T_{\text{final}})e^{-t/t_0}$ and the density $n = n_{\text{final}} - (n_{\text{final}} - n_0)e^{-t/t_0}$. Here $u_c = (v_c^3/v_{T0}^3 + 3\tau)^{1/3}$, where v_c is the critical velocity, v_{T0} is the thermal velocity before the disruption, τ is given by $\tau = \nu_0 \int_0^t n(t)/n_0 dt$, where ν_0 is the collision frequency before the disruption, t_0 is the thermal quench cooling time, and the subscripts '0' and 'final' of T and n mean the value at the beginning and the end of the thermal quench, respectively. Typical value of the thermal quench cooling time in TEXTOR disruptions is ~0.035 ms. The simulation results are shown in Figs 4(a) and (b) for typical TEXTOR parameters ($T_0 = 1.3$ keV, $T_{\text{final}} = 10$ eV, $n_0 = 2.0 \times 10^{19}$ m^{-3}, $n_{\text{final}} = 3.0 \times 10^{19}$ m^{-3}). It turns out the temperature history is highly consistent with the experimental observation but the electron density is not exactly the same as in the experiment, and therefore the value used in the model is a little lower than the experimental value because the line integrated density measured by the interferometer includes the region inside $q = 2$, which does not change a lot, and outside $q = 2$, which includes bumps in $q = 2$ and $q = 3$ surfaces (Thornton et al. 2012). For hot tail RE generation, only the region inside $q = 2$ is considered. The hot tail density is $n_{\text{RE-HT}} = 5.8 \times 10^{15}$ m^{-3} and the energy of hot tail electrons is several keV. Accelerated continually by the electric field, the electrons increase their energy to several MeV and the velocity is close to the speed of light, so the corresponding hot tail RE currents are $I_{\text{RE-HT}}$ ~57 kA, which should provide large amounts of seed REs. Actually, the value is overestimated for seed REs because there are several mechanisms that can constrain the energy or cause RE losses, especially radial diffusion losses due to magnetic turbulence during the thermal quench (Marmar et al. 2009) and current quench (Zeng et al. 2013).

Comparison of RE currents from hot tail generation with the model and measured RE currents is shown in Fig. 4(c). The experimental results are from the three discharges with the same toroidal field of $B_t = 2.4$ T, the same plasma current of $I_p = 350$ kA and the different densities of $n_e = 2.0 \times 10^{19}$, 2.5×10^{19} and 3×10^{19} m^{-3}, which correspond to the central temperatures of 1.30, 1.13 and 1.00 keV, respectively. Similar to Fig. 1, the RE tail increases with the increasing temperature before the thermal quench. The simulation results confirm the tendency found in the experiments. The difference between them could be understood by RE losses and the following RE avalanche during the current quench, where the avalanche gain is about 2.4. The Dreicer mechanism is not considered here.

Although it is difficult to measure the exact contribution from hot tail electrons directly in a disruption, the anomalous RE losses could be observed, shown in Fig. 5. A bump after the thermal quench (measured by the electron cyclotron emission diagnostic) results from confined REs for energies below ~3 MeV (Fig. 5(a)). A SXR spike following the ECE bump, indicated by an arrow in Fig. 5(b), is associated with bremsstrahlung from RE impact at the wall. The SXR spike refers to RE prompt loss and coincides with a decrease in ECE amplitude. REs via the hot tail mechanism could be the reason as the temperature of background plasma (~10 eV) is too low to emit such high X-ray radiation, and a much higher loop voltage of ~500 V would be needed in a short period of 0.8 ms for REs via the Dreicer mechanism to emit the relevant X-ray radiation. Similar results have also been reported from DIII-D (James et al. 2011; 2012).

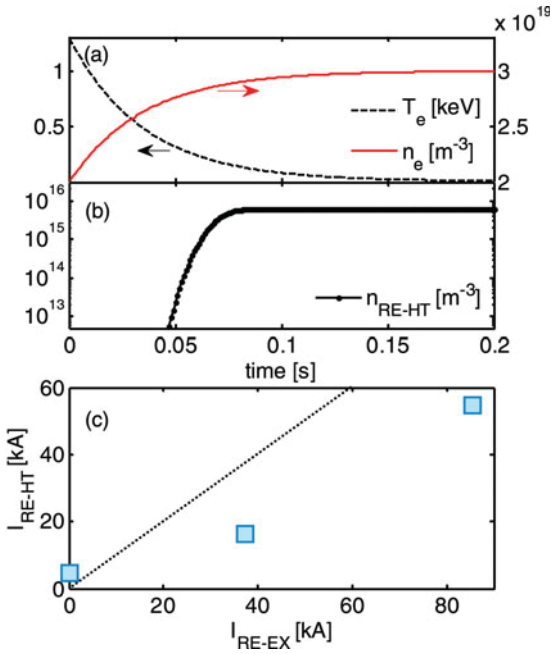

FIGURE 4. Time evolution during the thermal quench of (a) electron temperature and density and (b) the density of tail electrons in the RE region. (c) Comparison of RE currents from hot tail generation with the modelled $I_{\text{RE-HT}}$ and measured RE currents $I_{\text{RE-EX}}$ with the dashed line indicating equality.

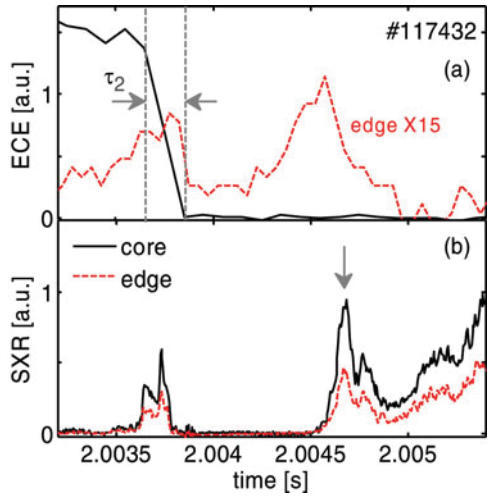

FIGURE 5. Time traces for shot 117 432 showing (a) electron temperature and (b) Soft X-ray emission measured by a core and an edge channel. The thermal quench time is indicated in (a) and the spike caused by RE losses is marked by the arrow in the (b).

4. Conclusions and discussion

Higher RE currents during TEXTOR disruptions are obtained in discharges with higher electron temperature before the disruption both in ohmic and NBI discharges. The presented evidence supports the theory of hot-tail RE generation. RE generation occurs only above a threshold for the toroidal magnetic field and below a threshold

of the electron density. The density threshold increases with the toroidal field but the toroidal magnetic field threshold decrease with the density decreasing. Actually, there is a temperature threshold instead of the density threshold. With higher temperature, more REs are generated via the hot tail mechanism during the thermal quench. Increasing the hot tail RE generation by increasing the temperature, an obvious RE plateau is observed even with low toroidal magnetic field (1.7 T), less than the previously reported toroidal field threshold of about 2 T on TEXTOR. The simulation results confirm the tendency seen in the experimental data.

Acknowledgement

Support from the Helmholtz Association in frame of the Helmholtz-University Young Investigators Group VH-NG-410, the National Magnetic Confinement Fusion Science Program of China under Contracts No. 2013GB106003 and 2014GB106004 and the Natural Science Foundation of China under Grant No. 11475221 is gratefully acknowledged.

REFERENCES

Bozhenkov, S. A. et al. 2007 Main characteristics of the fast disruption mitigation valve. *Rev. Sci. Instrum.* **78**, 033 503.

Bozhenkov, S. A. et al. 2008 Generation and suppression of runaway electrons in disruption mitigation experiments in TEXTOR. *Plasma Phys. Control. Fusion* **50**, 105 007.

Chiu, S. C., Rosenbluth, M. N., Harvey, R. W. and Chan, V. S. 1998 Fokker–Planck simulations mylb of knock-on electron runaway avalanche and bursts in tokamaks. *Nucl. Fusion* **38**, 1711.

Connor, J. W., Hastie, R. J. 1975 Relativistic limitations on runaway electrons. *Nucl. Fusion* **15**, 415.

Dreicer, H. 1959 Electron and ion runaway in a fully ionized gas: I. *Phys. Rev.* **115**, 238.

Dreicer, H. 1960 Electron and ion runaway in a fully ionized gas: II. *Phys. Rev.* **117**, 329.

Féher, T. et al. 2011 Simulation of runaway electron generation during plasma shutdown by impurity injection in ITER. *Plasma Phys. Control. Fusion* **53**, 035 014.

Granetz R. et al. 2015 An ITPA joint experiment to study runaway electron generation and suppression. *Phys. Plasma* **21**, 072 506.

Harvey, R. W. et al. 2000 Runaway electron production in DIII-D killer pellet experiments, calculated with the CQL3D/KPRAD model. *Phys. Plasmas* **7**, 4590.

Helander, P., Smith, H., Fülop, T. and Eriksson, L. G. 2004 Electron kinetics in a cooling plasma. *Phys. Plasmas* **11**, 5704.

Hender, T. C. et al. 2007 Progress in the ITER physics basis chapter 3: MHD stability, operational limits and disruptions. *Nucl. Fusion* **47**, S128.

ITER Physics Basis Editors et al. 1999 ITER physics basis chapter 1: overview and summary. *Nucl. Fusion* **39**, 2137.

James, A. N. 2011 Investigations of runaway electron generation, transport, and stability in the DIII-D tokamak. *PhD thesis*, University of California, San Diego, USA.

James, A. N. et al. 2012 Measurements of hard x-ray emission from runaway electrons in DIII-D. *Nucl. Fusion* **52**, 013 007.

Lehnen, M. et al. 2008 Suppression of runaway electrons by resonant magnetic perturbations in TEXTOR disruptions. *Phys. Rev. Lett.* **100**, 255 003.

Lehnen, M. et al. 2009 Runaway generation during disruptions in JET and TEXTOR. *J. Nucl. Mater.* **390–391**, 740.

Lehnen, M. et al. 2011 Disruption mitigation by massive gas injection in JET. *Nucl. Fusion* **51,** 123 010.

Lvovskiy, A. Koslowski, H. R. and Zeng, L. 2015 Suppression of the runaway electron generation by massive gas injection after induced disruptions on TEXTOR. *Submitted to J. Plasma Phys.*

Marmar, E. et al. 2009 Overview of the Alcator C-Mod research program. *Nucl. Fusion* **49**, 104 014.

Martin, G. 1998 Runaway electrons: from Tore-Supra to ITER. In: *Proc. 25th European Physical Society Conf. on Plasma Physics, Prague*, 1998, Vol. 22C. Prague, Czech Republic: European Physical Society, P3.006.

Pautasso, G. et al. 2007 Plasma shut-down with fast impurity puff on ASDEX Upgrade. *Nucl. Fusion* **47**, 900.

Rosenbluth, M. N. and Putvinski, S. V. 1997 Theory for avalanche of runaway electrons in tokamaks. *Nucl. Fusion* **37**, 1355.

Smith, H., Helander, P., Eriksson, L. G. and Fülop, T. 2005 Runaway electron generation in a cooling plasma. *Phys. Plasmas* **12**, 122 505.

Smith, H. and Verwichte, E. 2008 Hot tail runaway electron generation in tokamak disruptions. *Phys. Plasmas* **15**, 072 502.

Thornton, A. J. et al. 2012 Plasma profile evolution during disruption mitigation via massive gas injection on MAST. *Nucl. Fusion* **52**, 063 018.

Yoshino, R. 1995 Avoidance and softening of disruptions by control of plasma-surface interaction. *J. Nucl. Mater.* **220–222**, 132.

Yoshino, R., Tokuda, S. and Kawano, Y. 1999 Generation and termination of runaway electrons at major disruptions in JT-60U. *Nucl. Fusion* **39**, 151.

Zeng, L. et al. 2013 Experimental observation of a magnetic-turbulence threshold for runaway-electron generation in the TEXTOR tokamak. *Phys. Rev. Lett.* **110**, 235 003.

PUBLICATION 6

J. Plasma Phys. (2015), *vol.* 81, 475810501 © Cambridge University Press 2015
doi:10.1017/S0022377815000501

Mechanisms of plasma disruption and runaway electron losses in the TEXTOR tokamak

S. S. Abdullaev[1,†], K. H. Finken[2], K. Wongrach[2], M. Tokar[1], H. R. Koslowski[1], O. Willi[2], L. Zeng[3] and the TEXTOR team

[1]Forschungszentrum Jülich GmbH, Institut für Energie- und Klimaforschung – Plasmaphysik, D-52425 Jülich, Germany

[2]Institut für Laser- und Plasmaphysik, Heinrich-Heine Universität Düsseldorf, Germany

[3]Institute of Plasma Physics, Chinese Academy of Sciences, 230031 Hefei, China

(Received 5 January 2015; revised 10 April 2015; accepted 10 April 2015)

Based on the analysis of data from the numerous dedicated experiments on plasma disruptions in the TEXTOR tokamak the mechanisms of the formation of runaway electron (RE) beams and their losses are proposed. The plasma disruption is caused by a strong stochastic magnetic field formed due to nonlinearly excited low-mode-number magneto-hydro-dynamics (MHD) modes. It is hypothesized that the RE beam is formed in the central plasma region confined by an intact magnetic surface due to the acceleration of electrons by the inductive toroidal electric field. In the case of plasmas with the safety factor $q(0) < 1$ the most stable RE beams are formed by the outermost intact magnetic surface located between the magnetic surface $q = 1$ and the closest low-order rational surface $q = m/n > 1$ ($q = 5/4$, $q = 4/3$, ...). The thermal quench (TQ) time caused by the fast electron transport in a stochastic magnetic field is calculated using the collisional transport model. The current quench (CQ) stage is due to the particle transport in a stochastic magnetic field. The RE beam current is modelled as a sum of a toroidally symmetric part and a small-amplitude helical current with a predominant $m/n = 1/1$ component. The REs are lost due to two effects: (i) by outward drift of electrons in a toroidal electric field until they touch the wall and (ii) by the formation of a stochastic layer of REs at the beam edge. Such a stochastic layer for high-energy REs is formed in the presence of the $m/n = 1/1$ MHD mode. It has a mixed topological structure with a stochastic region open to the wall. The effect of external resonant magnetic perturbations on RE loss is discussed. A possible cause of the sudden MHD signals accompanied by RE bursts is explained by the redistribution of runaway current during the resonant interaction of high-energetic electron orbits with the $m/n = 1/1$ MHD mode.

1. Introduction

One of the severe consequences of the plasma disruptions in tokamaks is the generation of the runaway electron (RE) beams (see e.g. Wesson *et al.* 1989; Gill 1993; Schüller 1995; Gill *et al.* 2000, 2002; Wesson 2004; Boozer 2012; Papp *et al.* 2013 and references therein). The REs generated during the disruptions of tokamak

† Email address for correspondence: s.abdullaev@fz-juelich.de

plasmas may reach several tens of MeV and may contribute to a significant part of post-disruption plasma current. The prevention of such RE beams is of paramount importance in future tokamaks, especially in the ITER operation, since it may severely damage a device wall (Bécoulet *et al.* 2013).

At present there are several proposals to mitigate REs generated during plasma disruptions. The mitigation of REs by gas injections has been discussed (see e.g. Whyte *et al.* 2002, 2003; Bakhtiari *et al.* 2002, 2005; Granetz *et al.* 2007; Hender *et al.* 2007; Bozhenkov *et al.* 2008; Lehnen *et al.* 2009; Pautasso *et al.* 2009; Hollmann *et al.* 2010; Reux *et al.* 2010 and Lehnen *et al.* 2011). Suppression of REs by resonant magnetic perturbations (RMPs) has been also intensively discussed since the late 1990s (see e.g. Kawano *et al.* 1997; Tokuda and Yoshino 1999; Helander *et al.* 2000; Yoshino and Tokuda 2000; Lehnen *et al.* 2008, 2009; Hollmann *et al.* 2010 and Papp *et al.* 2011, 2012). However, up to now there is no regular strategy to solve this problem. One of the reasons is that the physical mechanisms of the formation of REs during plasma disruptions are still not well known. The different scenarios of runaway formation during plasma disruptions have been discussed in the literature. Particularly, in Fülöp *et al.* (2009), Fülöp and Newton (2014), the possible roles of whistler waves in the generation of REs and Alfvénic wave instabilities driven by REs have been discussed.

There were numerous dedicated experiments to study the problem of runaway current generation during plasma disruptions triggered by massive gas injections (MGIs) in the TEXTOR tokamak (see e.g. Forster *et al.* 2012; Zeng *et al.* 2013; Wongrach *et al.* 2014), in the KSTAR tokamak (Chen *et al.* 2013), in the JET tokamak (Plyusnin *et al.* 2006; Lehnen *et al.* 2011), in DIII-D (Hollmann *et al.* 2010; Commaux *et al.* 2011; Hollmann *et al.* 2013), in Alcator C-Mod (Olynyk *et al.* 2013), and others. In these works the dependences of RE generation on the toroidal magnetic field, on the magnetic field fluctuations, and on the species of injection gases have been investigated. Particularly, in the KSTAR tokamak (Chen *et al.* 2013), it has been found that there is no toroidal magnetic field threshold $B_T < 2$ T, as was indicated by previous experiments in other tokamaks. In Izzo *et al.* (2011, 2012), magneto-hydro-dynamics (MHD) simulations have been performed to study the confinement of REs generated during rapid disruptions by MGIs in DIII-D, Alcator C-Mod, and ITER. Such simulations with two different MHD codes have been carried out by Izzo *et al.* (2012) to analyse shot-to-shot variability of RE currents in DIII-D tokamak discharges.

These numerous experiments show the complex nature of plasma disruption processes, especially the formation of RE beams, and their evolution. One of the important features of this event is its irregularity and variability of RE beam parameters from one discharge to another. This indicates the sensitivity of disruption processes and RE beam formations to initial conditions, which is the characteristic feature of nonlinear processes, particularly, a deterministic chaotic system. Therefore, *ab initio* numerical simulations of these processes may not always be successful to understand their mechanisms because of the complexity of computer simulations of nonlinear processes (Kadanoff 2004). The problem of numerical simulations of plasma disruptions is comprehensively discussed by Boozer (2012). The present status of the theory of RE generation in ITER is reviewed in the recent paper by Boozer (2015).

In this work we intend to approach this problem from the point of view of Hamiltonian chaotic systems, mainly the magnetic stochasticity in magnetically confined plasmas (Abdullaev 2014). Based on the ideas of these systems and analyses of numerous experimental results, mainly obtained in the TEXTOR tokamak, we

propose possible mechanisms of formation and evolution of RE beams created during plasma disruptions. Since a self-consistent theoretical treatment of all these processes is very complicated, we developed theoretical models for each stage of a plasma disruption. These models are used to estimate the characteristic times of the thermal and current quenches (CQs), the spatial size of runaway plasma beams and their decay times, the speed of RE radial drifts, and the effect of magnetic perturbations.

It is believed that the plasma disruption starts due to a large-scale magnetic stochasticity caused by excited MHD modes with low poloidal m and toroidal n numbers ($m/n = 1/1, 2/1, 3/2, 5/2, \ldots$) (see e.g. Kadomtsev 1984; Gill 1993; Schüller 1995; Wesson 2004 and references therein). The heat and particle transports in the strongly chaotic magnetic field cause a fast temperature drop and stop the plasma current. However, at a certain spectrum of magnetic perturbations, for example at a sufficiently small amplitude of the $m/n = 1/1$ mode, the chaotic field lines may not extend to the central plasma region due to the creation of an intact magnetic surface. In the case of plasmas with the safety factor $q(0) < 1$ at magnetic axis $\rho = 0$ the intact magnetic surface can be located between the magnetic surface $q = 1$ and the nearest low-order rational surface $q = 5/4$ (or $q = 4/3, \ldots$). This intact magnetic surface confines particles in the central plasma region and serves as a transport barrier to particles during the CQ. Electrons in the confined region are accelerated due to the large toroidal electric field and form the relatively stable RE beams.

This occurs, for instance, when the plasma disruption is initiated by the heavy argon gas injection which does not penetrate deep into the plasma; therefore, it does not excite the $m/n = 1/1$ mode with a sufficiently large amplitude. On the contrary, the injection of the lighter noble gases neon and helium does not generate runaways. The reason is that light gases penetrate deeper into the plasma and excite the large-amplitude $m/n = 1/1$ mode.

The existence of an intact magnetic surface and its location depend on the radial profile of the safety factor and the spectrum of magnetic perturbations. The latter sensitively depends on the plasma disruption conditions and varies unpredictably from one discharge to another during plasma disruptions. This makes the RE formation process unpredictable and may explain a shot-to-shot variability of the parameters of RE beams.

The role of the safety factor profile in the formation of RE beams can be pronounced during disruptions of plasmas with reversed magnetic shear. In the plasmas with non-monotonic radial profiles of the safety factor there has been observed an improved confinement of energy and particles due to the internal transport barrier located near the minimal value of the safety factor, i.e. near the shearless magnetic surface (Levinton *et al.* 1995; Strait *et al.* 1995). During disruptions this magnetic surface acts as a robust magnetic barrier that separates a chaotic magnetic field formed in the outer region from penetration into the central plasma region. Electrons confined by the shearless magnetic surface can form a stable RE beam with a relatively large transversal size. Recently published results of the disruption experiments in the TFTR tokamak with the reversed magnetic shear indeed show the formation of a large RE beam with long confinement times (Fredrickson *et al.* 2015).

Based on this mechanism, we study the three main stages of the post-disruption plasma evolution: the fast thermal quench (TQ), the CQ, and the RE beam evolution. The physical processes during each of these stages will be studied by theoretical models. These processes are the formation of a stochastic magnetic field, heat and particle transport in a stochastic magnetic field, the acceleration of electrons by an inductive electric field, the loss mechanisms of REs, and the effect of internal and

external magnetic perturbations. A short report on this study is to be published in Abdullaev *et al.* (2015).

The paper consists of eight sections. Mathematical tools and models employed to study the problems are given in the Supplementary Part available at http://dx.doi.org/10.1017/S0022377815000501. The numerous data obtained during the dedicated experiments in the TEXTOR tokamak are analysed in § 2. Possible mechanisms of plasma disruptions with RE beam formation are proposed and analysed in § 3. The transport of heat and particles during the fast TQ and the CQ stages of plasma disruption are studied in § 4. The model of a post-disruption plasma beam is proposed in § 5. Using this model, the time evolution of guiding-centre (GC) orbits of electrons accelerated by the inductive toroidal electric field is studied in § 6. Particularly, the change of RE confinement conditions with decreasing plasma current and increasing electron energy and the outward drift of GC orbits are investigated. The effect of external and internal magnetic perturbations on the RE confinement are discussed in § 7. In the final § 8, we give a summary of the obtained results and discuss their consequences.

2. Description of plasma disruptions

The TEXTOR was a middle size limiter tokamak with the major radius $R_0 = 1.75$ m and the minor radius $a = 0.46$ cm. The toroidal field B_0 can be varied up to 2.8 T, and the plasma current taken up to 600 kA. In the experiments the plasma disruptions were triggered in a controlled way by gas injections using a fast disruption mitigation valve (DMV) (Bozhenkov *et al.* 2007; Finken *et al.* 2008, 2011; Bozhenkov *et al.* 2011). Particularly, the disruptions with REs were triggered by argon (Ar) injection. The runaway-free disruptions were triggered by either helium or neon (He/Ne) injection performed by the smaller valve. The effect of the externally applied RMPs on the RE generations has been investigated using the dynamic ergodic divertor (DED) installed in the TEXTOR tokamak.

Below we analyse the experimental results of discharges with the pre-disruption plasma current $I_p = 350$ kA and the toroidal field $B_t = 2.4$ T. Figure 1(*a*) illustrates typical disruptions of the discharges of the TEXTOR tokamak with and without RE generations. Specifically, it shows the time evolution of plasma parameters (the loop voltage V_{loop}, the electron cyclotron emission (ECE), the soft X-ray (SXR) signal, the Mirnov signal, and the scintillation probe (ScProbe) signal during disruptions of the discharges with REs (nos 117 434, 117 859, 119 978 and 120 140) and without REs (no. 117 444)).

There are also some discharges with untypical RE currents and shorter current decay times. The two examples of such discharges are shown in figure 1(*b*). We will discuss some features of these discharges at the end of the section.

The typical behaviour of the plasma during the disruptions is as follows. The gas (Ar or Ne/He) was injected at the time instant $t = 2$ s. One can distinguish three stages of the disruption with the REs: the first (or fast) stage in which a sudden temperature drop occurs, in the second stage the plasma current starts to decay with a higher rate, and in the third stage the current decay slows down and the current beam with the REs is formed.

2.1. *Thermal quench stage*

The first fast stage starts a few milliseconds (between 2 and 5 ms) after the gas injection and ends with a sudden temperature drop (a TQ) in a time interval of

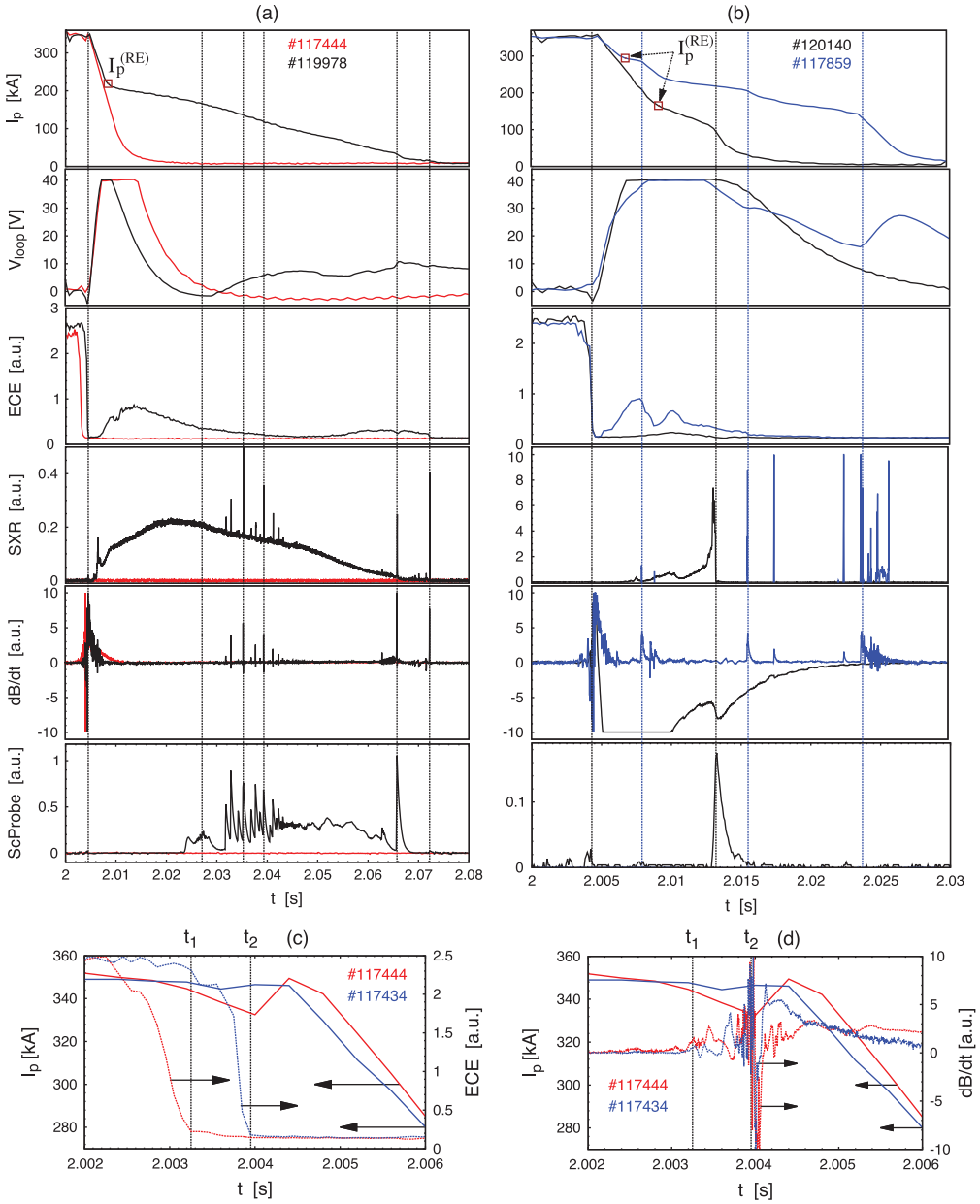

FIGURE 1. (*a*) Time evolution of the disruption of the TEXTOR shots no. 119 978 (black solid lines) and no. 117 444 (red curves) (from top to bottom): the plasma current, the loop voltage, the ECE signal, the SXR signal, the Mirnov signal, and the ScProbe signal. (*b*) The same but for the discharges no. 117 859 (blue curves) and no. 120 140 (black curves). (*c*) Initial stage of the temporal evolution of the plasma current (solid curve on the left-hand side axis) and ECE signal (right-hand side axis); (*d*) the Mirnov signal (right-hand side axis) during a plasma disruption with (nos 117 434 and 117 507) and without (no. 117 444) RE generations. $I_p^{(RE)}$ is the initial value of the plasma current with REs. Disruptions for discharges nos 117 434, 119 978, 117 507, 117 859 and 120 140 are initiated by Ar injections, and no. 117 444 by Ne injections.

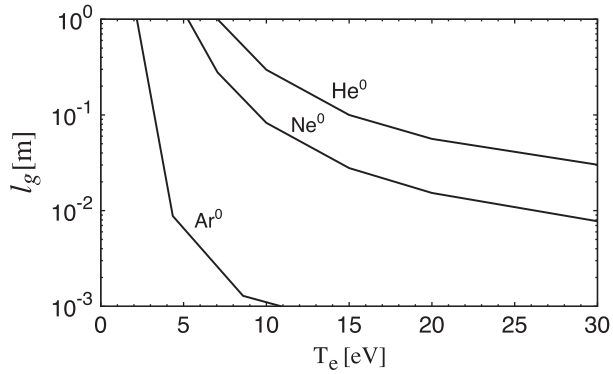

FIGURE 2. Dependence of the penetration length l_g on the electron temperature T_e for He, Ne, and Ar atoms. The electron density is $n_e = 10^{19}$ m^{-3}.

about 1 ms, as seen from the ECE signals shown in detail in figure 1(*c*). The Mirnov signals indicating magnetic activities start just before this time interval and they last a few milliseconds until a significant decay of the plasma current for the RE-free discharges or establishment of the current with the REs (see figure 1*a*). The close-up views of the ECE signals and the Mirnov signals in this stage for the discharges with REs (no. 117 434) and without REs (no. 117 444) are shown in figure 1(*c*,*d*), respectively. The end times t_1 and t_2 of the TQ stages for these discharges are shown by vertical lines.

For our study, it is of importance to analyse in detail the difference in the time development of the TQ stage of disruptions without REs and with REs, initiated by the massive injection of lighter (Ne) and heavier (Ar) noble gases. (i) In figure 1(*c*), one can see that the TQ starts roughly at 2.6 μs, in the former case, and at 3.7 μs, in the latter one, after the initiation of injection. The ratio of these delay times is $0.7 \approx 1/\sqrt{2}$ and can be well explained by the difference in the atomic weights A_g of the gases in question. Indeed, the flow velocity $V_g \sim 1/\sqrt{A_g}$ of neon atoms is a factor of $\sqrt{2}$ higher than that for argon and, thus, neon atoms enter the plasma after a respectively shorter time.

(ii) By comparing figure 1(*c*,*d*), we find that by injection of neon the TQ stage is finished (at time t_1) before MHD perturbations are triggered. That is, in this case, TQ is completely due to cooling induced by the presence of impurity atoms squeezed in a narrow jet and penetrating deep enough into the plasma core. The penetration depth of gas atoms is $l_g = V_g/(k^0_{ion} n_e)$, where k^0_{ion} is the ionization rate coefficient. Figure 2 displays l_g versus the electron temperature T_e with the electron density $n_e = 10^{19}$ m^{-3} computed for He, Ne, and Ar, by using the open atomic database ADAS (OPEN-ADAS: Atomic Data and Analysis Structure, http://open.adas.ac.uk/) for k^0_{ion} and assuming that the gas jet has a radial velocity of two sound speeds at the room temperature. One can see that for light gases, He and Ne, l_g can exceed the minor radius of TEXTOR of 0.46 m if inside the gas jet the plasma is cooled down to a temperature of several eV by energy losses on excitation and ionization of gas atoms and thermalization of generated electrons, as is demonstrated in Koltunov and Tokar (2011). The rest of the magnetic surfaces is cooled down by the heat conduction along magnetic field lines to the jet area (Tokar and Koltunov 2013). Thus, the plasma is cooled down as a whole during a time of $a/V_g \approx 0.5$–1 ms. Only later are tearing

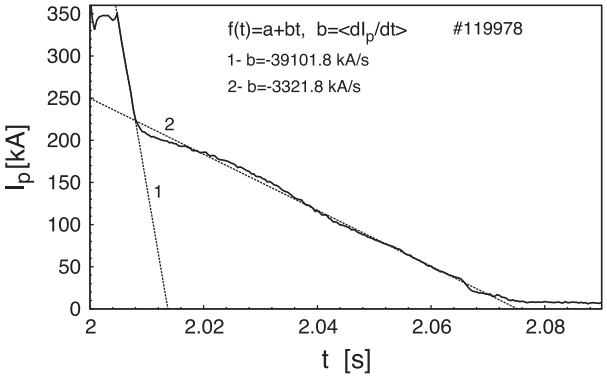

FIGURE 3. Determination of the average current decay rate $\langle dI_p/dt\rangle$ at the second and the third stages of the plasma disruptions. Solid curve describes the measured time evolution of the current $I_p(t)$, dashed straight line $f(t) = a - bt$ approximates the average current decay. The coefficient b gives the estimation of $|\langle dI_p/dt\rangle|$. Curve 1 corresponds to the current decay stage and curve 2 corresponds to the RE current decay stage.

modes excited on numerous resonant magnetic surfaces due to the growth, as $1/T_e^{3/2}$, of the plasma resistivity.

(iii) In the case of Ar, the penetration depth l_g is much smaller, mostly due to the much larger ionization rate, than for He and Ne atoms and Ar gas is ionized at the plasma edge. Due to edge cooling very sharp radial gradients of the plasma resistivity and plasma current density j are generated. Since the growth rate of tearing modes is $\sim(dj/d\rho)^{4/5}$ (Wesson 2004), MHD modes resonant mostly on outer magnetic surfaces with the safety factor noticeably larger than 1 are triggered. The magnetic field stochastization due to these modes leads to the fast cooling of the main plasma volume during a time of 0.1–0.2 ms (see § 4.1). This explains why in shot no. 117 434 with Ar injection the temperature drop happens although later but faster than in shot no. 117 444 with Ne, and MHD activity starts to develop even before the TQ; see figure 1(*c*,*d*).

2.2. *Current quench stage*

The second stage of the plasma disruption begins with the current decay within a millisecond after the TQ. Particularly, for the discharges nos 117 434 and 117 444, the current decay starts in 0.47×10^{-3} s and 0.87×10^{-3} s, respectively, after the temperature drop (see figure 1*a*,*c*). In discharges without the RE formation the current decays with the same rate until it completely disappears in a few milliseconds. In the discharges with the RE formation the strong current decay stops at a certain value of $I_p = I_p^{(RE)}$ and is replaced by a slower decay. The initial RE current $I_p^{(RE)}$ is shown in figure 1(*a*,*b*). In this stage the loop voltage starts to rise due to an inductive electric field opposing the current decay.

The time dependence of the plasma current I_p in this stage for all discharges is well approximated by the linear function of time $I_p = I_{p0} - bt$, where the coefficient $b = -\langle dI_p/dt\rangle$ determines the average current decay rate. The scheme of determination of $b = |\langle dI_p/dt\rangle|$ is shown in figure 3. The values of the current decay rate $\langle dI_p/dt\rangle$ during the CQ and RE plateau regimes and the initial RE current $I_p^{(RE)}$ for a number of discharges are listed in table 1. It also shows the time t_{max} when the applied RMP,

Discharge no.	Second stage	Third stage	$I_p^{(RE)}$ (kA)	DEDt_{max}, n, I_{ded}
117 434	40.2 ± 0.45	4.63 ± 0.09	220.1	No
117 444	47.8 ± 0.21	N/A	N/A	No
117 507	42.7 ± 0.71	4.29 ± 0.14	193.9	No
117 527	39.4 ± 0.29	5.65 ± 0.12	220.9	No
117 543	50.2 ± 0.19	NA	N/A	No
117 859	33.2 ± 1.11	11.70 ± 0.50	296.0	No
119 868	40.05 ± 0.31	2.45 ± 0.01	224.9	No
119 869	39.96 ± 0.67	2.20 ± 0.02	230.0	2.02 s, $n = 1$, 1 kA
119 870	36.5 ± 0.96	2.23 ± 0.01	254.8	2.02 s, $n = 1$, 1.5 kA
119 874	37.9 ± 0.60	2.25 ± 0.01	243.8	No
119 877	45.3 ± 0.47	25.13 ± 0.98	166.8	1.9 s, $n = 1$, 2 kA
119 978	38.8 ± 0.76	3.38 ± 0.02	218.4	No
119 990	41.98 ± 0.23	3.35 ± 0.03	204.0	No
120 106	42.8 ± 0.42	2.03 ± 0.03	196.0	2.0 s, $n = 2$, 4 kA
120 107	40.73 ± 0.29	2.52 ± 0.03	206.0	2.0 s, $n = 2$, 4 kA
120 108	42.71 ± 0.32	2.25 ± 0.02	191.0	1.9 s, $n = 2$, 4 kA
120 109	42.91 ± 0.35	1.93 ± 0.02	176.0	1.9 s, $n = 2$, 4 kA
120 123	36.4 ± 0.47	3.66 ± 0.01	236.0	No
120 126	43.3 ± 0.25	1.92 ± 0.03	176.0	2.0 s, $n = 2$, 7 kA
120 134	45.0 ± 0.97	2.99 ± 0.17	176.0	2.0 s, $n = 2$, 7 kA
120 135	44.3 ± 0.43	2.20 ± 0.05	177.0	2.0 s, $n = 2$, 7 kA
120 140	47.5 ± 0.86	13.91 ± 0.35	165.0	1.97 s, $n = 2$, 6 kA
120 141	42.2 ± 0.30	2.20 ± 0.03	194.8	2.07 s, $n = 2$, 6 kA

TABLE 1. Parameters of discharges: first column – the discharge number; second and third columns – the average decay rates $|\langle dIp/dt\rangle|$ (in MA s^{-1}) of the plasma current $I_p(t)$ in the second and the third stages; fourth column – the initial current of the RE beam $I_p^{(RE)}$; the fifth column shows the parameters of the RMPs, a time t_{max} when the DED current reaches its maximum value I_{ded}, and the toroidal mode n. Note that the discharges nos 117 444 and 117 543 are RE-free.

i.e. the DED current I_{ded}, reaches its maximal value, and the toroidal mode n of the RMPs.

The dependences of $|\langle dI_p/dt\rangle|$ on the initial RE current $I_p^{(RE)}$ for a number of discharges are plotted in figure 4(*a*,*b*) in the CQ regime and the RE current decay stage, respectively. The current decay rate $|\langle dI_p/dt\rangle|$ for all discharges is of the same order and lies between 32 and 50 (MA s^{-1}), as listed in the second column of table 1 and shown in figure 4(*a*). The highest value of $|\langle dI_p/dt\rangle|$ is observed for the discharges without REs and with the lowest values of the RE current $I_p^{(RE)}$. As one can see from figure 4, there is a clear regular dependence of the current decay rate on the initial RE current, which can be fitted by a linear function $|\langle dI_p/dt\rangle| \approx A - BI_p^{(RE)}$ with constant parameters A, B. In § 4.2, we will discuss the possible mechanism of such a current decay related with the transport of particles in a stochastic magnetic field.

2.3. *RE plateau stage*

In the third stage (RE plateau) of the disruption the rapid current decay is replaced by its slow decay and it starts the formation of the REs due to the acceleration of electrons in the inductive toroidal electric field and the secondary generation of REs.

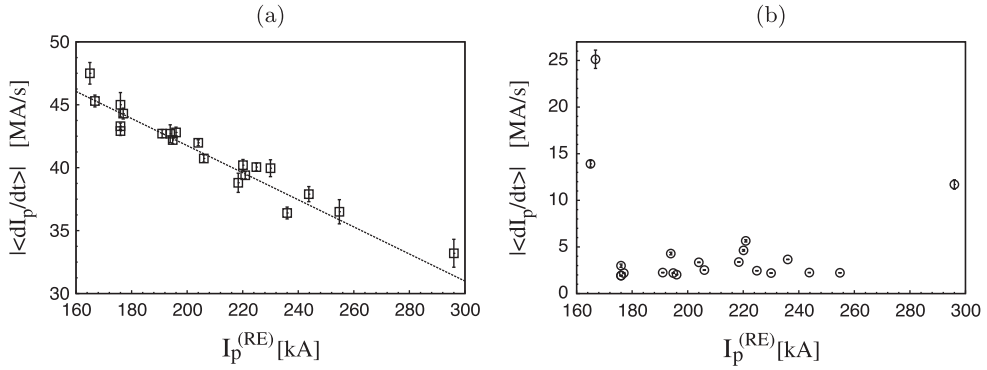

FIGURE 4. (*a*) Dependence of the average current decay rate $|\langle \mathrm{d}I_p/\mathrm{d}t\rangle|$ on the initial RE current $I_p^{(RE)}$ in the CQ regime for several discharges; (*b*) the same as in (*a*) but in the RE current decay stage.

The values of the current decay rate $|\langle \mathrm{d}I_p/\mathrm{d}t\rangle|$ along with the initial values of the plasma current $I_p^{(RE)}$ in this stage for several discharges are listed in the third and the fourth columns of table 1 and plotted in figure 4(*b*). The average values of $|\langle \mathrm{d}I_p/\mathrm{d}t\rangle|$ for almost all discharges are confined in the interval (2.2, 5.6) MA s^{-1}, i.e. one order lower than the current decay rate in the second stage. The values of $I_p^{(RE)}$ are also confined in the range between 170 and 260 kA, except for some untypical discharges, which will be discussed in the next subsection. These values of $|\langle \mathrm{d}I_p/\mathrm{d}t\rangle|$ and $I_p^{(RE)}$ are close to the ones observed in the similar experiments in the DIII-D tokamak (see e.g. Hollmann *et al.* 2010, 2013).

One should also note that in the RE plateau stage at certain time instants one also observes a sudden current drop accompanied by magnetic activity and RE bursts, as seen from figure 1(*a*,*b*) (see also e.g. Gill *et al.* 2000, Forster *et al.* 2012). These events are probably related to the nonlinear interaction of high-energetic electrons with MHD modes, which leads to formation of a stochastic layer at the beam edge open to the wall. We will discuss this phenomenon in § 7.3. In the final termination stage, one observes the quick RE current losses accompanied by magnetic activity.

2.4. *Untypical discharges with REs*

As was mentioned above, there are several untypical discharges for which the rates $\langle \mathrm{d}I_p/\mathrm{d}t\rangle$ take highest or lowest values (see figures 1(*b*), 4(*b*), and table 1). Particularly, the current decay rate (in the second stage) for no. 117 859 is lowest and highest for discharges nos 119 877 and 120 140. The RE current decay rate (in the third stage) for these discharges takes highest values. The quantity $I_p^{(RE)}$ takes the lowest value for the discharges nos 119 877 and 120 140 and the highest value for no. 117 859, as shown in figure 4(*b*). One can notice strong spikes in the SXR signals of these discharges compared to typical discharges (see figure 1*a*,*b*). Moreover, the above-mentioned bursts of REs accompanied by magnetic activities are more pronounced in these discharges. We will discuss the peculiarity of these discharges in §§ 3 and 5.

2.5. *Effect of the RMPs on RE generation*

In a number of discharges the effect of the DED of the TEXTOR (see § 5.2 of the Supplementary Part) on the RE generation has been studied. It was found that the

RMPs do not completely eliminate the RE formation, but they can increase the decay rate $\langle dI_p/dt\rangle$ and decrease $I_p^{(RE)}$. This effect depends on the operational mode n, the amplitude of the DED current I_{DED}, and the time t_{max} when the maximal DED current is reached. As seen from table 1, the maximal effect is obtained when the maximal I_{ded} is reached before the gas injection at $t = 2.0$ s, i.e. $t_{max} \leqslant t = 2.0$ s. However, at $t_{max} > t = 2.0$ s the RMPs do not affect it at all or it is very weak. Other experimental observations in the TEXTOR also confirm these observations (Koslowski *et al.* 2014). We will discuss this problem in § 7.2.

3. Formation of a confined plasma beam

3.1. *Main conjecture*

It is believed that the plasma disruption is caused by a large-scale magnetic stochasticity of field lines due to interactions of nonlinearly destabilized MHD modes (Carreras *et al.* 1980; Kadomtsev 1984; Lichtenberg 1984; Fukuyama *et al.* 1993; Wesson 2004; Kruger *et al.* 2005; White 2014). The global stochasticity is mainly due to the interactions of coupled MHD modes with low (m, n) numbers: $(m = 1, 2, \ldots, n = 1, 2, \ldots)$. The structure of a stochastic magnetic field mainly depends of the amplitudes B_{mn} of MHD modes and the radial profile of the safety factor $q(\rho)$, where ρ is the minor radius of a magnetic surface. Depending on these parameters, the stochastic magnetic field may fill entirely the plasma region so that the plasma particles are transported out along chaotic magnetic field lines, which leads to stopping of the plasma current. However, at certain conditions the stochastic magnetic field may not extend up to the central plasma region due to the formation of a magnetic barrier by the outermost intact magnetic surface at ρ_c. The electrons confined by this magnetic surface are accelerated by the toroidal electric field induced by the current decay from the outer plasma region, thus forming a RE beam. Let $I_p(\rho)$ be the plasma current flowing inside the magnetic surface of radius ρ,

$$I_p(\rho) = 2\pi \int_0^\rho j_\varphi(\rho)\rho \, d\rho, \tag{3.1}$$

where $j_\varphi(\rho)$ is the toroidal current density profile. Then the initial RE current $I_p^{(RE)}$ is mainly determined by the pre-disruption plasma current distribution $I_p(\rho)$ confined by the intact magnetic surface ρ_c, i.e. $I_p^{(RE)} \approx I_p(\rho_c)$.

As will be shown in §§ 6 and 7, the decay of the RE beam mainly depends on two effects: the outward drift of RE orbits induced by the toroidal electric field E_φ and their resonant interactions with helical magnetic perturbations. The outward drift velocity v_{dr} is determined by E_φ and the RE current $I_p^{(RE)}$ (see (6.2) and figure 15; see also Abdullaev 2015),

$$v_{dr} \propto E_\varphi / I_p^{(RE)} \propto E_\varphi / \rho_c^2. \tag{3.2}$$

The most stable RE beams are expected to form when the corresponding drift velocity is lowest and the low-order rational magnetic surfaces within the RE beam are absent or there is only one.

3.2. *Possible generic structures of stochastic magnetic fields*

Below we study possible structures of the stochastic magnetic field which may lead to the formation of the RE beams. We consider two types of the safety factor profiles of $q(\rho)$: (i) the monotonic radial profile and (ii) the non-monotonic radial profile, corresponding to the plasmas with the reversed magnetic shear.

The models for the radial profiles of the plasma current $I_p(\rho)$, the safety factor $q(\rho)$ of the pre-disruption equilibrium plasma, and the MHD magnetic perturbations are given in § 3 of the Supplementary Part. The perturbation magnetic field simulating low-mode-number MHD modes is given by the toroidal component of the vector potential

$$A_{\varphi}^{(1)}(R, Z, \varphi, t) = -\frac{R_0^2}{R} \sum_{mn} m^{-1} a_{mn}(\rho) \cos(m\vartheta - n\varphi + \Omega_{mn} t), \tag{3.3}$$

$$a_{mn}(\rho) = B_{mn} U_{mn}(\rho), \tag{3.4}$$

with the mode amplitudes B_{mn} and rotation frequencies Ω_{mn}. Here B_0 is the toroidal field strength, R_0 is the major radius R_0, and the functions $U_{mn}(\rho)$ describe the radial profiles of the modes.

One should note that the structure of the magnetic field lines in the presence of magnetic perturbations is less sensitive to the radial profiles of $U_{mn}(\rho)$. It is mainly determined by the safety factor profiles and the mode amplitudes $a_{mn}(\rho)$ at the resonant surfaces $\rho = \rho_{mn}$, $q(\rho_{mn}) = m/n$ (see § 7.2 of the Supplementary Part).

Monotonic radial profile of $q(\rho)$: *the case* $q(0) < 1$. The typical TEXTOR plasma has the monotonic safety factor profile with the value $q(0) < 1$ at the magnetic axis $\rho = 0$. In this plasma, the $m/n = 1/1$ mode should play an important role in the structure of stochastic field lines near the plasma centre. At low amplitudes of this mode the global stochastic field lines may not reach the $q = 1$ magnetic surface and may form a confined region about the plasma centre where REs can be generated. At high amplitudes of the $m/n = 1/1$ mode the stochastic field lines may cover the entire plasma region with no confined particles.

As was mentioned above, in the TEXTOR experiments plasma disruptions with REs were deliberately caused by the injection of Ar gas while the RE-free disruptions are triggered by He/Ne injection. Experiments show that the penetration lengths of atoms depend on their atomic weights (Bozhenkov *et al.* 2008): He (or Ne) atoms penetrate deeper into plasma than argon atoms. The injection of these gases may finally give rise to different spectra of amplitudes of MHD modes. One can expect that the amplitude of the $m/n = 1/1$ MHD mode excited by the He/Ne injection is higher than in the case of argon gas injection.

The two possible distinct generic structures of a stochastic magnetic field before the CQ with the RE-free discharge and with the RE discharge are shown in figure 5(*a*,*b*) by the Poincaré sections of magnetic field lines. It is assumed that the perturbation field contains several MHD modes: $m/n = 1/1$, $m/n = 2/1$, $m/n = 3/2$, and $m/n = 5/2$. In the case shown in figure 5(*a*), the normalized mode amplitudes $b_{mn} = B_{mn}/B_0$ are $(1, 1, 1, 1) \times \epsilon_{MHD}$, and in figure 5(*b*) they are $(1/2, 1, 1, 1) \times \epsilon_{MHD}$. The toroidal field magnitude is $B_0 = 2.5$ T and the dimensionless perturbation parameter $\epsilon_{MHD} = 10^{-4}$. As seen from figure 5(*a*), for the larger amplitude of the $m/n = 1/1$ mode the stochastic magnetic field extends up to the central plasma region destroying the separatrix of the $m = n = 1$ island. For the low amplitude of the $m/n = 1/1$ mode shown in figure 5(*b*), the stochastic magnetic field does not reach the $q = 1$ magnetic surface and covers the region outside the $q = 1$ magnetic surface. The last intact magnetic surface ρ_c (red curve) is located between the resonant surfaces $q(\rho_1) = 1$ and $q(\rho_3) = 4/3$ (blue curves).

As seen from figure 5, particles in the plasma core are confined by intact magnetic surfaces located between resonant surfaces $q = 4/3$ and $q = 1$. A plasma beam confined in this area is relatively stable. It contains only the $m/n = 1/1$ MHD mode, which does

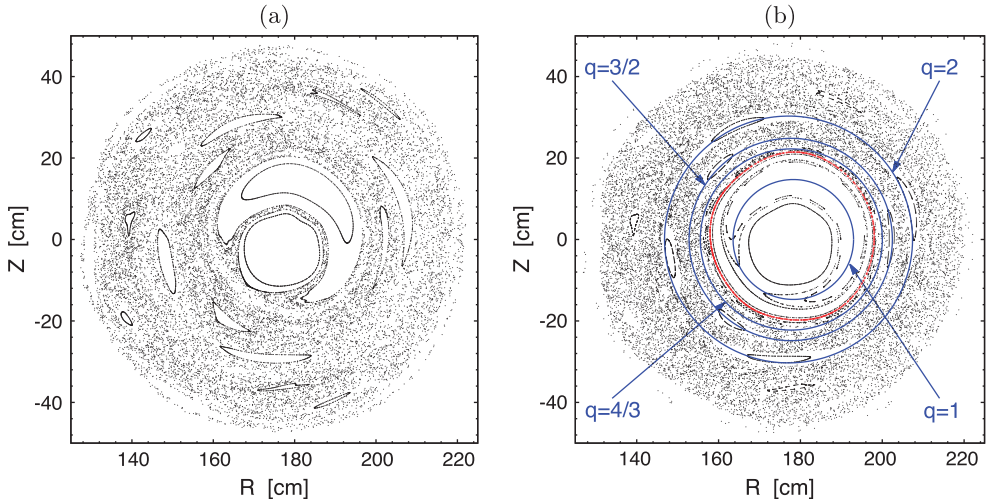

FIGURE 5. Poincaré sections of magnetic field lines in a pre-disruption plasma caused by several MHD modes: (*a*) the mode amplitudes $b_{mn} = B_{mn}/B_0$ are $(1, 1, 1, 1) \times \epsilon_{MHD}$; (*b*) $b_{mn} = B_{mn}/B_0$ are $(0.5, 1, 1, 1)\epsilon_{MHD}$. Red curve corresponds to the last intact magnetic surface, blue curves are the resonant magnetic surfaces $q = 1$, $q = 4/3$, $q = 3/2$, and $q = 2$, respectively. The dimensionless perturbation parameter $\epsilon_{MHD} = 1.5 \times 10^{-4}$. The plasma current is $I_p = 0.35$ MA, the toroidal field is $B_0 = 2.5$ T, and the safety factor at the magnetic axis is $q(0) = 0.8$.

not lead to a global stochasticity. The radial transport of particles from the confined area can take place only due to small-scale turbulent fluctuations and therefore it has a much smaller rate than those in the stochastic zone. The confinement time of these electrons is sufficiently long enough for them to be accelerated by the inductive electric field, thus creating a RE beam. The modelling of the current of this confined plasma will be discussed in § 5.

Monotonic radial profile of $q(\rho)$: *the case* $q(0) > 1$. In this case the $m/n = 1/1$ mode does not play a significant role in the formation of the stochastic zone in the plasma centre. However, the m/n modes with $n \geqslant 3$ contribute greatly to the growth of the stochastic zone and shrinkage of the intact magnetic surface ρ_c. The examples of such stochastic magnetic fields are shown in figure 6(*a*,*b*) corresponding to the values $q(0) = 1.1$ and $q(0) = 1.2$, respectively.

The outward drift velocity v_{dr} of such RE beams is significantly larger than the one in the case $q(0) < 1$. This is because of the smaller RE beam radius ρ_c and the higher toroidal electric field E_φ. Such RE beams decay in shorter times.

Plasma with reversed magnetic shear. In this case the safety factor $q(\rho)$ has a minimal value located at the normalized radius $\rho_m/a \sim 0.4$–0.6 and increases towards the centre and the plasma edge. Figure 7(*a*,*b*) show an example of the non-monotonic radial profile of the safety factor $q(\rho)$ and the corresponding Poincaré section of stochastic magnetic field lines (a more detailed description of this case is given in § 7.3 of the Supplementary Part). The intact magnetic surface located near the shearless magnetic surface (red curve), i.e. the magnetic surface with a minimal value of the safety factor $q(\rho)$, is not broken even at the relatively large magnetic perturbations. And, it confines electrons in the central plasma region.

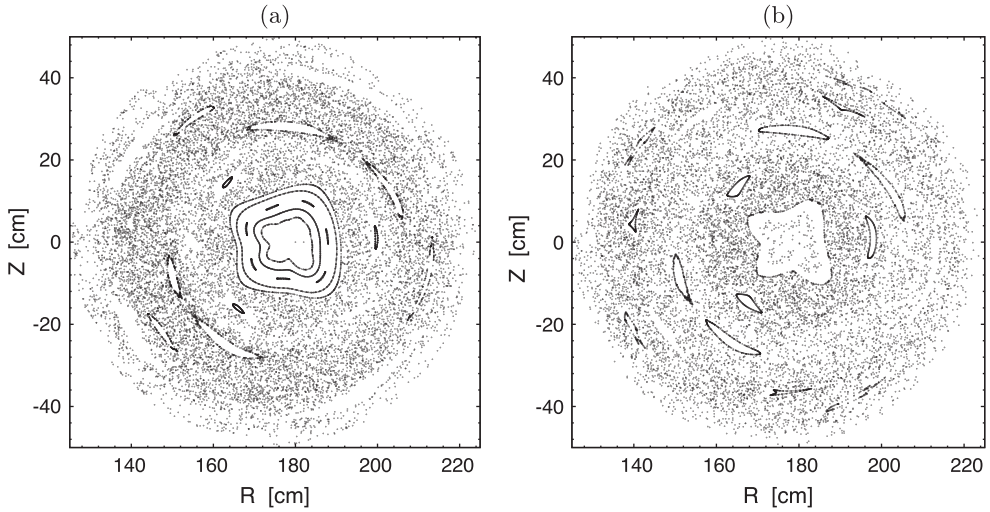

FIGURE 6. The same as in figure 5 but for the case $q(0) > 1$: (*a*) $q(0) = 1.1$; (*b*) $q(0) = 1.2$. It is assumed that the magnetic perturbation contains the m/n modes ($n = 1$–3, $m = 1$–8) with equal amplitudes. The dimensionless perturbation parameter $\epsilon_{MHD} = 1.0 \times 10^{-4}$. The plasma parameters are the same as in figure 5.

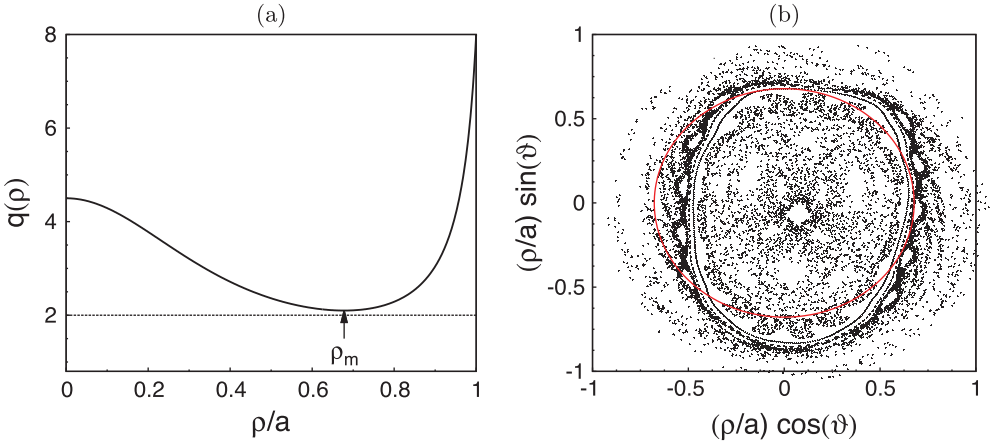

FIGURE 7. (*a*) Radial profiles of the safety factor $q(\rho)$ in the plasma with the reversed magnetic shear. (*b*) Poincaré sections of magnetic field lines in a pre-disruption plasma caused by several MHD modes. Red curve corresponds to the shearless magnetic surface.

Due to the relatively large confined area, the RE beam would carry a large current $I_p^{(RE)}$. According to (3.2), the decay rate of this RE beam owing to the outward drift would be small. This effect probably explains the large RE current with a long lifetime observed in the TFTR tokamak during the disruption of plasmas with the reversed magnetic shear (Fredrickson *et al.* 2015).

3.3. *Experimental evidences*

Existence of the finite interval of the RE currents $I_p^{(RE)}$. It follows from the conjecture above that the RE current $I_p^{(RE)}$ is mainly determined by the current distribution $I_p(\rho)$

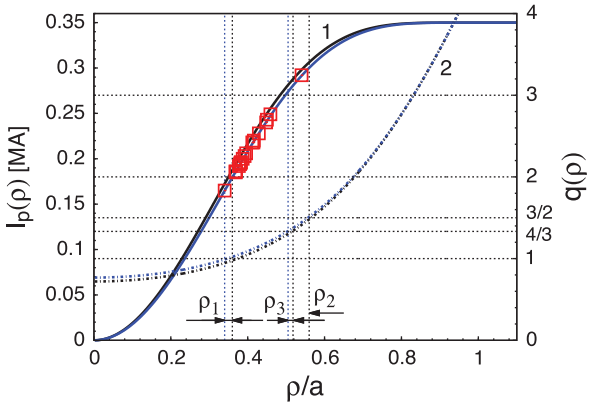

FIGURE 8. Radial profile of the plasma current $I_p(\rho)$ (3.1) (solid curves 1 on left-hand side axis) and the corresponding safety factor profile $q(\rho)$ (dotted curves 2 on right-hand side axis). The rectangular (red) dots correspond to the experimentally measured values of $I_p^{(RE)}$ for several TEXTOR discharges. The plasma parameters are $I_p = 350$ kA, $B_0 = 2.4$ T, $R_0 = 1.75$ m, and $a = 0.46$ m. The values of $q_0 = q(0)$ are 0.75 and 0.8, respectively. The radii ρ_1, ρ_2, and ρ_3 are the positions of the rational magnetic surfaces $q(\rho_1) = 1$, $q(\rho_2) = 3/2$, and $q(\rho_3) = 4/3$, respectively.

in the pre-disruption plasma confined by the intact magnetic surface ρ_c, i.e. $I_p^{(RE)} \approx I_p(\rho_c)$. Since ρ_c is located between the magnetic surfaces ρ_1 and ρ_3 corresponding to $q(\rho_1) = 1$ and $q(\rho_3) = 4/3$, the RE current $I_p^{(RE)}$ should be in a finite range. This expectation is in line with the experimental data presented in figure 4. One can see that the range of stable $I_p^{(RE)}$ values shown in figure 4(*b*) corresponds well to the space between resonant magnetic surfaces with $q(\rho_1) = 1$ and $q(\rho_3) = 4/3$ (or $q(\rho_2) = 3/2$). In figure 8, the radial profile of the pre-disruption plasma current $I_p(\rho)$ and the corresponding safety factor profile $q(\rho)$ are plotted. Also, values of $I_p^{(RE)}$ found in other experiments on TEXTOR, see Zeng *et al.* (2013), lie in the same range.

Since the q-value on the plasma axis $\rho = 0$ is one of the major causes for uncertainties in the $q(\rho)$-profile, in figure 8 we show I and q profiles for $q(0) = 0.75$ and $q(0) = 0.8$. These are in the range of $q(0)$-values experimentally measured between sawtooth crashes in the TEXTOR tokamak (Soltwisch and Stodiek 1987; Soltwisch *et al.* 1987) (see also Wesson (2004, p. 372)). The values of $q(0)$ measured after pellet injection in the DIII-D tokamak experiments are also close to these values (Izzo *et al.* 2012). Thus, small changes in $q(0)$ still keep the RE currents $I_p^{(RE)}$ in the interval $\rho_1 < \rho < \rho_3$. The highest and lowest values of $I_p^{(RE)}$ shown in figure 8 corresponding to the discharges nos 117 859 and 120 140, respectively, lie at the border of the region $\rho_1 < \rho < \rho_3, \rho_2$. They have the shortest duration time for the RE current decay (see table 1 and figures 1*b* and 4). The presence of several low-order $m/n = 4/3$, $m/n = 3/2$, and $m/n = 1/1$ resonant magnetic surfaces within the RE beam may lead to excitations of the corresponding MHD modes. The interactions of these modes may lead to the quick loss of REs due to the formation of a stochastic zone at the edge of the RE beam (see § 7).

Dependence on the level of magnetic perturbations. The existence of the intact magnetic surface ρ_c between the $q = 1$ and $q = 5/4$ (or $q = 4/3$) rational magnetic surfaces and its location depend on the level of the magnetic perturbation ϵ_{MHD}

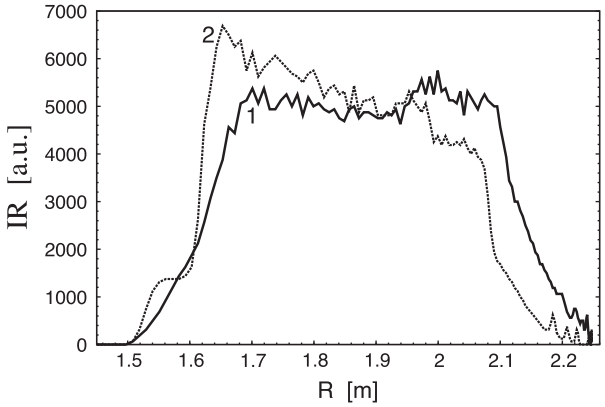

FIGURE 9. Radial profiles of the synchrotron radiation at the equatorial plane $z = 0$: curve 1 corresponds to the discharge no. 117 507 at the time instant $t = 2.034324$ s and curve 2 to no. 120 134 at $t = 2.050284$ s.

(more exactly, on the spectrum B_{mn}). With increase of ϵ_{MHD} the radius ρ_c shrinks and it can be broken at a certain critical perturbation level ϵ_{cr}. It leads to the total destruction of the confinement of plasma particles. This is in agreement with experimental observations on the existence of a critical magnetic perturbation level above which the runaway beams are not formed (Zeng *et al.* 2013).

The shrinkage of ρ_c with increasing magnetic perturbation ϵ_{MHD} leads to the decrease of the RE current $I_p^{(RE)}$, since $I_p^{(RE)} \approx I_p(\rho_c)$. On the other hand, if one assumes that the plasma current decay is caused by the radial transport of particles in the stochastic magnetic field, its decay rate $\mathrm{d}I_p/\mathrm{d}t$ should be proportional to the square of the magnetic perturbation level ϵ_{MHD}, $|\langle \mathrm{d}I_p/\mathrm{d}t\rangle| \propto |\epsilon_{MHD}|^2$ (see § 4.2). Therefore, one expects that the higher values of $|\langle \mathrm{d}I_p/\mathrm{d}t\rangle|$ correspond to the lower values of the RE current $I_p^{(RE)}$. This expectation is in agreement with the experimental values of these quantities presented in figure 4(*a*).

Synchrotron radiation pattern. The formation of the RE beam inside the intact magnetic surface can also be confirmed by the spatial profiles of the synchrotron radiation of high-energy REs with energies exceeding 25 MeV. Figure 9 shows the radial profiles of infrared radiation of the REs at the equatorial plane $z = 0$ for the two TEXTOR discharges. One can see that radiation is localized inside a finite radial extent corresponding to the central region of the plasma within the $q = 4/3$ magnetic surface (see figure 5*b*). One should note that the radiation from the plasma edge regions, $1.5 \lesssim R \lesssim 1.6$ and $2.1 \lesssim R \lesssim 2.2$, is due to thermal radiation of the wall elements. The outward shift of the radiation pattern is explained to some extent by the drift of RE beams discussed in § 6.1.

Another indication of the formation of a confined plasma beam is the rise of the temperature at the initial stage of the beam formation, as seen in the ECE signals shown in figure 1(*a*,*b*). It may occur due to the ohmic heating of confined plasma by the induced toroidal electric field or by superthermal emission from high-energy electrons. As thermal electrons are converted into runaway ones, the beam temperature goes down.

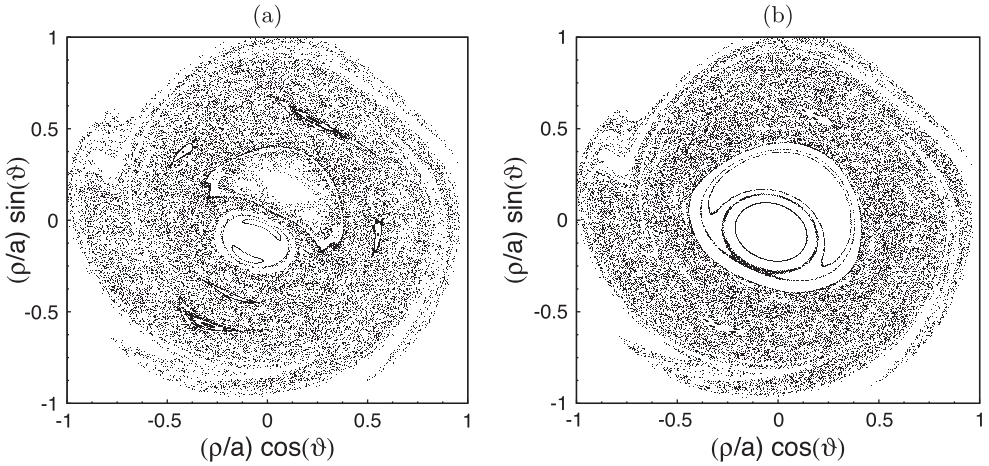

FIGURE 10. Poincaré sections of field lines in a pre-disruption plasma caused by several MHD modes: (*a*) runaway-free discharges; (*b*) with REs. The dimensionless MHD mode amplitudes are $\epsilon_{mn} = 8.68 \times 10^{-3} b_{mn}$ with $b_{mn} = 1$ for all modes in (*a*), and $b_{11} = 1/4$, $b_{mn} = 1$ for all other modes ($n = 1, 2$, $m =$ 1–5) in (*b*). The safety factor at the magnetic axis is $q(0) = 0.8$ and at the plasma edge $q_a = 4.7$.

4. Thermal and current quench stages

Our analysis in § 2.1 reveals that both the processes induced directly by injected atoms and strong radial transport along stochastic magnetic field lines created by MHD perturbations can lead to heat losses from the plasma in the TQ stage of disruption. During this stage the temperature drops on a time scale of several hundreds of microseconds; the current decay time is 4–6 ms in RE-free discharges and increases up to 0.1 s in discharges with RE generations.

As one can see in figure 1, the CQ stage before the formation of RE beams coincides well with the time interval where magnetic perturbations are significant and the particle transport in a stochastic magnetic field leads to the current decay. To study these processes, we use the models for stochastic magnetic field and collisional transport of test particles described in § 7 of the Supplementary Part.

Figure 10(*a*,*b*) show the typical Poincaré sections of field lines of this model in the runaway-free disruption case (*a*) and the case with RE generation (*b*). The perturbation amplitudes ϵ_{mn} of all MHD modes, except the ($m = 1, n = 1$) mode, correspond to a twice larger value of ϵ_{MHD} than the case shown in figure 5. For the ($m = 1, n = 1$) mode ϵ_{mn} corresponds to the same value of ϵ_{MHD}. The relation between ϵ_{mn} and ϵ_{MHD} is $\epsilon_{mn} = \epsilon_{MHD} b_{mn}/\Psi_a$, where Ψ_a is the toroidal magnetic flux at the plasma edge (see § 7 of the Supplementary Part).

In general, the transport of heat and particles in the presence of RMPs is a three-dimensional problem. Particularly, a stochastic magnetic field with the topological structures like ones in figure 10 leads to poloidally and toroidally localized heat and particle deposition patterns on the wall (Kruger *et al.* 2005). This is a general feature of open chaotic systems, which has been observed in ergodic divertor tokamaks (see e.g. Finken *et al.* 2005; Jakubowski *et al.* 2006 and Abdullaev 2014). The problem can be simplified when we are interested only in the radial transport rate. It can be done by introducing the radial diffusion coefficient averaged over a poloidal angle.

4.1. *Heat transport*

The electron heat conductivity in a stochastic magnetic field has been assessed by diverse approaches. We apply here the following formula for the electron heat diffusion χ_r deduced on the basis of simulations for transport of test particles, by taking into account coulomb collisions with background plasma species (Abdullaev 2013) (see also § 10.4 in Abdullaev 2014):

$$\chi_r(\rho, T_e) = \frac{v_\parallel D_{FL}(\rho)}{1 + L_c/\lambda_{mfp}}, \tag{4.1}$$

where $v_\parallel \approx v_{T_e} = 1.33 \times 10^7\, T_e^{1/2}$ is the thermal velocity of electrons, $D_{FL}(\rho)$ is the diffusion coefficient of field lines ($D_{FL}(\rho) \sim 10^{-5}$–$10^{-4}$ m), $\lambda_{mfp} = 8.5 \times 10^{21}\, T_e^2(\rho)/n(\rho)$ is the mean free path length of electrons with the temperature T_e and density $n(\rho)$ measured in keV and m^{-3}, respectively, and $L_c \approx \pi q(\rho) R_0$ is the characteristic connection length.

A characteristic heat diffusion time one can estimate as $\tau_H = a^2/2\chi_r$, where for χ_r we assume its magnitude at the radial position $\rho = 0.566a$. Before the disruption, the local temperature here is 0.6 keV. This provides $\chi_r = 287\ \mathrm{m}^2\ \mathrm{s}^{-1}$ and $\tau_H = 3.68 \times 10^{-4}$ s, i.e. of the order of the experimentally observed time, for the plasma temperature drop during the TQ after disruption.

For a quantitative analysis, we have modelled the time evolution of the radial profile for the electron temperature averaged over the poloidal θ and toroidal φ angles, $T(\rho, t)$. This is done by solving numerically the following diffusion equation:

$$\frac{\partial T}{\partial t} = \frac{1}{\rho}\frac{\partial}{\partial \rho}\left[\rho \chi_r(\rho, T)\frac{\partial T}{\partial \rho}\right], \tag{4.2}$$

where the heat diffusivity is given by (4.1) and the applied boundary conditions are: $\partial T(\rho)/\partial\rho = 0$ at $\rho = 0$ and $\partial T(\rho)/\partial\rho = -T/\delta_T$ at the plasma edge $\rho = a$, where $\delta_T \simeq 0.1$ m is the characteristic e-folding length for the temperature decay in the scrape-off layer.

Below we consider an example of heat transport in a fully chaotic magnetic field shown in figure 10(*a*). Figure 11(*a*,*b*) show the radial profiles of the heat conductivity and the temperature at different times. One can see in this case that the temperature drops and almost flattens within a time interval of order 0.5 ms.

In the situation with a partially stochastic magnetic field, see figure 10(*b*), anomalous turbulent transport in the very plasma core, $\rho \leqslant 0.3$, with intact magnetic surfaces is two orders of magnitude smaller than in the outer region. In this case the temperature drop in the central plasma region could be explained by the effect of parallel transport in the magnetic island created by the $m/n = 1/1$ MHD mode and some level of stochastization in a thin layer near the island separatrix (see a review by Schüller 1995 for more details).

4.2. *Current quench stage*

As was discussed in § 3.3, the current decay rate $\langle \mathrm{d}I_p/\mathrm{d}t\rangle$ depends on the initial RE current $I_p^{(RE)}$, which in turn depends on the level of magnetic perturbations. Therefore, one can assume that the current decay rate $\langle \mathrm{d}I_p/\mathrm{d}t\rangle$ may implicitly depend on the level of magnetic perturbations. This assumption, however, may contradict the traditional view that the current decay rate is determined by the time $\tau_{CQ} = R/L$, i.e. by the ratio of the plasma resistivity R to its inductance L: $\mathrm{d}I_p/\mathrm{d}t = -I_p/\tau_{CQ}$.

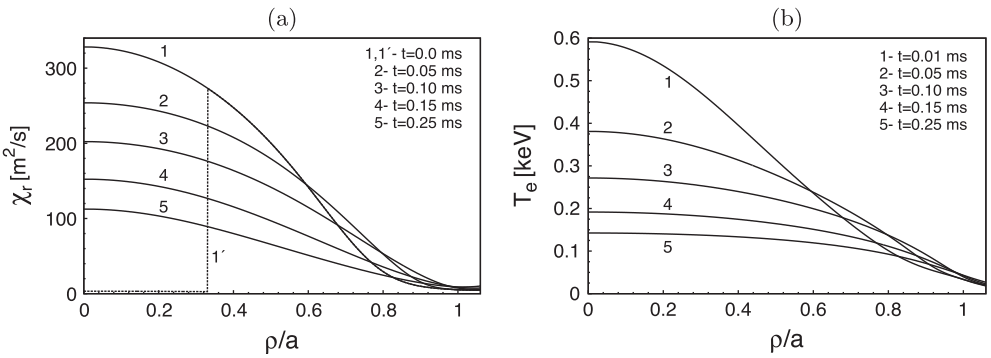

FIGURE 11. Radial profiles of the electron heat conductivity $\chi_r(\rho, t)$ computed according to (4.1), (*a*), and of the electron temperature averaged over toroidal and poloidal angles, $T_e(\rho, t)$, found by solving the heat conduction equation (4.2) numerically, (*b*), at different time moments after the disruption initiation.

In the simplest case when R and L are constants, it leads to the exponential decay law $I_p(t) \propto \exp(-t/\tau_{CQ})$. However, in many tokamaks, particularly in the TEXTOR tokamak, the current decay evolution is better fitted by the linear function $I_p = a - bt$ rather than by the exponential function (see figure 3). At present, the reason for such a dependence is not quite clear. So, other mechanisms may also play a role in the CQ (see e.g. Kadomtsev 1984; Gerhardt *et al.* 2009; Shibata *et al.* 2010 and references therein).

Particularly, one cannot exclude that the poloidal and toroidal variations of the plasma current imposed by the initial MHD modes in the TQ stage do not disappear immediately with the temperature drop (see also § 5 and (5.1) and (5.5)). This leads to the corresponding variations of the poloidal magnetic field, which acts as non-axisymmetric magnetic perturbations. Below we discuss a possible role of the radial transport of particles in a stochastic magnetic field created by such magnetic perturbations.

The magnetic field structure before the CQ has been assumed similar to the one shown in figure 10. The level of magnetic perturbations may be different from that during and after the TQ when strong magnetic fluctuations are present; see figure 1(*d*).

One should note that according to the mechanism of RE beam formation discussed above in § 3.1, at the CQ stage the plasma current is carried mainly by thermal electrons. The contribution of REs to the plasma current at this stage is still small. Those REs created outside the outermost intact magnetic surface ρ_c are quickly lost due to the fast transport along chaotic field lines. Electrons in the central plasma region $\rho < \rho_c$ confined by the outermost intact magnetic surface are sources for the RE beam.

The time scale of the current decay is determined by the rate of radial particle transport in a stochastic magnetic field. This process has an ambipolar nature and it is strongly collisional due to the low plasma temperature. On the other hand, one expects that the toroidal electric field induced by the current decay also strongly affects the particle transport. Below we give a rough estimation of the particle transport rate based on the collisional test particle transport model.

In table 2, we have listed the ambipolar diffusion coefficients D_p and the characteristic diffusion times τ_{CQ} of particles at the different plasma temperatures

T_i (keV)	D_p (m^2 s^{-1})	$\tau_{CQ} = a^2/2D_p$ (s)
0.005	0.0986057	1.072
0.050	0.386249	2.739×10^{-1}
0.100	1.01251	1.045×10^{-1}
0.500	6.46228	1.637×10^{-2}
1.000	9.51915	1.111×10^{-2}
2.000	13.1030	8.074×10^{-3}
4.000	17.8366	5.932×10^{-3}
5.000	23.7424	4.456×10^{-3}
10.00	27.0265	3.915×10^{-3}

TABLE 2. Ambipolar diffusion coefficients D_p of particles and the diffusion times $\tau_{CQ} = a^2/2D_p$ from the stochastic zone at the different effective plasma temperatures. The plasma radius $a = 0.46$ m.

in a stochastic magnetic field shown in figure 10. The typical plasma temperature after the TQ is about from 5 to 50 eV. The average particle confinement time τ_{CQ} at this temperature changes from 1 to 0.3 s. These time scales are shortened if the magnetic perturbation level ϵ^2 is larger. Since the diffusion coefficient $D_p \propto \epsilon^2$ and therefore $\tau_{CQ} \propto \epsilon^{-2}$, τ_{CQ} can be reduced to one order smaller value for three times larger perturbation than in figure 10. This time scale is still much longer than the experimentally observed values. However, this collisional model does not take account of the effect of the inductive toroidal electric field. One expects that the acceleration of electrons and ions by the electric field increases the radial transport of particles. To include this effect in the collisional model, one can assume that the effective temperature of the plasma is higher than the measured one. The particle diffusion time τ_{CQ} for the effective temperature 2 keV is about 8×10^{-3} s. This time scale gives the average current decay rate $|\mathrm{d}I_p/\mathrm{d}t| \approx \Delta I_p/\tau_{CQ} \sim I_p^{(0)}/\tau_{CQ} = 0.35$ MA$/(8.0 \times 10^{-3}$ s$) \approx 44.0$ MA s^{-1}, which is of the order of the experimental measured rates given in table 1. (Here $I_p^{(0)}$ is the full pre-disruption plasma current.)

A more rigorous approach to the particle transport in a stochastic magnetic field during the current decay stage would require a three-dimensional treatment of the problem. It should take into account not only the formation of the ambipolar electric potential (Spizzo *et al.* 2014) but also the inductive toroidal electric field which accompanies the process. The latter may lead to the directionality of the particle transport that eventually may influence the random vertical displacement of runaway beams. Of course, the study of these complicated processes is beyond the scope of the present work.

5. Modelling of post-disruption plasma

The described scenario of plasma disruption with a RE beam allows one to model a post-disruption plasma. After establishing the runaway beam the current is localized inside the area enclosed by the last intact magnetic surface. In general, the distribution of the current density j would depend not only on the radial coordinate ρ but also vary along the poloidal θ and the toroidal φ angles due to the presence of the $m/n = 1/1$ magnetic island. In such a post-disruption plasma the toroidal current density can be presented as a sum of two parts,

$$j_\varphi(\rho, \theta, \varphi) = j_0(\rho) + j_1(\rho, \theta, \varphi), \tag{5.1}$$

where $j_0(\rho)$ is the current density depending only on the radial coordinate ρ and $j_1(\rho, \theta, \varphi)$ is the helical current, which is a periodic function of the poloidal θ and toroidal φ angles.

The radial dependence of $j_0(\rho)$ can also be modelled by assuming that after the disruption the current is uniformly distributed over the confined area with a steep gradient at the beam edge ρ_c. Calculations show that electron orbits do not significantly depend on the specifics of the radial profile of $j_0(\rho)$. For our calculations of GC orbits, we choose the following profile:

$$j_0(\rho) = \begin{cases} J_0 \tanh[(\rho_c^2 - \rho^2)/\Delta_a], & \text{for } \rho < \rho_c, \\ 0, & \text{for } \rho > \rho_c, \end{cases} \tag{5.2}$$

where J_0 is a constant determined by the full current of the beam $I_p^{(RE)}$ and Δ_a is the steepness parameter. The current flowing inside the magnetic surface ρ, i.e. $I_p(\rho) = 2\pi J_0 \int_0^\rho j_0(\rho')\rho' \, \mathrm{d}\rho'$, is given by

$$I_p(\rho) = \begin{cases} I_p^{(RE)} \left[1 - \dfrac{\ln\cosh([\rho_c^2 - \rho^2]/\Delta_a)}{\ln\cosh(\rho_c^2/\Delta_a)}\right], & \text{for } \rho \leqslant \rho_c, \\ I_p^{(RE)}, & \text{for } \rho > \rho_c, \end{cases} \tag{5.3}$$

where $I_p^{(RE)}$ is the full current of the confined area.

One should also note the fact that after the TQ the plasma beam is shifted inwardly because of drop of plasma pressure. In the modelling this fact can be taken into account by assuming that the radial position of the centre R_a of the post-disruption plasma is different from the one of the pre-disruption plasma. The safety factor of the corresponding plasma is then given by

$$q(\rho) = q_{cyl}(\rho) C(\rho/R_a), \quad q_{cyl}(\rho) = \frac{2\pi\rho^2 B_0}{\mu_o R_a I_p(\rho)}, \tag{5.4}$$

where $q_{cyl}(\rho)$ is the safety factor of the cylindrical plasma; the function $C(x) = 1 + A_1 x + A_2 x^2 + \cdots$ is a function which takes into account the toroidicity of the plasma. The coefficients A_i, $(i = 1, 2, \ldots)$ depend on the plasma pressure (Abdullaev *et al.* 1999; Abdullaev 2006).

Figure 12 shows the radial profiles of $I_p(\rho)$ (solid curves 1–3 on the left-hand side axis) (5.3) and the safety factor (5.4) (dashed curves 1′–3′ on the right-hand side axis) for the three discharge parameters, respectively. Solid black curve 4 corresponds to the pre-disruption plasma current profile. We set the toroidal field magnitude $B_0 = 2.4$ T and the beam centre at $R_a = 1.7$ m. The plasma radius a is found from the condition $I_{p0}(a) = I_p^{(RE)}$, where $I_{p0}(r)$ is the current profile of the pre-disruption plasma. The vertical dashed colour arrows show the radial positions of the $q = 1$, $q = 4/3$, and $q = 3/2$ magnetic surfaces and the vertical solid arrows indicate the plasma radii a.

Note that the red curves 1 and 1′ and the green curves 3 and 3′ in figure 12 correspond to the discharges with the lowest and highest values of $I_p^{(RE)}$ shown in figure 1(*b*). For the lowest value of $I_p^{(RE)}$, the radial position of the $q = 1$ magnetic surface is very close to the RE beam radius ρ_c. For the highest value of $I_p^{(RE)}$, the magnetic surfaces with $q = 1$, $q = 4/3$, and $q = 3/2$ are located inside the plasma

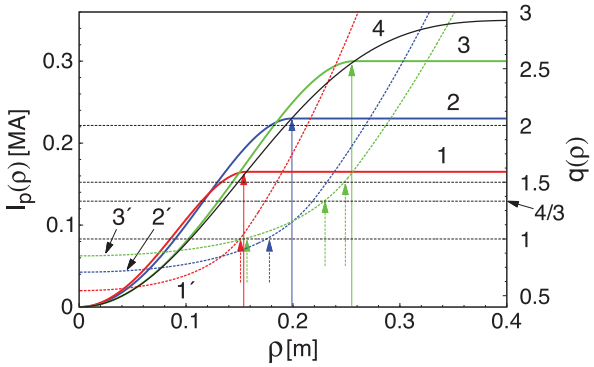

FIGURE 12. Radial profiles of the plasma current $I_p(\rho)$ (5.3) (solid curves 1–3 on left-hand side axis) and the safety factor profiles $q(\rho)$ (5.4) (dashed curves 1′–3′ on right-hand side axis); curve 4 corresponds to the pre-disruption plasma current. The red curves 1 and 1′ correspond to $I_p^{(RE)} = 165$ kA, blue curves 2 and 2′ correspond to $I_p^{(RE)} = 230$ kA, and green curves 3 and 3′ correspond to $I_p^{(RE)} = 300$ kA. The vertical solid arrows indicate the radii of the plasma beam a, the vertical dashed arrows indicate the positions of resonant magnetic surfaces $q = 1$ and $q = 3/2$. The toroidal magnetic field $B_t = 2.4$ T, $R_a = 1.7$ m, the pre-disruption plasma current $I_p = 350$ kA, and the radius $a_0 = 0.46$ m.

region $\rho < a$. However, the radial position of the magnetic surface $q = 3/2$ is at the plasma edge. For the typical discharges like the one shown by blue curves, the magnetic surface $q = 1$ is located relatively far from the plasma edge.

The Fourier expansion of the helical current, $j_1(\rho, \theta, \varphi)$,

$$j_1(\rho, \theta, \varphi) = \sum_{m,n} j_{mn}(\rho) \cos(m\theta - n\varphi + \phi_{mn}), \tag{5.5}$$

is mainly dominated by the $m/n = 1/1$ component. This assumption is based on the analysis of numerous disruptions in the JET tokamak (Gerasimov *et al.* 2014).

We should assume that the value of the safety factor at the beam axis $q(0)$ is less than unity. This assumption is supported by a number of experimental measurements of the current profile after the sawtooth crashes in the TEXTOR, TFTR, and JET tokamaks (Soltwisch *et al.* 1987; O'Rourke 1991; Yamada *et al.* 1994; Soltwisch and Koslowski 1995; Koslowski *et al.* 1996; Soltwisch and Koslowski 1997).

This model of the post-disruption plasma current describes only the initial stage of the RE beam. During acceleration of electrons in the toroidal electric field the RE orbits drift outward and their form evolves from a circular one to an oval one. This process changes in turn the RE beam form and its current. The self-consistent description of the time evolution of the RE beam is a difficult problem. It is beyond the scope of the present study.

6. Evolution of GC orbits during acceleration

Now we discuss the dynamics of RE orbits during the acceleration of electrons induced by the toroidal electric field in a toroidal post-disruption plasma. Mainly we study the outward drift of RE orbits and its role in the RE losses. However, we will not consider the processes of the generation and the proliferation of the RE population, the problems of stability of RE beams, and related issues. These problems have been much discussed in the literature.

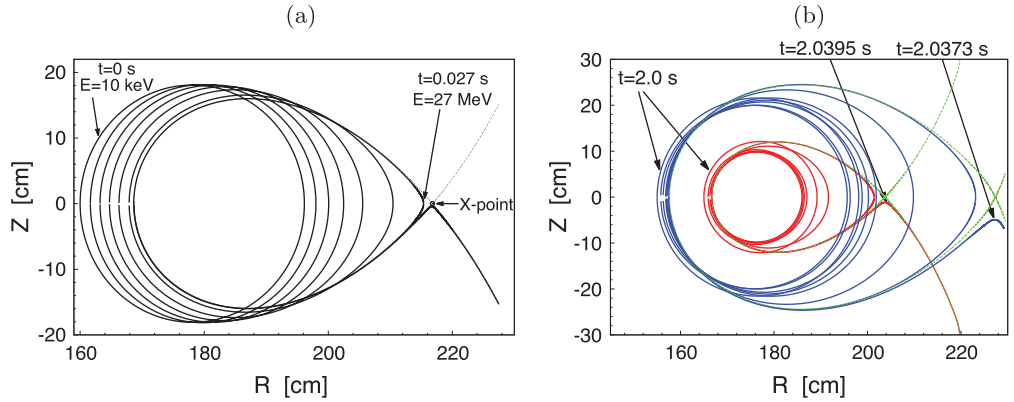

FIGURE 13. (*a*) Evolution of the GC orbit of accelerating electrons in the (R, Z)-plane at the constant plasma current $I_p = 100$ kA in the presence of a constant toroidal electric field with $V = 40$ V. Dashed curve corresponds to the separatrix of GC orbits of the electrons of energy $E = 27$ MeV. (*b*) The same as in (*a*) but for the two GC orbits of accelerating electrons for the time-varying current $I_p(t)$ and the loop voltage $V(t)$ corresponding to the TEXTOR discharge no. 117 527. Green curves correspond to the separatrices of GC orbits.

6.1. *Outward drift of RE orbits*

First we consider the case of an axisymmetric plasma beam neglecting the helical magnetic perturbations. The inductive toroidal electric field generated due to the current decay during the plasma disruption accelerates thermal electrons. This is an adiabatic process, since the characteristic time of significant variation of energy is much larger than the transit time of electrons. Therefore, the GC orbit slowly drifts outward without changing the area of the GC orbit in the poloidal plane, which is an adiabatic invariant J, or the action variable (see § 6.1 of the Supplementary Part). With increasing electron energy the topology of GC orbits also slowly changes from the circular one to the oval one. Starting from a certain critical energy E_{cr} the adiabaticity of the process breaks and the GC orbit bifurcates by creating an unstable stagnation point (or X-point) inside the plasma region. With the further increase of energy the GC orbit crosses the separatrix (a homoclinic orbit associated with the X-point) and becomes unconfined. The value E_{cr} depends on the plasma current I_p. The described phenomenon is an addition mechanism of confinement loss of REs. Figure 13(*a*) shows a typical evolution of a GC orbit in the presence of the toroidal electric field with the constant beam current $I_p = 100$ kA and the loop voltage $V = 40$ V.

One should note that the formation of the separatrix of RE GC orbits during the acceleration process in tokamaks has been first predicted in Zehrfeld *et al.* (1981). The numerical study of this process in a realistic tokamak configuration has been carried out in Wongrach *et al.* (2014). Particularly, it was shown that with increasing electron energy the area confined by the separatrix decreases and it vanishes when the energy exceeds a certain critical value $\mathcal{E}_{cr}$, i.e. such electrons cannot be confined. The critical energy $\mathcal{E}_{cr}$ is proportional to the square root of the plasma current I_p, $\mathcal{E}_{cr} \propto \sqrt{I_p}$.

The described evolution of RE orbits is in agreement with the experimental observation of the infrared radiation patterns observed in the experiment in the

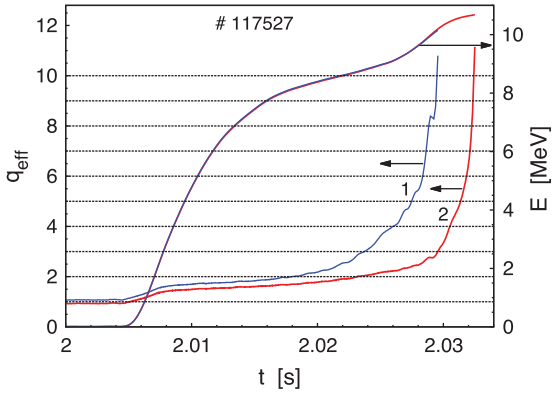

FIGURE 14. Time evolution of the effective safety factors q_{eff} (left-hand side axis) and electron energies (right-hand side axis) during the acceleration in the discharge no. 117 527. Blue curves correspond to the orbit launched at the coordinate ($R = 160$, $Z = 0$) cm and red curves to the one with ($R = 165$, $Z = 0$) cm. Horizontal lines correspond to $q(t) = m$, where $m = 1, 2, \ldots$ are integers.

TEXTOR tokamak (Wongrach *et al.* 2014) and in the DIII-D tokamak (Hollmann *et al.* 2013). The observations clearly show the evolution of the spatial form of RE beams from crescent ones into oval ones with increasing electron energies.

An example of the time evolution of GC orbits in the plasma beam with a time-varying current $I_p(t)$ and the loop voltage $V(t)$ corresponding to the TEXTOR discharge no. 117 527 is shown in figure 13(*b*). To simplify the calculations of orbits, we have assumed that the loop voltage $V(t)$ is uniform in the poloidal section, i.e. it does not depend on the radial coordinate r and is equal to the experimentally measured value at the limiter. However, this assumption only approximately describes the situation. To find the exact magnitude of the toroidal electric field during the runaway current decay one should solve the corresponding Maxwell equations.

One of the important parameters of the GC orbit is the effective safety factor q_{eff}, defined as a ratio $q_{eff} = \Delta\varphi/2\pi$, where $\Delta\varphi$ is the increment of the toroidal angle φ per one poloidal turn. It is a function of the action variable J and particle energy E. For low-energy electrons the quantity $q_{eff}(J, E)$ coincides with the safety factor $q(\rho)$ of the equilibrium magnetic field. With increasing electron energy the effective safety factor strongly deviates from $q(\rho)$. With RE energy E approaching the critical one E_{cr} it diverges as

$$q_{eff}(J, E) \propto -\ln|E - E_{cr}|. \tag{6.1}$$

Figure 14 shows the typical time evolutions of the effective safety factors q_{eff} of two GC orbits during the electron acceleration in the conditions of the TEXTOR discharge no. 117 527.

Figure 15 shows the time evolution of the outward drift velocity v_{dr} calculated numerically for the three different RE beam currents. It is quite well described by the formula derived in Abdullaev (2015) (see also § 4 of the Supplementary Part)

$$v_{dr} = \frac{R_0 E_\varphi}{R B_z^*}\left(1 - \frac{R T_{av}}{R_0 T}\right), \tag{6.2}$$

where $B_z^* = B_z + F(E)$ is the effective poloidal magnetic field, B_z is the z-component of the poloidal magnetic field at the equatorial plane $z = 0$, and $F(E)$ is a term depending

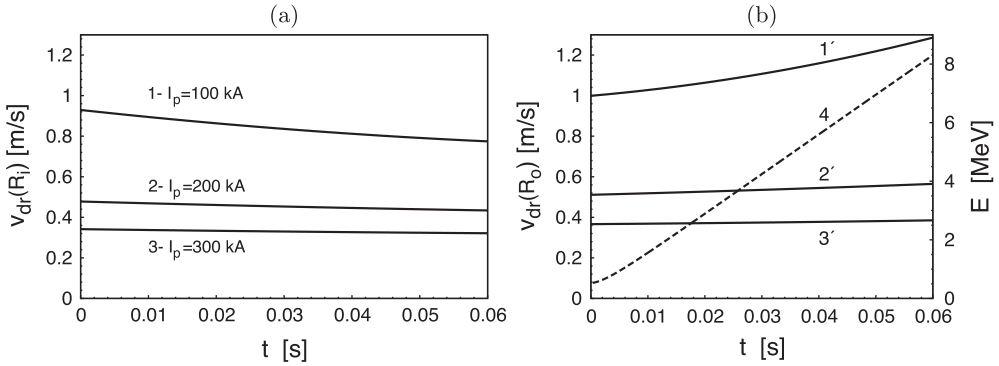

FIGURE 15. Drift velocities of innermost $v_{df}(R_i)$ (a) (curves 1, 2, and 3) and outermost $v_{df}(R_o)$ (b) (curves 1′, 2′, and 3′) points of orbits for the different plasma currents: curves 1 and 1′ correspond to the plasma current $I_p = 100$ kA, curves 2 and 2′ correspond to $I_p = 200$ kA, and curves 3 and 3′ correspond to $I_p = 300$ kA. Curve 4 describes the increase of energy E (right-hand axis). The toroidal field $B_t = 2.5$ T, major radius $R_0 = 175$ cm, minor radius $a = 46$ cm, and loop voltage $V_{loop} = 5$ V.

on the particle energy. The quantity

$$T_{av} = \frac{2\pi q_{eff} R_0}{v_\varphi} \tag{6.3}$$

is the average transit time, E_φ is the toroidal electric field strength, T is the transit time of the orbit, and v_φ is the toroidal velocity.

The expression (6.2) describes the creation of the X-point and the separatrix of RE orbits at the critical energy E_{cr}. This phenomenon is related with the appearance of zeroes of the effective poloidal magnetic field B_z^* at $E = E_{cr}$ and a certain radial distance $R = R_s$ within the plasma region (see Abdullaev 2015 for details).

At $|B_z| \gg |F(E)|$ and $T_{av} \approx T$, the formula (6.2) is reduced to

$$v_{dr} = \frac{qE_\varphi}{B_0} = -\frac{(R - R_0)E_\varphi}{RB_Z}, \tag{6.4}$$

obtained by Guan *et al.* (2010) and Qin *et al.* (2011) for the circular orbits. Here $q = (R - R_0)B_0/B_zR$ is the safety factor of the magnetic field. As seen from figure 15, the formulas (6.2) and (6.4) give the correct dependence of v_{dr} on the plasma current I_p, $v_{dr} \propto I_p^{-1}$, because $B_z \propto I_p$.

However, the formula (6.4) does not describe the situation when the GC orbits take an oval form with increasing energy similar to the ones shown in figure 13(*a*,*b*). From the latter, it follows that the average outward velocity v_{dr} of the innermost part of the orbit is approximately equal to 0.6 and 8 m s^{-1} of the outermost part of the orbit.

6.2. *RE current decay*

The rate $\mathrm{d}I_p/\mathrm{d}t$ of the runaway current loss due to the described outward drift of orbits can be roughly estimated as follows. This loss mechanism is mainly caused by the shrinkage of the beam radius ρ_c. The rate of such a shrinkage $\mathrm{d}\rho_c/\mathrm{d}t$ is of order of

the average outward velocity v_{dr}. Since $I_p \propto \rho_c^2$, we have

$$\frac{\mathrm{d}I_p}{\mathrm{d}t} = \frac{\mathrm{d}I_p}{\mathrm{d}\rho_c}\frac{\mathrm{d}\rho_c}{\mathrm{d}t} \sim \frac{2I_p}{\rho_c} v_{dr} \propto \frac{E_\varphi}{\rho_c}. \tag{6.5}$$

For the typical values of $I_p \approx 0.2$ MA, $\rho_c \approx 0.2$ m, and $v_{dr} \sim 1$ m s^{-1}, one has $\mathrm{d}I_p/\mathrm{d}t \approx$ 4 MA s^{-1}. This estimation is of order of the experimentally measured average decay rate of the runaway current listed in table 1.

Since the safety factor q, as well as q_{eff}, of RE beams is about unity, $q_{eff} \sim 1$, the outward drift may slow down for the higher values of the toroidal magnetic field B_0. However, the much higher toroidal electric field E_φ may compensate this effect, so that the decay time of RE currents in large tokamaks, like ITER, may have the same order as in smaller tokamaks.

One should also note that the outward drift velocity v_{dr} is proportional to the inverse aspect ratio of tokamaks, $v_{dr} \propto a/R_0$ (Abdullaev 2015). It means that the RE current loss due to the outward drift of orbits in spherical tokamaks would be larger than in standard tokamaks, so that the REs would cease faster. This effect could be one of the reasons of the absence of REs during disruptions in NSTX tokamaks (Gerhardt *et al.* 2009).

Besides outward orbit drifts, the RE current losses are also caused by the internal MHD mode, which will be discussed in the next section. The collisions of REs with neutral particles may also contribute to the RE losses.

7. Effect of magnetic perturbations

The effect of the magnetic perturbations on electrons in the post-disruption current beam strongly depends on its safety factor profile $q(\rho)$, the spectrum of magnetic perturbations, and the electron energy. To explain this effect, we consider a simplified version of GC motion equations in the presence of magnetic perturbations. (A rigorous consideration of this problem is given in § 6 of the Supplementary Part.)

The particle drift motion in the presence of perturbations can be represented by Hamiltonian equations similar to the equations for magnetic field lines,

$$\frac{\mathrm{d}\vartheta}{\mathrm{d}\varphi} = \frac{\partial K}{\partial J}, \quad \frac{\mathrm{d}J}{\mathrm{d}\varphi} = -\frac{\partial K}{\partial \vartheta_z}, \tag{7.1a,b}$$

with the Hamiltonian $K = K(\vartheta, J, E, \varphi)$ with the canonical variables (ϑ, J), and the toroidal φ as the time-like variable. In the absence of perturbations GC orbits wind around the drift surfaces $J = \text{const.}$ and the poloidal angle ϑ is a linear function of φ, $\vartheta = \varphi/q_{eff}(J, E) + \vartheta$. In the presence of perturbations the Hamiltonian H can be represented as a sum

$$K = \int \frac{\mathrm{d}J}{q_{eff}(J, E)} + \epsilon K_1(\vartheta_z, J, E, \varphi). \tag{7.2}$$

Since the perturbations are periodic in poloidal and toroidal angles and in time, it can be represented by a Fourier series

$$K_1(\vartheta_z, J, E, \varphi) = \sum_{mn} K_{mn}(J, E) \exp[\mathrm{i}(m\vartheta - n\varphi)]. \tag{7.3}$$

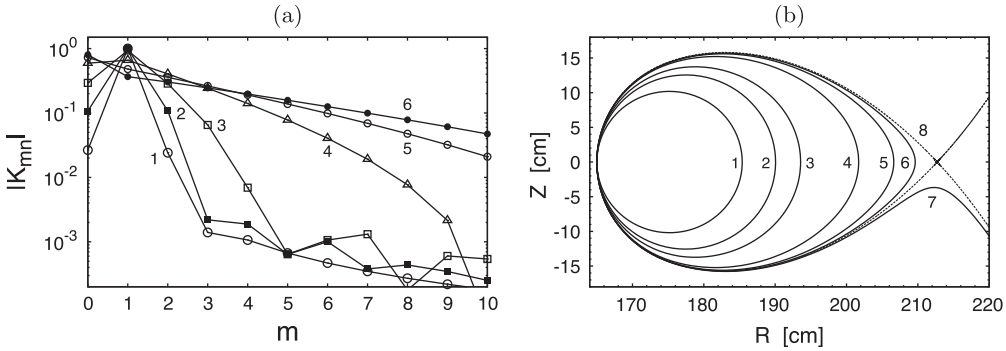

FIGURE 16. (*a*) Spectrum of perturbations K_{mn} and (*b*) corresponding RE orbits with different energies E. Curves 1–7 correspond to RE energies 10 keV, 20 MeV, 30 MeV, 40 MeV, 42 MeV, 42.5 MeV, and 42.7 MeV, respectively. Curve 8 corresponds to the separatrix with the critical energy $E_{cr} = 42.646$ MeV. The plasma current $I_p = 150$ kA, the toroidal field $B_0 = 2.5$ T, and the toroidal mode number $n = 1$.

The strongest influence of perturbations on particles takes place on the (m, n) resonant drift surfaces, i.e.

$$m = nq_{eff}(J, E), \tag{7.4}$$

originating from the (m, n) term in (7.3) with the amplitude $K_{mn}(J, E)$. They are determined by the magnetic perturbation spectrum b_{mn},

$$K_{mn}(J, E) \propto \sum_{m'} b_{m'n} \int_0^{2\pi} \mathrm{d}\vartheta \, \exp[\mathrm{i}(m\vartheta - m'\vartheta_M)], \tag{7.5}$$

where ϑ_M, the poloidal angle associated with magnetic field lines, is a function of ϑ as well as the particle energy E.

For low-energy electrons (up to 5 MeV) the spectrum of amplitudes $K_{mn}(J, E)$ weakly depends on energy E and is close to the spectrum of magnetic perturbations b_{mn} of the (m, n)th modes. With increasing energy the spectrum of perturbations $K_{mn}(J, E)$ deviates from b_{mn} and acquires more higher poloidal harmonics m. An example of the poloidal spectra of perturbations $K_{mn}(J, E)$ for different particle energies is shown in figure 16(*a*). The corresponding unperturbed orbits are plotted in figure 16(*b*). It is assumed that the magnetic perturbation contains a single $(m = 1, n = 1)$ mode. For the low-energy electrons with $E < 10$ MeV, the spectrum K_{mn} contains the predominant $m = 1$ mode.

With increasing energy the amplitudes K_{mn} of higher m also grow and the width of the poloidal spectrum K_{mn} in m becomes wider, as shown in figure 16(*b*). For the spectrum K_{mn}, one can obtain the following asymptotic formula for the orbits close to the separatrix (see § 3.4 in Abdullaev 2014)

$$K_{mn} \propto \frac{1}{q_{eff}} \exp\left(-\frac{mC}{q_{eff}}\right), \tag{7.6}$$

where C is a finite constant, and the effective safety factor q_{eff} diverges as (6.1).

As was shown in § 5 (see also figure 12), the typical values of $q(\rho)$ vary over $q(0) \approx 0.7$–0.8 at the magnetic axis and $q(a) < 1.5$ at the plasma edge. Therefore, the

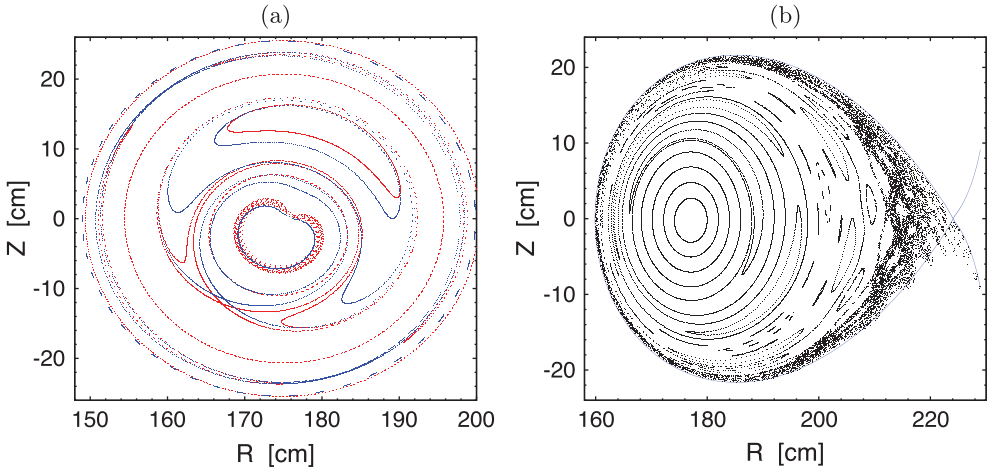

FIGURE 17. Poincaré sections of RE orbits in the (R, Z)-plane: red dots correspond to RE orbits with energies $E = 1$ MeV (a) and $E = 20$ MeV (b). [In (a) blue dots correspond to magnetic field lines, green dots is the separatrix.] The perturbation parameter $\epsilon = 10^{-5}$, the plasma current $I_p = 200$ kA (a) and $I_p = 100$ kA (b).

strongest effect of the RMPs on electron orbits may be expected if its spectrum b_{mn} contains a sufficient number of (m, n)-components that are resonant to the magnetic surfaces with q in the interval $q(0) < q = m/n < q(a)$ that would create a stochastic zone of magnetic field lines. The electrons from this stochastic layer would then be radially transported to the wall.

Below we discuss the influence of magnetic perturbations on RE orbits for two specific cases. First we consider the effect of an internal single helical magnetic field and then we analyse the effect of the external RMPs, namely, the TEXTOR-DED, on the confinement of REs.

7.1. *Effect of a single helical magnetic field*

Assume that the magnetic perturbation (3.3) contains the single $(m = 1, n = 1)$ MHD mode, as was proposed in the model of the post-disruption current beam described in § 5. For the low-energy electrons it creates a single island structure, since the deviations of their GC orbits from the magnetic surfaces is small. Such a system is *stable* because the single MHD mode does not create stochasticity of magnetic field lines. An example of this case is shown in figure 17(a) by the Poincaré sections of RE orbits (red dots) and magnetic field lines (blue dots).

With increasing energy of the electrons and decreasing beam current the electrons' GC orbits strongly deviate from the magnetic field lines. The effective safety factor q_{eff} of the GC orbit increases as the electron energy grows, as was shown in figure 14. At certain time instants the value of q_{eff} reaches an integer value, so that a resonant condition may be satisfied for the higher harmonics $(m > 1, n > 1)$ of the GC orbits with the $(m = 1, n = 1)$ magnetic perturbation. This generates a number of island chains of GC orbits. The interaction of several such island structures may even lead to the formation of a stochastic layer near the separatrices (see figure 13a,b).

Figure 17(b) illustrates a typical structure of high-energy electrons in the presence of the internal helical magnetic field with a single $(m = 1, n = 1)$ mode. Such a

structure leads to a widening area of loss of electrons and decreasing of the critical energy E_{cr}. The characteristic escape time of REs from the stochastic layer is of order of 10 μs. Sudden RE bursts in many discharges is probably related with the loss of REs from the stochastic layer. The occurrence of the MHD mode signals accompanying these events will be discussed in § 7.3.

As was discussed above in §§ 2 and 5 (see also figures 1*b* and 12), there are some exceptional discharges (for example no. 117 859) with the highest RE current and several low-order rational surfaces within the plasma beam. Such a beam can be easily destabilized by the magnetic perturbations containing several MHD modes with low-order (m, n) numbers. Such a magnetic perturbation may strongly affect the electrons, creating a chaotic zone at the beam edge open to the wall. Such an effect probably explains the sudden loss of REs at certain times seen in figure 1(*b*).

7.2. *Influence of the TEXTOR-DED*

The coil configuration of the TEXTOR-DED is designed to have the poloidal spectra of magnetic perturbations localized near the magnetic surface $q = 3$ of the flat-top plasma discharges (see § 5.2 of the Supplementary Part). Therefore, these perturbations do not contain the necessary number of resonant components to create a stochastic zone of magnetic field lines in the post-disruption current beam with the safety factor q lying between $q(0) < 1$ and $q(a) < 1.5$.

In the so-called 3/1 operational mode with the predominant toroidal mode $n = 1$ there is only one $(m = 1, n = 1)$ component resonant to the magnetic surface $q = 1$. A similar situation takes place in the 6/2 mode $(n = 2)$ with the resonant component $(m = 2, n = 2)$. (There are no magnetic surfaces in the plasma region that are resonant to the components $(m = 1, n = 2)$ and $(m = 3, n = 2)$.) On the other hand, this resonant component of the DED field is weak, since it is located away from the maximum of the spectrum. Therefore, the effect of the DED on the RE beam does not create a stochastic zone of magnetic field lines from which electrons would escape to the wall as in the case of the stochastic zone in a flat-top plasma operation. Only the $m/n = 1/1$ component of the DED perturbations may create an island structure near the $q = 1$ magnetic surface similar to the one shown in figure 17(*a*).

With increasing energy of REs and decreasing plasma current the DED perturbation starts to affect the REs because of the appearance of high-mode resonances $q_{eff} = m/n$ similar to the case discussed in § 7.1. It generates structures with islands and a stochastic layer. Figure 18(*a*,*b*) show the typical Poincaré sections of GC orbits of energetic electrons affected by the TEXTOR-DED: (*a*) corresponds to the 3/1 mode with the DED current $I_{ded} = 3$ kA; (*b*) corresponds to the 6/2 mode with $I_{ded} = 7$ kA. The particle energy is taken as $E = 20$ MeV, the plasma current $I_p = 94$ kA, and the toroidal field $B_0 = 2.5$ T. These structures explain the fast decay of RE current in its final stage accompanied by spikes in the scintillation probe (see figure 1*b*).

The structures of RE orbits shown in figures 17(*b*) and 18 correspond to the final termination stages of RE current. They have features which are characteristic for the so-called stable and unstable manifolds created by the splitting of separatrices (see e.g. Abdullaev 2014). They lead to the toroidally and poloidally localized deposition patterns of REs on the wall. Toroidal peaking and spatial–temporal evolution of hard X-ray emission in the final stage of RE current loss observed in DIII-D experiments (James *et al.* 2012) is consistent with the described topology of REs.

The experimental observations in the TEXTOR-DED have indeed showed that the RMP field, which is switched on just after the TQ, does not affect the radial transport

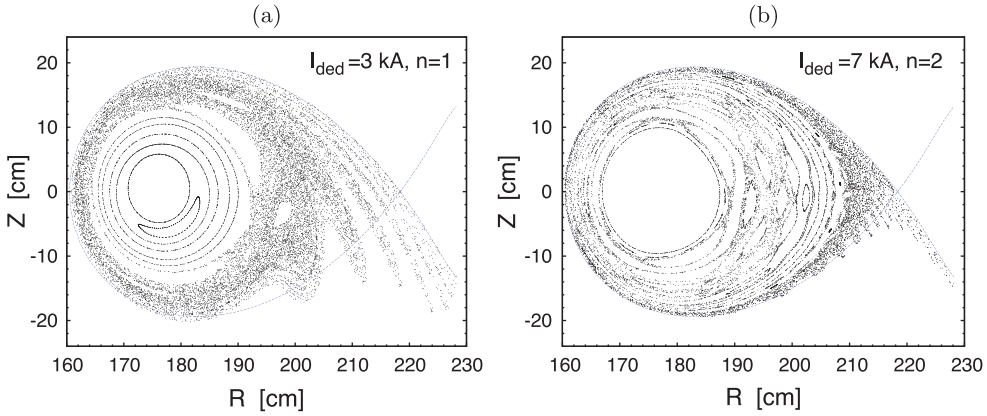

FIGURE 18. Poincaré sections of RE orbits in the (R, Z)-plane of the RE orbits of energy $E = 20$ MeV in the presence of the magnetic perturbations of the TEXTOR-DED. (a) corresponds to the $n = 1$ mode and the DED current $I_{ded} = 3$ kA; (b) corresponds to the $n = 2$ mode and $I_{ded} = 7$ kA. The plasma current $I_p = 94$ kA and the toroidal field $B_0 = 2.4$ T.

and the loss of low-energy electrons (Koslowski *et al.* 2014; Wongrach *et al.* 2015) (see also table 1). This is mainly because of the mentioned features of the poloidal and toroidal spectra of the DED field.

7.3. *Generation of magnetic perturbations by high-energy electrons*

As mentioned in § 2, the occurrence of the MHD activities during the sudden RE bursts can be explained by the nonlinear interaction of high-energy electrons with the $(m = 1, n = 1)$ MHD mode. The MHD magnetic perturbations with mode numbers (m, n) higher than the initial $(m = 1, n = 1)$ mode can be generated during the acceleration process of the REs. At a certain energy of REs their orbits strongly deviate from the magnetic surfaces, which creates in turn higher (m, n)-harmonics, $(m > 1, n > 1)$, of the MHD $(m = 1, n = 1)$ mode (7.5). The resonant interaction of RE orbits with these harmonics leads to the redistribution of the corresponding current near these orbits according to the helicity of these modes. Therefore, the current density (5.5) acquires higher (m, n)-components j_{mn}, which in turn generates the corresponding MHD modes. The bursts of magnetic activities accompanied by sudden runaway current drops observed in experiments (see figure 1*a*,*b*) are probably related to the described phenomenon.

8. Summary

Based on the analysis of numerous experimental data obtained in the TEXTOR tokamak we have proposed a possible mechanism of the plasma disruption with the formation of RE beams. The plasma disruption starts due to a large-scale magnetic stochasticity caused by nonlinearly excited MHD modes with low (m, n) numbers $(m/n = 1/1, 2/1, 3/2, 5/2, \ldots)$. The RE beam is formed in the central plasma region confined by the intact magnetic surface. Its location depends on the safety factor profile $q(\rho)$ and the spectrum of the MHD modes. In the cases of plasmas with a monotonic profile of $q(\rho)$ and at a sufficiently small amplitude of the $m/n = 1/1$ mode

the most stable RE beams are formed by the intact magnetic surface located between the magnetic surface $q = 1$ and the closest low-order rational surface $q = m/n > 1$. Depending on the spectrum of the magnetic perturbations, this rational magnetic surface could be one of these ones: $q = 4/3$, $q = 5/4$, or $q = 3/2$.

Such an outermost intact magnetic surface forms a transport barrier for particles in the central plasma region. Electrons in this confined region are accelerated by the inductive toroidal electric field. Such a situation occurs, for instance, in plasma disruptions with runaway beams initiated by argon gas injection. Heavy argon atoms do not penetrate sufficiently deeply into the plasma and therefore they do not excite the $m/n = 1/1$ mode with an amplitude necessary to create a fully chaotic magnetic field. On the other hand, the injection of the lighter noble gases neon and helium does not generate runaways, since the light gases penetrate deeper into the plasma and excite the large-amplitude $m/n = 1/1$ mode.

During disruptions of tokamak plasmas with the reversed magnetic shear, RE beams can be formed in the central plasma region confined by the shearless magnetic surface. The latter cannot be broken even at relatively large magnetic perturbations and it acts as a robust transport barrier to the parallel motion of particles along chaotic magnetic field lines. One expects that electrons confined by this intact magnetic surface form a relatively stable RE beam with a large transversal size. Experimental observations of RE beams with long confinement times during disruptions of plasma with the reversed magnetic shear in the TFTR tokamak (Fredrickson *et al.* 2015), probably, support this expectation.

Based on this scenario, we proposed models of the pre-disruption and post-disruption plasmas with REs to study the processes of thermal, CQ, and runaway current losses. A model of the magnetic field was proposed to describe the large-scale magnetic stochasticity due to interaction of low-mode-number MHD modes. The radial transport of heat and particles in a stochastic magnetic field was studied using collisional diffusional models. It was shown that the temperature drop during the fast phase of disruption is caused by the radial heat transport determined by the collisional electron transport in a stochastic magnetic field. We have estimated a current decay time using the ambipolar collisional particle transport model. The dynamics of RE orbits in a post-disruption plasma in the presence of the inductive toroidal electric field was investigated by integrating the equations of guiding centre motion. We analysed the effect of the internal MHD mode and external RMPs on the topology of RE orbits.

The new model reproduces for the first time remarkably well the essential features of the measurements, as follows.

(*a*) The outer part of the plasma is clearly ergodized while the inner section is still intact. This agrees with the observation that the runaways are only seen in the inner half of the torus while they are obviously quickly lost from the outer part.

(*b*) One observes a short tiny spike during the energy quench; we have described this spike previously; this spike is attributed to the loss of runaways born at the start up of the discharge from the ergodic zone.

(*c*) In the case of disruptions caused by injection of light He and Ne gases the energy quench is due to processes directly related to the penetration of neutral impurities into the plasma; if heavier Ar is injected fast electron transport in a stochastic magnetic field is of more importance. Stochastic motion of plasma particles is also responsible for the current decay; however, due to the ambipolarity of particle losses, the ion motion essentially affects the duration of the CQ stage.

The estimations of the energy quench and the current decay times based on the models presented agree well with observations.

(*d*) The slow decay of the RE current in the plateau phase is explained by the loss of runaways due to two effects: (i) an outward shift of the runaways due to their continuous acceleration and the subsequent loss at the wall; (ii) by the formation of a stochastic layer of high-energy REs at the beam edge in the presence of the $m/n = 1/1$ MHD mode.

(*e*) The effect of external resonant magnetic perturbations on low-energy electrons (up to 5–10 MeV) is weak and does not cause their loss.

The new mechanism explains well the observed disruptions in present-day tokamaks. One can expect the following consequences, e.g. for ITER.

(*a*) The structure of the stochastic zone during the TQ allows persistence of pre-existing runaways through this phase such that they act as seeds during the following phase of high loop voltage.

(*b*) The decay phase of the REs is rather long such that REs can acquire very high energy.

(*c*) External magnetic perturbations acting on REs seem little promising unless the core of a RE beam can be ergodized.

(*d*) A means for eliminating the REs completely is the injection of about 10^{25} molecules of H_2 or D_2 into the discharge (Hender *et al.* 2007). This MGI may impose a heavy load on the cryo-pumping system.

Acknowledgements

The authors gratefully acknowledge valuable discussions with W. Biel, S. Brezinsek, O. Marchuk, Ph. Mertens, D. Reiser, D. Reiter, A. Rogister, and U. Samm. S.S.A. thanks V. Igochine for consulting on the MHD mode structure in tokamaks. We also thank the anonymous referees for their constructive criticisms, comments, and valuable suggestions.

Supplementary data

Supplementary data is available at http://dx.doi.org/10.1017/S0022377815000501.

REFERENCES

ABDULLAEV, S. S. 2006 *Construction of Mappings for Hamiltonian Systems and their Applications*. Springer.

ABDULLAEV, S. S. 2013 On collisional diffusion in a stochastic magnetic field. *Phys. Plasmas* **20**, 082507.

ABDULLAEV, S. S. 2014 *Magnetic Stochasticity in Magnetically Confined Fusion Plasmas*. Springer.

ABDULLAEV, S. S. 2015 Drifts of electron orbits induced by toroidal electric field in tokamaks. *Phys. Plasmas* **22**, 030702.

ABDULLAEV, S. S., FINKEN, K. H. & SPATSCHEK, K. H. 1999 Asymptotical and mapping methods in study of ergodic divertor magnetic field in a toroidal system. *Phys. Plasmas* **6**, 153–174.

ABDULLAEV, S. S., FINKEN, K. H., WONGRACH, K., TOKAR, M., KOSLOWSKI, H. R., WILLI, O., ZHENG, L. & THE TEXTOR TEAM 2015 Mechanism of runaway electron formation during plasma disruptions in tokamaks. *Phys. Plasmas* **22**, 040704.

BAKHTIARI, M., KAWANO, Y., TAMAI, H., MIURA, Y., YOSHINO, R. & NISHIDA, Y. 2002 Fast plasma shutdown scenarios in the JT-60U tokamak using intense mixed gas puffing. *Nucl. Fusion* **42** (10), 1197–1204.

BAKHTIARI, M., TAMAI, H., KAWANO, Y., KRAMER, G. J., ISAYAMA, A., NAKANO, T., KAMIYA, Y., YOSHINO, R., MIURA, Y. & NISHIDA, Y. 2005 Study of plasma termination using high-*Z* noble gas puffing in the JT-60U tokamak. *Nucl. Fusion* **45** (10), 318–325.

BÉCOULET, A., HOANG, G. T., ABITEBOUL, J., ACHARD, J., ALARCON, T., ALBA-DURAN, J., ALLEGRETTI, L., ALLFREY, S., AMIEL, S., ANE, J. M., ANIEL, T., ANTAR, G., ARGOUARCH, A., ARMITANO, A., ARNAUD, J., ARRANGER, D., ARTAUD, J. F., AUDISIO, D., AUMEUNIER, M., AUTISSIER, E., AZCONA, L., BACK, A., BAHAT, A., BAI, X., BAIOCCHI, B., BALAGUER, D., BALME, S., BALORIN, C., BARANA, O., BARBIER, D., BARBUTI, A., BASIUK, V., BAULAIGUE, O., BAYETTI, P., BAYLARD, C., BEAUFILS, S., BEAUTE, A., BÉCOULET, M., BEJ, Z., BENKADDA, S., BENOIT, F., BERGER-BY, G., BERNARD, J. M., BERNE, A., BERTRAND, B., BERTRAND, E., BEYER, P., BIGAND, A., BONHOMME, G., BOREL, G., BORON, A., BOTTEREAU, C., BOTTOLLIER-CURTET, H., BOUCHAND, C., BOUQUEY, F., BOURDELLE, C., BOURG, J., BOURMAUD, S., BRÉMOND, S., BRIBIESCA ARGOMEDO, F., BRIEU, M., BRUN, C., BRUNO, V., BUCALOSSI, J., BUFFERAND, H., BURAVAND, Y., CAI, L., CANTONE, V., CANTONE, B., CAPRIN, E., CARTIER-MICHAUD, T., CASTAGLIOLO, A., BELO, J., CATHERINE-DUMONT, V., CAULIER, G., CHAIX, J., CHANTANT, M., CHATELIER, M., CHAUVIN, D., CHENEVOIS, J., CHOULI, B., CHRISTIN, L., CIAZYNSKI, D., CIRAOLO, G., CLAIRET, F., CLAPIER, R., CLOEZ, H., COATANEA-GOUACHET, M., COLAS, L., COLLEDANI, G., COMMIN, L., COQUILLAT, P., CORBEL, E., CORRE, Y., COTTET, J., COTTIER, P., COURTOIS, X., CREST, I., DACHICOURT, R., DAPENA FEBRER, M., DAUMAS, C., DE ESCH, H. P. L., DE GENTILE, B., DECHELLE, C., DECKER, J., DECOOL, P., DEGHAYE, V., DELAPLANCHE, J., DELCHAMBRE-DEMONCHEAUX, E., DELPECH, L., DESGRANGES, C., DEVYNCK, P., DIAS PEREIRA BERNARDO, J., DIF-PRADALIER, G., DOCEUL, L., DONG, Y., DOUAI, D., DOUGNAC, H., DUBUIT, N., DUCHATEAU, J.-L., DUCOBU, L., DUGUE, B., DUMAS, N., DUMONT, R., DUROCHER, A., DUROCHER, A., DUTHOIT, F., EKEDAHL, A., ELBEZE, D., ESCARGUEL, A., ESCOP, J., FAÏSSE, F., FALCHETTO, G., FARJON, J., FAURY, M., FEDORZACK, N., FÉJOZ, P., FENZI, C., FERLAY, F., FIET, P., FIRDAOUSS, M., FRANCISQUEZ, M., FRANEL, B., FRAUCHE, J., FRAUEL, Y., FUTTERSACK, R., GARBET, X., GARCIA, J., GARDAREIN, J., GARGIULO, L., GARIBALDI, P., GARIN, P., GARNIER, D., GAUTHIER, E., GAYE, O., GERAUD, A., GEROME, M., GERVAISE, V., GEYNET, M., GHENDRIH, P., GIACALONE, I., GIBERT, S., GIL, C., GINOUX, S., GIOVANNANGELO, L., GIRARD, S., GIRUZZI, G., GOLETTO, C., GONCALVES, R., GONDE, R., GONICHE, M., GOSWAMI, R., GRAND, C., GRANDGIRARD, V., GRAVIL, B., GRISOLIA, C., GROS, G., GROSMAN, A., GUIGUE, J., GUILHEM, D., GUILLEMAUT, C., GUILLERMINET, B., GUIMARAES FILHO, Z., GUIRLET, R., GUNN, J. P., GURCAN, O., GUZMAN, F., HACQUIN, S., HARIRI, F., HASENBECK, F., HATCHRESSIAN, J. C., HENNEQUIN, P., HERNANDEZ, C., HERTOUT, P., HEURAUX, S., HILLAIRET, J., HONORE, C., HORNUNG, G., HOURY, M., HUNSTAD, I., HUTTER, T., HUYNH, P., ICARD, V., IMBEAUX, F., IRISHKIN, M., ISOARDI, L., JACQUINOT, J., JACQUOT, J., JIOLAT, G., JOANNY, M., JOFFRIN, E., JOHNER, J., JOUBERT, P., JOURD'HEUIL, L., JOUVE, M., JUNIQUE, C., KELLER, D., KLEPPER, C., KOGUT, D., KUBIČ, M., LABASSE, F., LACROIX, B., LALLIER, Y., LAMAISON, V., LAMBERT, R., LARROQUE, S., LATU, G., LAUSENAZ, Y., LAVIRON, C., LE, R., LE LUYER, A., LE NILIOT, C., LE TONQUEZE, Y., LEBOURG, P., LEFEVRE, T., LEROUX, F., LETELLIER, L., LI, Y., LIPA, M., LISTER, J., LITAUDON, X., LIU, F., LOARER, T., LOMBARD, G., LOTTE, P., LOZANO, M., LUCAS, J., LÜTJENS, H., MAGAUD, P., MAGET, P., MAGNE, R., MAHIEU, J.-F., MAINI, P., MALARD, P., MANENC, L., MARANDET, Y., MARBACH, G., MARECHAL, J.-L., MARFISI, L., MARLE, M., MARTIN, C., MARTIN, V., MARTIN, G., MARTINEZ, A., MARTINO, P., MASSET, R., MAZON, D., MELLET, N., MERCADIER, L., MERLE, A., MESHCHERIAKOV, D., MESSINA, P., MEYER, O., MILLON, L., MISSIRLIAN, M., MOEREL, J., MOLINA, D., MOLLARD, P., MONCADA, V., MONIER-GARBET, P., MOREAU, D., MOREAU, M., MOREAU, P., MOREL, P., MORIYAMA, T., MOTASSIM, Y., MOUGEOLLE, G., MOULTON, D., MOUREAU, G., MOUYON, D., NAIM HABIB, M., NARDON, E., NÉGRIER, V., NEMETH, J., NGUYEN, C., NGUYEN, M., NICOLAS, L., NICOLAS, T., NICOLLET, S., NILSSON, E., N'KONGA, B., NOEL, F.,

NOOMAN, A., NORSCINI, C., NOUAILLETAS, R., ODDON, P., OHSAKO, T., ORAIN, F., OTTAVIANI, M., PAGANO, M., PALERMO, F., PANAYOTIS, S., PARRAT, H., PASCAL, J.-Y., PASSERON, C., PASTOR, P., PATTERLINI, J., PAVY, K., PECQUET, A.-L., PÉGOURIÉ, B., PEINTURIER, C., PELLETIER, T., PELUSO, B., PETRZILKA, V., PEYSSON, Y., PIGNOLY, E., PIROLA, R., POCHEAU, C., POITEVIN, E., POLI, V., POLI, S., POMPON, F., PORCHY, I., PORTAFAIX, C., PREYNAS, M., PROCHET, P., PROU, M., RATNANI, A., RAULIN, D., RAVENEL, N., RENARD, S., RICAUD, B., RICHOU, M., RITZ, G., ROCHE, H., ROUBIN, P., ROUX, C., RUIZ, K., SABATHIER, F., SABOT, R., SAILLE, A., SAINT-LAURENT, F., SAKAMOTO, R., SALASCA, S., SALMON, T., SALMON, T., SAMAILLE, F., SANCHEZ, S., SANTAGIUSTINA, A., SAOUTIC, B., SARAZIN, Y., SARDAIN, P., SCHLOSSER, J., SCHNEIDER, M., SCHWOB, J., SEGUI, J., SEGUIN, N., SELIG, G., SERRET, D., SIGNORET, J., SIGNORET, J., SIMONIN, A., SOLDAINI, M., SOLER, B., SOLTANE, C., SONG, S., SOURBIER, F., SPARAGNA, J., SPITZ, P., SPUIG, P., STORELLI, A., STRUGAREK, A., TAMAIN, P., TENA, M., THEIS, J., THOMINE, O., THOUVENIN, D., TORRE, A., TOULOUSE, L., TRAVÉRE, J., TSITRONE, E., TURCK, B., URBAN, J., VALLET, J.-C., VALLORY, J., VALOGNES, A., VAN HELVOIRT, J., VARTANIAN, S., VERGER, J.-M., VERMARE, L., VERMARE, C., VEZINET, D., VICENTE, K., VIDAL, J., VIGNAL, N., VIGNE, T., VILLECROZE, F., VILLEDIEU, E., VINCENT, B., VOLPE, B., VOLPE, D., VOLPE, R., WAGREZ, J., WANG, H., WAUTERS, T., WINTERSDORFF, O., WITTEBOL, E., ZAGO, B., ZANI, L., ZARZOSO, D., ZHANG, Y., ZHONG, W. & ZOU, X. L. 2013 Science and technology research and development in support to ITER and the broader approach at CEA. *Nucl. Fusion* **53** (10), 104023.

BOOZER, A. H. 2012 Theory of tokamak disruptions. *Phys. Plasmas* **19**, 058101.

BOOZER, A. H. 2015 Theory of runaway electrons in ITER: equations, important parameters, and implications for mitigation. *Phys. Plasmas* **22**, 032504.

BOZHENKOV, S. A., FINKEN, K. H., LEHNEN, M. & WOLF, R. C. 2007 Main characteristics of the fast disruption mitigation valve. *Rev. Sci. Instrum.* **78**, 033503.

BOZHENKOV, S. A., LEHNEN, M., FINKEN, K. H., BERTSCHINGER, G., KOSLOWSKI, H. R., REITER, D., WOLF, R. C. & THE TEXTOR TEAM 2011 Fuelling efficiency of massive gas injection in TEXTOR: mass scaling and importance of gas flow dynamics. *Nucl. Fusion* **51**, 083033.

BOZHENKOV, S. A., LEHNEN, M., FINKEN, K. H., JAKUBOWSKI, M. W., WOLF, R. C., JASPERS, R., KANTOR, M., MARCHUK, O. V., UZGEL, E., VANWASSENHOVE, G., ZIMMERMANN, O., REITER, D. & THE TEXTOR TEAM 2008 Generation and suppression of runaway electrons in disruption mitigation experiments in TEXTOR. *Plasma Phys. Control. Fusion* **50**, 105007.

CARRERAS, B., HICKS, H. R., HOLMES, J. A. & WADDELL, B. V. 1980 Nonlinear coupling of tearing modes with self-consistent resistivity evolution in tokamaks. *Phys. Fluids* **23** (9), 1811–1826.

CHEN, Z. Y., KIM, W. C., YU, Y. W., ENGLAND, A. C., YOO, J. W., HAHN, S. H., YOON, S. W., LEE, Y. K., OH, Y. K., KWAK, J. G. & KWON, M. 2013 Study of runaway current generation following disruptions in KSTAR. *Plasma Phys. Control. Fusion* **55**, 035007.

COMMAUX, N., BAYLOR, L. R., COMBS, S. K., EIDIETIS, N. W., EVANS, T. E., FOUST, C. R., HOLLMANN, E. M., HUMPHREYS, D. A., IZZO, V. A., JAMES, A. N., JERNIGAN, T. C., MEITNER, S. J., PARKS, P. B., WESLEY, J. C. & YU, J. H. 2011 Novel rapid shutdown strategies for runaway electron suppression in DIII-D. *Nucl. Fusion* **51** (10), 103001.

FINKEN, K. H., ABDULLAEV, S. S., JAKUBOWSKI, M., LEHNEN, M., NICOLAI, A. & SPATSCHEK, K. H. 2005 *The Structure of Magnetic Field in the TEXTOR-DED. Energy Technology.* Vol. 45. Forschungszentrum Jülich.

FINKEN, K. H., LEHNEN, M. & BOZHENKOV, S. A. 2008 Gas flow analysis of a disruption mitigation valve (DMV). *Nucl. Fusion* **48**, 115001.

FINKEN, K. H., LEHNEN, M. & BOZHENKOV, S. A. 2011 A new disruption mitigation valve (DMV) and gas flow in guiding tubes of different diameter. *Nucl. Fusion* **51**, 033007.

FORSTER, M., FINKEN, K. H., KUDYAKOV, T., LEHNEN, M., WILLI, O., XU, Y., ZENG, L. & THE TEXTOR TEAM 2012 Temporal and spectral evolution of runaway electron bursts in TEXTOR disruptions. *Phys. Plasmas* **19**, 092513.

FREDRICKSON, E. D., BELL, M. G., TAYLOR, G. & MEDLEY, S. S. 2015 Control of disruption-generated runaway plasmas in TFTR. *Nucl. Fusion* **55** (1), 013006.

FUKUYAMA, A., ITOH, K., ITOH, S. I., TSUJI, S. & LICHTENBERG, A. J. 1993 Stochasticity driven disruptive phenomena in tokamaks. In *Proc. 14th IAEA Int. Conf. on Plasma Physics and Controlled Nuclear Fusion Research, Würzburg, Germany, 30 September–7 October 1992*. Vol. 2, pp. 363–370. IAEA, IAEA-CN-56/D-4-21.

FÜLÖP, T. & NEWTON, S. 2014 Alfvénic instabilities driven by runaways in fusion plasmas. *Phys. Plasmas* **21** (8), 080702.

FÜLÖP, T., SMITH, H. M. & POKOL, G. 2009 Magnetic field threshold for runaway generation in tokamak disruptions. *Phys. Plasmas* **16**, 022502.

GERASIMOV, S. N., HENDER, T. C., MORRIS, J., RICCARDO, V., ZAKHAROV, L. E. & JET EFDA CONTRIBUTORS 2014 Plasma current asymmetries during disruptions in JET. *Nucl. Fusion* **54** (7), 073009.

GERHARDT, S. P., MENARD, J. E. & THE NSTX TEAM 2009 Characterization of the plasma current quench during disruptions in the National Spherical Torus Experiment. *Nucl. Fusion* **49** (2), 025005.

GILL, R. D. 1993 Generation and loss of runaway electrons following disruptions in JET. *Nucl. Fusion* **33** (11), 1613–1625.

GILL, R. D., ALPER, B., DE BAAR, M., HENDER, T. C., JOHNSON, M. F., RICCARDO, V. & CONTRIBUTORS TO THE EFDA-JET WORKPROGRAMME 2002 Behaviour of disruption generated runaways in JET. *Nucl. Fusion* **42**, 1039–1046.

GILL, R. D., ALPER, B., EDWARDS, A. W., INGESSON, L. C., JOHNSON, M. F. & WARD, D. J. 2000 Direct observations of runaway electrons during disruptions in the JET tokamak. *Nucl. Fusion* **40** (2), 163–174.

GRANETZ, R. S., HOLLMANN, E. M., WHYTE, D. G., IZZO, V. A., ANTAR, G. Y., BADER, A., BAKHTIARI, M., BIEWER, T., BOEDO, J. A., EVANS, T. E., HUTCHINSON, I. H. & JERNIGAN, T. C. 2007 Gas jet disruption mitigation studies on Alcator C-mod and DIII-D. *Nucl. Fusion* **47**, 1086.

GUAN, X., QIN, H. & FISCH, N. J. 2010 Phase-space dynamics of runaway electrons in tokamaks. *Phys. Plasmas* **17** (9), 092502.

HELANDER, P., ERIKSSON, L.-G. & ANDERSSON, F. 2000 Suppression of runaway electron avalanches by radial diffusion. *Phys. Plasmas* **7** (10), 4106–4111.

HENDER, T. C., WESLEY, J. C., BIALEK, J., BONDESON, A., BOOZER, A. H., BUTTERY, R. J., GAROFALO, A., GOODMAN, T. P., GRANETZ, R. S., GRIBOV, Y., GRUBER, O., GRYAZNEVICH, M., GIRUZZI, G., GÜNTER, S., HAYASHI, N., HELANDER, P., HEGNA, C. C., HOWELL, D. F., HUMPHREYS, D. A., HUYSMANS, G. T. A., HYATT, A. W., ISAYAMA, A., JARDIN, S. C., KAWANO, Y., KELLMAN, A., KESSEL, C., KOSLOWSKI, H. R., LA HAYE, R. J., LAZZARO, E., LIU, Y. Q., LUKASH, V., MANICKAM, J., MEDVEDEV, S., MERTENS, V., MIRNOV, S. V., NAKAMURA, Y., NAVRATIL, G., OKABAYASHI, M., OZEKI, T., PACCAGNELLA, R., PAUTASSO, G., PORCELLI, F., PUSTOVITOV, V. D., RICCARDO, V., SATO, M., SAUTER, O., SCHAFFER, M. J., SHIMADA, M., SONATO, P., STRAIT, E. J., SUGIHARA, M., TAKECHI, M., TURNBULL, A. D., WESTERHOF, E., WHYTE, D. G., YOSHINO, R., ZOHM, H. & THE ITPA MHD, DISRUPTION AND MAGNETIC CONTROL TOPICAL GROUP 2007 Progress in the ITER physics basis. *Nucl. Fusion* **47**, S128–S202; Chapter 3: MHD stability, operational limits and disruptions.

HOLLMANN, E. M., COMMAUX, N., EIDIETIS, N. W., EVANS, T. E., HUMPHREYS, D. A., JAMES, A. N., JERNIGAN, T. C., PARKS, P. B., STRAIT, E. J., WESLEY, J. C., YU, J. H.,

AUSTIN, M. E., BAYLOR, L. R., BROOKS, N. H., IZZO, V. A., JACKSON, G. L., VAN ZEELAND, M. A. & WU, W. 2010 Experiments in DIII-D toward achieving rapid shutdown with RE suppression. *Phys. Plasmas* **17** (5), 056117.

HOLLMANN, E. M., AUSTIN, M. E., BOEDO, J. A., BROOKS, N. H., COMMAUX, N., EIDIETIS, N. W., HUMPHREYS, D. A., IZZO, V. A., JAMES, A. N., JERNIGAN, T. C., LOARTE, A., MARTIN-SOLIS, J., MOYER, R. A., MUÑOZ-BURGOS, J. M., PARKS, P. B., RUDAKOV, D. L., STRAIT, E. J., TSUI, C., VAN ZEELAND, M. A., WESLEY, J. C. & YU, J. H. 2013 Control and dissipation of runaway electron beams created during rapid shutdown experiments in DIII-D. *Nucl. Fusion* **53** (8), 083004.

IZZO, V. A., HOLLMANN, E. M., JAMES, A. N., YU, J. H., HUMPHREYS, D. A., LAO, L. L., PARKS, P. B., SIECK, P. E., WESLEY, J. C., GRANETZ, R. S., OLYNYK, G. M. & WHYTE, D. G. 2011 Runaway electron confinement modelling for rapid shutdown scenarios in DIII-D, Alcator C-Mod and ITER. *Nucl. Fusion* **51** (6), 063032.

IZZO, V. A., HUMPHREYS, D. A. & KORNBLUTH, M. 2012 Analysis of shot-to-shot variability in post-disruption runaway electron currents for diverted DIII-D discharges. *Plasma Phys. Control. Fusion* **54** (9), 095002.

JAKUBOWSKI, M. W., SCHMITZ, O., ABDULLAEV, S. S., BREZINSEK, S., FINKEN, K. H., KRÄMER-FLECKEN, A., LEHNEN, M., SAMM, U., SPATSCHEK, K. H., UNTERBERG, B., WOLF, R. C. & THE TEXTOR TEAM 2006 Change of the magnetic-field topology by an ergodic divertor and the effect on the plasma structure and transport. *Phys. Rev. Lett.* **96**, 035004.

JAMES, A. N., AUSTIN, M. E., COMMAUX, N., EIDIETIS, N. W., EVANS, T. E., HOLLMANN, E. M., HUMPHREYS, D. A., HYATT, A. W., IZZO, V. A., JERNIGAN, T. C., LA HAYE, R. J., PARKS, P. B., STRAIT, E. J., TYNAN, G. R., WESLEY, J. C. & YU, J. H. 2012 Measurements of hard X-ray emission from runaway electrons in DIII-D. *Nucl. Fusion* **52** (1), 013007.

KADANOFF, L. P. 2004 Excellence in computer simulation. *Perspect. Comput. Sci.* (IEEE-CS and AIP), March/April, 57–67.

KADOMTSEV, B. B. 1984 Behavior of disruptions in tokamaks. *Plasma Phys. Control. Fusion* **26**, 217–226.

KAWANO, Y., YOSHINO, R., KONDOH, T., ISEI, N., ISHIDA, S., TOBITA, K., HATAE, T., ITAMI, K., SAKASAI, S. & THE JT-60 TEAM 1997 Suppression of runaways – electron generation during disruptive discharge – termination in JT-60U. In *Controlled Fusion and Plasma Physics. Proc. 24th Eur. Conf., Berchtesgaden, 1997. Vol. 21A*, pp. 501–504. European Physical Society.

KOLTUNOV, M. & TOKAR, M. Z. 2011 Modification of local plasma parameters by impurity injection. *Plasma Phys. Control. Fusion* **53** (6), 065015.

KOSLOWSKI, H. R., SOLTWISCH, H. & STODIEK, W. 1996 Polarimetric measurement of $m = 1$ sawtooth precursor oscillations in the TEXTOR tokamak. *Plasma Phys. Control. Fusion* **38** (3), 271–278.

KOSLOWSKI, H. R., ZENG, L., LEHNEN, M., LVOVSKIY, A., WONGRACH, K. & THE TEXTOR TEAM 2014 Influence of massive gas injection and resonant magnetic perturbations on the generation of runaway electrons during disruptions in TEXTOR. In *Proc. 41st EPS Conf. on Plasma Physics, Berlin, 22–28 June 2014*, P5.028.

KRUGER, S. E., SCHNAK, D. D. & SOVINEC, C. R. 2005 Dynamics of the major disruption of a DIII-D plasma. *Phys. Plasmas* **12**, 056113.

LEHNEN, M., ALONSO, A., ARNOUX, G., BAUMGARTEN, N., BOZHENKOV, S. A., BREZINSEK, S., BRIX, M., EICH, T., GERASIMOV, S. N., HUBER, A., JACHMICH, S., KRUEZI, U., MORGAN, P. D., PLYUSNIN, V. V., REUX, C., RICCARDO, V., SERGIENKO, G., STAMP, M. F. & CONTRIBUTORS, JET EFDA 2011 Disruption mitigation by massive gas injection in JET. *Nucl. Fusion* **51** (12), 123010.

LEHNEN, M., ABDULLAEV, S. S., ARNOUX, G., BOZHENKOV, S. A., JAKUBOWSKI, M. W., JASPERS, R., PLYUSNIN, V. V., RICCARDO, V., SAMM, U., JET EFDA CONTRIBUTORS & THE TEXTOR TEAM 2009 Runaway generation during disruptions in JET and TEXTOR. *J. Nucl. Mater.* **390–391**, 740–746.

LEHNEN, M., BOZHENKOV, S. A., ABDULLAEV, S. S., JAKUBOWSKI, M. W. & THE TEXTOR TEAM 2008 Suppression of runaway electrons by resonant magnetic perturbations in TEXTOR disruptions. *Phys. Rev. Lett.* **100**, 255003.

LEVINTON, F. M., ZARNSTORFF, M. C., BATHA, S. H., BELL, M., BELL, R. E., BUDNY, R. V., BUSH, C., CHANG, Z., FREDRICKSON, E., JANOS, A., MANICKAM, J., RAMSEY, A., SABBAGH, S. A., SCHMIDT, G. L., SYNAKOWSKI, E. J. & TAYLOR, G. 1995 Improved confinement with reversed magnetic shear in TFTR. *Phys. Rev. Lett.* **75** (24), 4417–4420.

LICHTENBERG, A. J. 1984 Stochasticity as the mechanism for the disruptive phase of the $m = 1$ tokamak oscillations. *Nucl. Fusion* **24**, 1277–1289.

OLYNYK, G. M., GRANETZ, R. S., REINKE, M. L., WHYTE, D. G., GOLFINOPOULOS, T., HUGHES, J. W., WALK, J. R., IZZO, V. A., COMBS, S. K., MILORA, S. L. & BROOKMAN, M. W. 2013 Rapid shutdown experiments with one and two gas jets on Alcator C-Mod. *Nucl. Fusion* **53** (9), 092001.

O'ROURKE, J. 1991 The change in the safety factor profile at a sawtooth collapse. *Plasma Phys. Control. Fusion* **33**, 289–296.

PAPP, G., DREVLAK, M., FÜLÖP, T., HELANDER, P. & POKOL, G.-I. 2011 Runaway electron losses caused by resonant magnetic perturbations in ITER. *Plasma Phys. Control. Fusion* **53**, 095004.

PAPP, G., DREVLAK, M., FÜLÖP, T. & POKOL, G.-I. 2012 The effect of resonant magnetic perturbations on runaway electron transport in ITER. *Plasma Phys. Control. Fusion* **54**, 125008.

PAPP, G., FÜLÖP, T., FEHÉR, T., DE VRIES, P. C., RICCARDO, V., REUX, C., LEHNEN, M., KIPTILY, V., PLYUSIN, V. V., ALPER, B. & JET-EFDA CONTRIBUTORS 2013 The effect of ITER-like wall on runaway electron generation in JET. *Nucl. Fusion* **53**, 123017.

PAUTASSO, G., COSTER, D., EICH, TH., FUCHS, J. C., GRUBER, O., GUDE, A., HERRMANN, A., IGOCHINE, V., KONZ, C., KURZAN, B., LACKNER, K., LUNT, T., MARASCHECK, M., MLYNEK, A., REITER, B., ROHDE, V., ZHANG, Y., BONNIN, X., BECK, M., PRAUSNER, G. & THE ASDEX UPGRADE TEAM 2009 Disruption studies in ASDEX Upgrade in view of ITER. *Plasma Phys. Control. Fusion* **51**, 124056.

PLYUSNIN, V. V., RICCARDO, V., JASPERS, R., ALPER, B., KIPTILY, V. G., MLYNAR, J., POPOVICHEV, S., DE LA LUNA, E., ANDERSSON, F. & JET EFDA CONTRIBUTORS 2006 Study of runaway electron generation during major disruptions in JET. *Nucl. Fusion* **46**, 277–284.

QIN, H., GUAN, X. & FISCH, N. J. 2011 Neoclassical drift of circulating orbits due to toroidal electric field in tokamaks. *Tech. Rep.* PPPL-4639. Princeton Plasma Physics Laboratory, Princeton.

REUX, C., BUCALOSSI, J., SAINT-LAURENT, F., GIL, C., MOREAU, P. & MAGET, P. 2010 Experimental study of disruption mitigation using massive injection of noble gases on Tore Supra. *Nucl. Fusion* **50**, 095006.

SCHÜLLER, F. C. 1995 Disruptions in tokamaks. *Plasma Phys. Control. Fusion* **37**, A135–A162.

SHIBATA, Y., WATANABE, K.Y., OHNO, N., OKAMOTO, M., ISAYAMA, A., KURIHARA, K., NAKANO, T., OYAMA, N., KAWANO, Y., MATSUNAGA, G., SAKAKIBARA, S., SUGIHARA, M., KAMADA, Y. & THE JT-60 TEAM 2010 Study of current decay time during disruption in JT-60U tokamak. *Nucl. Fusion* **50**, 025015.

SOLTWISCH, H. & KOSLOWSKI, H. R. 1995 Sawtooth modulation of the poloidal field in TEXTOR under ohmic heating conditions. *Plasma Phys. Control. Fusion* **37** (6), 667–678.

SOLTWISCH, H. & KOSLOWSKI, H. R. 1997 Observation of magnetic field perturbations during sawtooth activity in tokamak plasmas. *Plasma Phys. Control. Fusion* **39** (5A), A341–A349.

SOLTWISCH, H. & STODIEK, W. 1987 Polarimetric measurement of safety factor changes during a sawtooth cycle in the TEXTOR tokamak under ohmic heating conditions. *Bull. Amer. Phys. Soc.* **32** (9), 1929. *Proc. 29th Annu. Meet. of the APS Division of Plasma Physics*. San Diego.

SOLTWISCH, H., STODIEK, W., MANICKAM, J. & SCHLÜTER, J. 1987 Current density profiles in the TEXTOR tokamak. In *Proc. 11th IAEA Conf. on Plasma Physics and Controlled Fusion Research, Kyoto, 13–20 November 1986, Vol. 1*, pp. 263–273. IAEA, IAEA-CN-47/A-V-1.

SPIZZO, G., VIANELLO, N., WHITE, R. B., ABDULLAEV, S. S., AGOSTINI, M., CAVAZZANA, R., CIACCIO, G., PUIATTI, M. E., SCARIN, P., SCHMITZ, O., SPOLAORE, M., TERRANOVA, D. & RFX AND TEXTOR TEAMS 2014 Edge ambipolar potential in toroidal fusion plasmas. *Phys. Plasmas* **21** (5), 056102.

STRAIT, E. J., LAO, L. L., MAUEL, M. E., RICE, B. W., TAYLOR, T. S., BURRELL, K. H., CHU, M. S., LAZARUS, E. A., OSBORNE, T. H., THOMPSON, S. J. & TURNBULL, A. D. 1995 Enhanced confinement and stability in DIII-D discharges with reversed magnetic shear. *Phys. Rev. Lett.* **75** (24), 4421–4424.

TOKAR, M. Z. & KOLTUNOV, M. 2013 Modelling of the plasma global response to a local cooling. *Plasma Phys. Control. Fusion* **55** (4), 045013.

TOKUDA, S. & YOSHINO, R. 1999 Simulation study on collisionless loss of runaway electrons by magnetic perturbations in a tokamak. *Nucl. Fusion* **39**, 1123–1132.

WESSON, J. 2004 *Tokamaks*, 3rd edn, Clarendon.

WESSON, J. A., GILL, R. D., HUGON, M., SCHÜLLER, F. C., SNIPES, J. A., WARD, D. J., BARTLETT, D. V., CAMPBELL, D. J., DUPERREX, P. A., EDWARDS, A. W., GRANETZ, R. S., GOTTARDI, N. A. O., HENDER, T. C., LAZZARO, E., LOMAS, P. J., LOPES CARDOZO, N., MAST, K. F., NAVE, M. F. F., SALMON, N. A., SMEULDERS, P., THOMAS, P. R., TUBBING, B. J. D., TURNER, M. F. & WELLER, A. 1989 Disruptions in JET. *Nucl. Fusion* **29** (4), 641–666.

WHITE, R. B. 2014 *The Theory of Toroidally Confined Plasmas*, 3rd edn, Imperial College Press.

WHYTE, D. G., JERNIGAN, T. C., HUMPHREYS, D. A., HYATT, A. W., LASNIER, C. J., PARKS, P. B., EVANS, T. E., ROSENBLUTH, M. N., TAYLOR, P. L., KELLMAN, A. G., GRAY, D. S., HOLLMANN, E. M. & COMBSET, S. K. 2002 Mitigation of tokamak disruptions using high-pressure gas injection. *Phys. Rev. Lett.* **89** (5), 055001.

WHYTE, D. G., JERNIGAN, T. C., HUMPHREYS, D. A., HYATT, A. W., LASNIER, C. J., PARKS, P. B., EVANS, T. E., TAYLOR, P. L., KELLMAN, A. G., GRAY, D. S. & HOLLMANNET, E. M. 2003 Disruption mitigation with high-pressure noble gas injection. *J. Nucl. Mater.* **313–316**, 1239.

WONGRACH, K., FINKEN, K. H., ABDULLAEV, S. S., KOSLOWSKI, R., WILLI, O., ZENG, L. & THE TEXTOR TEAM 2014 Measurement of synchrotron radiation from runaway electrons during TEXTOR tokamak disruptions. *Nucl. Fusion* **54**, 043011.

WONGRACH, K., FINKEN, K. H., ABDULLAEV, S. S., WILLI, O., ZENG, L., XU, Y. & THE TEXTOR TEAM 2015 Runaway electron studies in TEXTOR. *Nucl. Fusion* **55**, 053008.

YAMADA, M., LIVINTON, F. M., POMPHREY, N., BUDNY, R., MANICKAM, J. & NAGAYAMA, Y. 1994 Investigation of magnetic reconnection during a sawtooth crash in a high-temperature tokamak plasma. *Phys. Plasmas* **1**, 3269–3276.

YOSHINO, R. & TOKUDA, S. 2000 Runaway electrons in magnetic turbulence and runaway current termination in tokamak discharge. *Nucl. Fusion* **40** (7), 1293–1309.

ZEHRFELD, H. P., FUSSMANN, G. & GREEN, B. J. 1981 Electric field effects on relativistic charged particle motion in tokamaks. *Plasma Phys.* **23** (5), 473–489.

ZENG, L., KOSLOWSKI, H. R., LIANG, Y., LVOVSKIY, A., LEHNEN, M., NICOLAI, D., PEARSON, J., RACK, M., JAEGERS, H., FINKEN, K. H., WONGRACH, K. & XU, Y. 2013 Experimental observation of a magnetic-turbulence threshold for runaway generation in the TEXTOR tokamak. *Phys. Rev. Lett.* **110**, 235003.

PUBLICATION 7

Synchrotron radiation pattern of the runaway beam during induced disruptions in TEXTOR

K. Wongarch[1], K.H. Finken[1,2], R. Koslowski[2], S.S. Abdullaev[2], O. Willi[1] and L. Zeng[2,3]

[1]*Institut für Laser- und Plasmaphysik, Heinrich-Heine Universität Düsseldorf, Germany*

[2]*Institut für Energie- und Klimaforschung, Forschungszentrum Jülich GmbH, EURATOM Association, Jülich, Germany*

[3]*Institute of Plasma Physics, Chinese Academy of Sciences, Hefei, China*

Introduction

Tokamak plasmas are prone to disruptions, an abrupt termination of the discharge. During a disruption upto 80% of the initial plasma current is carried by runaway electrons [1]. The runaways can gain energies as high as tens of MeV. When the high-energy electrons are lost, they can penetrate deep inside the materials and cause a severe damage to the plasma facing components (PCFs). Most of techniques employed to diagnose the runaway electrons provide an indirect measurement. These methods are based on detecting X-ray, gamma ray or neutrons, which are generated by runaway-wall interactions. One of the most promising runaway diagnostic methods is the measurement of synchrotron radiation. Since the high-energy electrons emit synchrotron radiation highly collimated in the direction of flight [2], this technique enables an observation of the shape of the high-energy runaway beam, its location and dynamics.

Experimental Setup

In the circular cross-section limiter tokamak TEXTOR (R_0 = 1.75 m, a = 0.46 m), the synchrotron radiation emitted by runaway electrons is observed by an infrared (IR) camera, which is located at the equatorial plan of the tokamak. The camera views the plasma tangentially in the electron approach direction. Its viewing area covers the plasma at the low-field side (LFS) of the torus, whereas the high-field side (HFS) is vignetted. The operational wavelength range of the camera is 3-5 μm. The camera is, therefore, sensitive not only to the synchrotron radiation emitted by runaway electrons but also the IR radiation emitted from other sources such as thermal radiation. However, the characteristic features of each source enables to differentiate between the synchrotron radiation and IR radiation from other sources.

The TEXTOR plasma position are controlled by 3 different magnetic coil systems. The vertical field coils and the radial position control coils generate the vertical fields which is responsible for the plasma horizontal position. The vertical position is controlled by the plasma vertical position control coil system. Each coil has own power supply and can be operated independently

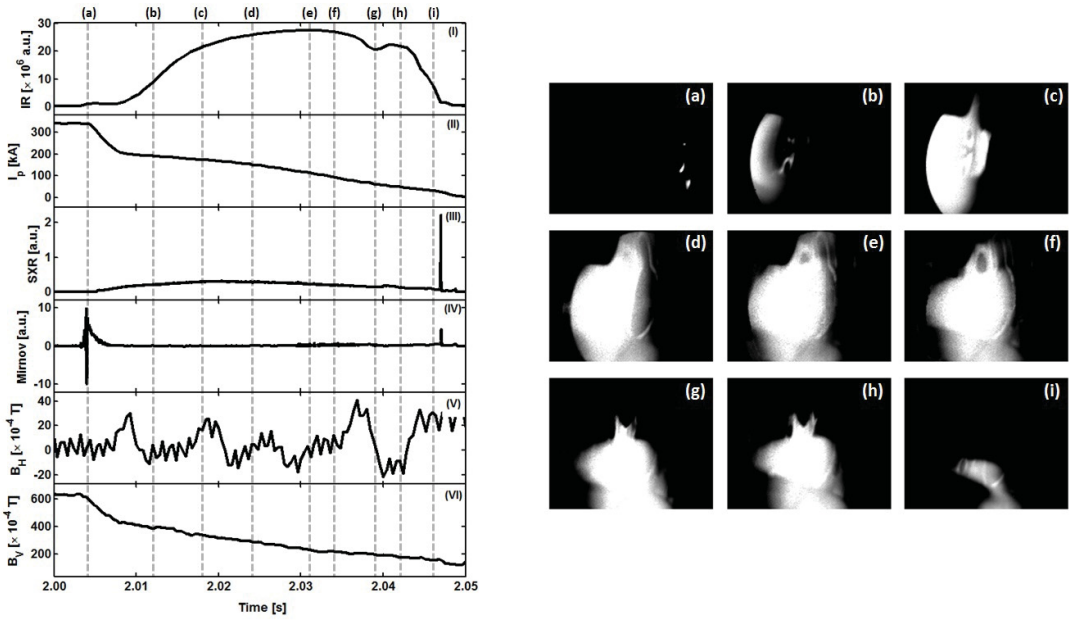

Figure 1: *left* - time traces of the discharge 117434: (top to bottom) the IR radiation intensity summed over all the camera viewing area, the plasma current, the soft X-ray emission, the Mirnov signal, the horizontal field and the total vertical field during an induced disruption. *Right* - temporal evolution of IR radiation pattern observed by the camera.

in the feed-forward mode [3].

Observation of the Synchrotron radiation pattern during disruptions

In the experimental campaign, disruptions are initiated by Ar injection performed by a fast valve [4]. In the discharge 117434, the current of the radial position control coils is switched to its limiting value of -3.5 kA and the current of the vertical position control coils is set to +1 kA shortly after the initiation of the disruption. The temporal evolution of the IR radiation, the plasma current, the soft X-ray signal, the Mirnov signal, the horizontal field and the vertical field during disruption of the discharge 117434 are shown in figure 1. The energy quench takes place at 3 ms after the gas injection. A strong Mirnov spike is present. The plasma thermal energy is lost to the PFCs. The heated components are seen by the IR camera as shown in figure 1 (a). About 10 ms after the thermal quench the runaway electrons gain high enough energies to become visible at the left side of figure 1 (b). The runaway beam develops and moves toward LFS until it reach its maximum intensity at t = 2.031 s (see figure 1 (e)). The negative field generated by the radial position control coils leads to the movement toward LFS of the beam. Figure 1 (e) - (i) shows that the runaway beam shrinks and its intensity decreases with increasing time. At the end of the discharge a sharp SXR spike and the Mirnov signal spike are present. The runaways are completely lost to the wall within less than 1 ms. A structure present in the

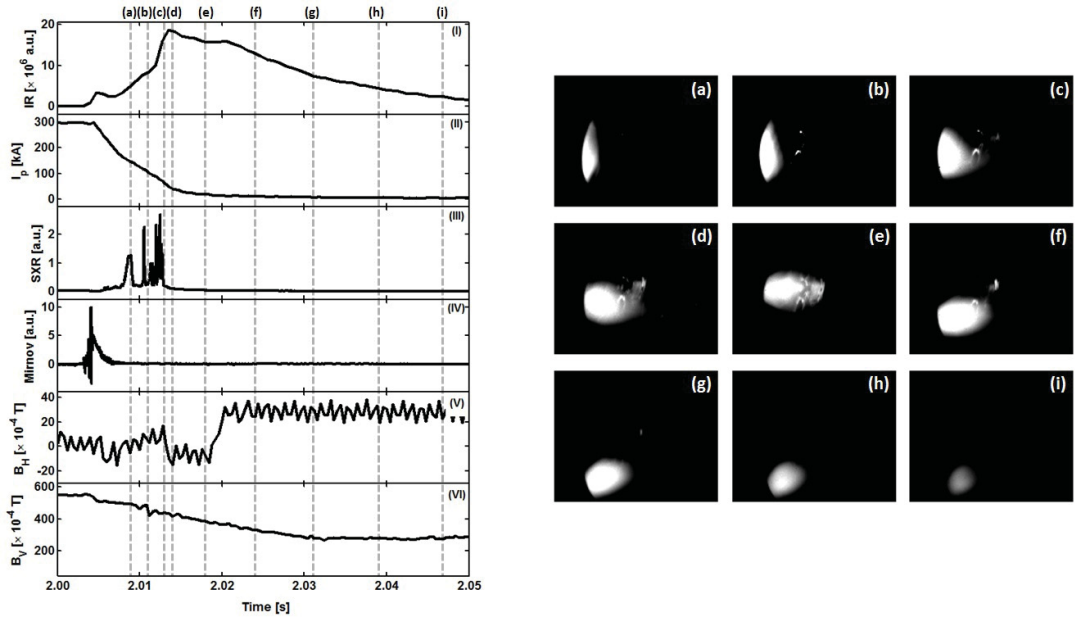

Figure 2: *left* - time traces of the discharge 117828: (top to bottom) the IR radiation intensity summed over all the camera viewing area, the plasma current, the soft X-ray emission, the Mirnov signal, the horizontal field and the total vertical field during an induced disruption. *Right* - temporal evolution of IR radiation pattern observed by the camera.

IR images in figure 1 is a reflection from one of the big opening ports of TEXTOR.

In the discharge 117828, the current of the vertical position control coils is also switched to +1 kA but the current of the radial position control coils is set to +3.5 kA. The runaway beam, similar to the previous case, develops at the left side of the image. However, the beam remain at the HFS until the end of the current plateau due to the positive field generated by the radial position control coils (see figure 2 (a) - (c)). During this phase SXR spikes which indicate the runaway loss are observed. After the plateau phase the plasma current drops rapidly. The poloidal field, therefore, decreases immediately. This results in a charge separation. The $E \times B$ force leads to the drift of the runaway beam toward LFS as seen in figure 2 (d). In figure 2 (d) - (i), the runaway beam moves upward and downward under the influence of the negative and the positive horizontal fields, respectively (see also figure 2 (V)). Although the plasma current drops to almost zero after the plateau termination, part of the runaway beam persists over a few tens of milliseconds. The beam decays gradually until it completely disappears at $t \approx 2.57$ s. Neither a SXR spike nor a Mirnov oscillation are observed during this phase.

Runaway parameters and critical plasma current

The runaway parameters, i.e., the pitch angle (θ) and the radius of the runaway beam (r_{beam}) can be deduced from the synchrotron radiation image [5]. From the analysis of figure 1 (e)

we obtain r_{beam} = 283 mm and θ = 52 mrad. The maximum number of the runaway electron observed by the IR camera is 1.6 $\times 10^{16}$. The number of the high energy runaways is affected with an error margin of about 20%. The total number of runaway electrons estimated from the runaway current in figure 1 (II) is N_{tot} = 2.82 $\times 10^{16}$.

As can be seen from the synchrotron radiation in the second example, a significant amount of the high-energy runaway electrons are still confined after the current drop. The maximum number of the runaway electron observed by the IR camera after the current drop is 6.4 $\times 10^{15}$. Our numerical calculation shows that the minimum current required to sustain the runaway electron beam is proportional to the square of the runaway energy. The runaway electrons with energies of 25 MeV can survive the plateau termination at the low plasma current of about 20 kA.

Conclusion

The synchrotron radiation measuring system on the TEXTOR tokamak serves as an important runaway diagnostic method. This technique provides information on beam position and profile of the high-energy runaways. We have found that the magnetic fields generated by position control coils have a significant influence on the dynamics of the runaway beam even after the current decay. Generally, it has been supposed that runaway electrons are completely lost to the wall at the time the plasma current drops rapidly to almost zero [6]. However, the detection of the synchrotron radiation shows that a substantial number of high-energy runaway electrons survives the current plateau termination. Additionally, the pitch angle and the radius of the runaway beam are obtained from the IR image analysis.

Acknowledgement

This work was supported by the Royal Thai Government, an R&D contract and the Trilateral Euregio Cluster (TEC). The authors thank O. Schmitz and the TEXTOR team for their support.

References

[1] J.R. Martin-Solis, B. Esposito, et al.,Phys. Rev. Lett. **97**, 165002 (2006).
[2] K.H. Finken, S.S. Abdullaev, M.W. Jakubowski, et al., Nucl. Fusion **47**, 91 (2007).
[3] O. Neubauer, G. Czymek, B. Giesen, et al., Fusion Sci. and Tech **47**,76 (2005).
[4] A. Savtchkov, K.H. Finken and G. Mank, Rev. of Sci. Instrum **70**, 3490 (2002).
[5] K.H. Finken, J.G. Watkins, D. Rusbüldt, et al., Nucl. Fusion **30**, 859 (1990).
[6] N. W. Eidietis, N. Commaux, E.M. Hollmann, et al., Phys. of plasma **19**, 056109 (2012).

PUBLICATION 8

Experimental observation of runaway electron related relaxation phenomena during disruptions in the TEXTOR tokamak

L. Zeng[1, 2*], H.R. Koslowski[1], Y. Liang[1], A. Lvovskiy[1], M. Lehnen[3], D. Nicolai[1], J. Pearson[1], M. Rack[1], P. Denner[1], K.H. Finken[4], K. Wongrach[4], and the TEXTOR team

[1] *Forschungszentrum Jülich GmbH, Institute of Energy and Climate Research - Plasma Physics (IEK-4), Association EURATOM-FZJ, Trilateral Euregio Cluster, 52425 Jülich, Germany*
[2] *Institute of Plasma Physics, Chinese Academy of Sciences, 230031 Hefei, China*
[3] *ITER Organization, Route de Vinon sur Verdon, 13115 St Paul Lez Durance, France*
[4] *Institut für Laser- und Plasmaphysik, Heinrich-Heine-Universität Düsseldorf, 40225 Düsseldorf, Germany*
** E-mail: l.zeng@fz-juelich.de*

1. Introduction

Runaway electron (RE) currents of several mega amperes are expected to be generated in ITER disruptions due to avalanche multiplication [1]. An uncontrolled loss of these high-energy electrons to the plasma facing components might cause serious damage [2]. However, the loss process has not yet been clarified. We present here observations of the RE related relaxation phenomena during disruptions in the TEXTOR tokamak.

2. Experimental observations

Figure 1 shows a typical discharge (#117991) with a RE plateau during a deliberated disruption in TEXTOR. Figures 1(a)-(d) illustrate the plasma current, toroidal loop voltage, soft X-ray emission, and magnetic turbulence, respectively. There are four phases during the disruption, (I) the thermal quench, (II) the current quench, (III) the RE plateau, and (IV) final termination. Magnetic activity in the latter three phases will be discussed in this paper.

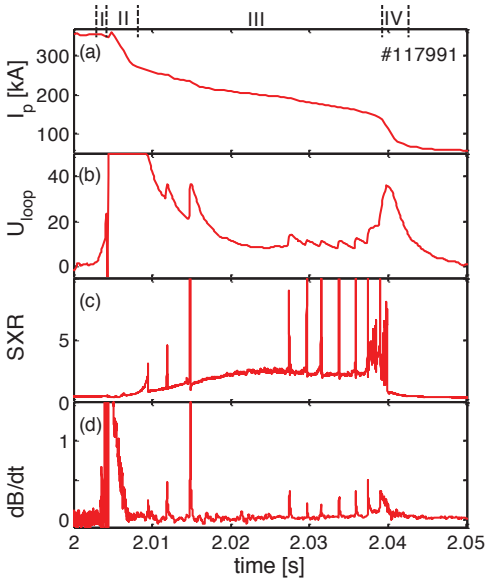

Fig. 1 Time traces in shot 117991showing (a) plasma current, (b) toroidal loop voltage, (c) soft X-ray emission, and (d) magnetic turbulence.

2.1 *Magnetic turbulence during current quench*

Figure 2 compares two discharges, #117833 develops a RE current plateau during the current quench while #117849 does not. The parameters of both shots are the same except for the toroidal magnetic field (B_t = 1.8 T for #117849 and B_t = 2.4 T for #117833). Obvious magnetic turbulence is seen during the current quench in the magnetic pick-up coil signals, shown in Fig. 2 (b) and (c). The magnetic turbulence lasts from 4 to 8 ms and the level initially increases and then decreases. A typical frequency spectrum of magnetic turbulence is shown in Fig. 2 (d). The turbulence frequency has a large distribution with most

of the power in the range from 60 to 260 kHz. The magnetic turbulence level with B_t = 1.8 T is at least twice of that with B_t = 2.4 T. The RE tail is not always reproducible, even with the same toroidal magnetic field, in which the magnetic turbulence level (δB) is also different. These suggest that magnetic turbulence during the current quench plays the dominant role in this stage and is the cause of the different observed RE tails.

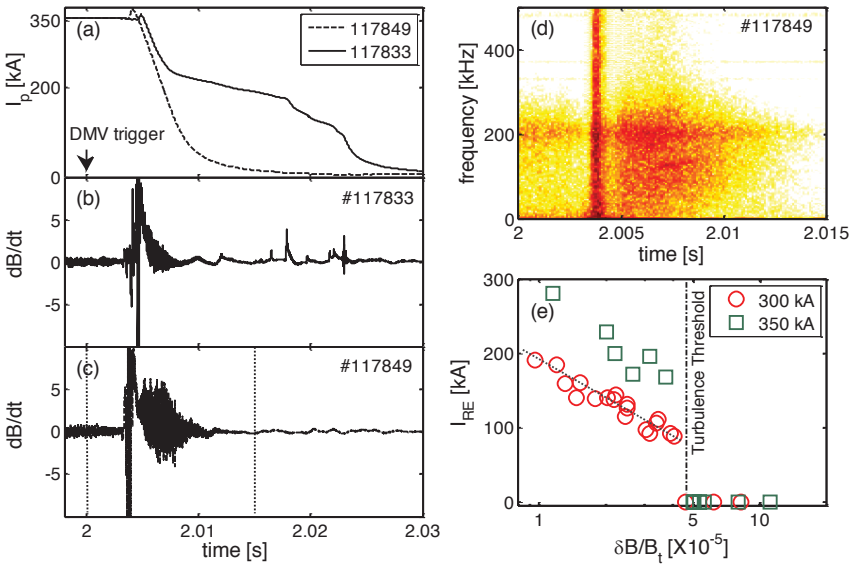

Fig. 2 Time traces showing (a) plasma current, (b) magnetic turbulence in shot 117833, (c) magnetic turbulence in shot 117849, and (d) spectrum of magnetic turbulence in shot 117849. (e) RE current in TEXTOR disruptions as a function of normalized magnetic turbulence level.

In Fig. 2 (e), a survey of several discharges shows that in TEXTOR the RE plateau is always visible unless the normalized magnetic turbulence level exceeds the threshold of $\delta B/B_t \sim 4.8 \times 10^{-5}$ for both the I_p = 300 and 350 kA cases [3]. The REs (which may be produced in the current quench) are quickly lost within the first 5 ms of the current quench. For shots with lower magnetic turbulence levels than the threshold, it is found that the RE current (I_{RE}) decreases linearly with $\delta B/B_t$ for I_p = 300 kA and also for I_p = 350 kA, but in the latter case the RE current is larger. The value of the critical fluctuation amplitude seems to depend mainly on the toroidal field and not on the plasma current. From the analysis above it follows that there is clear evidence that the development of a RE beam depends strongly on the level of magnetic turbulence during the current quench.

2.2 *Magnetic activities during RE plateau*

Burst-like relaxations during the RE plateau cause large RE losses, seen by spikes in the signals of soft X-ray arrays, shown in Fig. 1(a) and 1(c). RE losses will reduce the current and, as a consequence, induce a positive voltage spike (Fig. 1(b)). A series of bursting activities are also observed on the Mirnov coils, consistent with the spikes on the SXR arrays, shown in Fig. 1(d). The physical mechanisms for the magnetic bursts are complex and at least two distinct types are found: i) RE beam interaction with the inner wall and ii) RE beam interaction with the outer wall.

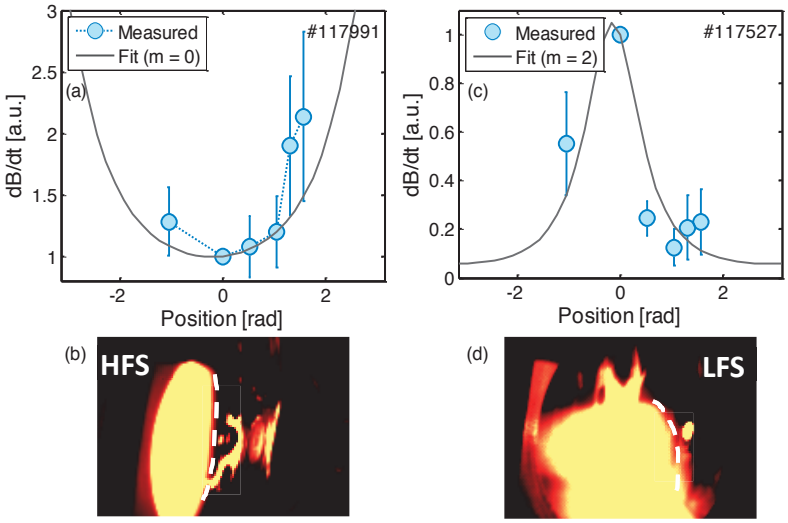

Fig. 3 (a) and (c) Comparison of magnetic turbulence level at different poloidal angles in shots 117991 and 117527. (b) and (d) IR radiation observed by the camera in shots 117993 and 117434.

i) RE beam interaction with the inner wall. — For the interaction with the inner wall, the magnetic spikes can be found at every phases of the RE beam lifetime, i.e., the whole RE, plateau and final termination. The poloidal and toroidal mode numbers are both 0. The time periods for the duration and the intervals between the spikes are ~100 μs and ~2 ms, respectively. Moreover, high frequency fluctuations (~200 kHz) followed by the spikes are often observed by the coils, at the end of the RE plateau and final termination, and the toroidal mode number is 1. Similar to the signal distributions of the Mirnov coils during the current quench (Fig. 3 in Ref. [3]), the magnetic spikes are poloidally asymmetric. The level at the top of the inner wall is about 2 times larger than at the low field side. This can be explained by the inward movement of the plasma. Indeed, the magnetic fluctuations decay as $r^{-(m+1)}$ in the vacuum. Assuming an inward movement of 25 cm, a reduction of the minor radius from 0.45 m to 0.25 m and $m = 0$, the simulated signals agree with the measured one, shown in Fig. 3(a). The RE beam is located on the high field side as has been observed by measuring the synchrotron emission with an infrared camera in TEXTOR, which is also consistent with the assumptions for our simulations (Fig. 3(b)).

ii) RE beam interaction with the outer wall. — For the interaction with the outer wall, the spikes can usually be found at the end of the RE plateau and final termination. The poloidal mode number is 2 or 3 and the toroidal mode number is still 0. The magnetic spikes are usually observed initially and then these develop to continuous fluctuations, with a frequency up to ~10 kHz. The magnetic spike is also poloidally asymmetric but the peak is found at the low field side. Assuming an outward movement of 20 cm and $m = 2$, the simulated signals agree with the measured one (Fig. 3(c)). This suggests RE beam is located on the low field side. The results can also be confirmed by measuring the synchrotron emission with an infrared camera (Fig. 3(d)).

During the RE current plateau, most of the current are carried by REs. RE drift orbits, shifted outward from the magnetic flux surfaces, depend on the electron energy. This is illustrated in

Fig. 4 where poloidal sections of the drift surfaces of the REs with different energies are plotted. For the HFS case, background plasma and low energy electrons do firstly interact with the inner wall. Another possibility is that closed magnetic surfaces are firstly broken, due to the interaction with the inner wall, and then the REs confined on these surfaces are lost immediately. For the LFS case, high energy electrons interact with the outer wall and the whole plasma with the RE beam is still well-confined. But the phase difference seen in the poloidal Mirnov coil signals could not be understood by this.

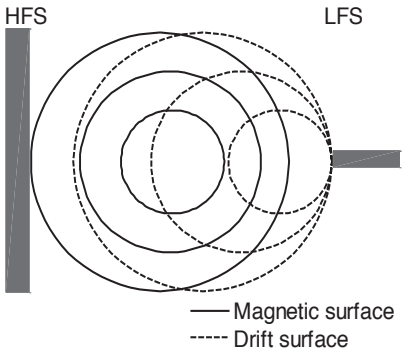

Fig. 4 Drift orbits of runaway electrons on different magnetic flux surfaces.

2.3 *Magnetic turbulence during final termination*

During final termination, several kinds of magnetic turbulence are also observed on the Mirnov coils. Some of them are similar to the magnetic turbulence during current quench. In some other cases, regular fluctuations are observed both on the Mirnov coils and SXR signals, shown in Fig. 5(a)-(b). The frequency spectrum of magnetic turbulence (#115208) is shown in Fig. 5(c) and the turbulence frequency changes from ~100 kHz to ~60 kHz in 0.8 ms. The toroidal mode number is 1. Similar behavior is also found during the current quench in some discharges without a RE plateau. These suggest the modes are likely to be from the interaction between the high-energetic REs and the background plasma.

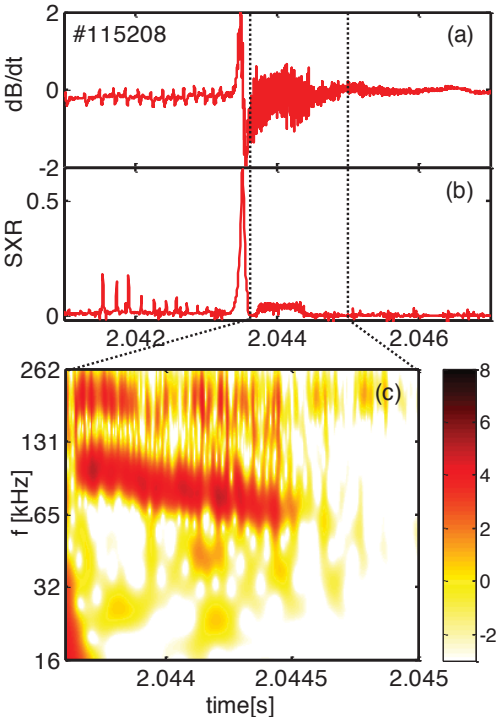

Fig. 5 Time traces showing (a) magnetic turbulence, (b) SXR emission, and (c) spectrum of magnetic turbulence in shot 115208.

Acknowledgement. — Support from the Helmholtz Association in the frame of the Helmholtz-University Young Investigators Group VH-NG-410, the National Magnetic Confinement Fusion Science Program of China under Contracts No. 2013GB106003, and the Natural Science Foundation of China under Grant No. 11105184 is gratefully acknowledged.

References.

[1] T. C. Hender *et al.*, Nucl. Fusion 47, S128 (2007)

[2] M. Lehnen, S. S. Abdullaev, G. Arnoux *et al.*, J. Nucl. Mater. 390–391, 740 (2009)

[3] L. Zeng, H. R. Koslowski, Y. Liang *et al.*, Phys. Rev. Lett. 110, 235003 (2013)

PUBLICATION 9

Structure of the runaway electron loss during induced disruptions in TEXTOR

K. Wongrach[1], K.H. Finken[1], S.S. Abdullaev[2], O. Willi[1], L. Zeng[3] and Y. Xu[4]
[1]*Institut für Laser- und Plasmaphysik, Heinrich-Heine Universität Düsseldorf, Düsseldorf 40225, Germany*
[2]*Institut für Energie- und Klimaforschung, Forschungszentrum Jülich GmbH, Jülich 52428, Germany*
[3]*Institute of Plasma Physics, Chinese Academy of Sciences, Hefei, Anhui 230031, People's Republic of China*
[4]*Southwestern Institute of Physics, Chengdu 610041, People's Republic of China*

The loss of runaway electrons during an induced disruption is recorded by a synchrotron imaging technique using a fast infrared CCD camera. The loss is predominantly diffuse. During the "spiky-loss phase" when the runaway beam moves close to the wall, a narrow channel between the runaway column and a scintillator probe is formed and lasts until the runaway beam is terminated. In some cases the processed images show a stripe pattern at the plasma edge. A comparison between the MHD dominated disruptions and the MHD-free disruption is performed. A new mechanism of plasma disruptions with the runaway electron generation and a novel model which reproduces many characteristic features of the plasma beam evolution during a disruption are briefly described.

PACS numbers: 52.55.Fa, 52.70.-m, 52.55.-s
Submit to Physics of Plasmas

I. INTRODUCTION

In the development of fusion based on tokamaks, runaway electrons (REs) generated during disruptions are of major concern as they travel with high velocities that exceed the friction force and can be freely accelerated. In the present tokamaks, REs can gain energies up to several tens of MeV. The high energy electrons may cause severe damage to the vessel walls and other components inside the torus. This problem becomes more important, e.g. in ITER because runaways with energies up to $\sim$ 100 MeV are expected [1]. However, the REs with energies of the order of 10 MeV become dominant when the avalanching commences [2]. Studies of REs generated during disruptions have been performed at nearly all major tokamaks. The toroidal magnetic field plays an important role in runaway generation. No REs are observed for disruptions when the magnetic field is below the magnetic threshold [3, 4]. With decreasing magnetic field the level of magnetic fluctuation increases [5]. In the presence of micromagnetic turbulence and low m/n mode magnetic islands in stochastic sea, REs are better confined than the thermal electrons. Macroscale magnetic turbulence, conversely, degrades the runaway confinement [6]. In DIII-D, the runaway current depends critically on MHD fluctuations, particularly the radial profile of the $n = 1$ mode [7].

Disruptions with a substantial runaway population show at first a rapid decay of the plasma current followed by a plateau like formation with a reduced decay rate. During the first strong decay phase, the loop voltage is enhanced acting as the driving force for the REs. In addition to the continuous decay during the plateau phase, a small stepwise decays of the plasma current and loss spikes accompanied by MHD activity are observed [8]. The main emphasis of this article is laid on an imaging of the plasma cross section by the synchrotron radiation measurement in order to understand the mechanism behind the loss. We also try to show similarities and differences between the observations during the runaway plateau phase of two different groups of disruptions.

II. EXPERIMENTAL SETUP

A CCD IR-camera has been installed at the low field side of the torus oriented tangentially in the electron approach direction and has been used to record images of synchrotron radiation emitted by high energy REs (see figure 1). The camera is sensitive only to electrons which have energies exceeding 25 MeV with an instantaneous velocity vector in the direction of the camera entrance optics. This restricts the synchrotron image to a narrow area [9] with a toroidal integration length of about 10 cm. As the field of observation of the plasma at the high field side is vignetted the camera detects only synchrotron radiation emitted by REs at the low field side. The camera is operated at a frame rate of 1253 frames per second, corresponding to the time distance between consecutive images of 0.8 ms, with an integration time of 2 μs.

The REs at the plasma edge are measured by the scintillator probe [10], which is placed at the last closed flux surface ($r = 46$ cm) shortly before the disruption is triggered. The probe consists of 9 scintillating YSO crystals, which are partially shielded by layers if iron of different thickness; therefore they are sensitive to REs with different energies from 3 MeV to about 22 MeV. The probe is covered by a 5 mm thick CFC mantle such that neither light nor electrons with energies below 3 MeV can hit the scintillator crystals. During the pre-programmed disruptions, the radial position control coils are operated in a feed-forward mode.

At TEXTOR, reproducible disruptions with REs can be initiated by a fast injection of argon gas [11–13]. The disruptions reported in this paper are induced by argon injection at $t = 2$ s performed by a fast valve. The dis-

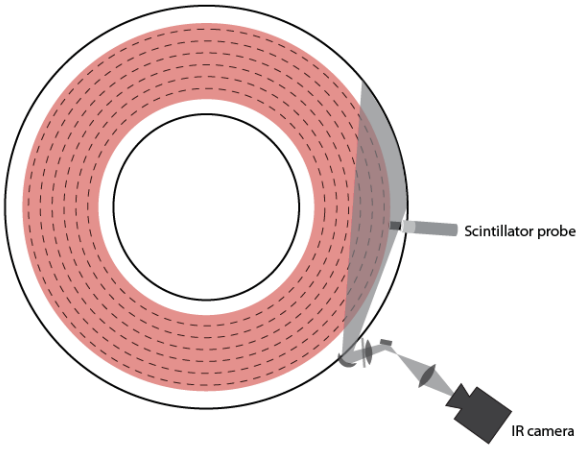

FIG. 1. Schematic top view of experimental setup. Solid black lines indicate the vacuum chamber wall. A gray area represents the field of view of the IR camera. The scintillator probe is placed at the last closed flux surface.

charge conditions are: a stationary, ohmic discharge with circular cross section at a major radius of $R_0 = 1.75$ m, and a minor radius of $a = 0.46$ m. The plasma current is $I_p = 350$ kA, the toroidal field strength is $B_T = 2.4$ T and the line average density before the disruption is $n_e = 1.5 \times 10^{19}$ m^{-3}.

III. RUNAWAY LOSS DURING INDUCED DISRUPTION

Although the same conditions were applied to all disruptions in the recent experiments, two distinct groups of disruptions have been observed. The first group consists of a MHD-dominated plateau phase, during which the MHD activity is observed. The other group, the MHD-free runaway disruption, has a smooth runaway plateau phase. Neither runaway bursts nor SXR and Mirnov signal spikes are present. The existence of the spikes is independent of the presence of the scintillator probe near the plasma edge.

A. MHD-dominated plateau phase

A typical example of an induced disruption with MHD activity in the TEXTOR tokamak is shown in Fig. 2. The current plateau as seen in the first sub-figure (black curve) typically indicates the presence of REs. In the discharge without runaways, one observes only the exponential decay (red curve). The second sub-figure shows the difference between the current traces with and without REs and thus gives the pure contribution of the runaways to the plasma current. The plateau phase of the current is initially flat until the spiky bursts are present between $t = 2.032$ s and $t = 2.045$ s. The spikes are

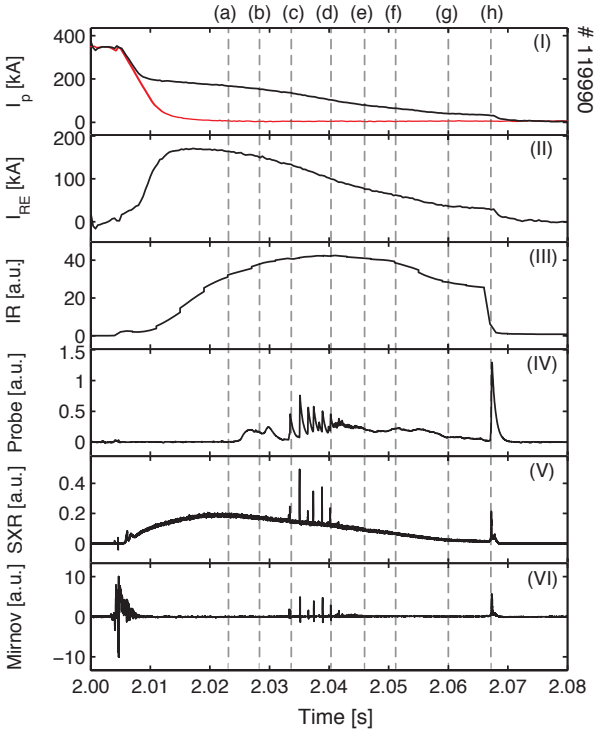

FIG. 2. Temporal evolution of disruption discharge # 119990 (top to bottom): (I) time trace of the plasma current (black curve) and of the current without REs (red curve), (II) the runaway current, (III) the spatially integrated synchrotron radiation, (IV) the scintillator probe signal for REs with energies above 11 MeV, (V) the soft X-ray signal and (VI) the Mirnov signal.

observed in the probe, the SXR and the Mirnov signals at the same time. However, the amplitudes of the spikes are different indicating that the spikes are probably local and not uniform around the torus. The integrated synchrotron signal starts to increase after a delay with respect to the runaway current because the synchrotron measuring system is sensitive to the electrons with energies above 25 MeV. The integrated synchrotron signal increases until the spiky loss starts. Afterwards, it decays smoothly. At the end, we observe a sudden loss of the synchrotron radiation.

In Fig. 3, a compilation of images of the synchrotron light recorded in the discharge # 119990 is shown in false color. As already mentioned, the images show a cross section of the high energy runaway beam. The left side of the images represent the high field side which is partially vignetted. Therefore, one cannot see the radial extend of the runaways in the first frames of the disruption. Later, the runaway beam is shifted more towards the low field side allowing the whole beam to be seen. The runaway column is spatially rather smooth and has a circular shape. The radius of the runaways is about 20 cm. The "horn like" double structure which one sees on the upper part of the image is an artifact from reflec-

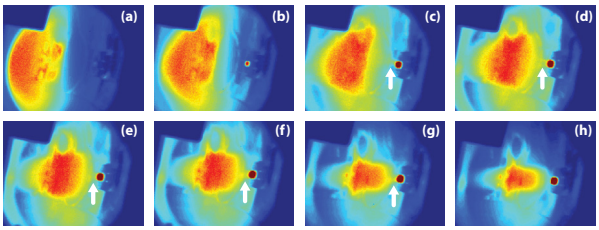

FIG. 3. Temporal evolution of IR radiation patterns of the discharge # 119990 taken at (a) $t = 2.023$ s, (b) $t = 2.028$ s, (c) $t = 2.033$ s, (d) $t = 2.040$ s, (e) $t = 2.046$ s, (f) $t = 2.051$ s, (g) $t = 2.060$ s, and (h) $t = 2.068$ s. A small red spot at the right side of the image represents the heated scintillator probe tip. The white arrows in sub-figures (c) - (g) indicate the channel between the core runaways and the probe tip.

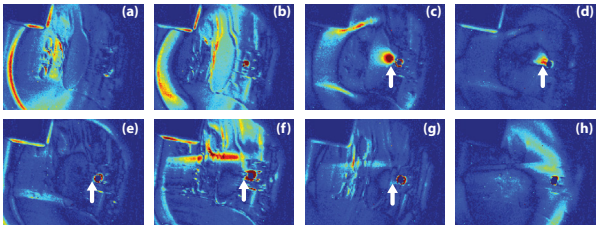

FIG. 4. The images obtained from subtracting consecutive images of the discharge # 119990 corresponding to the images shown in Fig. 3. In sub-figures (c) and (d), i.e. at the time of the MHD spikes, the channel is clearly visible. The white arrows in sub-figures (c) - (g) indicate the position of the channel between the core runaways and the probe tip.

tions of the wall (from the stiffening ring at a window). The IR structure remains fixed in space. At the low field side one sees a small red dot at the edge of the runaway beam. This dot is the tip of the scintillator probe which is heated by the lost REs and runaway halo. Later in the disruption when the plasma current is already low, the runaway beam shrinks and takes an oval shape oriented horizontally before it suddenly disappears at the end of the discharge, i.e. within 80 μs.

To our surprise, we did not observe special structures in the runaway beam during the spiky phase but a rather diffuse loss. Nevertheless, when the runaway beam is shifted close to the probe a small channel which connects the runaway column to the probe is observed. The channel is formed at the beginning of the spiky phase and lasts until the runaway beam is terminated (see sub-figures (c) - (g)). However, there was no indication of fast variations during the individual spikes.

In order to detect weak local structures which vary in time, we have developed a technique to subtract each image from its previous image. This technique is close to a time derivative of the images or related to a stroboscopic method; it visualizes in particular events which are quickly developing. This technique enables an observation of the runaway beam structures, which change on the time scale of the image recording time. Fig. 4

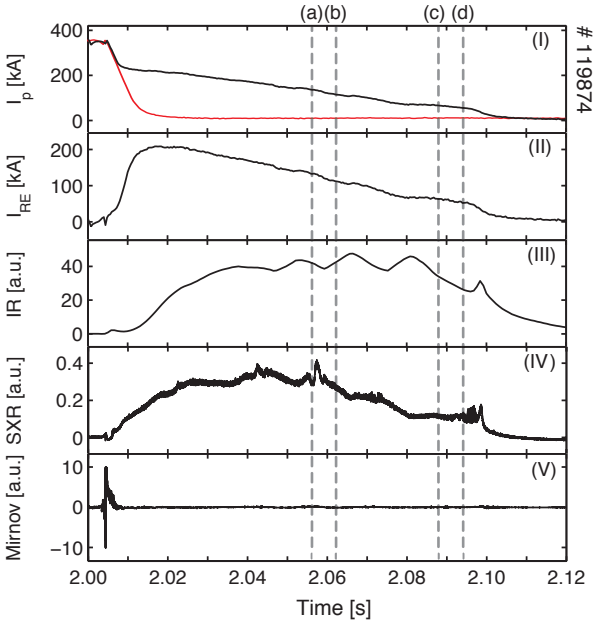

FIG. 5. Temporal evolution of the disruption of the discharge # 119874 (top to bottom): (I) time trace of the plasma current (black curve) and of the current without runaway electrons (red curve), (II) the runaway current, (III) the spatially integrated synchrotron radiation, (IV) the soft X-ray signal and (V) the Mirnov signal.

shows the absolute values of the differences between the consecutive images related to the images shown in Fig. 3. The intensity of the color code is increased by a factor of 10. Sub-figure (a) shows an enhanced intensity because the number of high energy electrons is increasing. In sub-figure (b), an intensity of synchrotron radiation at the low field side increases due to an outwards movement of the beam. Sub-figures (c) and (d), are taken during the spiky phase. One sees that the influence zone of the probe is well restricted to few centimeters only and does not influence the central runaway population. Some narrow stripes at the top and bottom of the beam presented in sub-figure (c) - (e) may indicate an enhanced loss during the spikes.

B. MHD-free runaway disruptions

Fig. 5 shows an example of a "smooth" disruption with runaways. One sees only week signs of MHD activity. No SXR and Mirnov spikes are detected. The scintillator probe was absent during this experiment. A slow radial oscillation of the runaway beam results in the variations of the IR signal and the plasma current. The image of the synchrotron radiation is not spectacular and develops slowly. Therefore, we have selected only 4 images (see Fig. 6). The radius of the runaway beam in this example is 26 cm. It is larger than the radius in the previous example. No loss channel connecting between the

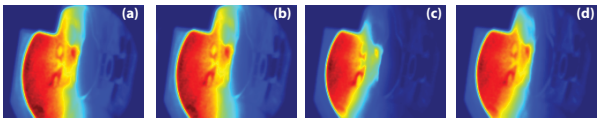

FIG. 6. Temporal evolution of the IR radiation patterns of the discharge # 119874 taken at (a) $t = 2.057$ s, (b) $t = 2.062$ s, (c) $t = 2.088$ s and (d) $t = 2.093$ s. A small red spot at the right field side of the image presents the heated scintillator probe tip.

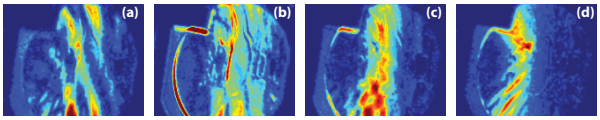

FIG. 7. The images obtained from subtracting consecutive images of the discharge # 119874 corresponding to the images shown in figure 6.

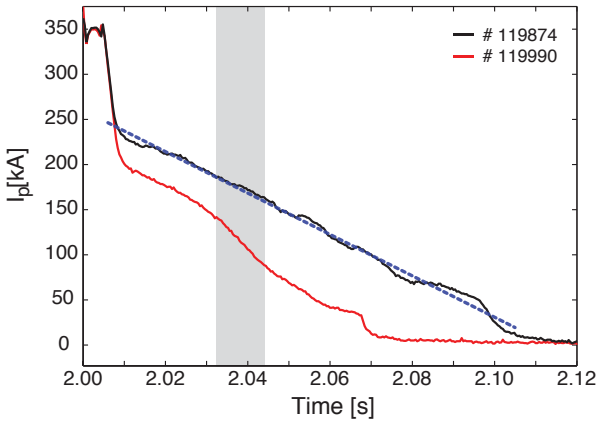

FIG. 8. The plasma current of the discharges # 119874 (black - quiet disruption) and # 119990 (red - spiky disruption). A dashed blue line represents a linear fit of the current of the discharges # 119874. A gray are indicates the spiky phase.

runaway beam and wall elements is observed. The images obtained from subtracting consecutive images shown in Fig. 7 are surprising. We find, after a smooth beginning phase, the development of a stripe pattern at the edge of the runaway column. The stripes are inclined with respect to the expected magnetic flux surfaces. Inclinations in both directions as well as a superposition of the stripes are observed at the edge of the beam.

C. Comparison of runaways with and without MHD activity

The plasma current of a discharge without MHD activity (black) in comparison with that of a discharge with MHD activity (red) is shown in Fig. 8. The current decay during the runaway plateau phase in case of discharge without MHD activity can be described by a linear function of time with a decay rate of 2.3 MA/s (see dashed blue line). In case of a discharge with MHD activity, the current starts to decrease with the same rate as the current in the previous case. However, during the spiky phase, the decay rate increases to 4.1 MA/s. The variation of the plasma current due to the slight movement of the beam is minor in comparison with the current drop during the spiky phase.

Although the runaway loss is substantially enhanced, no significant change of synchrotron radiation is observed. The major part of the high energy runaways remains confined in the plasma as can be seen in Fig. 3 (c) - (e) and Fig. 4 (c) - (e). The lost runaways are mainly the REs in low and energy range. This is consistent with the earlier publication [8], in which the energy spectrum of the lost RE was analyzed by the different channel of the scintillator probe. The spectrum of the lost runaways was described by an exponential decay function the an exponent of $n_{r_0} \sim 10$ MeV. At that time the probe was well calibrated. At present, the calibration is old and no longer reliable because the probe housing was modified.

It has been observed that runaway disruptions with MHD-activity often show channels between the main runaway beam and the probe or other wall elements. During runaway disruptions without MHD-activity we have never seen those channels even when the beam moves close to the probe and the probe is continuously heated by the beam halo. However, it has to be stated that these channels are not visible in all spiky disruptions, probably because they are out of sight of the IR-camera. There are disruptions, during which the spikes are present when the runaway beam moves toward the wall at the HFS. The loss channel connecting between the wall and the beam are probably created. But this part is located outside the camera field of view. We, therefore cannot see whether the channels exist or not.

During some smooth disruptions, the stripe structure like in Fig. 7. In runaway disruptions with MHD-activity we have not yet seen these stripe pattern. It is still unclear, whether the stripe structure is systematically connected to MHD-free disruptions or whether it was just an accident that we found it only there. We suspect that the plasma rotation frequencies in case of spiky disruptions and smooth disruptions are different. The rotation frequency in the former case possibly does not match the recording frequency of the camera. The observed structures are smeared out and hence the smooth runaway beam is detected.

IV. STRUCTURE OF RUNAWAY ELECTRON ORBITS

The stripes are a characteristic feature for an ergodic system and related to the so-called laminar zones [14, 15]. To explain the observed stripes in synchrotron radiation patterns, we have created a model which describes prac-

tically topological features in the plasma. According to our assumptions, the most stable RE beams are created in plasmas with the central safety factor $q(0) < 1$ [16, 17]. They are formed in the central plasma region confined inside the intact magnetic surface located between the rational magnetic surface $q = 1$ and the closest low-order rational magnetic surface $q = 5/4$ (or $q = 4/3, \dots$). Heat and plasma particles outside this region are lost due to transport in a strong stochastic magnetic field formed due to nonlinearly excited low-mode number MHD modes. Electrons in the confined region are accelerated by the inductive toroidal electric field.

Based on the new model, REs are mainly lost due to two effects. The smooth decay of RE current is related to the outward drift of electron orbits induced by a toroidal electric field [18, 19]. This loss mechanism plays an important role for high energy REs since they have large drift orbit displacement. The sudden losses of REs are caused by the nonlinear interactions of high energy runaway orbits with the $m/n = 1/1$ helical magnetic perturbation leading to the formation of stochastic layer of REs at the beam edge. The typical Poincaré section of RE orbits in the presence of the $m/n = 1/1$ mode is shown in Fig. 9. The presence of the ergodic layer is consistent with the observation that the runaway beam fills only about half of the predisruptive plasma diameter while one sees a larger runaway beam in typical low density runaway discharges [9]. In Fig. 9 mixed topological structures are observed: the large intact area inside the $q = 1$ surface and a series of stable islands embedded into a stochastic layer near the separatrix that open to the wall. The high energy REs is less sensitive to the magnetic turbulence due to their strong drift [20]. Therefore, the lost REs are mainly from the low energy range. The characteristic escape time of REs from the stochastic layer is of order of 10 μs. However, REs trapped by the stability islands stay longer and their synchrotron radiation can be seen. Due to the rotation of the $m/n = 1/1$ helical magnetic perturbation, the stability islands also rotate. This can explain the observed stripes in subtracted synchrotron radiation patterns.

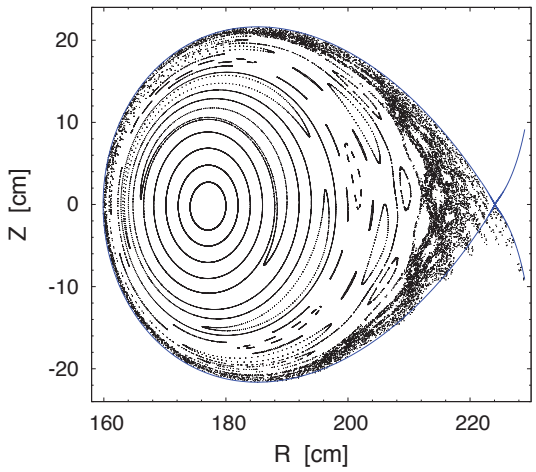

FIG. 9. Poincaré section of the RE guiding center. The RE energy $E = 20$ MeV and he RE beam current of $I_p = 100$ kA.

V. SUMMARY AND CONCLUSIONS

During TEXTOR disruptions, REs and in particular their loss have been measured - besides by the standard diagnostics - by synchrotron radiation imaging and by a scintillator probe positioned close to the plasma edge. The synchrotron radiation in the observed wavelength range is emitted from REs with energies exceeding 25 MeV while scintillator probe is most sensitive for electron energies in the range of 3 MeV to 22 MeV. REs with energies below 3 MeV as well as low energy particles are stopped by a CFC light tight mantle beyond the probe head.

The disruptions are initiated by massive injection of Ar-gas and the initial conditions are constant. In nearly all cases after the thermal quench the development of a a runaway plateau is observed. In the plateau phase we distinguish the case with MHD-activity in the form of short spikes and the case of MHD-free plateau phase. One aim of the investigations by the synchrotron imaging is to find special "structures" in the runaway beam which are responsible for the MHD-spikes. As a result, a channel between the runaway beam and the probe head is identified. However, MHD activity is also present although the probe is not applied and no channel is detected. The loss is best described as a diffusive loss.

Without MHD activity, the loss is again best described as a diffusive process. However, by a special synchrotron image subtraction method we find stripe-structures which resemble the laminar zone of an open ergodic system. The observed stripes in the subtracted IR-pictures may result from the rotation of the mixed topological structure of the stochastic layer created by the resonant interactions of high energy RE orbits with the $m/n = 1/1$ helical magnetic perturbation.

The observation of the laminar pattern leads to the development of a model, which explains many of the observed features: During the energy quench, low m/n modes are created including $m/n = 1/1$ and $m/n = 5/4$ (or4/3..). The REs generated in the large islands of those modes survive; this model explains the size of the runaway column of roughly half of the predisruptive plasma size, the diffusive loss of the runaways, the current decay rate of the plasma current and also the development of the MHD spikes as an interaction of the runaways with the background modes.

ACKNOWLEDGEMENTS

This work was supported by the Royal Thai Government, a Jülich R&D contract, the Trilateral Euregio Cluster (TEC), and the DFG program GRK 1203.

The authors would like to thank Dr. H.R. Koslowski, M. Forster, M. Rack, Dr. O. Schmitz and the TEXTOR team for their support.

[1] J.R. Martiín-Solís, B. Esposito, R. Sánchez, and J.D. Alvarez, Phys. Plasmas **6**, 238 (1999).
[2] G. Papp, M. Drevlak, T. Fülöp, P. Helander and G.I. Pokol, Plasma Phys. Control. Fusion **53**, 095004 (2011).
[3] R.D. Gill, B. Alper, M. de Baar, T.C. Hender, M.F. Johnson, V. Riccardo and contributors to the EFDA-JET Workprogramme Nucl. Fusion **42**, 1039 (2002).
[4] M. Lehnen, S.S. Abdullaev, G. Arnoux, S.A. Bozhenkov, M.W. Jakubowski, R. Jaspers, V.V. Plyusnin, V. Riccardo, U. Samm, JET EFDA Contributors and The TEXTOR Team, Nucl. Fusion **36**, 367 (1996). J. Nucl. Mater. **390391**, 740 (2009).
[5] T. Kudyakov, S.S. Abdullaev, S.A. Bozhenkov, K.H. Finken, M.W. Jakubowski, M. Lehnen, G. Sewell, O. Willi, Y. Xu and the TEXTOR team Nuclear Fusion **52**, 023025 (2012).
[6] R. Yoshino, S. Takuda Nuclear Fusion **40**, 1293 (2000).
[7] V.A. Izzo, D.A. Humphreys and M. Kornbluth, Plasma Phys. Control. Fusion **54**, 095002 (2012).
[8] M. Forster, K. H. Finken, T. Kudyakov, M. Lehnen, O. Willi, Y. Xu, L. Zeng and the TEXTOR Team, Phys. Plasmas **19**, 092513 (2012).
[9] K.H. Finken, J.G. Watkins, D. Rusbüldt, W.J. Corbett, K.H. Dippel, D.M. Goebel and R.A. Moyer, Nucl. Fusion **30**, 859 (1990).
[10] T. Kudyakov, A. Jochmann, K. Zeil, S. Kraft, K.H. Finken, U. Schramm and O. Willi, Rev. Sci. Instrum, **80**, 076106 (2009).
[11] S.A. Bozhenkov, M. Lehnen, K.H. Finken, M.W. Jakubowski, R. C. Wolf, R. Jaspers, M. Kantor, O.V. Marchuk, E. Uzgel, G. Van Wassenhove, O. Zimmermann, D. Reiter and the TEXTOR team, Plasma Phys. Control. Fusion **50**, 105007 (2008).
[12] M. Lehnen, S.A. Bozhenkov, S.S. Abdullaev and M. W. Jakubowski, Phys. Rev. Lett. **100**, 255003 (2008).
[13] A. Savtchkov, K.H. Finken and G. Mank, Rev. Sci. Instrum **73**, 3490 (2002).
[14] K.H. Finken, S.S. Abdullaev, M. Jakubowski, R. Jaspers, M. Lehnen and O. Zimmermann, Nucl. Fusion **46**, S139 (2006).
[15] S.S. Abdullaev, *Magnetic stochasticity in magnetically confined fusion plasmas*, (Springer, Cham, 2014).
[16] S.S. Abdullaev, K.H. Finken, K. Wongrach, M. Tokar, H.R. Koslowski, O. Willi, L.Zeng and the TEXTOR team Phys. Plasmas **22**, 040704 (2015).
[17] S.S. Abdullaev, K.H. Finken, K. Wongrach, M. Tokar, H.R. Koslowski, O. Willi, L.Zeng and the TEXTOR team, J. Plasma Phys. **81**, 475810501 (2015).
[18] X. Guan, H. Qin, and N. Fisch, Phys. Plasmas **17**, 092502 (2010).
[19] S.S. Abdullaev, Phys. Plasmas, **22**, 030702 (2015).
[20] J.R. Myra and P. J. Catto, Phys. Fluids B, **4**, 176 (1992).

Declaration of Academic Honesty (Eidesstattliche Versicherung)

Ich versichere an Eides statt, dass die Dissertation von mir selbständig und ohne unzulässige fremde Hilfe unter Beachtung der "Grundsätze zur Sicherung guter wissenschaftlicher Praxis an der Heinrich-Heine-Universität Düsseldorf" erstellt worden ist.

Die Dissertation wurde in der vorgelegten oder in ähnlicher Form noch bei keiner anderen Institution eingereicht. Ich habe bisher keinen erfolglosen Promotionsversuch unternommen.

(Datum) (Unterschrift)